Nonlinear information processing in early vestibular pathways

Adam David Schneider

Doctor of Philosophy

Department of Physics

McGill University

Montréal, Québec

May 2016

A thesis submitted to McGill University in partial fulfilment of the requirements of the degree of Doctor of Philosophy

DEDICATION

This thesis is dedicated to all the friends and family who have supported me along the way. You know who you are.

ACKNOWLEDGEMENTS

Firstly I am eternally thankful that Dr. Maurice Chacron and Dr. Kathleen Cullen were in the unique position to allow me to study computational neuroscience while pursuing a PhD in physics. I would also like to thank the Fonds de Recherche Nature et Technoligies (FQRNT) and the Centre for Applied Math in Bioscience and Medicine (CAMBAM) for providing me with some funding to carry out my research.

A special thanks goes to Dr. Corentin Massot for collecting such high quality data for me to analyze, as well as my colleagues and co-authors Dr. Jerome Carriot and Dr. Mohsen Jamali; I could have never survived without their continuous support, feedback and discussions. Further thanks go to my numerous colleagues and lab mates and all for useful discussions over the years: Dr. Soroush Sadeghi, Diana Mitchell, Alexis Paez, Amy Wong, Dr. Isabelle Mackrous, Dr. Guillaume Ducharme, Dr. Oscar Avila Akerberg, Dr. Jens Kroeger, Dr. Tara Deemyad, Dr. Navid Khosravi, Dr. Katrin Vonderschen, Melissa Savard, Michael Sproule, Dr. Michael Metzen, Greg Stacey, Ashkan Golzar and Fred Simard. And of course to the excellent technicians Walter Kucharski and Steve Nuara. I would also like to thank Dr. Michael Guevara for the critical feedback on my final chapter, and Dr. Erik Cook for the continuing support and encouragement to finish this thesis.

I would especially like to thank my parents for always supporting me unconditionally during this perilous journey.

ABSTRACT

We study nonlinear sensory information processing in the peripheral vestibular system. As the vestibular system is one of the oldest and most evolutionarily conserved sensory systems in the animal kingdom, we explore the idea that the system is optimized for the natural sensory environment to which an animal is exposed. We record the natural head movements of free moving monkeys, as well as characterize the linear-nonlinear transformations performed by vestibular afferents, with previously recorded afferent data. Using information theoretic techniques, we calculate how well different classes of vestibular afferents are optimized for the statistics of natural stimuli. We also consider the constraints of energy consumption and functional goals on the optimal coding strategy used. Additionally, we consider effects of nonlinear processing in the first stage within the brain, the vestibular nuclei (VN). Both afferents and VN neurons are explicitly tested for nonlinear effects other than the expected saturation and rectification, through the use of stimuli with combined frequencies. A boosting nonlinearity was found in VN neurons but not afferents, which was shown to explain the results for combined frequency stimulation. We adapt an in vitro model of VN neurons, and find that they can produce linear rate coding due to the high conductance state of neurons in vivo. Furthermore, it can also produce a boosting nonlinearity for certain combinations of parameters. Finally, we simplify the neuron model to a generalized quadratic integrate-and-fire model in order to find an analytic equation for the input-output nonlinearity found both experimentally in neurons, as well as theoretically in model VN neurons.

ABRÉGÉ

Nous avons étudié le traitement des informations sensorielles nonlinaires au niveau du système vestibulaire périphérique. Comme le système vestibulaire est l'un des plus vieux systèmes et l'un des mieux conservé dans le royaume animal, nous explorons l'idée que ce système est optimisé pour l'environnement sensoriel dans lequel l'animal évolue. Nous avons enregistré les mouvements naturels de la tête chez un singe se déplaçant librement. Nous avons aussi caractérisé les transformations linéaires et non linéaires effectuées par les afférents vestibulaires grâce aux données enregistrées précédemment. Grâce aux techniques de la théorie de l'information, nous avons calculé comment les différentes classes d'afférents vestibulaires sont optimisées pour les statistiques des stimuli naturels. Nous avons aussi considéré les contraintes de consommation d'énergie et le but fonctionnel des stratégies de codage. De plus, nous avons considéré les effets des processus nonlinéaires au premier niveau central et au niveau du noyau vestibulaire (VN). Les afférents et les neurones centraux sont testés explicitement pour les effets nonlinéaires, autre que la saturation et la rectification attendues, par l'utilisation de stimuli avec des fréquences combinées. Une augmentation de la non linéarité a été trouvée pour les neurones centraux, mais pas pour les afférents. Cette observation peut expliquer les résultats obtenus pendant les stimulations avec des fréquences combinées. Pour les neurones centraux, nous avons adapté un modèle in vitro et nous avons trouvé que nous pouvions produire un codage par fréquence de décharge dû à l'état de haute conductance des neurones in vivo. De plus, le modèle peut aussi produire une augmentation de la non linéarité pour

certaines combinaisons de paramètres. Finalement, nous avons simplifié le modèle de neurones pour un “integrate-and-fire” quadratique général dans le but d’etablir une équation analytique pour l’entrée-sortie nonlinéaire trouvée expérimentalement et théoriquement avec le modèle.

AUTHOR CONTRIBUTIONS

In **Chapter 2** the following publication is presented: ***Schneider, AD****, Jamali, M, Carriot, J, Chacron, MJ, Cullen, KE, The Increased Sensitivity of Irregular Canal and Otolith Afferents Optimizes their Encoding of Natural Stimuli. Journal of Neuroscience Vol. 35 (14) pp. 5522-5536 (2015).* Afferent data used in this study was previously collected by Dr. Soroush Sadeghi (canals) and Dr. Mohsen Jamali (otoliths) for other purposes. Natural head movement data was collected by ADS, JC, MJ and animal technician Steve Nuara: The animals were handled by JC, MJ, and SN, while different behavioural activities were filmed by ADS. All subsequent analysis of natural head movement data, as well as afferent data analysis and information theoretic calculations were carried out by ADS (Although MJ also performed data analysis on the otolith afferents he recorded, the analysis used in this paper was carried out by ADS). Some analysis justifying experimental stimuli used as "naturalistic" in response to reviewers was done by MJ and JC. All figures were made by ADS, except with Figure 2.4C&D, and some changes for reviewers to Figure 2.1 made by MJ and JC. All monkey images (i.e. Figure 2.4B and 2.1A) were made by JC. All authors contributed to the writing of this manuscript.

In **Chapter 3** the following publication is presented: ***Schneider, AD****, Cullen, KE, Chacron, MJ, In Vivo Conditions Induce Faithful Encoding of Stimuli by Reducing Nonlinear Synchronization in Vestibular Sensory Neurons. PLoS Computational Biology Vol. 7 (7), e1002120 (2011).* All research for this paper was carried out by

ADS under the guidance of KEC and MJC, and all authors contributed to its writing.

Chapter 4 - In this chapter the following paper is presented: ***Schneider, AD****, Model Vestibular Nuclei Neurons can Exhibit a Boosting Nonlinearity due to an Adaptation Current Regulated by Spike-Triggered Calcium and Calcium-Activated Potassium Channels. PLoS One (in press), DOI:10.1371/journal.pone.0159300.* All research involved in this paper was done by ADS.

In **Appendices A-D**, additional data analysis and information theoretic calculations pertaining to the material in chapter 2 (performed by ADS) is presented.

In **Appendix E** the following publication is presented: *Massot, C,* ***Schneider, AD****, Chacron, MJ, Cullen, KE, The Vestibular System Implements a Linear-Nonlinear Transformation in Order to Encode Self-Motion. PLoS Biology Vol. 10 (7), e1001365 (2012).* The experiment in this paper was designed by MJC and KEC, carried out and analyzed by CM under their supervision. A model, explanation, and manuscript were written and submitted, but it was not accepted in that form. A new model was then proposed by ADS, who re-analyzed the data to validate and fit the new model, according to Equations E.7, E.16, and E.17. The model and theory were conceptually developed by ADS and MJC, with the formalization of Equations E.8-E.15 done by MJC. CM contributed Figures E.1-4 and E.S1-4, while MCJ made Figure E.5 ADS contributed Figures E.6, E.7 and E.S5-8, and contributed to editing Figures E.3B-E and E.4. While CM and ADS analyzed the data in their own Figures, both also did each others analysis independently as confirmation. CM was the first to perform the SR-coherence and gain analysis, while ADS was the first to perform the

input-output nonlinearity and LN model analysis. The text was originally written by KEC, MJC, and CM, with contributions of ADS pertaining to figures he created. In **Appendix F** to this chapter contains additional analysis done by ADS, on this dataset collected by CM for Appendix E, to further investigate the relationship between nonlinear and temporal coding.

TABLE OF CONTENTS

DEDICATION ii

ACKNOWLEDGEMENTS iii

ABSTRACT iv

ABRÉGÉ v

AUTHOR CONTRIBUTIONS vii

LIST OF TABLES xvi

LIST OF FIGURES xvii

1 General Introduction: Background & Methods 1

1.1 Sensory-Motor Systems 1
1.1.1 Cracking the neural code 1
1.1.2 Optimal coding: A general principle of neuroscience? 4
1.2 The Vestibular System 7
1.2.1 Peripheral Sensors: Hair cells & afferents 9
1.2.2 Central pathways: The vestibular nuclei 13
1.3 Methods of Analysis 17
1.3.1 Firing rate estimation 18
1.3.2 Traditional linear-nonlinear systems identification 19
1.3.3 Information Theory 24
1.4 Methods of Neuron Modelling 29
1.4.1 Biophysically detailed models 29
1.4.2 Phenomenological models 36
1.4.3 Vestibular neuron models 38
1.5 Research Goals and Thesis Outline 40

2 The increased sensitivity of irregular peripheral canal and otolith afferents optimizes their encoding of natural stimuli 43

2.1 Introduction . . . 46
2.2 Materials & Methods . . . 47
2.2.1 Experimental Preparation . . . 47
2.2.2 Head movement recording . . . 48
2.2.3 Single-unit recording . . . 49
2.2.4 Statistical analysis of natural head movements . . . 52
2.2.5 Linear models of vestibular afferent responses . . . 52
2.2.6 Linear-nonlinear cascade models. . . . 54
2.2.7 Optimal stimulus distribution that maximizes information . 55
2.2.8 Quantifying the distance between probability distributions 57
2.3 Results . . . 57
2.3.1 Statistics of natural vestibular stimuli . . . 57
2.3.2 Traditional linear models of vestibular processing cannot accurately predict responses to natural stimuli . . . 61
2.3.3 Building LN models of peripheral vestibular afferent responses to naturalistic stimuli . . . 66
2.3.4 Neural heterogeneities in tuning and in trial-to-trial variability influence optimal coding . . . 72
2.3.5 Irregular afferents are better optimized to code for natural stimuli than regular afferents . . . 77
2.4 Discussion . . . 80
2.4.1 Summary of Results . . . 80
2.4.2 Irregular afferents are better optimized to process natural stimuli . . . 81
2.4.3 Nature of the neural code used by the vestibular system to transmit information about natural stimuli . . . 82
2.4.4 Role of variability in neural coding . . . 83
2.4.5 Coding natural stimuli by otolith versus semicircular canal afferent populations . . . 83
2.4.6 Implications for higher order processing of natural vestibular stimuli . . . 84

3 *In vivo* conditions induce faithful encoding of stimuli by reducing nonlinear synchronization in vestibular sensory neurons . . . 86

3.1 Introduction . . . 87
3.2 Results . . . 89
3.2.1 Intrinsic membrane conductances give rise to damped membrane potential oscillations in the presence of perturbations 91

3.2.2 Membrane potential oscillations induce a resonance in the spiking activity. 96
3.2.3 Increasing variability promotes faithful encoding of the stimulus time course through changes in firing rate . . . 100
3.3 Discussion 112
3.3.1 Summary of results 112
3.3.2 Correspondence between anatomy and function in VN . . . 114
3.3.3 Sources of variability in VN 117
3.3.4 Differences between *in vivo* and *in vitro* conditions in VN neuronal activity 118
3.3.5 Stochastic resonance in VN neurons promotes linear coding: functional consequences 121
3.4 Methods 122
3.4.1 Measures 126
3.4.2 Linearized Model 129
3.5 Supporting Information 130

4 Model vestibular nuclei neurons can exhibit a boosting nonlinearity due to an adaptation current regulated by spike-triggered calcium and calcium-activated potassium channels 135

4.1 Introduction 136
4.2 Results 138
4.2.1 HH model produces boosting nonlinearity with AHP and bifurcation through bursting separating low and high gain regions. 138
4.2.2 QIF reduction of HH model can preserve subthreshold bifurcation structure, boosting nonlinearity, and bifurcation through bursting. 142
4.2.3 Does boosting require bursting? 146
4.2.4 Analytic firing rate and gain curves for the QIF model, with fixed gating variable reset. 150
4.2.5 Theoretical firing rate for the QIF model with spike generated resets: convergent iterative predictions 159
4.3 Conclusions 165
4.3.1 Comparison to other two- and three-variable adaptive models. 166
4.3.2 Correspondence to vestibular nuclei neuron data. 168
4.3.3 Implications for sensory information processing in the vestibular system. 169

4.4 Models and Methods . . . 171
4.4.1 Full HH model . . . 171
4.4.2 Simplified QIF model . . . 174
4.4.3 Slow gating variable approximation for fixed reset conditions. 177
4.4.4 Iterative Theoretical Predictions: Stable and Unstable Limit Cycles . . . 183

5 Conclusions . . . 186

5.1 Summary of Results . . . 186
5.1.1 Irregular afferents are more optimized for the statistics of natural vestibular stimuli than regular afferents . . . 186
5.1.2 High conductance state of neurons *in vivo* explains differences in behaviour observed *in vitro* . . . 187
5.1.3 VO model neuron exhibits boosting nonlinearity due to spike-triggered adaptation current governed by calcium and calcium-activated potassium channels . . . 188
5.2 Optimal Coding in the Vestibular System . . . 189
5.2.1 Statistical Structure of Natural Stimuli . . . 189
5.2.2 Maximizing Mutual Information or Minimizing Energy Consumption . . . 189
5.2.3 Dynamic Stimuli and the Mutual Information Rate . . . 191
5.2.4 Functional Constraints: Active versus Passive stimuli . . . 192
5.3 Coexistence of Rate and Temporal Coding in the Vestibular system 194
5.3.1 Advantage of a Boosting Nonlinearity . . . 194
5.3.2 Role of Variability . . . 194
5.3.3 Single Neuron versus Population Coding . . . 195
5.4 Future Directions . . . 196

A Sigmoidal and exponential f-I curve fitting. . . . 199

B Derivation of the optimal stimulus distribution, with and without constraints, in the low noise limit. . . . 203

B.1 The Cramer-Rao Bound . . . 203
B.2 Relationship between Fisher and Mutual Information . . . 204
B.3 Calculating Fisher Information . . . 205
B.4 Information Maximization: The Optimal Stimulus Distribution . . 206
B.5 Entropy Maximization with Constraints . . . 208

C Optimal stimulus distribution in the high noise limit: Blahut-Arimoto algorithm . . . 214

D Frequency Content of Natural Stimuli and Whitening . . . 219

E The Vestibular System Implements a Linear-Nonlinear Transformation In Order to Encode Self-Motion . . . 226

E.1 Introduction . . . 227
E.2 Results . . . 229
E.2.1 Central Vestibular Neurons Respond Nonlinearly to Self-Motion . . . 229
E.2.2 Peripheral Vestibular Afferents Respond Linearly to Sums of Low and High Frequency Motion . . . 234
E.2.3 Central Vestibular Neurons Display Nonlinear Responses to High Frequency But Not Low Frequency Head Rotations When These Are Applied in Isolation . . . 235
E.2.4 The Greater Afferent Firing Rate Modulations Elicited by High Frequency Stimuli Elicit Nonlinear Responses in Central Vestibular Neurons . . . 240
E.2.5 Modeling and Predicting Central Vestibular Neuron Responses to Sums of Arbitrary Stimuli . . . 246
E.2.6 A Linear-Nonlinear Cascade Model Verifies That Central Vestibular Neurons Display a Static Boosting Nonlinearity 250
E.2.7 How Does a Static Boosting Nonlinearity Give Rise to Suppressed Response to Low Frequency Stimuli in the Presence of High Frequency Stimuli? . . . 252
E.3 Discussion . . . 258
E.3.1 Summary of Results . . . 258
E.3.2 Origins of the Nonlinear Processing in Early Vestibular Pathways . . . 259
E.3.3 Consequences of Nonlinear Central Vestibular Processing for Higher Vestibular Pathways and Perception . . . 261
E.3.4 The Emergence of Feature Extraction: Function and General Principles Across Systems . . . 264
E.4 Materials & Methods . . . 266
E.4.1 Data Acquisition . . . 267
E.4.2 Experimental Design . . . 267
E.4.3 Traditional Linear System Analysis . . . 268

E.4.4 Coherence Measures 269
E.4.5 Stationarity 270
E.4.6 Normalization 270
E.4.7 Attenuation 270
E.4.8 Input-Output Relationships 271
E.4.9 Rescaled Input-Output Relationships 271
E.4.10 Model 273
E.4.11 Linear Nonlinear Cascade Model 276
E.4.12 Statistics 277
E.5 Supporting Information 277
E.6 Author Contributions 289

F Coherence and spike timing jitter analysis reveal potential for temporally encoded information that cannot be decoded linearly. 291

References 300

LIST OF TABLES

Table page

2.1 Averaged mean, SD, and kurtosis values of natural movements during low, medium, high, and all levels of activity 64

LIST OF FIGURES

Figure		page
1.1	Vestibular Anatomy.	8
1.2	Peripheral vestibular neuron properties.	12
1.3	Schematic summarizing optimal linear filters for stimulus and response estimation.	23
1.4	Fixed point bifurcation analysis of two-dimensional spiking neuron model.	34
2.1	Statistics of natural vestibular stimuli in nonhuman primates.	59
2.3	Traditional linear models cannot accurately predict vestibular afferent responses to natural stimuli.	62
2.2	Natural vestibular stimulus statistics during low-, medium-, and high-activity behaviors.	63
2.4	LN models can correctly predict vestibular afferent responses to naturalistic stimuli.	69
2.5	Regular and irregular canal and otolith afferents are well described by LN models.	71
2.6	Hypothetical effects of neural heterogeneities in tuning and in trial-to-trial variability on optimal coding.	73
2.7	Effects of experimentally measured trial-to-trial variability on information transmission.	76
2.8	Irregular afferents are better optimized to code for natural stimuli than regular afferents.	79
3.1	Vestibular anatomy and model description.	90

3.2 The model displays damped membrane potential oscillations in response to step current input. 93

3.3 Effects of increased leak conductance on membrane potential oscillations. 95

3.4 Membrane potential responses to zap current input are greatest for a given frequency. 97

3.5 Spiking responses to zap current input display a resonance. 99

3.6 Synchronization to sinusoidal input and its consequences on faithful encoding of this input through changes in firing rate. 102

3.7 Effects of the bias current and noise intensity on resting discharge rate and variability, and resonance strength and frequency. 105

3.8 Effects of low intensity noise on synchronization to sinusoidal input and its consequences on faithful encoding of this input through changes in firing rate. 107

3.9 Effects of high intensity noise on synchronization to sinusoidal input and its consequences on faithful encoding of this input through changes in firing rate. 109

3.10 Effects of varying noise intensity on the VAF and PLI. 112

3.S1 Effects of increased persistent sodium conductance on membrane potential oscillations. 131

3.S2 The linearized model's response to step input agrees quantitatively with that of the full model. 132

3.S3 A nonlinearity index (NI) gives qualitatively similar results to those obtained with the PLI measure. 133

3.S4 Synchronization to sinusoidal conductance input and the effects of noise. 134

4.1 Calium and calcium-activated potassium currents induce boosting nonlinearity, AHP, and bifurcation through bursting. 140

4.2 Reduced QIF model captures subthreshold bifurcation structure, boosting nonlinearity, and bursting bifurcation of HH model. 144

4.3 Boosting nonlinearity and bursting depend on reset boundary conditions, not only subthreshold bifurcation structure. 148

4.4 WV phase space projection of trajectories at low and high gain μ values, for QIF with $X_r = 0.1$ and $C_r = C_\infty(V_r, X_r)$ 152

4.5 Steady state firing rate, simulations and theory: QIF with $X_{reset} = 0.1$ and $C_{reset} = C_\infty(V_{reset}, X_{reset})$. 155

4.6 f-I curve gain, simulations and theory: QIF with $X_{reset} = 0.1$ and $C_{reset} = C_\infty(V_{reset}, X_{reset})$. 157

4.7 Comparison between results from the full theoretical and approximate gain equations. 158

4.8 WV phase space projection for QIF model with spike waveform, and convergent iterative theoretical predictions for $\mu > \mu^*$ and $\mu \to 0$. . 161

4.9 Iterative theoretical predictions for QIF model with spike waveform: stable and unstable 1-spike limit cycles. 164

A.1 Sigmoidal versus exponential f-I curve fitting. 201

B.1 Vestibular afferents and natural stimulus statistics are more consistent with *constrained* optimal coding. 212

C.1 Optimal stimulus distribution in the high noise limit: Blahut-Arimoto algorithm. 218

D.1 Linear head accelerations obey a power law, while angular head velocity does not. 224

D.2 Irregular afferent transfer functions whiten frequency spectra more than regular, consistent with their being *more* optimal. 225

E.1 Central vestibular neurons respond nonlinearly to sums of noise stimuli. 232

E.2 Afferents respond linearly to sums of noise stimuli. 236

E.3 Central vestibular neurons but not afferents display a nonlinear relationship between output firing rate and input head velocity. . . 238

E.4 Central neurons display a static nonlinear relationship between their output firing rate and their afferent input. 244

E.5 A simple model accurately predicts nonlinear central VO neuron responses to sums of low and high frequency stimuli. 248

E.6 A linear-nonlinear (LN) cascade model reveals that central vestibular neurons respond nonlinearly to broadband noise stimulation. 255

E.7 Schematic showing how a nonlinear static relationship between input and output can lead to attenuated sensitivity to sums of low and high frequency stimuli. 256

E.S1 Central VO neurons but not afferents respond nonlinearly to sums of low and high frequency noise stimuli as quantified by coherence measures. 278

E.S2 Central vestibular neurons respond nonlinearly to sums of sinusoidal stimuli. 279

E.S3 Analysis of unfiltered spike trains confirms that central vestibular neurons respond nonlinearly to sums of sinusoidal stimuli. 281

E.S4 Central VO neurons as well as afferents do not show rectification and/or saturation when stimulated by the low and high frequency head rotations used in this study. 282

E.S5 Afferents display a linear relationship between output firing rate and input head velocity. 284

E.S6 Individual central neurons display nonlinear responses. 286

E.S7 Characterization of central VO neurons and afferents by LN cascade models. 287

E.S8 LN analysis reveals that central vestibular neurons but not afferents display a static nonlinearity in response to different self-motion stimuli. 289

F.1 Stimuli which elicit nonlinear range of FI curve of VO neurons, results in information which can not be linearly decoded. 296

F.2 Spike timing jitter analysis reveals nature of temporally encoded information. 298

CHAPTER 1
General Introduction: Background & Methods

1.1 Sensory-Motor Systems

For an organism to survive in a dynamic, competitive environment with limited resources, it should have a sensory system to collect information about its environment, and a motor system to move within its environment. To this end, sensory information must first be detected by the peripheral sensors, and subsequently processed through the nervous system's networks of neurons, before driving the appropriate motor outputs. An important question is thus, what information is represented by various populations of neural activity, and how? Furthermore, how are these representations transformed from one brain region to the next? This is generally referred to as "the neural code", although it is of course thought to have emerged naturally rather than by intelligent design.

1.1.1 Cracking the neural code

While it had been known since the 1700s that electricity could cause a frogs legs to twitch, it was not until the works of Lord Adrian starting in 1926 [1–4] that the foundations of the neural code would be laid [5]. The first and primary assumption of the neural code is that neurons communicate primarily via action potentials, or spikes in their membrane voltage, which are stereotyped all-or-none events. Although different types of neurons can exhibit action potentials with different shapes, within one type they generally do not. The second principle of the neural code

is that increases/decreases in the strength of some static stimulus input results in increases/decreases in the neurons rate of spiking output. This is a fundamental concept of sensory information processing known as *rate coding*, in which only the number of spikes occurring in a time window carries information about the stimulus. A competing possibility is in turn the concept of *temporal coding* [6], in which it is the precise timing of the spike patterns within the time window that carries information. One difficulty in distinguishing rate and temporal codes lies in the size of the windows used to count the spikes, a point we will come back to.

Understanding how stimulus information is represented by a neural responses can further be separated into two components: *encoding* and *decoding*. First of all sensory neurons at the periphery receive a stimulus input and generate a spiking response, into which some stimulus information is *encoded*. However, even if information has been encoded into a spike train, it is only useful if that information can be *decoded* by downstream neurons. An experimenter can present a stimulus for many seconds and count the number of resulting spikes over the entire time period, and estimate the stimulus. However, a downstream neuron's response is generally only sensitive to shorter time windows on the order of tens to hundreds of milliseconds. As a result, the output spike rate should be considered to change, on a similar timescale. A continuous firing rate can then be defined by counting the spikes in a small window that slides across the spike train in time, however a smoother estimate is generally made by convolving the spike train with a Gaussian shaped window defined by its width.

For a neuron to transform a constant (i.e. in time) current input into an oscillating membrane voltage, a *nonlinear* system of differential equations is needed (see section 1.4). However, once the spiking membrane voltage is converted into a continuous firing rate (i.e. threshold spikes and convolve with Gaussian filter; see section 1.3), it is often possible to find a *linear* filter that can be convolved with the stimulus input time-series to produce the firing rate output time-series, known as a *transfer function* (see section 1.3). In this case, a related *linear* filter can also be used to estimate the stimulus input time-series from convolution with the output spike train time-series, known as the *optimal reconstruction filter* (see section 1.3). If such linear filters can predict well the stimulus from the spike train response (i.e. with minimal squared difference between the stimulus and its estimate), as well as the firing rate from the stimulus, a rate code is generally said to be in use. If there is additional information in the spike trains that cannot be decoded by such linear filters, this can be indicative of a temporal code that can be assessed using a stimulus-response coherence technique that will be discussed in the section 1.3.

To further complicate things, neurons generally behave stochastically, responding differently to repeated presentations of the same stimulus, likely using a combination of both linear and nonlinear rate and temporal codes. Furthermore information can be distributed over populations of neurons that can be difficult to record from simultaneously. While this might seem to make things hopeless, we will review some basic signal processing techniques that are commonly used in computational neuroscience (and will be used in this thesis) in the Introductory Methods section. Although these are useful in identifying and describing what type of code may be

used, we also seek an underlying and unifying principle of neuroscience to explain why different codes appear in different regions.

1.1.2 Optimal coding: A general principle of neuroscience?

After describing the way in which neurons transform their stimulus inputs into response outputs, the big picture question is *why* do neurons behave in the way that they do. This includes both the underlying cellular mechanisms that endow a neuron with its particular behaviour, as well as the functional role these properties play in the organisms ultimate goal of survival. A goal of neuroscience is therefore to find a general principle that can universally explain why the types of codes found across different sensory modalities are there. An analogy to Newton's Laws could be the observation of different types of planetary orbits, and explaining them as different solutions to the same differential equation. Similarly, as the equations of motion come from the principle of least action [7], one might expect the neuronal dynamics of sensory systems to be the result of optimizing something, such as sensory information.

To this end, information theory has recently been applied to quantify the precise amount of information a neuron's response contains about the stimulus by which it was elicited, with the universal units of bits (or bits/sec) (described in detail in the Intro Methods). The equation defining the information transmitted by a neuron depends on both the properties of the neuronal transformation, as well as the *statistics of the stimulus* being applied. This has lead to the proposal of the principle of optimal (or efficient) coding [8], suggesting that the neuronal properties have evolved to maximize the information transmitted about the *natural sensory*

environment to which an organism is exposed. For single neurons this can amount to having a neural transformation that ensures all available responses are being used equally [9–11], or that successive action potentials contain independent information from one another (i.e. reduce redundancy) [12]. At the population level, however, redundancy reduction is achieved by each neuron encoding independent features of a stimulus [13, 14]. More recently, however, a positive role for redundancy has been considered [15], along with the role of behavioural constraints such as energy consumption [16].

The action potentials by which neurons generally communicate, do in fact cost a neuron some metabolic energy to generate [17]. This can result in a trade off, where neurons can transmit more information, at the cost of using more spikes per second and in turn more energy. This leads to the hypothesis that neurons maximize information transmission while keeping the output firing rate at a fixed mean, or energy consumption rate, for which there has been some evidence in cortex [18]. In general, it has been observed that sensory neurons at the periphery tend to have higher firing rates and population redundancy, while through subsequent stages of processing mean firing rates and population redundancy are reduced, as sensory information is distributed and integrated more efficiently across populations in cortex.

While it is clear that the characteristics of the neural transforms are essential to understanding the neural code, what is often overlooked is the statistical structure of of the natural stimulus environment in which the organism has evolved. Rieke et al. [12] give a nice summary of how temporal and spatial correlations in natural auditory and visual scenes exhibit power law scaling in their frequency content.

While the origins of this statistical structure is very interesting, the optimal neural transformations for processing them are perhaps more relevant. Rieke et al. [12] go on to explain how a high-pass "whitening" filter maximizes information by decorrelation, maximizing response entropy, while combination with a low pass filter can additionally reduce noise entropy due to high frequencies where the noise variance exceeds the signal variance. However, the stimulus is not uniquely characterized by its power spectrum, also requiring a probability distribution of the values from which it comes. In many cases such distributions can approach Gaussian, as might be expected from some form of the central limit theorem. The contrast distributions of natural images, however, were found to have heavy tails which can decay exponentially [19]. Interestingly, natural images with whitened power spectra maintain much of their perceived structure, compared to synthetic images with natural power law spectra but pixels drawn from Gaussian contrast distributions. This suggests that some stimulus statistics are more relevant to perception/behaviour than others.

While considerable support for the efficient coding of sensory information has been found [5, 12, 20–22], it does not address what the information might be used for, if at all. For example, the auditory environment in the jungle includes a mixture of a variety of different animals with different vocalizations. Yet animals have been found to be adapted to specific subsets of behaviourally relevant sounds, such as predators or potential mates [23]. Furthermore, predator sounds may best trigger an escape response requiring just enough information to identify the stimulus and generate the required reflex. While a mating call, on the other hand, may need to be analyzed in more detail to assess the quality of the mate, requiring more

stimulus information. These examples illustrate how the behavioural and functional constraints of the system can also be relevant to the sensory coding strategies in use [24]. In this thesis we will consider all of these aspects of information processing in one of the oldest (yet commonly unknown) sensory systems: The vestibular system.

1.2 The Vestibular System

The vestibular system is one of the oldest and most evolutionarily conserved sensory systems, detecting head movements used to maintain stable gaze, posture and spatial orientation [25]. It comprises three semicircular canals that sense angular velocity, and two otolith organs that sense linear acceleration, via hair cells synapsed onto afferent neurons. These afferent neurons (in the VIIIth nerve) project to the vestibular nuclei (VN), located in the brainstem, the first central stage of vestibular processing within the brain. The VN house a variety of cell types, project outputs to a range of areas (see Figure 1.1A) including spinal cord (for postural reflexes), cerebellum (for fine reflex calibration), and cortex (spatial orientation perception), but it also receive massive amounts of feedback from these regions as well [26]. Different network connections (i.e. neural circuitry) serve different functional roles driving different behavioural responses. In addition to network effects, each single neuron is a complex nonlinear dynamical system of interacting ion channels, various combinations of which can lead to very different response properties, potentially serving a variety of functional roles [27]. In this thesis, we focus primarily on the peripheral vestibular afferents and central vestibular nuclei neurons.

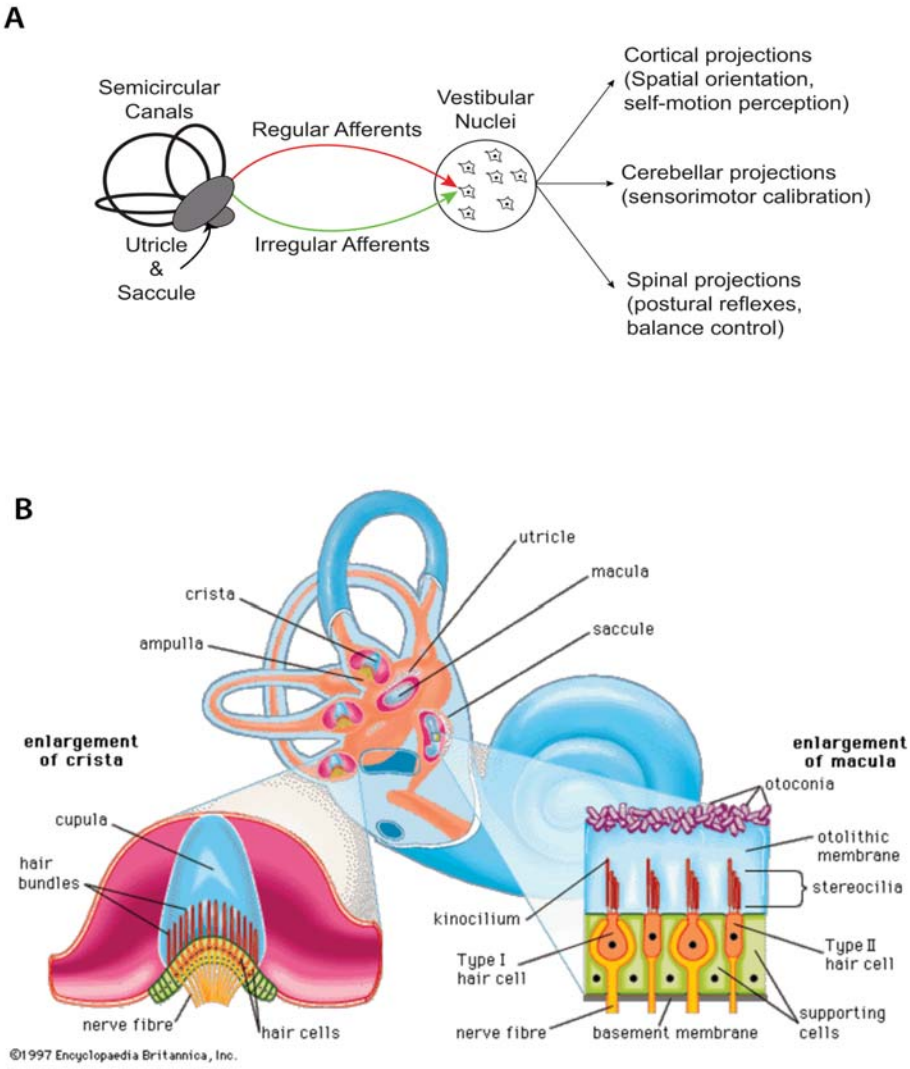

Figure 1.1. Vestibular Anatomy. A) Schematic of basic vestibular periphery, with connectivity relevant to this thesis. B) Detailed anatomy of vestibular sensors with otolith and semicircular canals and hair cells. (Image from online Encyclopedia Britannica)

1.2.1 Peripheral Sensors: Hair cells & afferents

Anatomy

Head motion is detected by two types of sensory organs, the semicircular canals and the otoliths. There are two types of otolith organs, the utricle and the saccule, which sense *linear acceleration* in the horizontal and vertical planes, respectively [28]. Each organ consists of a layer of hair cells (see Figure 1.1B), the cilia of which extend into a gelatinous layer containing small calcium carbonate crystals known as otoconia [29]. During linear acceleration, the hair cells move before the crystals due to their increased inertia. This results in a bending of the cilia which cause K+ channels to open or close (depending on the direction of bending), leading to either an increase (termed depolarization) or decrease (termed hyperpolarization) of the membrane potential of the hair cell. The combination of the utricle and saccule provide a 3-dimensional representation of linear acceleration, which, it should be noted, includes the direction and magnitude of *gravity* [30, 31].

The semicircular canals, on the other hand, sense *angular velocity* [32]. There are three canals oriented nearly orthogonally to one another, located in the inner ear on both sides of the brain. One plane is oriented (very nearly) horizontally and is sensitive to rotations in the yaw plane (i.e. about earth vertical when standing upright). The other two canals are vertically oriented, but rotated by $\pm 45^\circ$ from the fore/aft and inter-aural axes [33]. Each canal forms a circular tube filled with a fluid called endolymph. At the widest part of the canal, known as the ampulla, an impermeable but flexible membrane, called the cupula, blocks the continuous flow of endolymph through the canal. During head rotations, the head and canals move

while the endolymph lags, due to its inertia, causing a deflection of the cupula. The cupula is embedded with hair cells which are also deflected along with it, resulting in either depolarization or hyperpolarization of the hair cells membrane voltages (similarly to otolith hair cells) [34]. Although it is truly the angular acceleration which provides the force that drives fluid motion, due to the small diameter of the canals and the high viscosity of the endolymph, the canals effectively encode angular velocity, and by convention we henceforth refer to them in terms of their head velocity inputs.

Spiking Activity

Vestibular afferents fire spontaneously, when there is no head motion, with a baseline firing rate of about 80-100 spk/s [35]. The variability of spike times in this spontaneous discharge is quantified by the coefficient of variation (CV) of the inter-spike-intervals (ISIs), with values generally ranging from 0.01 to 1 [36]. Because otolith afferents change their baseline firing rate with static changes in head tilt, and we want CV to be an unchanging property of a neuron, an empirical formula is used to generate CV^* such that CV^* does not change with spontaneous firing rate across populations of cells [35]. Based on this CV^* value, vestibular afferents are generally divided into two classes (see Figure 1.2 A&B): regular afferents ($CV^* < 0.1$) and irregular afferents ($CV^* > 0.1$). While the exact cutoff value used varies slightly across the literature, the distribution of CV^* values has been shown to be significantly bimodal [36]. This classification is further justified by the existence of two morphologically distinct hair cell bodies know as type I and II [29]. In general, regular afferents synapse onto type II hair cells, while irregular afferents synapse onto

type I hair cells. Not only these differences in morphology, but also the distribution of different ion channels have been found to contribute to the different levels of spiking variability of the regular and irregular vestibular afferents [37].

In addition to their different baseline activity, vestibular afferents have also been well characterized using sinusoidal stimuli and traditional linear techniques detailed in the section 1.3 [36]. For both canal and otolith afferents, irregular afferents have significantly higher gains that are high pass as a function of frequency, compared to regular afferents which have relatively flat gain curves by comparison (see Figure 1.2C&D). While this might suggest that irregular afferents transmit more information, this does not account for their differences in variability quantified by CV^*. A more recent study used white noise stimuli to estimate the mutual information density (see Introductory Methods), and indeed found regular afferents to exhibit a higher signal-to-noise ratio than their irregular counterparts, across all frequencies [38] (see Figure 1.2E). Another study also found the linearity in response to sine waves at higher frequencies to break down, and a nonlinear phase locking to occur, for irregular but not regular afferents [39].

It should also be noted that the type I hair cells (primarily irregular afferents) is evolutionarily newer than the type II cells (primarily regular afferents), suggesting that the irregular afferents are further developed and should exhibit an improved performance than their regular counterparts [29]. The newer type I hair cells began to appear as animals left the water to walk on land, where the low viscosity of air allowed them to move much faster. The current hypothesis is therefore that the dynamics of irregular afferents are more specialized for the detection of high frequency

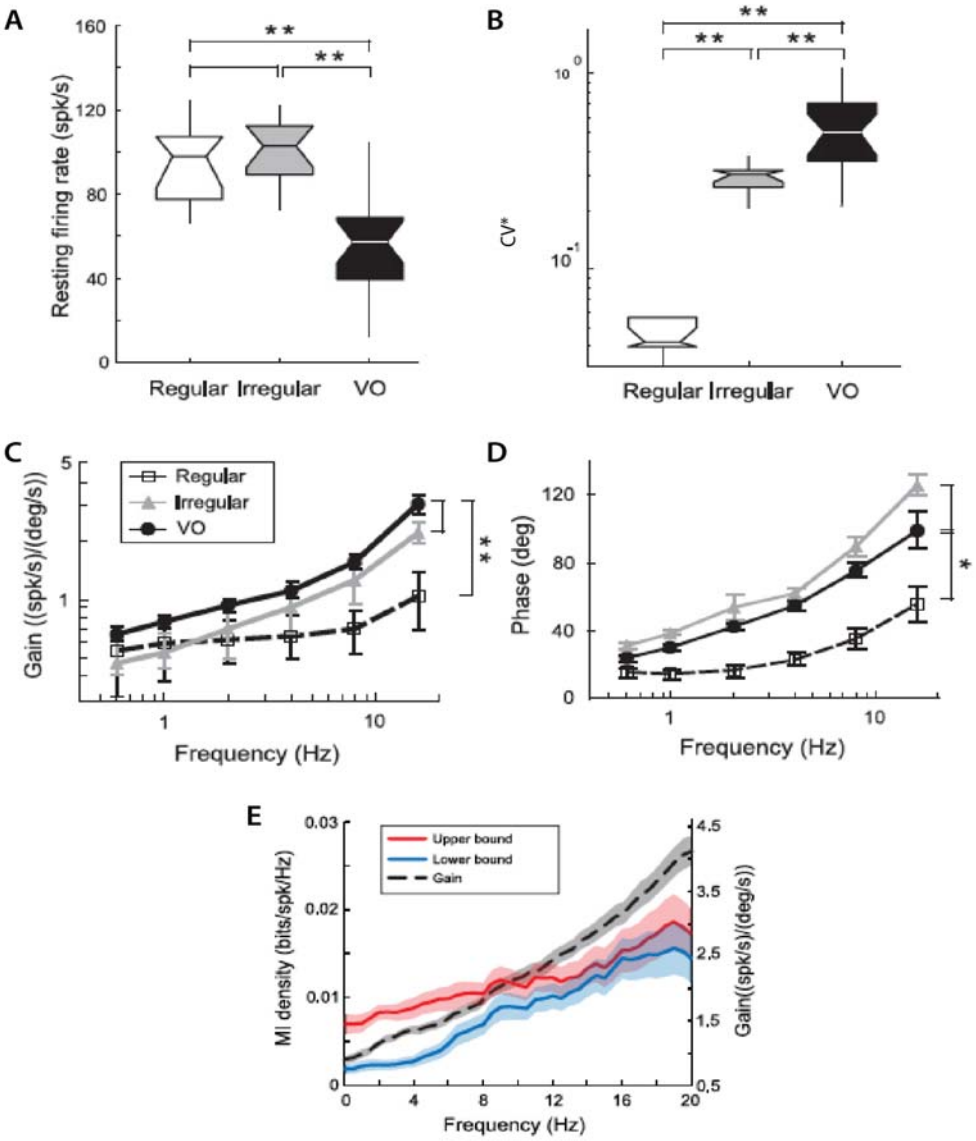

Figure 1.2. Peripheral vestibular neuron properties. Population averaged A) spontaneous firing rate, B) CV^*, C) Gain, and D) Phase, for regular and irregular afferents, as well as VO cells. E) Mutual information lower and upper bound for VO cells, with gap at low frequencies indicative of potential nonlinearity other than saturation and rectification. (Figures adapted from Massot et al. (2011) [35]).

"features" [38], while the regular afferents precisely track the entire stimulus time course. However, both types of afferents can converge onto the same downstream cells in the vestibular nuclei, making it unclear how such downstream neurons could somehow benefit from these two seemingly opposite afferent representations.

1.2.2 Central pathways: The vestibular nuclei

Anatomy

The first central stage of vestibular information processing occurs in the vestibular nuclei (VN) of the brainstem, the primary target of afferent projections (see Figure 1.1A). Although the VN then send output connections to other brain regions, they also receive inputs from other brain regions as well. Over the past 40 years, several anatomical and single unit studies have identified the various regions contributing inputs driving VN activity: from several regions of cortex (parieto-insular vestibular cortex, premotor cortex 6/6pa, anterior cingulate cortex, somatosensory cortex 3a, intraparietal sulcus area 3v, superior temporal cortex; [40–43]), cerebellum (rostral fastigial nuclei, nodulus/uvula, anterior vermis, flocculus; [44–53]), oculomotor regions (nucleus of the optic tract, superior colliculus, nucleus prepositus; [54,55]), and areas encoding proprioception (external cuneate, central cervical nuclei; [56–59]).

Although the inputs to the VN are surely related to their functional role, the regions to which their outputs project are perhaps even more illustrative of their function. In order to maintain stable gaze and posture, vestibulo-motor transformations must correctly drive both the vestibuloocular reflex (VOR) with projections to oculomotor nuclei in the brainstem [60–64], as well as vestibulo-spinal reflexes with

projections to the spinal cord [65–72]. Additionally projections to the various cerebellar regions (rostral fastigial nuclei, nodulus/uvula, anterior vermis, flocculus; [44–53]) are thought to ensure proper calibration of these motor reflexes. Finally, projections to thalamus [73] and in turn cortex [43, 74] are thought to underly orientation and self-motion perception.

With the anatomy reasonably well known, we briefly classify different VN cell types with their neural response characteristics, which has been done under both *in vivo* and *in vitro* conditions.

***In vivo* characterization: Behavioural functions**

In order for the vestibular system to appropriately integrate all of its inputs and generate the appropriate outputs and behavioural responses, the vestibular nuclei are populated by multiple neuron types, each serving different functional roles [33]. *In vivo* recordings performed in alert behaving primates allow cell types to be identified by their responses to both head and eye movements. Two cell types found in VN are known as 'eye-head' neurons, because they respond to eye and head velocity, and 'position-vestibular-pause', because they respond to eye position, head velocity, and pause during fast eye movements. These two neuron types project to the eye motoneurons, contributing to pursuit eye movements as well as the vestibulooccular reflex (VOR), in order to maintain stable gaze [39].

Another type of neuron in the VN is known as 'vestibular-only' (VO) because they respond to head movements, but not eye movements. Rather than projecting to the eye muscles, VO neurons are found to project to the spinal cord [75,76] and likely mediate vestibulo-spinal reflexes to maintain stable posture. Furthermore, because

vestibular neurons in cortex tend to show little to no response to eye movements [77, 78], VO neurons are also presumed to project to thalamus and cortex, contributing to perception of self-motion and spatial orientation. Additionally there are two types of VO neurons, termed type I and type II [33]. Considering yaw rotations as an example, vestibular afferents on either side of the brain respond with increases in firing to ipsilateral rotations (i.e. rotations towards the same side as the neurons location), and decreased to contralateral rotations (i.e. rotations towards the opposite side as the neurons location). For VO neurons the situation is slightly more complex: Type I neurons respond with increases in firing rate to ipsilateral movements, while type II neurons respond with increases in firing rate to contralateral movements. Both type I and II VO neurons can be found on both sides of the brain. While type I VOs respond in the same way as the afferents on the same side of the brain (from which they get their input), type II VOs on one side of the brain receive their inputs from type I VO neurons on the other side of the brain.

Once a neuron has been isolated *in vivo* and identified based on the presence of eye movement related responses its baseline activity and linear response properties are characterized and compared to others across the population studied (see Figure 1.2). In this thesis we will be primarily concerned with VO neurons, which have been found to have slightly lower baseline firing rates (60-70 Hz) and higher CV values than even irregular afferents [35]. Furthermore their gain curves have been found to be even more high pass than irregular afferents. Studies have also used noise stimuli to estimate their mutual information and again find a similar trend to irregulars [35]. However, a difference between lower and upper bounds on information

was observed at low frequencies (see Figure 1.2E), which is indicative of a nonlinearity (see Introductory Methods), and is a primary topic explored in this thesis.

Finally, it should be noted that these response characteristics are only valid for stimuli passively applied by the experimenter, while for natural self-generated movement VO responses are attenuated by $\sim 70\%$. This effect is, however, not seen in their afferent inputs. Although we will not study this phenomenon directly in this thesis, it is an important issue studied in the lab, and is relevant to understanding the functional goal of VO neurons, and in turn interpreting their information coding properties.

***In vitro* characterization: Intrinsic membrane dynamics**

Much work on the characterization of vestibular anatomy and function has also been done using *in vitro* techniques, whereby a slice of (or whole) brain containing the neurons of interest is removed from an animal and isolated in a dish. This technique has the advantage of being able to visually identify neurons while recording, as well as facilitating intracellular recordings which precisely measure the the membrane voltage of a cell, rather than simply inferring spike times, as is done for extracellular recordings *in vivo* (Note, intracellular recordings *in vivo* are possible, but significantly more difficult). The main disadvantage of *in vitro* techniques is that the animal is no longer alive and behaving during recordings, which in turn prevents the classification of cell types based on their response to eye movements, or natural self-generated head movements. For this reason, VN neurons recorded *in vitro* are classified based on the precise time course of the membrane voltage during each action potential, along with the usual linear systems techniques (see section 1.3). Additionally, more

diagnostic step and ramp stimuli, along with pharmacological ion channel blockers allows identification of the specific ion channels involved in shaping the neuronal responses [27]. Such studies allow for building more detailed models than *in vivo* data alone (discussed in the Neural Modelling section), however we will see that it is somewhat of an art in deciding what levels of detail one wishes to include. In general one includes as little detail as possible and as much as necessary to reproduce the neural response properties, observed either *in vitro* or *in vivo*. Before discussing neuron models, we will first discuss methods of characterizing their properties of interest.

1.3 Methods of Analysis

Neurons are often thought of simply as input-output devices, in reality receiving thousands of synaptic inputs to their dendrites, which are transformed, via the complex nonlinear dynamics of ion channels distributed throughout their cellular membrane, to output a spiking membrane voltage (or firing rate) transmitted down an axon to other neurons. To characterize this entire process by which a neuron transforms a sensory signal from its input to its output, classical linear-nonlinear signal processing techniques are typically used. Although some neurons, such as the elusive "Jennifer Aniston" neuron which responds only to images of Jennifer Aniston but no other television celebrities, have responses that are highly nonlinear functions of the sensor inputs at the retina, while more peripheral sensory neurons (such as those studied in this thesis) tend to fire spontaneous with a baseline firing rate which can be modulated up and down by the sensor inputs to linearly encode

stimulus changes. These are the type of neurons we will consider in the vestibular system.

1.3.1 Firing rate estimation

If a constant stimulus is applied (perhaps of zero for spontaneously active neurons), one can simply count the number of spikes in a time window to estimate the average firing rate. If the stimulus instead slowly changes we can expect the firing rate to slowly change as well, but it is then not as obvious how to estimate the time dependent firing rate, r(t). Because repeated presentations of the same stimulus result in different spike train responses each time, they can be averaged to generate what is known as a post-stimulus time histogram (PSTH), that can be normalized to give either the probability of spiking at different phases of the stimulus or the average firing rate in spk/s. The PSTH works best when you can repeat a short stimulus *many* times. To estimate the firing rate in a single trial, one can use a short sliding window to count spikes, or analogously convolve with a Gaussian filter. However, the width of the Gaussian filter is not always easily chosen. Imagine the firing rate is 1 spk/s for 1 sec: a broad enough filter says that the firing rate is constant at 1 spk/s for 1 s, while a sufficiently narrow filter could say that the firing rate is 1000 spk/s for 1 ms and 0 spk/s the rest of the time. This is further complicated when the firing rate is changing in time. An alternative measure of the firing rate that uses only the spike times is to simply invert the inter-spike intervals (ISIs), 1/ISI, however it is only defined at the spike times, and doesn't give a continuous estimate. Spiking variability is also quantified by $CV = \sigma_{ISI}/\mu_{ISI}$, for spontaneous activity.

1.3.2 Traditional linear-nonlinear systems identification

Consider a spontaneously active neuron whose firing rate can be modulated by some stimulus input. A *linear transformation*, by definition, cannot change the frequency of a signal. For this reason, linear modulations can most simply be characterized by the application of sinusoidal stimuli, $s(t) = A_s \sin(2\pi f t)$, over a range of frequencies, the responses to which must also be sine waves, $r(t) = A_r(f) \sin(2\pi f t + \phi(f))$, shifted in time and scaled in amplitude. Such stimulus and response data can then be used to generate a *transfer function* which combines the "gain", $g(f) = A_r(f)/A_s$, and phase shift, $\phi(f)$, into a complex function of frequency, $H(f) = g(f)e^{i\phi(f)}$. With a neuron's linear transfer function, one can then in principle predict the neurons response to other arbitrarily complex dynamic stimuli, as long as the neuron remains linear. We can then take the inverse Fourier transform to get the transfer function filter (or impulse response function) in the time domain, $h(t) = \mathcal{F}^{-1}\{H(f)\}$, and the response can be estimated from the stimulus by the convolution integral, $\hat{r}(t) = \int d\tau h(t-\tau)s(\tau)$. However, in the frequency domain this can be simply written as $\hat{R} = H * S$, where $S, R(f) = \mathcal{F}\{s, r(t)\}$.

Although sine waves spanning a range of frequencies are perhaps the simplest stimuli with which to measure a neuron's transfer functions, one can also use Gaussian noise stimuli over the desired frequency range, essentially combining all frequencies into one stimulus. In this case, as long as the neuron remains linear, the entire transfer function can be calculated via the stimulus-response cross-spectral density,

according to

$$\begin{aligned} H(f) &= \frac{\langle S(f)^* R(f) \rangle}{\langle S(f)^* S(f) \rangle} \\ &= \frac{P_{SR}(f)}{P_{SS}(f)}, \end{aligned} \tag{1.1}$$

where $\langle . \rangle$ denotes averaging, and * indicates the complex conjugate. The numerator and denominator are also written explicitly as the stimulus-response cross spectrum, and stimulus power spectrum, respectively. Similarly, the linear filter which provides the best estimate of the stimulus, the *optimal reconstruction filter* is

$$\begin{aligned} K(f) &= \frac{\langle R(f)^* S(f) \rangle}{\langle R(f)^* R(f) \rangle} \\ &= \frac{P_{SR}(-f)}{P_{RR}(f)}, \end{aligned} \tag{1.2}$$

such that $\hat{S} = K * R$, where K is chosen to minimize $(S - \hat{S})^2$. We will come back to this filter later. A schematic summarizing these optimal linear filters is shown in Figure 1.3.

Such linear transfer functions can also be derived analytically from the differential equations of simple systems, such as the torsion pendulum model of cupula motion in the semicircular canals. In this simple model, the cupula motion is described by a second order differential equation of the form $m\ddot{x} + c\dot{x} + kx = f(x,t)$, where x represents the cupula position, m is a mass coefficient, c is a damping coefficient, k is a spring constant and f is a driving force that depends on x and time. By applying a Laplace transform, the time variable changes to a frequency variable $s = i2\pi f$, and derivatives in time result in multiplicative factors of s, resulting in $(ms^2 + cs + k)X(s) = F(s)$ which can be solved algebraically to give the transfer

function, $H(s) \equiv X(s)/F(s) = 1/(ms^2 + cs + k)$. This transfer function is in a polynomial form, but can be factored into a more intuitive zero-pole notation as $H(s) = 1/(1 + T_1 s)(1 + T_2 s)$, where the coefficients have been redefined as time constants, which can actually be measured.

Although spontaneously active neurons can modulate their firing rate linearly, they are inherently *nonlinear* due to their spike generation mechanism (see Methods of Modeling Neurons) and having a minimum possible firing rate of zero. Similarly neurons *must* have a maximum possible firing rate, due to physical limitations on the ion channels in the cellular membrane. Although neurons generally have a broad *linear range* within which linear transfer functions are sufficient, increasingly large amplitude stimuli will eventually drive them into nonlinear rectification (i.e. zero firing rate) and saturation (i.e. maximum firing rate). In the absence of stimuli, vetibular neurons return to their baseline firing rate in their linear response regime. This is often be modeled by combining a linear transfer function with a subsequent sigmoidal nonlinear function, known as a linear-nonlinear (LN) cascade model. To estimate from a stimulus and response, whether a nonlinear function is needed, one can use the neural data to estimate H(f), then plot the response estimate, $\hat{r}(t)$, versus the actual response, r(t). If they lie on a line with slope of one the response estimate is good, otherwise a nonlinear function, $\hat{r}_{nlin} = T(\hat{r})$, can be fit to the data. Similarly, the firing rate response can be plotted versus the stimulus directly, if the frequency dependence is negligible.

Many other neurons commonly found in higher levels of cortex, however, exist primarily at subthreshold voltages and only very specific stimulus features can cause

them to fire spikes. Some of these neurons can still be characterized with white noise, using reverse-correlation techniques, commonly referred to as spike-triggered averaging. This results in linear temporal filters (or kernels) selective for the stimulus features to which the neuron is sensitive, with a nonlinearity that says how strongly it encodes each feature. This is essentially another form of LN model, in which the response spends more time in the rectified state (i.e. zero firing rate), until its preferred stimulus drives it to spiking. The neurons that we will study in this thesis are, however, of the spontaneously active type. In either case, the understanding and modelling of neural systems requires a combination of their *linear* and *nonlinear* properties. Although these LN models can explain the responses elicited from the stimuli, we would like a more general measure of how well the stimulus is represented by a neurons response, for which neuroscientists have turned to information theory.

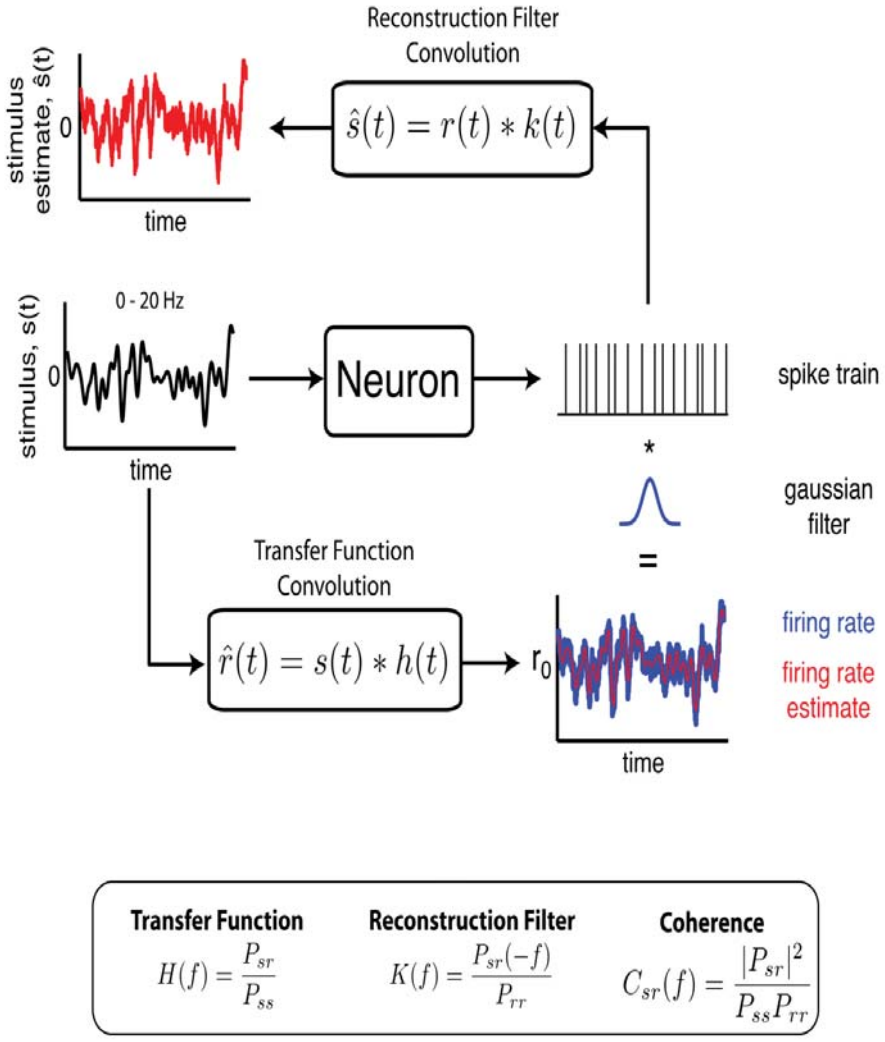

Transfer Function	Reconstruction Filter	Coherence
$H(f) = \frac{P_{sr}}{P_{ss}}$	$K(f) = \frac{P_{sr}(-f)}{P_{rr}}$	$C_{sr}(f) = \frac{\lvert P_{sr}\rvert^2}{P_{ss}P_{rr}}$

Figure 1.3. Schematic summarizing optimal linear filters for stimulus and response estimation. This diagram illustrates that a neuron produces a spiking response to a stimulus, which can be convolved with a Gaussian to produce a continuous, but noisy, firing rate. Furthermore, it summarizes the filters that are used to estimate the stimulus from the spike train, as well as estimate the firing rate from the stimulus (but using the spike train). These two filters combine to give the SR-coherence, which can be used to provide a lower bound on the mutual information between stimulus and response.

1.3.3 Information Theory

Information theory [79] was developed around the time telecommunication via Morse code became widespread, in order to quantify the information content of each message in a mathematically rigorous way. Although the inventor himself, Claude Shannon, advised caution in its application to other fields, its use by neuroscientists has brought progress in understanding the neural code [5].

Neurons respond differently to repeated presentations of the same stimulus, making it is natural to think of them probabilistically: such as, the distributions of responses that can be elicited from a particular stimulus value, or (perhaps more relevant to behaviour) the distribution of stimuli which may have occurred given the observation of a particular firing rate response. Information theory quantifies the uncertainty (or variability) in these distributions by their entropy, a precise measure proportional to the negative log-probability of their values occurring: the more unlikely an event, the higher its entropy. The log is to ensure that the entropy of two systems adds when they are combined, while their probability distributions multiply. The mutual information between a stimulus and response distributions can then be defined as the reduction of stimulus uncertainty given the observation of a particular stimulus, averaged over all possible stimuli:

$$\begin{aligned} I(S,R) &\equiv H(S) - H(S|R) = H(R) - H(R|S) \\ &= \int_{s\in S, r\in R} ds\, dr\, p(r|s)p(s) \log_2 \frac{p(r|s)}{p(r)} \\ &= \int_{s\in S, r\in R} ds\, dr\, p(s,r) \log_2 \frac{p(s,r)}{p(s)p(r)} \end{aligned} \tag{1.3}$$

where $H(R) = -\int drp(r)\log_2 p(r)$ is the entropy of the response distribution, $H(R|S) = \int dsp(s)drp(r|s)\log_2 p(r|s)$ is called the "noise entropy", and $p(r|s)$ is the conditional response probability. In the final line, $p(s,r)$ is the joint probability distribution, where $p(s,r) = p(s|r)p(r) = p(r|s)p(s)$.

The Noisy Gaussian Channel

As an illustrative example, we assume that the stimulus comes from a Gaussian distribution with zero mean and variance of σ_s^2, and that the neuron performs a linear transformation and adds some noise from a Gaussian distribution with zero mean and variance of σ_η^2. In this case the response is, $r = g \cdot s + \eta$, where g is the "gain", and the conditional distribution can be written as [5]

$$\begin{aligned} p(r|s) &= p(\eta = y - g \cdot s) \\ &= \frac{1}{\sqrt{2\pi\sigma_\eta^2}} \exp\left[-\frac{(y - g \cdot s)^2}{2\sigma_\eta^2} \right] \end{aligned} \tag{1.4}$$

Plugging this into equation 1.3 and doing some calculations, the mutual information for the Gaussian channel can be reduced to

$$I = \frac{1}{2}\log_2 \left[1 + \underbrace{\frac{\sigma_s^2}{\sigma_{\eta,eff}^2}}_{\text{SNR}} \right] \text{ bits}, \tag{1.5}$$

where $\sigma_s^2/\sigma_{\eta,eff}^2$ is the signal-to-noise ratio (SNR), in which the variance of the noise has been scaled by the gain to give the "effective noise" variance $\sigma_{\eta,eff}^2 = \sigma_\eta^2/g$, and we have now expressed the units of mutual information as bits (due to the log of base 2).

To have a better intuition for the units of information, consider a coin toss of two possible outcomes with equal probability, in this case the entropy of the coin toss can be calculated to be 1 bit, which is needed to represent the events two possible outcomes. Similarly, if the mutual information between stimulus and response is 1 bit, a response carries on average enough information to distinguish between two possible stimuli, or divide the stimulus distribution in two and predict which side the stimulus came from. Neurons, however, typically receive dynamic stimuli that result in dynamic responses which must be considered in order to properly estimate the *information rate* [5].

Dynamic Stimuli

In the case of coin flips, each is statistically independent from the next making the entropy and information additive across flips (and time). For dynamic stimuli and responses we must discretize time, but sequences of stimulus and response points come from stationary probability distributions, they are not generally statistically independent (unless they appear as white noise). An excellent derivation accounting for the entropy of spike trains and dynamic stimuli is presented here [5], and reviewed by Borst and Theunissen [80]. Starting with our linear Gaussian channel, the *information rate* can be shown to be

$$R_{info} = \int_0^\infty df \log_2 \Big[1 + \mathrm{SNR}(f)\Big] bits/sec. \tag{1.6}$$

Instead of integrating over frequency, we can consider the *information rate density* as a function of frequency

$$I(f) = \log_2 \Big[1 + \mathrm{SNR}(f)\Big], \tag{1.7}$$

however we must now still calculate the frequency dependent SNR(f). Although there are methods of calculating the mutual information directly without assuming linearity or Gaussian distributions, they often require unreasonably large amounts of experimental data. As such, we use a method to estimate lower and upper bounds.

Lower and Upper Bounds: SR- &$\sqrt{RR}$-coherence

To get a lower bound on the SNR, the optimal stimulus reconstruction filter is used to get the stimulus estimate, then defining the "noise" as the signal reconstruction error, $N = S - \hat{S}$. We can then define the lower bound of the SNR as

$$\begin{aligned} SNR_{LB}(f) &= \frac{\langle \hat{S}^* \hat{S} \rangle}{\langle N^* N \rangle} \\ &= \frac{\langle (KR)^* KR \rangle}{\langle (S^* - R^* K^*)(S - KR) \rangle} \\ &= \frac{C_{SR}}{1 - C_{SR}}, \end{aligned} \tag{1.8}$$

where C_{SR} is the stimulus-response coherence function

$$\begin{aligned} C_{SR} &= \frac{\langle S^* R \rangle \langle R^* S \rangle}{\langle S^* S \rangle \langle R^* R \rangle} \\ &= \frac{|P_{SR}|^2}{P_{SS} P_{RR}}. \end{aligned} \tag{1.9}$$

Here we can see that the SR-coherence is really just the combination of the two linear prediction filters, H(f) and K(f), as summarized in the bottom of Figure 1.3. C_{SR} is in fact a measure of the linear correlation between the stimulus and response,

giving a value between 0 and 1. For a linear noiseless transformation, the coherence would be 1. For Gaussian stimuli and noise, increasing noise intensity will reduce the coherence, but a nonlinearity will also reduce the linear correlation and hence SR-coherence, by altering the Gaussianity of the stimulus distribution and shifting power into its higher moments. However, for repeated presentations of the same stimulus the noise should be different each time, while the nonlinearity should do the same thing each time. These two factors can be separated by calculating the RR-coherence, which for 4 repetitions of the stimulus results in

$$C_{RR} = \frac{\left| \frac{1}{6} \sum_{i=2}^{4} \sum_{j=1}^{i-1} P_{R_i R_j} \right|}{P_{RR}}, \tag{1.10}$$

where $P_{R_i R_j}$ is the cross-spectrum between the i^{th} and j^{th} responses. It has been shown [81] that the square root of the RR-coherence is always greater than the SR-coherence, yet less than one: $0 \leq C_{SR} \leq \sqrt{C_{RR}}$. A difference between these two curves can therefore tell us if there may be any additional information that cannot be decoded linearly, as well as its frequency content, potentially indicative of temporal coding [80]. For sufficiently Gaussian stimulus, response and noise distributions, the $\sqrt{RR}$-coherence provides an upper bound on the MI:

$$I_{UB}(f) = -\log_2(1 - \sqrt{C_{RR}}). \tag{1.11}$$

Although nonlinearities will often result in temporally encoded information that cannot be decoded linearly (resulting in differences between C_{SR} and $\sqrt{C_{RR}}$), they

also tend to result in non-Gaussian response distributions which can invalidate their use as an upper bound on mutual information, requiring caution in its use.

Once we have characterized a neurons behaviour, we would like to further understand it by reproducing it with a model.

1.4 Methods of Neuron Modelling

Over one hundred year ago, Lapicque proposed that a neuron generates an action potential by integrating its sensory or synaptic inputs until a threshold value is reached [82]. Although this does not explain the biophysical details of how a neuron actually does this, the concept of 'integrate-and-fire' remains one of the most influential models in neurobiology primarily due to its simple mechanistic nature. However, this is of course far from explaining how neurons actually work, ignoring the neurons dendritic morphology, distribution of synaptic inputs, as well as the distribution and composition of the myriad ion channels that can interact to generate action potentials. This illustrates the point that there are clearly various levels of abstraction with which neurons can be described, such that choosing the level of detail to include in a model somewhat of an art form. The achievements of models with various levels of detail are summarized by Herz et al. [83], two broad classes of which will be described below, followed by a summary of the various models used for vestibular neurons.

1.4.1 Biophysically detailed models

While biophysically detailed models can include tremendous amounts of details including the dendritic morphology with synapses and neurotransmitters, here we will only consider the details necessary for spike generation. It had been long known

that the electrical currents input to a neuron could cause it to generate action potentials, but it was the work of Hodgkin and Huxley that identified the current-voltage activation curves for the sodium and potassium channels involved [84]. A single patch of neuron membrane will have thousands of channels of various types, but we model current flowing through them as a function of time. At an instant in time, the average current is generally defined as $I_{ions} = g_{ions} \cdot x^a(V) \cdot (V - V_{rev})$, where g_{ions} is the maximum conductance of the ion channel when it is completely open, and $x^a(V)$, is a voltage dependent gating variable (generally sigmoidal in voltage) which can take values from 0 to 1, indicating the proportion of channels that are open, with 1 indicating that the maximum conductance (and current) is achieved. This gating variable represents an activation variable which must equal 1 for current to flow, however inactivation variables are also possible in which a 0 indicates that the channel is de-inactivated and that current can flow. Finally, a reversal potential, V_{rev}, sets the direction of current flow (based on the electrochemical equilibrium) in the last term in the current equation above. The Hodgkin-Huxley equations for a spiking neuron involve a potassium current with an activation variable, n, as well as a sodium current that has both activation and inactivation (i.e. must be lower for current to flow) variables, m and h, respectively, resulting in the system of equations:

$$\begin{aligned} C_m \frac{dV}{dt} &= \underbrace{g_{Na} m^3 h (V - V_{Na})}_{I_{Na}} + \underbrace{g_K n^4 (V - V_K)}_{I_K} + \underbrace{g_{Leak} (V - V_{Leak})}_{I_{Leak}} + I_{input} \\ \frac{dn}{dt} &= [n_\infty(V) - n]/\tau_n(V), \\ \frac{dm}{dt} &= [m_\infty(V) - m]/\tau_m(V), \\ \frac{dh}{dt} &= [h_\infty(V) - h]/\tau_h(V), \end{aligned} \tag{1.12}$$

where the gating variables have their own first order dynamical equations, in which the gating variable x is driven towards the voltage dependent equilibrium point, $x_\infty(V)$, with a timescale set by the time constant, $\tau_x(V)$, for $x \in \{n, m, h\}$. Model parameters include the membrane capacitance, C_m, the maximum conductance for each channel type, g_{Na}, g_K, and g_{Leak}, as well as their reversal potentials, V_{Na}, V_K, and V_{Leak}. The average resting potential of such neurons when not producing action potentials is around -70 mV, which is generally close to V_{Leak}. As such, the reversal potential for sodium (which enters the cell) makes its current drive the voltage upwards (termed depolarizing), while the potassium (which generally exits the cell) makes its current drive the voltage downwards (termed hyperpolarizing). The leak current represents the cells overall permeability to a mixture of ions, but primarily to chloride.

These parameters describe the behavior of many ion channels together, however, we do know more details about the microscopic structure of each individual ion channel as well. A potassium channel, for example, is a protein through the cell membrane, which has two possible states, open and closed. These proteins often have multiple binding sites, each of which can be empty or full, and all of which must be full for the channel to open. In this case, the n^4 term would indicate probability that all four binding sites are occupied and the channel is open, while n indicates the probability that one binding site is occupied. Under this interpretation, the individual binding variable dynamics are often defined as

$$\frac{dn}{dt} = \alpha_n(V)(1-n) - \beta_n(V)(n) \tag{1.13}$$

where $\alpha(V)_n$ and $\beta(V)_n$ are voltage dependent transition rates from closed-to-open and open-to-closed, respectively. The two pictures are translated according to $n_\infty = \alpha_n/(\alpha_n+\beta_n)$, and $\tau_n = 1/(\alpha_n+\beta_n)$ (and similarly for the other activation variables).

One of the fabled triumphs of the Hodgkin-Huxley (HH) equations is the n^4 term, which would suggest the potassium channel could require four activation gates each with the probability n of being open, making n^4 the probability of all four being open simultaneously. Indeed it was found that the sodium channels do have four gates which must be activated, it is in all likelihood a fluke that Hodgkin and Huxley only tried to fit the model up to a power of four due to their lack of computational power!

Regardless of the interpretation with respect to further microscopic details, simulations of these equations with appropriately tuned parameters can reproduce the spiking activity of several classes of neurons. However the four-dimensional dynamical system is somewhat difficult to understand intuitively, as well as analyze its phase space trajectories and bifurcations. In order to understand more clearly the mechanism required to generate periodic spiking activity, the HH model can be simplified by noticing that m is very fast allowing $m \approx m_\infty(V)$, as well as that $h \approx 1-n$. This results in the simple two-dimensional spiking system:

$$\begin{aligned} C_m\frac{dV}{dt} &= g_{Na}m_\infty^3(1-n)(V-V_{Na}) + g_K n^4(V-V_K) + g_{Leak}(V-V_{Leak}) + I_{input} \\ \frac{dn}{dt} &= [n_\infty(V)-n]/\tau_n(V) \end{aligned} \tag{1.14}$$

For this simplified two-variable model, some details in the shape of the action potentials are lost, but there are now only two variables, the membrane voltage V, and the "recovery variable", n.

Fixed points and limit cycles

The simplified two-variable spiking model is significantly more tractable for a phase space analysis of fixed points and bifurcations, as the two variables can be plotted and visualized simultaneously in a 2D plane. The fixed points of a system are found by setting the two differential equations to zero: $\dot{V} = \dot{n} = 0$. This gives two equations for two curves called *nullclines*, the intersection points of which correspond to fixed points of the system, where neither variable is changing [85]. Furthermore, such fixed points can be either stable or unstable, as indicated by the eigenvalues of the linear stability matrix at that fixed point. It is simple to see that the n-nullcline is simply the sigmoidal curve corresponding to $n_\infty(V)$. The V-nullcline on the other hand has been shown to have a cubic shape, like an 's' rotated clockwise, which is shifted up and down by changes in the input bias current (see Figure 1.4). It is then relatively easy to see that for lower bias currents, the curves will intersect in three places (Figure 1.4A), and as the bias current is increased, two intersection points will disappear leaving only one (Figure 1.4B). An analysis of the stability of such fixed points has revealed two main bifurcation types that can lead to spontaneous periodic spiking for some bias current value, $I_{input} > I^*$.

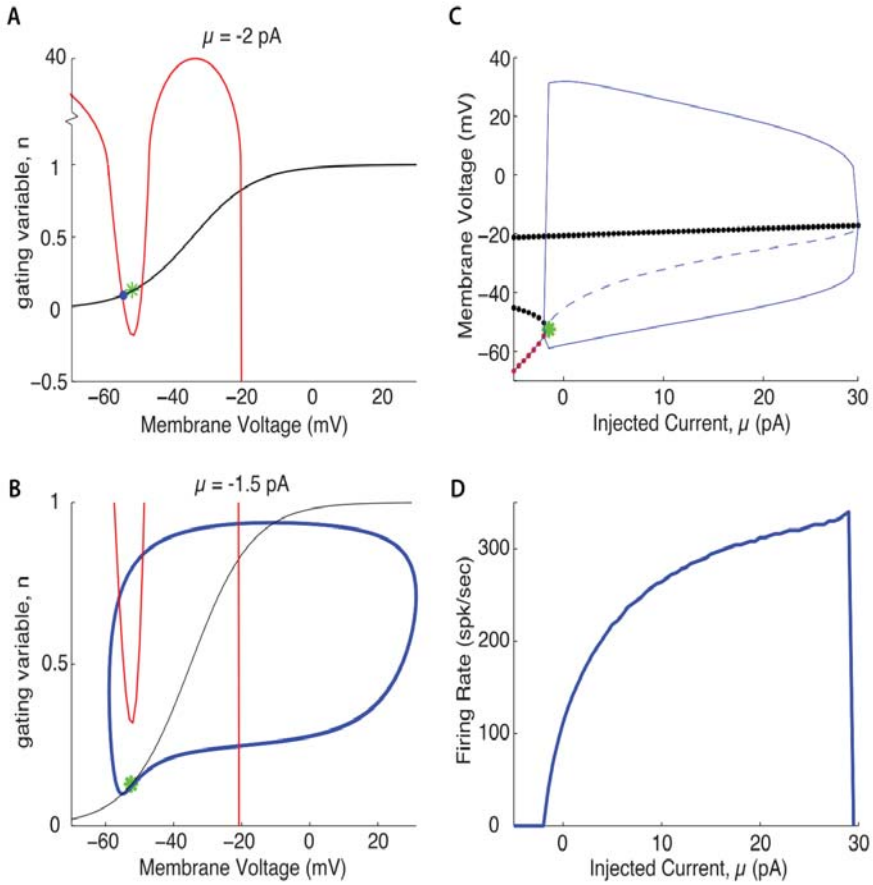

Figure 1.4. Fixed point bifurcation analysis of two-dimensional spiking neuron model. Panels (A-B) show n-nullclines (black) and V-nullclines (red) of the neuron model in Equation 1.14, for two bias current values. In (A) the bias current is below threshold and the voltage is a constant at the resting potential corresponding to the leftmost intersection point (blue dot). In (B) the only intersection point is unstable, as the voltage oscillates around it in a stable limit cycle (blue) (C) Bifurcation diagram of all fixed points, either stable (red dots) or unstable (black dots). The green star indicates a saddle node bifurcation point where the two fixed points annihilate and spiking begins. The blue line indicates the maximum and minimum values of the spiking limit cycle as a function of bias current. The dashed blue line indicates the voltage mean. (D) The firing rate, or 1/period of the limit cycle orbit.

In both scenarios, at low bias current the lowest of the three voltage fixed points will be stable, and the membrane voltage will be stable at rest, only firing a spike if sufficiently perturbed. In the first scenario, as the bias current is increased, the two fixed points with lowest voltage, one stable and one unstable, will come together and annihilate in a *saddle-node bifurcation* leaving only the high voltage fixed point which is unstable and oscillatory. This gives rise to a stable limit cycle encircling the one remaining fixed point, and a neuron which spikes periodically for a constant current input, a highly nonlinear phenomenon. This is the mechanism illustrated in Figure 1.4C. In the second scenario, as the bias is increased, the stable fixed point looses its stability and becomes oscillatory via a *Hopf bifurcation*, before annihilating with the second lowest fixed point. Although these two bifurcation scenarios both transition from non-spiking to spontaneously spiking states, they result in two classes of excitability, class 1 and class 2, respectively. In *class 1 excitable* systems, the f-I curve shows a continuous change from zero firing rate to non-zero firing rate, with arbitrarily low rates possible for a precisely tuned bias currents. In *class 2 excitable* systems, the f-I curve shows a discontinuous change from zero firing rate to non-zero firing rate, where the onset firing rate is determined primarily by the model parameters and imaginary eigenvalue components, insensitive to the precise input current. Furthermore, these two classes of excitability have been found to give rise to different information processing properties, providing a link between the underlying ion channel dynamics of a neuron, and its ability to process sensory information [86].

While these are some of the simplest biophysically realistic models which can explain the phenomenon of excitability and the generation of action potentials, they

can be further complicated by the addition of various other conductance-based ion channels uncovered by various experiments, all of which contribute to the type of spiking activity models exhibit. One approach is then to accurately model neurons by putting in all the various ion channels found and tuning parameters to see how they all contribute to shaping the action potentials and spiking dynamics. While this approach is likely to capture the rich and subtle differences in neural dynamics, it has been shown that many different biophysically detailed models and parameter combinations can give rise to qualitatively similar "types" of activity [87]. An alternate approach is therefore to start with the simplest possible mathematical models necessary (rather than simply sufficient) to reproduce the various types of spiking activity.

1.4.2 Phenomenological models

On the other end of the modelling spectrum, instead of including the details of each ionic current and fine tuning parameters to explain the different spiking mechanisms, integrate-and-fire (IF) models completely remove the actual spikes, to focus on their timing and the subthreshold dynamics responsible. As the name would suggest, an IF model integrates its input current to drive the membrane dynamics towards a *threshold voltage*, at which point a spike is said to occur and the voltage is set to a *reset voltage* and held fixed for a *refractory period*. Although this model cannot explain how a neuron generates an action potential, it does capture the basic neural properties of of a sigmoidal saturating and rectifying nonlinearity, along with a roughly linear spiking regime. Although, these models tend to fail at reproducing

the subthreshold membrane potential time course between spikes, details can then be added back systematically to recover the particular features of interest.

The simplicity of the IF model is that it has a single variable for the membrane voltage, V, governed by the equation $\dot{V} = F(V)$. The simplest case is the perfect IF model, which has only an input current, resulting in $F(V) = \mu$. The main problem with this model is that if a stimulus brings the neuron close to threshold but is removed, the voltage will remain close to threshold until any new stimulus causes it to spike. This can be fixed by adding back the linear leak current, resulting in $F(V) = \mu + g_{Leak}(V - V_{Leak})$, a leaky IF (LIF) model. In this model the voltage now decays back to a resting potential, set by V_{Leak}. These models, however, can still not reproduce the depolarizing upstroke in membrane potential prior to a spike. The simplest possible remedy is to add a quadratic term that rises for both increasing and decreasing V, resulting in a QIF model. While the quadratic term maintains as much simplicity as possible, a much better fit (to data and detailed models) can generally be achieved with an exponential IF model (EIF). While producing significantly more realistic models, the additional exponential term also reduces the analytic tractability of the model, highlighting the tradeoff in realism and simplicity.

Although these simplified IF-type models can explain a range of spiking activities, there do remain neuronal properties which require a second variable to reproduce, such as bursting, subthreshold membrane oscillations, and the Hopf bifurcation found in type II excitable neurons. In this case, IF-type models can be further generalized to include any extra conductance-based currents of the form $I = g \cdot x^a(V) \cdot (V - V_{rev})$, even if this requires additional dynamic equations for

their own activation variables, such as $dx/dt = [x_\infty(V) - x]/\tau_x(V)$. Although it may seem counter productive to add back such complexities after simplifying the neuron models in the first place, we will later see that this can in fact be necessary for the analytic treatment and intuitive understanding of more complex spiking neuron models.

1.4.3 Vestibular neuron models

Indeed models with various levels of detail have been used to represent various neurons in the vestibular system, for various purposes which we will briefly review here. In the 80s and 90s, as computational resources increased, and *in vitro* recording techniques improved at identifying the cell morphology and ion channels, a trend in detailed conductance-based models rose in hopes of putting every detail into the model to simply simulate and see how it works. *In vivo* recordings on the other hand can give access to the neural activity of the awake behaving animal. However, they tend not to give access to the more cellular details or the actual membrane potential, only the spike times, driving the development of more phenomenological models.

Afferent Models

The most common vestibular afferent models fit to spiking data are linear transfer functions characterizing their different gain and phase profiles [88,89]. Parametrized analytic forms for these models have also been related back to the material properties of the sensors, such as the torsion pendulum model of the cupula [90]. However these linear transfer function models do not account for the increased variability of irregular afferents. It was a model of Smith and Goldberg in 1986 [91] that first adopted a conductance-based spiking model of an AHP due to particular potassium

channels combined with synaptic shot noise that gave rise to their increased variability. However, more recent afferent studies using white noise stimuli were modeled using simple IF models, with an added first-order high-pass filter to account for the dynamics, and an additive noise current to account for the variability [38]. Although these models were not developed to explain the mechanistic origins of the gain and variability, they were sufficient to explain the resulting information transmission properties in the linear response regime. Although sigmoidal nonlinearities have been fit to afferent data [36], and nonlinear phase-locking observed [92], these nonlinear afferent properties have not yet been modeled explicitly.

Vestibular Nuclei Models

In Vitro studies of vestibular nuclei neurons identify and classify neurons as type A or B based on the shape of their action potentials, as well as their transfer functions, and responses to step current injections [27]. These studies have additionally found the ion channel distributions underlying these properties, and built conductance-based models to reproduce them. In 1994, Quadroni and Knopfel developed detailed conductance-based models with extensive dendritic compartments [93], however, in 1999, Av-Ron showed that these membrane properties could be reproduced by a single compartment model, with different ion channel combinations [94]. In particular, type B neurons have a high-pass gain profile, as well as an AHP in their membrane potential giving rise to increase spiking variability. *In vivo* VN neurons are again typically only modeled with linear transfer functions, with VO neurons having a high-pass profile [35], making their *in vitro* corespondents most likely Type

B. However, type B neurons exhibit some nonlinear effects (such as phase locking), that have not yet been reported *in vivo*.

1.5 Research Goals and Thesis Outline

The overall goal of doctoral research was to explore the nature of the neural code used in early vestibular pathways, and whether it is somehow optimized for the natural conditions to which it is exposed. This is relevant to the field of vestibular research as we are the first to have characterized the natural head movements of freely moving monkeys, as well as an explicit nonlinearity in central vestibular neurons. Furthermore my research is important for the field of computational neuroscience in general, as we are the first to consider optimal coding in the vestibular system, shedding light on such general theories of brain function. Finally my research provides insights into the complementary roles of rate and temporal codes, and the underlying molecular mechanisms that may regulate them. The organization of this thesis is as follows.

In *chapter 2*, a paper is presented where we explore the statistics of the natural stimuli to which the vestibular system is exposed in order to see whether afferent neurons have evolved to process such stimuli in an optimal way. To this end, we record and characterize the natural head movements of monkeys. We then fit LN cascade models to spiking otolith and canal afferent data previously recorded for other projects, in order to use information theoretic techniques to calculate the optimal stimulus distributions for each afferent class. Finally, we quantify whether the optimal stimulus distribution of regular or irregular afferents are better matched to

those of natural stimuli (for both canal and otolith afferents), showing that indeed the irregular afferents are better optimized than the regular afferents.

In *chapter 3*, a paper is presented where we seek to bridge the gap between *in vitro* and *in vivo* experiments by adapting a detailed conductance-based model of type B *in vitro* neurons to model the behavior of VO data recorded *in vivo*. To this end, we mimic the high conductance state of neurons *in vivo* with an increased leak conductance and additive current noise. We find the effects of *in vivo*-like conditions on the model neuron's response properties allow it to linearly encode stimuli within the experimentally tested range of stimulus frequencies and amplitudes, in its firing rate modulations. This provides us with a detailed VO neuron model that can next be used to further explore VO neurons nonlinear response properties to larger amplitude stimuli.

In *chapter 4*, in a paper in preparation, we show that the interplay of calcium and calcium activated-potassium channels can cause the f-I curve, of the VO model from Chapter 3, to exhibit a similar nonlinearity to one recently found in VO data (which is presented in Appendix E). I further reduce the model to a generalized QIF model which is more analytically tractable, while preserving the desired features of the original model, in order to reveal the mechanistic origins of f-I curve's nonlinear shape.

In the Conclusions section, the results of each chapter will be briefly summarized, and the implications of the findings to the field of computational neuroscience in the vestibular system will be considered, along with future possible directions in which these projects could be continued. In summary, my research has applied novel

methods of data analysis and neuron modelling in early vestibular pathways, to provide new insights into the nature of the neural code being used.

Because the works presented in chapters 2&3 are published papers with multiple authors, many written words and choices of analysis are the work of co-authors. For this reason, some additional justification of analysis and clarification of opinions are presented in their opening paragraphs.

CHAPTER 2
The increased sensitivity of irregular peripheral canal and otolith afferents optimizes their encoding of natural stimuli

The main goal of this chapter is to explore whether the vestibular system has evolved neural coding properties that are somehow optimized to the statistical structure of the natural vestibular stimuli to which it has been exposed over evolutionary time scales. To this end, we first record and characterize the natural head movements of monkeys, which were found to be non-Gaussian due heavy tails quantified by a high-kurtosis. It should be noted however that kurtosis can also be increased due to a sharp central peak as well, so higher kurtosis values do not guarantee larger tails of the distributions. We then develop linear-nonlinear (LN) cascade models of vestibular afferents, the first neurons exposed to the natural stimuli (see Appendix A for a comparison of the effects of different nonlinear function parameterizations). A published paper [95] is presented, in which we use these afferent LN models to estimate their optimal stimulus distributions (i.e. those which result in maximizing mutual information; see Appendix B for details of derivations) to assess which afferents are better optimized to process the statistics of natural vestibular stimuli. Although this approach incorporates the afferent transfer function filtering, it is based on maximizing the mutual information between the stimulus and response probability distributions, assuming low levels of firing rate variability (see Appendix C for additional effects of high variability levels). Irregulars are found to be more

optimized than regulars due to their larger gain (even more so for otoliths than canals).

In the first sentence of the second paragraph of section 2.3.4, author MJC wrote "Theoretically, one potential optimal coding strategy is to devote the most neural resources to code for stimuli that will occur most frequently in the natural environment, which maximizes information transmission [9,11,97]". Similarly, in Metzen and Chacron [96], MJC writes, "optimal coding theory predicts that sensory neurons should should be best tuned to stimuli that occur most frequently in the natural environment", citing [9,11] to infer that "a one-to-one match between the gain... and the power content of the natural [stimuli]...[is] consistent with optimal coding." What [9,11] actually says is that under noise-free conditions, the stimulus should be the derivative of the tuning curve, such that it results in the uniform response distribution. Accordingly if the distribution is broader the gain should be lower, and if the distribution is narrower the gain should be higher, for this to happen. If we consider the information rate for time dependent stimuli, Rieke et al. [5] explain that the optimal transfer function will "whiten" the stimulus, by having a high pass filter for low pass stimuli. This is to amplify most the stimuli which occur least often, and amplify least the most commonly occurring stimuli. It is Appendix D that contains additional analysis of the frequency content of natural stimuli, and presents considerations of maximizing the *information rate* via "whitening".

Finally, the following paper draws the conclusion that irregular afferents are better optimized than regular afferents, but it does not consider the possibility that energy constraints play as much of a role as information maximization. The author

of this thesis considers this to be a more plausible hypothesis that is discussed in further detail in Appendix B.

2.1 Introduction

Efficient processing of sensory input is critical for an organism's survival. Because some stimuli are more likely to be encountered than others, it is commonly assumed that the statistics of the natural sensory environment influence the brain's coding strategies [9, 15, 97, 98]. However, this hypothesis remains untested for the vestibular system, which processes head motion information and thus plays a vital role in the stabilization of gaze and control of balance and posture, as well as perception of spatial orientation and self-motion. Notably, addressing whether the coding strategies used by the vestibular system are optimized to process natural stimuli first requires knowledge of the head motion experienced during natural behaviors. The vestibular system is phylogenetically the oldest part of the inner ear and is highly conserved throughout evolution [99]. Vestibular end organ sensors detect head motion across six dimensions (three axes of translation detected by the otoliths and three axes of rotation detected by the semicircular canals; [25,100]. In the absence of motion, afferents display a wide range of resting discharge variability and are characterized as regular or irregular; a classification that correlates with differences in morphological features and response dynamics [26, 27, 101, 102]. Afferent response dynamics have been traditionally measured using artificial self-motion stimuli such as sinusoids or noise with low intensity to ensure that neurons are constrained to their linear ranges [26, 38, 103]. To date only a few studies have reported nonlinear responses to high-intensity vestibular stimuli [30, 31, 36]. However, a recent study performed in humans has revealed that vestibular stimuli can reach large intensities during everyday activities that could elicit nonlinear responses from afferents [104].

Thus, it currently remains unknown whether peripheral vestibular neural responses to natural input can be determined from those to artificial stimuli and whether coding strategies are constrained by the statistics of the natural environment. Here we characterized for the first time the structure of self-motion signals that are experienced by rhesus monkeys during typical natural behaviors. Existing linear models of peripheral processing incorrectly predicted that such stimuli elicit neural responses outside of the physiological range. Accordingly, we then recorded from afferents and developed new models incorporating static nonlinearities that accurately described responses to naturalistic stimuli. Finally, using these models, we tested whether coding by peripheral afferents is constrained by natural stimulus statistics. We found that irregular afferents, because of their higher sensitivities, were more optimized to process natural stimuli than their regular counterparts. Our results therefore have important implications for understanding the contributions of different classes of peripheral sensory neurons to the encoding of natural stimuli, and further provide evidence supporting the hypothesis that the neural coding strategies used by the vestibular system are matched to the statistics of natural stimuli.

2.2 Materials & Methods

2.2.1 Experimental Preparation

All experimental protocols were approved by the McGill University Animal Care Committee and were in compliance with the guidelines of the Canadian Council on Animal Care. Two male macaque monkeys (Macaca fascicularis) were prepared for chronic extracellular recording using aseptic surgical techniques. The surgical preparation was similar to that previously described [105]. Briefly, using aseptic

surgical techniques and under isoflurane anesthesia (0.8-1.5%), a stainless steel post was secured to the animal's skull with stainless steel screws and dental acrylic resin, allowing complete immobilization of the head during the experiments. The implant also held in place a recording chamber oriented stereotaxically toward the vestibular nerve where it emerges from the internal auditory meatus. Finally, an 18-19 mm diameter eye coil (three loops of Teflon-coated stainless steel wire) was implanted in the right eye behind the conjunctiva. After the surgery, buprenorphine (0.01 mg/kg, i.m.) was administered as postoperative analgesia every 12 h for 2-5 d depending on the animal's pain level, and Anafen (2 mg/kg, then 1 mg/kg subsequent days) was used as an anti-inflammatory. In addition, cefazolin (25 mg/kg, i.m.) was injected twice daily for 10 d. Animals were given at least 2 weeks to recuperate from the surgery before any experiments began.

2.2.2 Head movement recording

Head movements were recorded using a microelectromechanical systems (MEMS) module (iNEMO platform, STEVAL-MKI062V2; STMicroelectronics), as done recently for humans [104]. The module combined three linear accelerometers (recording linear accelerations along the fore-aft, lateral, and vertical axes) and three gyroscopes (recording angular velocity about pitch, roll, and yaw). To extend the velocity range to $2000 deg/s$, the MEMS module was augmented with a STEVAL-MKI107V2 three-axis gyroscope. The MEMS module, a battery, and and microSD card were encased in an extremely light (64 g) and small (35x35x15 mm) enclosure, which was firmly secured to the head posts of two macaque monkeys. Specifically, the plane spanned by the fore-aft and lateral axes of the MEMS module was set parallel to the horizontal

stereotaxic plane (i.e., the plane passing through the inferior margin of the orbit to the external auditory meatus; [104]). Data from each of the six sensors were sampled at 100 Hz and recorded wirelessly on an microSD card. Since we were interested in afferent responses to linear motion, we recorded the total gravito-inertial acceleration (GIA; i.e., the sum of gravity and linear motion), which is henceforth referred to as linear acceleration. Note that the data were reported in sensor coordinates in Figures 2.1 and 2.2.

Each monkey was released separately into a large familiar play cage ($9.5m^3$, with a multilevel wooden platform) where it was able to freely move and interact with another monkey from our colony for 160 min while a camera was recording its behavior. We segregated activities into three groups: (1) behaviors associated with low levels of activity that included monkey sitting observing its environment, holding and playing with objects, or grooming; (2) behaviors associated with medium levels of activity that included walking around and foraging; and (3) behaviors associated with high levels of activity that included running, jumping, and climbing, as well as rapid head shaking.

2.2.3 Single-unit recording

During the experiment, the head-restrained monkey was seated in a primate chair mounted on top of a vestibular table in a dimly lit room. The vestibular nerve was approached through the floccular lobe of the cerebellum, as identified by its eye-movement related activity [36, 103, 106]; entry to the nerve was preceded by a silence, indicating that the electrode had left the cerebellum. Extracellular single-unit activity of semicircular canal and otolith afferents was recorded using glass

microelectrodes (24-27 $M\Omega$), the depth of which was controlled using a precision hydraulic microdrive (Narishige). Rotational head velocity and linear acceleration were measured using an angular velocity sensor (Watson) and a linear accelerometer (ADXL330Z; Analog Devices) sensor firmly secured to the animal's head post. Note that vestibular afferents could not be recorded during natural movements due to the technical difficulty of maintaining isolation from single eighth nerve afferents using high-impedance glass micropipettes while the animal underwent such complex and high-intensity dynamic stimuli. Therefore, we used naturalistic stimuli whose time course mimicked that of the natural stimuli. These were generated as done previously [28, 107]. As both naturalistic and natural stimuli tended to consist of excursions whose time course was approximately bell shaped, we quantified them using the following measures: intensity I (maximum value), the full width at half maximum (FWHM), and area under the curve (AuC), which were all computed from the absolute value of the stimulus.

Natural rotation stimuli displayed large heterogeneities as all three quantities were distributed over large intervals (I: 100-1500 deg/s, FWHM: 84-582 ms, AuC: 13-173 deg). The characteristics of our naturalistic rotation stimuli were all within these ranges ($I = 35 \pm 641 deg/s$, $FWHM = 277 \pm 19 ms$, and $AuC = 100 \pm 8 deg$). Natural translation stimuli also displayed large heterogeneities (I: 0.8-8 G, FWHM: 24-228 ms, and AuC: 0.9-5.8 m/s). The characteristics of our naturalistic translational stimuli were also all within these ranges ($I = 0.87 \pm 0.35 G$, $FWHM = 146 \pm 30 ms$, and $AuC = 1.2 \pm 0.3 m/s$).

These stimuli were applied manually since the required velocities and accelerations were beyond the range of our controller. We focused our analysis on horizontal canal afferents ($N = 11$ regular and $N = 25$ irregular) and utricle otolith afferents ($N = 26$ regular and $N = 27$ irregular), since our motion platform was designed to apply stimuli along these axes of motion. For each afferent, stimuli were applied along the preferred axis of rotation (i.e., yaw) or translation (horizontal) as previously described [36, 103]. For otolith afferents, this was achieved by rotating the monkey's head such that the neuron's preferred direction was aligned with the apparatus' axis of translation. During experimental sessions, unit activity, horizontal and vertical eye positions, and head-velocity signals were recorded on digital audiotape for later playback. During playback, action potentials from extracellular recordings were discriminated using a windowing circuit (BAK Electronics). Eye position and head-velocity signals were low-pass filtered at 250 Hz (eight-pole Bessel filter) and sampled at 1 kHz.

We generated binary spike trains, with 1 kHz sampling rate for each afferent. Periods of spontaneous activity (i.e., no head movement) were used to classify afferents as regular or irregular according to the variability in their baseline spiking activity as quantified by the coefficient of variation, $CV = \sigma_{ISI}/\mu_{ISI}$, where μ_{ISI} is the mean inter-spike interval (ISI) and σ_{ISI} is the SD of the ISIs. Because CV varies with mean, the mean ISI, a normalized coefficient of variation (CV^*), was computed using the ISI distribution to quantify resting discharge variability as described previously [108]. Afferents with $CV^* < 0.1$ were classified as regular, while those with $CV^* \geq 0.1$ were classified as irregular as done previously [36, 103]. The firing rate

r(t) was obtained by convolving the binary spike train with a Gaussian centred on the spike time with 10 ms SD. For the purposes of illustration only, we computed the cross-correlation function between the firing rate r(t) and the stimulus s(t) and noted the lag at which it was maximal. This lag was then used to align the response with the stimulus.

2.2.4 Statistical analysis of natural head movements

To test whether natural head movement signals were characterized by probability distributions that differed significantly from Normal, surrogate datasets of the same length with the same mean and variance but drawn from a Gaussian distribution were generated. Probability distributions for both the data and the surrogate datasets were generated with bin widths of 20 deg/s for angular velocities and 0.1 G for linear accelerations. The deviation from normality was quantified using the kurtosis $k = \langle (x(t) - \mu)^4 \rangle / \sigma^4$, where x(t) is the signal, μ is the mean, and σ is the SD. We note that $k = 3$ for a Gaussian distribution. The signals were divided into 20 segments each lasting 8 min and the kurtosis values were obtained for each segment. The kurtosis values obtained from our dataset were then compared with kurtosis values obtained from the Gaussian surrogates.

2.2.5 Linear models of vestibular afferent responses

We first used previously established linear models to predict afferent responses to the experimentally recorded natural stimuli. Specifically, we assumed that the output firing rate $r(t)$ in response to stimulus s(t) is given by the following: $r(t) = H * s(t) + r_0$, where the asterisk denotes a convolution with a filter $H(t)$ and r_0 is the baseline (i.e., in the absence of stimulation) firing rate. We used $r_0 = 104$ Hz for canal

afferents and 79 Hz for otolith afferents, which corresponds to average baseline firing rates observed experimentally [38,103]. Before filtering with these transfer functions, natural angular velocity recorded was projected onto the horizontal semicircular canal plane as done previously [104] using an angle of 22 deg nose down [109]. For canal afferents, the Fourier transform of $H(t)$ (i.e., the transfer function) is given by the following:

$$H_{canal}(s) = k(s(s + 1/T_1))/((s + 1/T_c)(s + 1/T_2)) \tag{2.1}$$

with $S = i2\pi f$. For regular afferents, parameter values were as follows: $k = 2.83(spk/s)/(deg/s)$, $T_1 = 0.0175s$, $T_2 = 0.0027s$, and $T_c = 5.7s$. For irregular afferents, parameter values were as follows: $k = 27.09(spk/s)/(deg/s)$, $T_1 = 0.03s$, $T_2 = 0.0006s$, and $T_c = 5.7s$. Overall, these parameter values are similar to those used previously [89] and were chosen to best match available experimental data [38, 92]. For otoliths, we used the following transfer function [88]:

$$H_{otolith}(s) = k\frac{s^{k_1}(1 + as)^{k_2}}{(1 + bs)} \tag{2.2}$$

with $k = 59.0106(spk/s)/G$; $k_1 = 0.0643$, $k_2 = 2.208$, $a = 0.0138s$, and $b = 0.0255s$ for regular afferents; and $k = 112.7417(spk/s)/G$, $k_1 = 0.3084$, $k_2 = 2.6834$, $a = 0.0136s$, and $b = 0.0318s$ for irregular afferents. As for canal afferents, parameter values were chosen to best match available experimental data [103]. These expressions were used to generate the linear predictions of firing rate responses to natural stimuli shown in Figure 2.3.

2.2.6 Linear-nonlinear cascade models.

To characterize our experimentally observed nonlinear responses of vestibular afferents to naturalistic stimuli, we used linear-nonlinear (LN) cascade models [110, 111] in which the firing rate response $r(t)$ is given by the following:

$$r(t) = T((H * s)(t) + r_0) \tag{2.3}$$

where T is a nonlinear function. We note that, unlike previously used one-stage nonlinear models in which the firing rate at a given time is a nonlinear function of the current stimulus value [30, 38], LN models explicitly take into account neuronal temporal filtering properties [110] that are known to be prevalent in vestibular afferents (for review, see [26]). The LN model was fit to each individual recorded afferent and was used in Figures 2.4 and 2.5. We first estimated the transfer function $H(f)$ using:

$$H(f) = P_{sr}(f)/P_{ss}(f), \tag{2.4}$$

where $P_{sr}(f)$ is the cross-spectrum between the stimulus $s(t)$ and binary spike train response, and $P_{ss}(f)$ is the power spectrum of the stimulus $s(t)$. Note that we only used low-amplitude portions of the stimulus to ensure that the afferent was constrained to its linear regime. The baseline firing rate was then added to this to form the linear prediction $r_L(t)$, which was then plotted as a function of the experimentally observed firing rate $r(t)$ to reveal the shape of the nonlinear function T as done previously [111]. We found that the experimental data could be well fit

by a sigmoidal function:

$$T_{sig}(x) = \frac{c_3}{2}[1 + \mathrm{erf}\left(\frac{x - c_2}{\sqrt{2}c_1}\right)] \tag{2.5}$$

in which c_1, c_2, and c_3, are fit parameters, and erf$(\cdot)$ is the error function. Based on published results [31,38] the parameter c_3, which determines the maximum firing rate, was always 70 spk/s. We also found that the variance of the firing rate distribution could be well fit by a combination of error functions:

$$V(x) = c_1[\mathrm{erf}\left(\frac{x - c_2}{2c_3^2}\right) + \mathrm{erf}\left(\frac{x - c_4}{2c_5^2}\right)] \tag{2.6}$$

In practice, the first half of the experimental data was used to obtain the transfer function and the shape of the nonlinear function T. The LN model was then used to generate a prediction of the response to the second half of the stimulus that was compared with the experimental data. The model's performance was quantified using R^2. The linear model was generated by assuming that $T(x) = x$ instead and was used to generate a linear prediction of the response that was then also compared with the experimental data and its performance was also quantified using R^2. Note that the functions plotted in Figure 2.5 are population averages.

2.2.7 Optimal stimulus distribution that maximizes information

We used the LN model described above for which the response is given by the following:

$$r(t) = T_{sig}((H * s)(t) + r_0) \tag{2.7}$$

with T_{sig} as a nonlinear sigmoidal function. Assuming a stimulus with probability distribution $p(s)$ and a response with probability distribution $p(r)$, the mutual

information between stimulus and response is given as follows [5, 79]:

$$\begin{aligned} I(s,r) &= H(r) - H(r|s) \\ &= \int ds\, dr\, p(r|s)p(s) \log_2 \frac{p(r|s)}{p(r)} \end{aligned} \tag{2.8}$$

where $H(r) = -\int dr\, p(r) \log_2 p(r)$ is the response entropy, $H(r|s) = \int ds\, p(s)\, dr\, p(r|s) \log_2 p(r|s)$ is the noise entropy, and $p(r|s)$ is the conditional response probability. As deterministic linear transformations preserve information, we have $I(s,r) = I(r_L, r)$. Thus, we will only consider the information between the linear prediction $r_L(t) = (H * s)(t) + r_0$ and the response $r(t) = T_{sig}(r_L(t))$. In the noise-free case, there is a deterministic relationship between the linear prediction and the response and we have $p(r|r_L) = T_{sig}(r_L)\delta(r - r_L)$. The mutual information is then given by the following: $I(r_L, r) = H(r)$ and is maximum when [9, 11]:

$$p(r_L) = p_{opt} = T'_{sig}(r_L) / \int_{-\infty}^{+\infty} dz\, T'_{sig}(z), \tag{2.9}$$

where T'_{sig} is the derivative of T_{sig}. If we consider that there is noise, it is not possible to find an analytical expression for the probability distribution $p_{opt}(r_L)$ for which the mutual information is maximum. However, previous studies have found an approximate solution if we assume that $r = T_{sig}(r_L) + \sqrt{V(r_L)}\xi$, where ξ is a Normally distributed random variable with zero mean and variance unity. If the variance $V(r_L)$ is sufficiently small, then the optimal distribution is given by the following [112, 113]:

$$p_{opt} = \frac{T'_{sig}(r_L)}{\sqrt{V(r_L)}} / \int_{-\infty}^{+\infty} dz\, \frac{T'_{sig}(z)}{\sqrt{V(r_L)}}, \tag{2.10}$$

In comparing the expressions obtained with and without noise, it is interesting to note that the noise only appears as a normalization factor. Thus, if the noise variance is constant, then any noise intensity will not alter the shape of the optimal probability distribution.

Finally, to compute the optimal stimulus distribution $p_{opt}(s)$, we inverse filtered a signal with probability distribution $p_{opt}(r_L)$ whose power spectrum was equal to that of the filtered natural stimulus.

2.2.8 Quantifying the distance between probability distributions

To quantify the distance between two probability distributions $p(x)$ and $q(x)$, we used the Jensen-Shannon (JS) divergence defined by the following: $D_{JS}(p||q) = [D_{KL}(p||m) + D_{KL}(q||m)]/2$, where $m(x) = [p(x) + q(x)]/2$ and D_{KL} is the Kullback-Leibler divergence defined by the following:

$$D_{KL}(p||q) = \int_{\infty}^{\infty} dx\, p(x) \log_2 \frac{p(x)}{q(x)} \tag{2.11}$$

2.3 Results

2.3.1 Statistics of natural vestibular stimuli

We recorded the vestibular input experienced by freely moving rhesus monkeys during natural behaviors using a MEMS module that was attached to their heads (Fig. 2.1A; see Materials and Methods). The MEMS module consisted of three linear accelerometers measuring linear acceleration along the fore-aft, lateral, and vertical axes and three gyroscopes measuring angular velocity of rotations along these axes (i.e., pitch, roll, and yaw). We note that the linear acceleration signals that we recorded correspond to the total GIA (i.e., the sum of gravity and linear motion).

We found that natural vestibular stimuli reached large intensities in all six axes of motion (Fig. 2.1B, left), and were described by probability densities that were not Gaussian as they displayed characteristically long tails (Fig. 2.1B, right). This was quantified by large kurtosis values that were all significantly greater than that obtained for a Gaussian distribution (Fig. 2.1C, compare black and red bars), as seen in other sensory modalities [98].

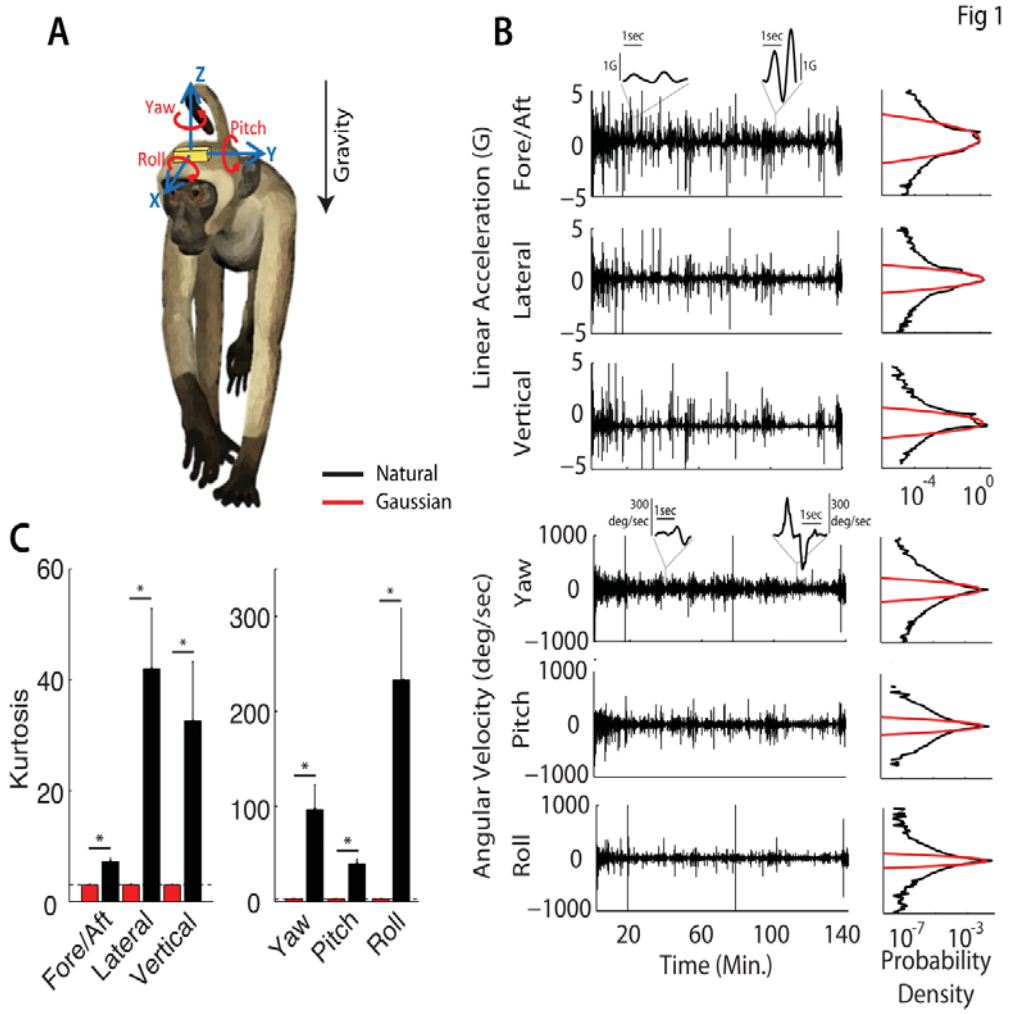

Figure 2.1. Statistics of natural vestibular stimuli in nonhuman primates. A, A MEMS module (gold box) was mounted to the monkey's head. This module recorded linear acceleration along three axes (fore/aft, lateral, and vertical) as well as angular velocity about these three axes (yaw, pitch, and roll).

Figure 2.1 ***(previous page).*** B, Example time series for linear acceleration (top) and angular velocity (bottom) during natural motion. Natural signals displayed probability distributions (black lines) that decayed more slowly than Normal distributions (red lines). Insets show time-expanded example low-amplitude (left) and high-amplitude (right) waveforms. C, Mean kurtosis values for natural stimuli (black) and surrogate Gaussian datasets (red). Note that a Gaussian distribution has a kurtosis equal to 3 by definition. $*p = 0.01$ level. This figure is copied from Schneider et al. [95]

To test whether specific behaviors influence stimulus statistics, we next grouped behaviors into three categories associated with low, medium, and high levels of activity and quantified the statistics of the vestibular input corresponding to each category (Fig. 2.2A; see Materials and Methods). Specifically, periods where the monkey was sedentary and observing its environment, holding and playing with objects, or grooming behaviors were associated with low levels of activity, while those where the monkey was walking around and/or foraging were associated with medium levels of activity. Periods where the monkey was running, jumping, climbing, and was rapidly shaking its head were associated with high levels of activity. Overall, low, medium, and high levels accounted for 63, 28, and 9% of all activities, respectively. We found that the vestibular input experienced during behaviors associated with all three categories displayed probability densities that were for the most part not Gaussian (Fig. 2.2B) as quantified by large kurtosis values (Fig. 2.2C). As expected, vestibular signals associated with low, medium, and high levels of activity were distributed over progressively larger ranges across all six motion dimensions (Fig. 2.2B). The mean, SD, and kurtosis values obtained across low, medium, and high levels of activity for all six motion dimensions are given in Table 2.1.

2.3.2 Traditional linear models of vestibular processing cannot accurately predict responses to natural stimuli

We next tested whether previously published models of early vestibular processing that have been shown to accurately reproduce the responses of peripheral otolith and semicircular canal afferents to artificial stimuli [26,35,36,100,103,111,114] could accurately predict responses to natural stimuli. Linear systems identification techniques were used to find the optimal transfer function that best captures the input-output relationship between head motion and firing rate and predict the firing rate response, henceforth referred to as the linear prediction (Fig. 2.3A). We used established expressions for the transfer functions of regular and irregular semicircular canal and otolith afferents [88, 111] and fitted these to available data [36, 103]. Specifically, prior studies have shown striking differences between the neural coding strategies used by semicircular canal and otolith afferents [36, 103]. Most notably, while the neural sensitivities for irregular afferents are larger than those of their regular counterparts, this difference is much more pronounced for otolith than for semicircular canal afferents (Fig. 2.3B).

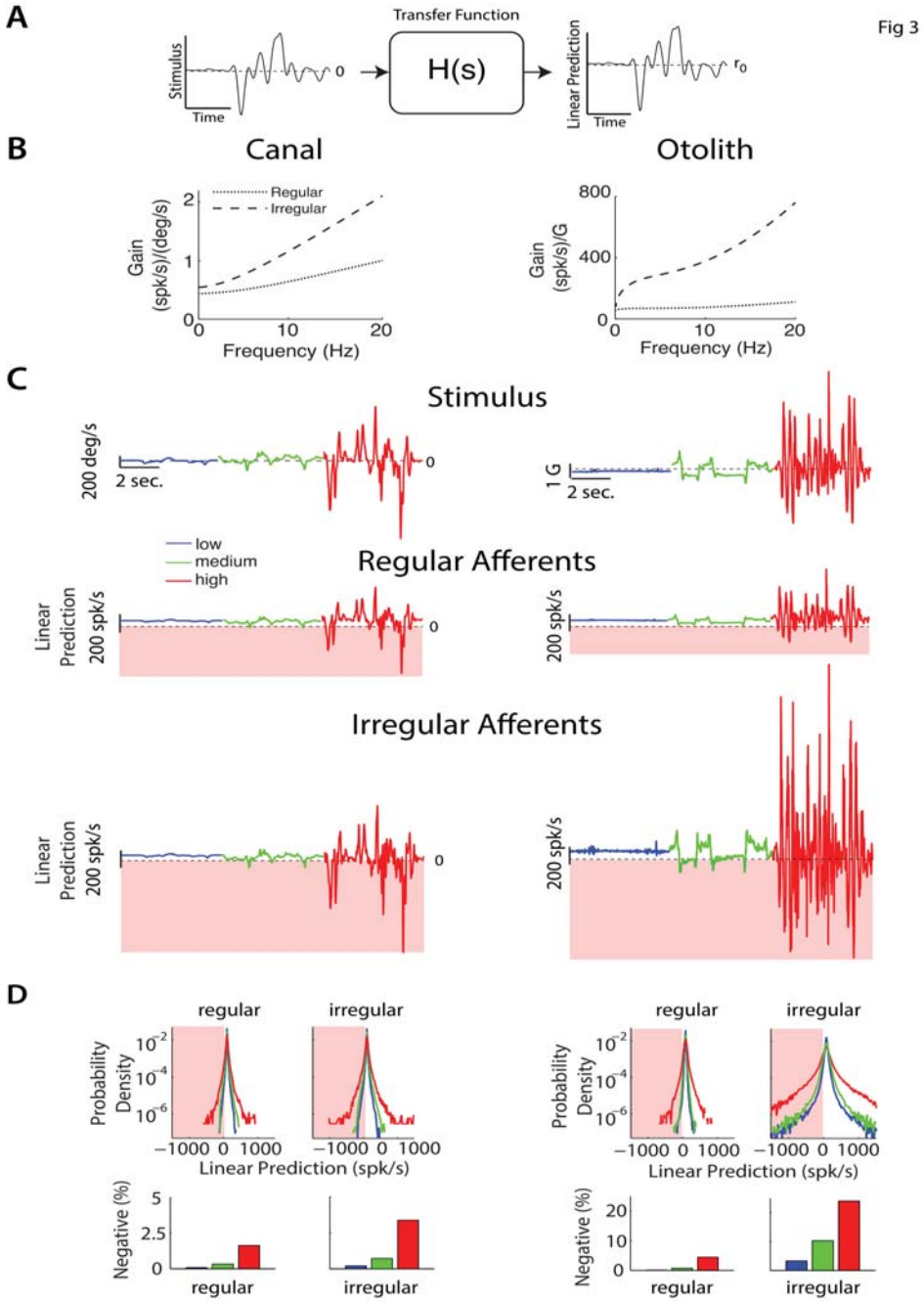

Figure 2.3. Traditional linear models cannot accurately predict vestibular afferent responses to natural stimuli. A, Traditional linear models assume, to obtain the output firing rate, the stimulus is filtered by a transfer function to which a baseline value is added.

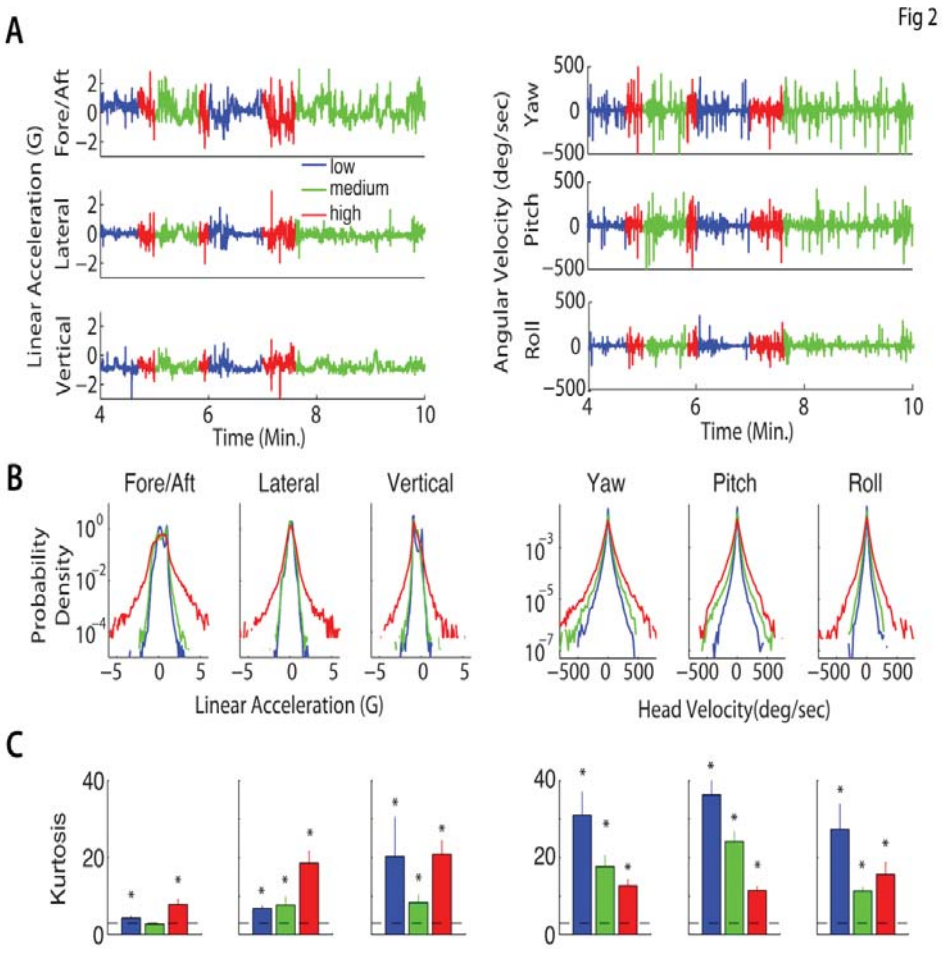

Figure 2.2. Natural vestibular stimulus statistics during low-, medium-, and high-activity behaviors. A, Example time series showing natural head acceleration and velocity traces during low (blue), medium (green), and high (red) levels of activity. B, Probability distributions of natural signals associated with low, medium, and high levels of activity. C, Mean kurtosis values for natural stimuli during low (blue), medium (green), and high (red) levels of activity. The horizontal dashed line indicates the kurtosis value for a normal distribution. Asterisk indicates that the kurtosis is significantly different than that of a normal distribution using a Wilcoxon rank sum test at the $p < 0.05$ level. The kurtosis was always significantly greater than that of a normal distribution except for stimuli-encountered medium levels of activity in the fore-aft translation axis. This figure is copied from Schneider et al. [95]

Table 2.1. Averaged mean, SD, and kurtosis values of natural movements during low, medium, high, and all levels of activity

	Mean ± SE	SD ± SE	Kurtosis ± SE
Fore-aft			
All	0.34 ± 0.05	0.44 ± 0.02	7.18 ± 0.72
Low	0.37 ± 0.06	0.31 ± 0.02	4.30 ± 0.56
Medium	0.36 ± 0.04	0.48 ± 0.02	2.81 ± 0.20
High	0.28 ± 0.05	0.68 ± 0.03	7.86 ± 1.13
Lateral			
All	0.12 ± 0.03	0.25 ± 0.02	42.00 ± 10.84
Low	0.12 ± 0.03	0.17 ± 0.01	6.80 ± 0.71
Medium	0.07 ± 0.03	0.20 ± 0.01	7.69 ± 2.11
High	0.11 ± 0.03	0.41 ± 0.03	18.59 ± 3.03
Vertical			
All	-0.71 ± 0.05	0.27 ± 0.02	32.57 ± 10.73
Low	-0.71 ± 0.06	0.22 ± 0.03	20.26 ± 10.24
Medium	-0.72 ± 0.02	0.23 ± 0.01	8.36 ± 1.93
High	-0.70 ± 0.02	0.36 ± 0.02	20.89 ± 3.45
Yaw			
All	-0.04 ± 0.02	42.07 ± 3.77	96.69 ± 25.77
Low	-0.13 ± 0.07	25.45 ± 2.08	31.00 ± 6.07
Medium	0.23 ± 0.26	43.05 ± 2.43	17.71 ± 2.77
High	-0.58 ± 0.93	74.08 ± 7.87	12.75 ± 1.49
Pitch			
All	0.05 ± 0.01	31.34 ± 2.22	39.72 ± 4.66
Low	0.04 ± 0.04	17.94 ± 1.45	36.31 ± 6.82
Medium	0.18 ± 0.09	35.40 ± 1.91	24.16 ± 2.57
High	-0.34 ± 0.45	65.02 ± 3.05	11.47 ± 0.96
Roll			
All	-0.04 ± 0.01	25.45 ± 2.09	233.11 ± 75.32
Low	0.05 ± 0.06	13.10 ± 0.97	27.35 ± 6.55
Medium	-0.00 ± 0.19	24.35 ± 1.26	11.34 ± 0.93
High	-0.65 ± 0.58	51.43 ± 5.39	15.64 ± 3.06

Figure 2.3 ***(previous page).*** B, Sensitivity of regular (dotted) and irregular (dashed) afferents as a function of frequency for canal (left) and otolith (right) afferents. C, Top, Example time series showing natural stimuli associated with low (blue),medium(green), and high (red) levels of activity, for yaw rotations (left) and fore-aft translations (right). Middle, Predicted firing rate responses from the linear model for regular canal (left) and otolith (right) afferents. In all cases, the model incorrectly predicts negative firing rates (denoted by the shaded red region) during large-amplitude stimulation associated with high levels of activity. Bottom, Predicted firing rate responses from the linear model for irregular canal (left) and otolith (right) afferents. In all cases, the model incorrectly predicts negative firing rates (denoted by the shaded red region) during large-amplitude stimulation associated with high levels of activity. D, Probability distributions of the linear model predictions with the shaded red region showing negative firing rates (top) and percentage of time that the firing rate signal is negative (bottom) for canal and otolith afferents for periods of low, medium, and high levels of activity (i.e., blue, green, and red curves, respectively). Data for regular and irregular afferents are shown on the left and right, respectively. Note that, in C and D,we only show data from yaw and fore-aft motion for simplicity. Similar results were observed for the other four motion dimensions. This figure is copied from Schneider et al. [95]

To test whether these linear models could give rise to physiologically realistic responses during natural behaviors, we used all stimulus waveforms measured during low, medium, and high levels of activity for both rotations and translations. Example stimulus waveforms used are shown in the top of Figure 2.3C for yaw rotations (left) and fore-aft translations (right). We found negative linear firing rate predictions for both otolith and semicircular canal afferents, which is of course outside of the physiological range. The middle and bottom of Figure 2.3C show the responses of regular and irregular semicircular canal (left) and otolith (right) afferents to the example waveforms, respectively. Moreover, the models' tendency to incorrectly predict negative firing rates was greater for stimuli encountered during high levels

of activity (e.g., 1500 deg/s and 8 G). For the same stimulation, linear models also showed a greater tendency to incorrectly predict negative firing rates for irregular afferents due to their larger sensitivities. Quantification of the percentage of time during which the firing rate prediction is negative revealed low values (5%) across all six motion dimensions for regular afferents. However, for irregular afferents, these values exceeded 20% for high levels of activity (Fig. 2.3D). We conclude that existing linear models of vestibular afferent responses (for review, see [26] cannot reliably predict responses to natural stimuli, and that this is especially the case for irregular afferents during the high-amplitude stimuli associated with high levels of activity.

2.3.3 Building LN models of peripheral vestibular afferent responses to naturalistic stimuli

It follows that if our conclusion above is correct, then natural stimuli will elicit nonlinear responses from vestibular afferents. To explicitly test this, we recorded afferent responses to high intensity naturalistic stimuli consisting of either rotation or linear motion whose time course mimicked that seen during natural movements (Fig. 2.1B, insets). We then used LN models [110] to characterize the nature of the nonlinearity in the input-output relationship of vestibular afferents (Fig. 2.4A). These models assume that the output firing rate is calculated by first linearly filtering the input stimulus via a transfer function and then passing the resulting linear prediction through a static nonlinear function (Fig. 2.4A, nonlinear prediction; see Materials and Methods). In practise, for each canal and otolith afferent (Fig. 2.4B), we estimated the transfer function from the response to the low-amplitude portions of the stimulus (see Materials and Methods). We then estimated the shape of the

nonlinearity by plotting the actual firing rate as a function of the linear prediction from the whole dataset. Figure 2.4C compares the performance of both linear and LN models when predicting the firing rate response of an example irregular otolith afferent to naturalistic stimuli. We found that both models provided comparable predictions for low-amplitude stimulus segments (Fig. 2.4C, left). In contrast, we found that the LN model gave a better prediction of the response to high-amplitude stimulus segments (Fig. 2.4C, right) as quantified by more than a twofold larger R^2 value (Fig. 2.4D, inset). This is because the afferent displays cutoff (i.e., ceases to fire action potentials) and saturation during the large negative and positive portions of the stimulus, respectively, which cannot be predicted from the linear model alone (Fig. 2.4C). Consequently, the firing rate response as a function of the linear prediction showed strong deviations from the identity line that were well fit by a sigmoidal function (Fig. 2.4D). Qualitatively similar results were seen for an example irregular canal afferent (Fig. 2.4E,F). Thus, LN cascade models can accurately predict afferent responses to high-amplitude naturalistic stimuli mimicking natural signals. Figure 2.5 shows the results of this same analysis for our populations of canal and otolith afferents where the population-averaged actual firing rate is plotted as a function of the linear prediction. On average, the goodness of fit of LN models was always significantly larger than that of linear models for both regular (Fig. 2.5A,C) and irregular (Fig. 2.5B,D) afferents. However, this difference was most striking for irregular afferents (Fig. 2.5, compare A, B and C, D). Accordingly, consistent with our original hypothesis, we conclude that vestibular afferents do indeed display nonlinear

responses to high-amplitude naturalistic stimuli that can be accurately described by LN models.

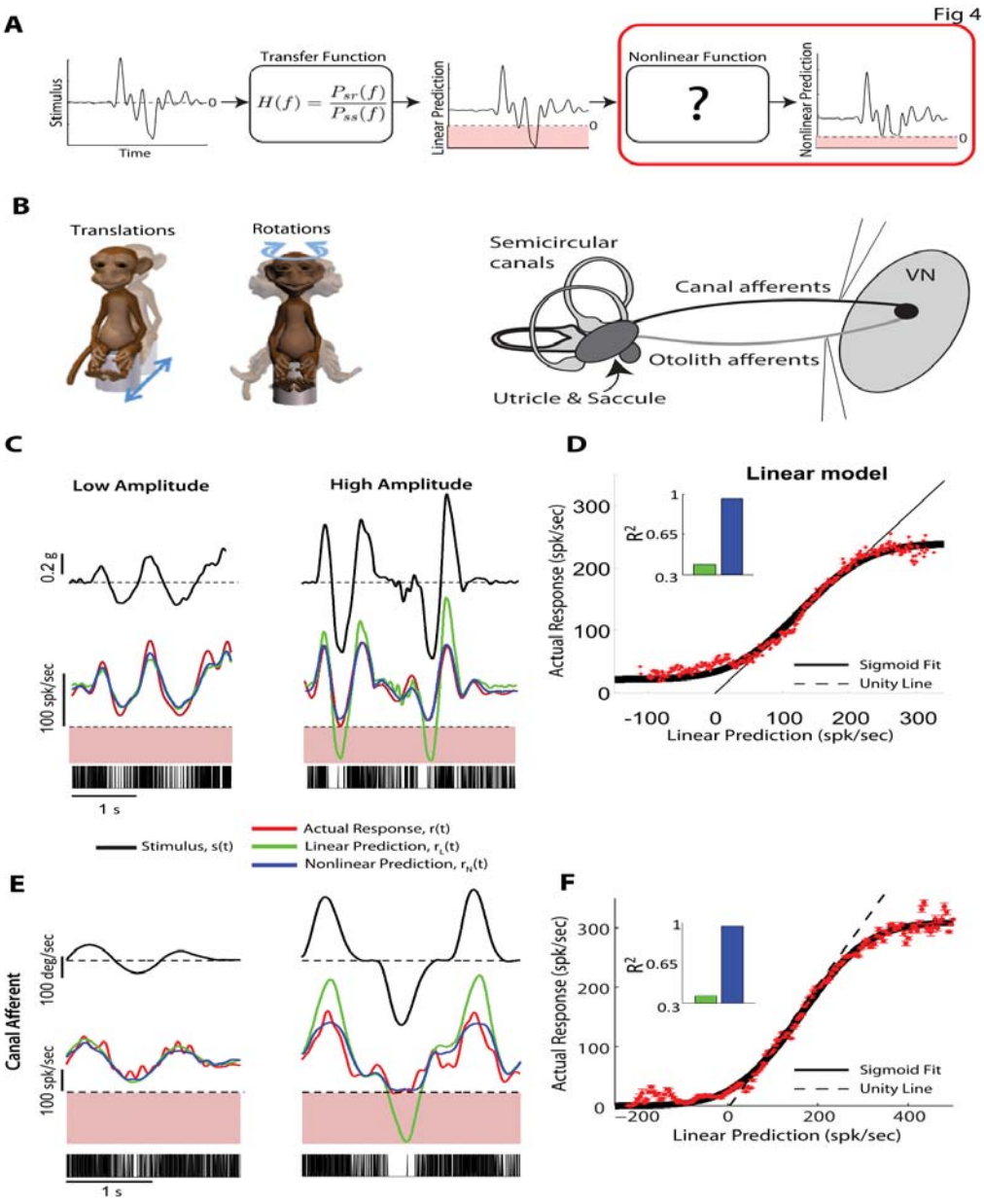

Figure 2.4. LN models can correctly predict vestibular afferent responses to naturalistic stimuli.

Figure 2.4 ***(previous page).*** A, Schematic showing the LN model consisting of first filtering the stimulus with a transfer function to get a linear prediction of firing rate that is then passed through a static nonlinearity to obtain the nonlinear prediction. B, We recorded the responses of both otolith and canal afferent responses to naturalistic rotational and translational stimuli, respectively. VN, Vestibular nuclei. C, Low-amplitude (upper left) and high amplitude (upper right) segments of naturalistic linear acceleration stimuli (compare with insets in Fig. 2.1B). The bottom part shows the actual responses of an example otolith afferent (red), the linear prediction (green), and the nonlinear prediction (blue) to the low-amplitude segment (left) and to the high-amplitude segment (right). The dashed line indicates a firing rate of zero and the shaded red region indicates negative firing rates that are of course physiologically unrealistic. Also shown is the actual spiking response of the afferent (black bars). D, Actual firing rate response as a function of the linear prediction for this otolith afferent reveals that the nonlinear function can be fitted by a sigmoid (black line) and deviates from the unity line (dashed). Inset, Performance as quantified by R^2 of the linear (black) and nonlinear (blue) predictions. E, Low-amplitude (upper left) and high-amplitude (upper right) segments of naturalistic head velocity stimuli (compare with insets in Fig. 2.1B). Bottom, Shows the actual responses of an example canal afferent (red), the linear prediction (green), and the nonlinear prediction (blue) to the low-amplitude segment (left) and to the high-amplitude segment (right). The dashed line indicates a firing rate of zero and the shaded red region indicates negative firing rates that are of course physiologically unrealistic. Also shown is the actual spiking response of the afferent (black bars). F, Actual firing rate response as a function of the linear prediction for this canal afferent reveals that the nonlinear function can be fitted by a sigmoid (black line) and deviates from the unity line (dashed). Inset, Performance as quantified by R^2 of the linear (green) and nonlinear (blue) predictions. This figure is copied from Schneider et al. [95]

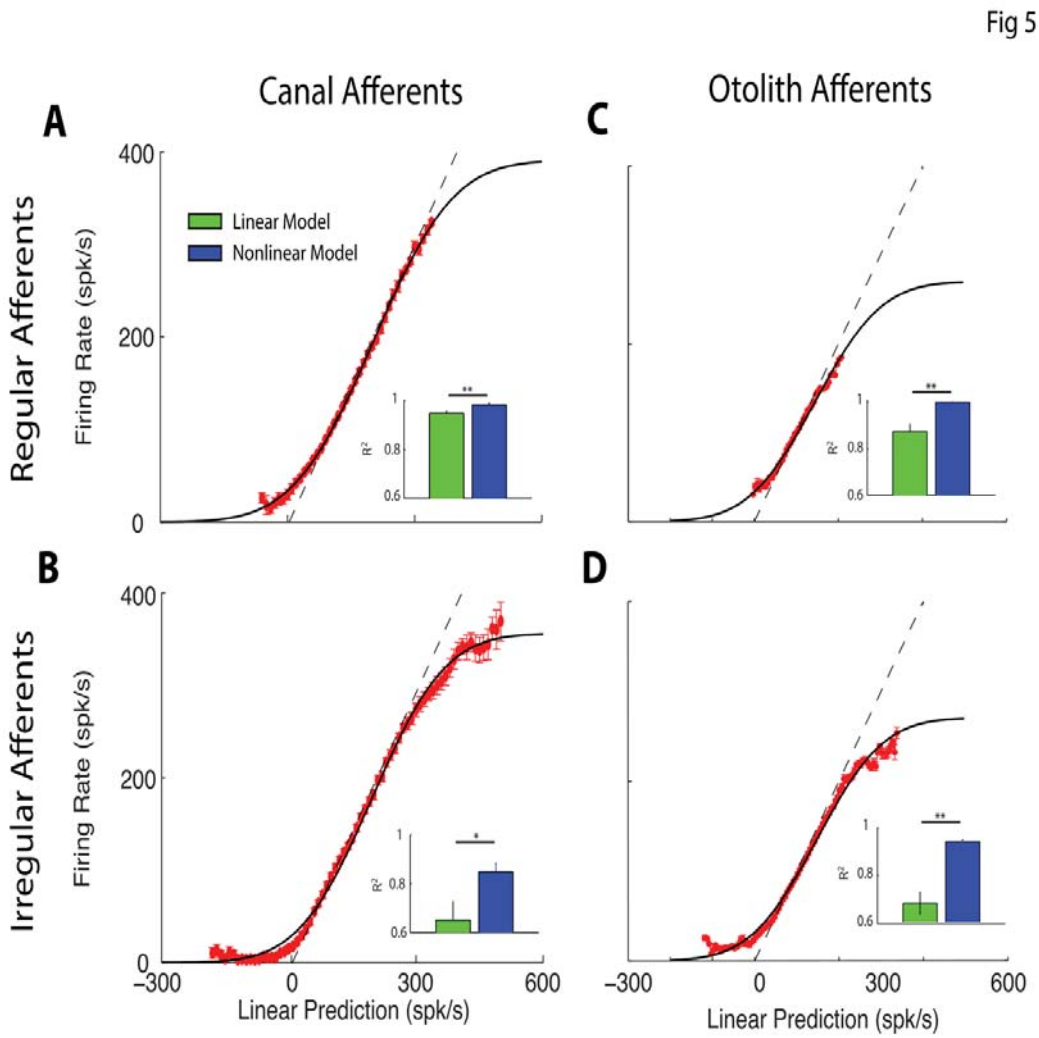

Figure 2.5. Regular and irregular canal and otolith afferents are well described by LN models. A-D, Population-averaged actual response as a function of the linear prediction with best-fit sigmoid (black line) and unity line (dashed) for regular canal (A; $N = 11$), irregular canal (B; $N = 25$), regular otolith (C; $N = 26$), irregular otolith (D; $N = 27$) afferents. $^*p < 0.05$ level using a Wilcoxon rank sum test. This figure is copied from Schneider et al. [95]

2.3.4 Neural heterogeneities in tuning and in trial-to-trial variability influence optimal coding

Our above analyses of canal and otolith afferents demonstrated that those with more irregular resting discharges are likely to be driven into a nonlinear regime during naturalistic stimulation. Thus, peripheral vestibular neural responses to natural input cannot be predicted from those to low-intensity artificial stimuli. We next asked whether, and if so, how the observed differences in coding between regular and irregular afferents (i.e., likelihood of entering the nonlinear regime) as well as those seen between canal and otolith afferents (i.e., differences in sensitivity) are constrained by the statistics of natural sensory input to optimize information transmission. Specifically, are differences in resting discharge variability optimized to code for different features of natural input? Moreover, is such optimization different for canal and otolith afferents?

Theoretically, one potential optimal coding strategy is to devote the most neural resources to code for stimuli that will occur most frequently in the natural environment, which maximizes information transmission [9,11,98]. If we neglect trial-to-trial variability in the neural response (i.e., deterministic), then information is maximized when the firing rate response is uniformly distributed (see Materials and Methods). In this case, the stimulus distribution that maximizes information transmission (i.e., the optimal stimulus distribution; see Eq. 2.9) is simply the derivative of the neuron's input-output relationship (Fig. 2.6A). Figure 2.6B shows two different hypothetical sigmoidal input-output relationships characterized by different levels of steepness. It is thus expected that regular and irregular afferents will have different optimal stimulus distributions due to their differences in sensitivity (Fig. 2.3B).

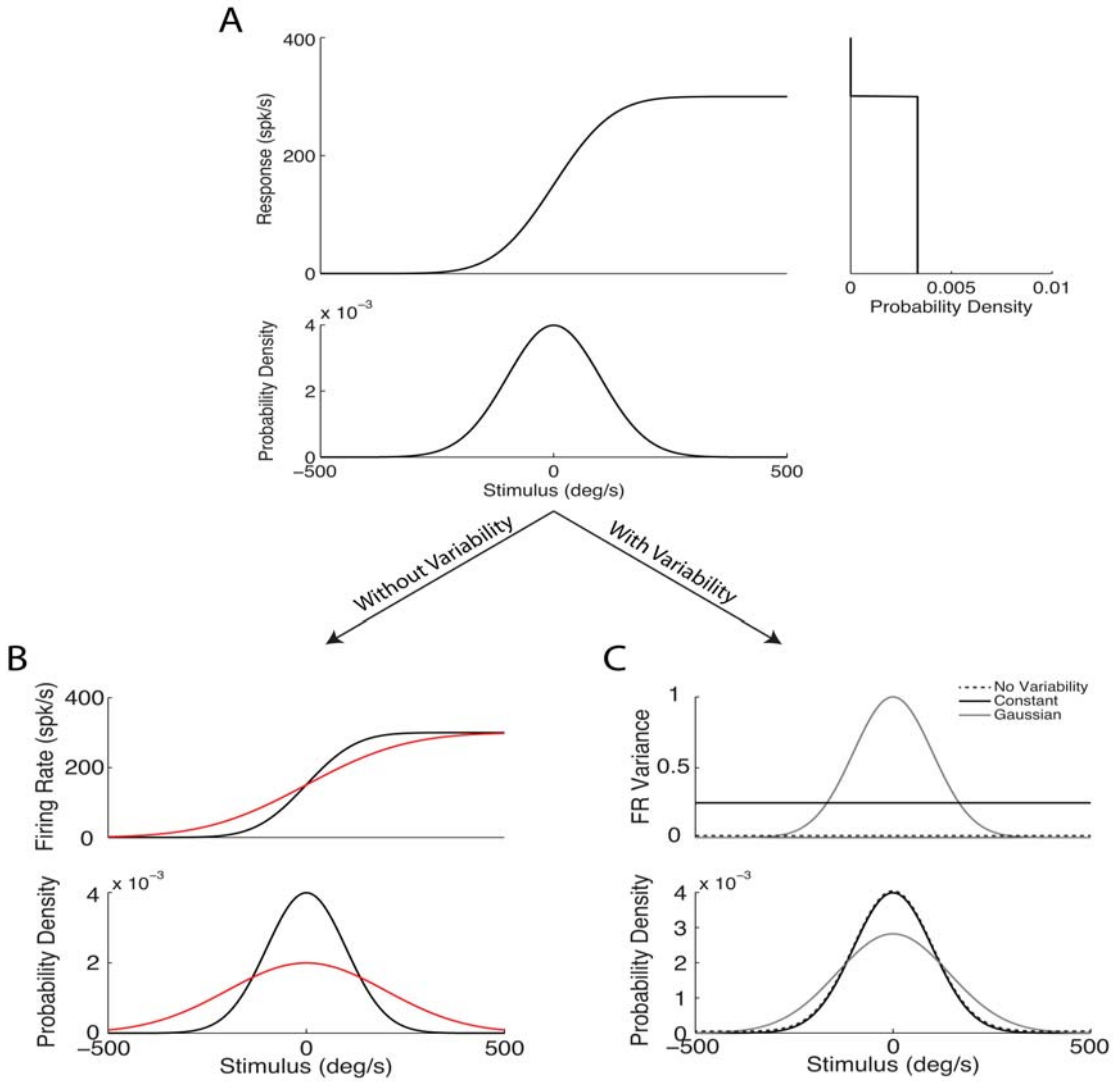

Figure 2.6. Hypothetical effects of neural heterogeneities in tuning and in trial-to-trial variability on optimal coding. A, Differentiating the neuron's input-output relationship (top) provides the optimal stimulus distribution (bottom) that gives rise to a uniform response distribution (upper right), which maximizes information.

Figure 2.6 ***(previous page).*** B, Input-output relationships (top) and their corresponding optimal stimulus distributions (bottom) assuming that variability is negligible. Note that the optimal stimulus distribution becomes narrower as the steepness of the input-output relationships increases (compare red and black curves). C, Input-output relationships (top) and their corresponding optimal stimulus distributions (bottom) when taking variability into account. If the firing rate variance is uniformly distributed (dashed), the optimal stimulus distribution is identical to that obtained when variability is neglected (black). In contrast, if firing rate variance is normally distributed (gray), then the optimal stimulus distribution is wider than that obtained in the deterministic case (compare gray and dashed curves). This figure is copied from Schneider et al. [95]

Additionally, it is well known that regular and irregular afferents display different amounts of trial-to-trial variability. It is thus important to consider the influence of such variability on the optimal stimulus distribution. Theoretical studies have derived an approximate expression for the optimal stimulus distribution taking into account trial-to-trial variability in the form of variance in the firing rate response to a given stimulus [112, 113] (see Materials and Methods). Figure 2.6C shows different distributions for the firing rate variance and how they influence the optimal stimulus distribution for the input-output relationship shown in Figure 2.6A. In particular, if the firing rate variance is normally distributed, then the optimal stimulus distribution is wider than that obtained in the deterministic case (Fig. 2.6C, compare black and gray curves). In contrast, a uniform firing rate variance distribution does not alter the optimal stimulus distribution (Fig. 2.6C, compare black and dashed curves).

Thus, to compute the optimal stimulus distributions for different afferent classes, it is first necessary to characterize, from experimentally recorded afferent responses, the firing rate variance as a function of the stimulus to naturalistic motion. Figure

2.7A shows the firing rate variance as a function of the stimulus for regular canal (top left), irregular canal (bottom left), regular otolith (top right), and irregular otolith (bottom right). Notably, as expected, irregular afferents displayed larger firing rate variances than regular afferents. Importantly, however, the firing rate variance decreased sharply for stimulus intensities that elicit either rectification or saturation (Fig. 2.5). This effect was most pronounced for irregular afferents. Figure 2.7B shows the optimal stimulus distribution neglecting trial-to-trial variability (black curves) and taking into account the variance distributions shown in Figure 2.7A (dashed curves). While some differences are apparent in that the distributions taking into account trial-to-trial variability had slightly larger extent than those obtained by neglecting trial-to-trial variability, both distributions had the same shape and largely overlapped for all afferent classes. To quantify the similarity between distributions, we computed the JS divergence (see Materials and Methods). We found that the JS divergence between regular and irregular afferents with variability was significantly greater than that obtained for either regular or irregular afferents with and without variability ($p \ll 10^{-3}$ in all cases, Wilcoxon rank sum tests with Bonferroni correction; Fig. 2.7B, insets). Thus, we conclude that the different levels of trial-to-trial variability displayed by both regular and irregular canal and otolith afferents have minimal influence on the stimulus distributions that maximize information transmission.

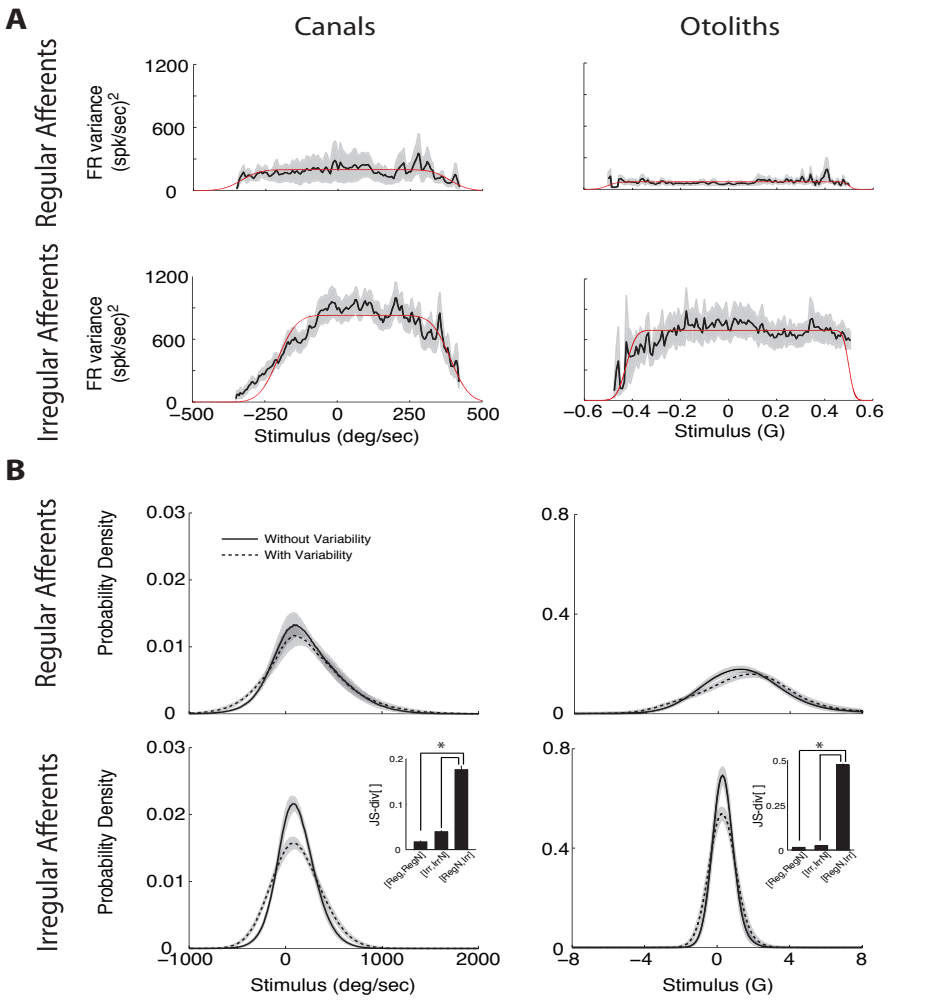

Figure 2.7. Effects of experimentally measured trial-to-trial variability on information transmission. A, Firing rate variance as a function of stimulus amplitude for canal (left) and otolith (right) afferents. Regular afferents (top) displayed less firing rate variance than irregular afferents (bottom). The red lines show the best fits (see Materials and Methods). B, Including the effects of the measured firing rate variance only has minor effects on the shape of the optimal stimulus distribution as can be seen by comparing the dashed (with variability) and black (without variability) curves for regular (top) and irregular (bottom) canal (left) and otolith (right) afferents. The insets show that the population-averaged JS divergence values between regular afferents (with and without variability) and irregular afferents (with and without variability) are significantly greater than those computed between regular and irregular afferents (with variability). $^*p < 0.05$ level using a Wilcoxon rank sum test with Bonferroni correction. This figure is copied from Schneider et al. [95]

2.3.5 Irregular afferents are better optimized to code for natural stimuli than regular afferents

We next explicitly tested whether and how the neural coding strategies used by the peripheral vestibular system are constrained by the statistics of stimuli encountered in the natural environment by comparing the optimal stimulus distributions obtained for each afferent class to the natural distributions. While differences in the trial-to-trial variability do not have much impact on the shape of the optimal distribution (Fig. 2.7B), we hypothesized that the large differences in sensitivity observed for regular and irregular afferents should strongly impact their optimal stimulus distributions. Specifically, as illustrated above in Figure 2.6B, we expected that the larger sensitivities of irregular afferents should lead to narrower optimal stimulus distributions. Figure 2.8A shows the population-averaged optimal stimulus distributions with variability for regular (red) and irregular canal afferents (green), as well as when both populations are combined (cyan), with the natural stimulus distribution (black) superimposed. To facilitate comparison with Figure 2.7, these distributions are also plotted on a linear scale in the inset of Figure 2.8A. Consistent with our hypothesis, the optimal stimulus distribution for irregular afferents was indeed narrower than that obtained for regular afferents. Importantly, we further found that the optimal stimulus distribution of irregular afferents was closer to natural stimulus distribution. Overall, the JS divergence between the optimal stimulus distribution with variability and the natural distribution was always significantly lower for irregular afferents than regular afferents. This was true when we considered either the stimuli arising from all levels of activity or the stimuli arising from either low, medium, or high levels of activity alone (Fig. 2.8B). We performed a comparable analysis on our population

of otolith afferents and obtained qualitatively similar results. Notably, the optimal stimulus distribution (with variability) of irregular otolith afferents was significantly narrower and better matched to the natural distribution in the fore-aft direction when compared with that obtained for regular afferents (Fig. 2.8C) as quantified by significantly lower JS values (Fig. 2.8D). Qualitatively similar results were obtained when comparing the optimal stimulus distributions of irregular and regular otolith afferents to the natural distribution in the lateral direction (population-averaged JS divergence values for irregular vs regular afferents; low: 0.39 ± 0.08 vs 0.73 ± 0.05, medium: 0.33 ± 0.07 vs 0.70 ± 0.04, high: 0.15 ± 0.06 vs 0.56 ± 0.07, all: 0.30 ± 0.07 vs 0.67 ± 0.05, $p < 0.05$ in all cases). Further, the optimal stimulus distributions obtained by pooling across all afferents (i.e., including both regular and irregular subgroups) were not better matched to the natural stimulus distribution than those obtained when only considering irregular afferents (Fig. 2.8A,C, compare green and cyan curves). Finally, we note that irregular otolith afferents were more optimized than irregular canal afferents (Fig. 2.8, compare A, C) as quantified by significantly lower JS values ($p \ll 10^{-3}$ in all cases, Wilcoxon rank sum tests).

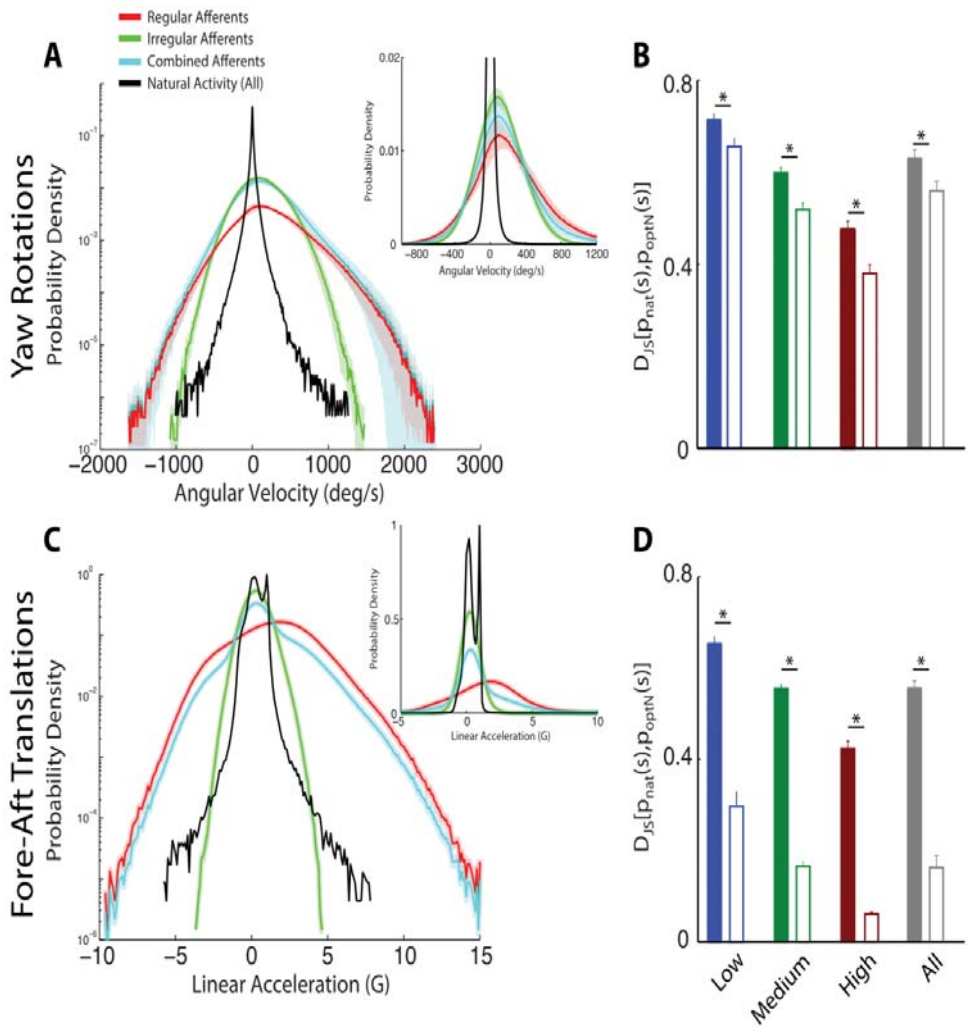

Figure 2.8. Irregular afferents are better optimized to code for natural stimuli than regular afferents. A, Population-averaged optimal stimulus distribution for regular (red) and irregular (green), as well as for both (cyan) canal afferents. The natural stimulus distribution (solid black) is also shown. The bands show ±1 SEM. The inset shows the same distributions plotted on a linear scale. B, Population-averaged JS divergence values quantifying the distance between the optimal stimulus distribution and the natural stimulus distribution for regular (solid bar) and irregular (empty bar) canal afferents for low (blue), medium (green), high (red), and all (black) activities. C, D, Same as A and B, but for otolith afferents, respectively. $^*p < 0.05$ level using a Wilcoxon rank sum test. This figure is copied from Schneider et al. [95]

2.4 Discussion

2.4.1 Summary of Results

Here we studied the statistics of natural vestibular signals experienced by monkeys to determine whether coding is optimized for such stimuli. We found that natural vestibular inputs reached large intensities as evidenced by probability distributions with long tails across all six motion dimensions, similar to those described by [104] for humans. We further found that well established linear models of early vestibular processing could not predict semicircular canal or otolith afferent responses to natural vestibular stimuli. Instead they incorrectly predicted physiologically impossible negative firing rates in response to large-amplitude "off-direction" movements. This was particularly true for the coding of high-intensity activities (e.g., running, jumping, climbing, etc.) by irregular afferents. Accordingly, to develop accurate models, we recorded from afferents during naturalistic rotational and linear motion. We found that linear-nonlinear cascade models could accurately describe neural responses. Thus, we used these models to determine whether afferent coding strategies are constrained by natural stimulus statistics by computing the optimal stimulus distribution that maximizes information. We found that irregular otolith and semicircular canal afferents, due to their higher sensitivities, were better optimized to process natural stimuli. It is therefore likely that the neural coding strategies used by the vestibular system have developed to match the statistics of natural stimuli.

2.4.2 Irregular afferents are better optimized to process natural stimuli

There is growing evidence that sensory systems have evolved coding strategies that are adapted to optimally process natural sensory input [9], for review, see [11]. For example, in the fly visual system, [9] compared the experimentally measured neuronal input-output relationship to that which maximizes information transmission about the natural luminance distribution and found excellent agreement between the two. Here we used a similar approach to compare the natural stimulus distribution to that which maximizes information transmission given the experimentally measured neuronal input-output relationship (Fig. 2.8) and found that irregular afferents better optimized to code for natural stimuli.

Interestingly, the evolution from stem tetrapods to amniotes was accompanied by the appearance of type I vestibular hair cells and a novel afferent terminal with a calyceal ending (for review, see [29]). Previous studies have shown that afferents supplied by type I hair cells tend to be more irregular in their resting discharges [115–117]. It has been hypothesized that type I hair cells evolved in amniotes as an adaptation to changes in natural stimulus statistics resulting from (1) the transition from water (i.e., characterized by resistive hydrodynamic forces) to a land-based environment [29] and (2) neck elongation in amniotes [118]. While it has been suggested these two factors lead to higher amplitude motion in amniotes, at least some anamniote species experience vestibular stimuli with extremely large intensities during natural self-motion (e.g., > 1000 deg/s in the spiny dogfish [119] and 15 G in the swimming pike (for review, see [120]. Thus, it is possible that other factors also contributed to the evolution of the vestibular periphery. For example,

aquatic species might experience more constant vestibular stimulation due to water currents. Further studies comparing the statistics of natural motion across amniotes versus anamniotes are needed to address this important issue.

2.4.3 Nature of the neural code used by the vestibular system to transmit information about natural stimuli

It is generally thought that neurons within early vestibular pathways transmit information about head-motion stimuli in a linear fashion through their time-varying firing rates (i.e., a rate code) rather than through precise timing of action potentials (i.e., a temporal code) [26, 35, 36, 111]. However, previous studies have mostly focused on characterizing neuronal responses to low-amplitude artificial stimuli. As a result modulations in the firing rate were largely constrained to the neuron's linear regime and did not elicit static nonlinearities such as saturation or rectification. Interestingly, our results show that this is also often applicable to the afferent coding of natural vestibular stimuli because monkeys spend much of their time engaged in activities characterized by relatively low-amplitude head motion (i.e., sitting, grooming). However, we found that this was not true for the vestibular stimuli experienced during intermittent high-activity behaviors, such as running, because of their large amplitudes. For such behaviors, the likelihood of nonlinearities (e.g., rectification, phase locking, saturation), open the interesting possibility that the neural code used by the vestibular system to process high-amplitude stimuli is inherently different than that used for low-amplitude stimuli. Further studies will also be needed to test this interesting hypothesis.

2.4.4 Role of variability in neural coding

Neural variability is seen ubiquitously in the CNS but its role in neural coding is highly debated [121, 122]. The peripheral vestibular system is particularly well suited for studying the effects of variability on neural coding because regular and irregular afferents display low and high amounts of variability, respectively. While previous studies have found that variability plays an important role in vestibular coding [26, 35, 36, 103, 111], our results show that sensitivity largely determines the corresponding optimal stimulus distribution (Figs. 2.7, 2.8). Thus, from this point of view, the increased variability of irregular afferents might just be a consequence of their increased gain: the detrimental effects of such increased variability on coding and feature detection can then be reduced by averaging the activities of large afferent populations [36, 103]. The fact that the increased variability and sensitivity are strongly correlated in the vestibular system [103], as they most likely originate from intrinsic properties [37, 91], support this hypothesis. Alternatively, it is theoretically possible that there is a source of sensory noise that is common to all afferents and that is greater for irregular afferents because of their larger sensitivity. Further studies will be needed to test these possibilities.

2.4.5 Coding natural stimuli by otolith versus semicircular canal afferent populations

Previous results have shown that the coding strategies used by otolith afferents to encode linear motion differ markedly from those used by semicircular canal afferents to encode rotational motion [36, 103]. Notably, strong correlations between trial-to-trial variability and sensitivity in otolith afferents are such that their ratio remains constant. As a consequence, neural detection thresholds (i.e., the minimum

stimulus intensity that elicits a detectable change in neural activity) are independent of either resting discharge variability or frequency [103]. In contrast, although a strong positive correlation between variability and sensitivity is also observed for semicircular canal afferents [26], the increased sensitivity displayed by irregular semicircular canal afferents is not sufficient to compensate for their substantially higher trial-to-trial variability. As a result, irregular semicircular canal afferents display higher detection thresholds than regular ones [35,36]. Interestingly, supporting these differences, we found that irregular otoliths are more optimized than irregular canal afferents, which was primarily due to the fact that the differences in sensitivity are far more pronounced in the otolith system. Nevertheless, despite these differences, we further found that both irregular semicircular canal and otolith afferents are more optimized to process natural stimuli when compared with regular afferents, thereby suggesting that both the semicircular and otolith systems have adapted to natural stimulus statistics through common principles.

2.4.6 Implications for higher order processing of natural vestibular stimuli

Our results have important implications for downstream processing and behavior. We have recently shown that vestibular sensory information encoded by eighth nerve afferents is nonlinearly integrated by postsynaptic neurons at the first central stage of vestibular processing (i.e., in the vestibular nuclei [111]). Notably, this nonlinearity generates an intensity-dependent bias in the output firing rate, when low- and high amplitude (or frequency) stimuli are presented concurrently. We speculate that this nonlinear effect will be particularly significant for high-intensity natural behaviors. Finally, we note that although irregular afferents are better optimized

to encode natural stimuli, the combined activities of both regular and irregular afferents most likely contribute to vestibular perception. Previous results obtained using artificial stimuli have led to the hypothesis that regular afferents are better suited to estimate the detailed time course of the stimulus while irregular afferents are instead better suited to detect high frequency features [26, 35, 36]. Such parallel processing of sensory information is a common strategy used across modalities including auditory [123–125], visual [126–128], and electrosensory [129–131], to code for different stimulus attributes. Further studies are needed to test the interesting hypothesis that the vestibular system uses distinct channels of peripheral input to encode different features of natural vestibular stimuli.

CHAPTER 3
In vivo conditions induce faithful encoding of stimuli by reducing nonlinear synchronization in vestibular sensory neurons

In the previous chapter we explored possible afferent responses to natural vestibular stimuli and the range of responses we can expect from them, which form the input to the second stage of vestibular processing: the vestibular nuclei. In this chapter I present a publication [132], in which a conductance-based vestibular nuclei (VN) neuron model originally developed to capture spiking activity recorded *in vitro*, is successfully modified to mimic *in vivo* conditions and shown to be able to reproduce VN neuron activity recorded *in vivo*. This has reconciled a long standing discrepancy in the behaviour of neurons recorded under different conditions, revealing that they may in fact be consistent properties of the same neuron. This provides us with a biophysically detailed model which can be used to potentially explain other VN neuron properties observed *in vivo* (see Appendix E), in terms of their underlying biophysical mechanisms.

Although we show that the increased variability of spiking *in vivo* disrupts the nonlinear phase-locking, allowing the mean firing rate to better track the stimulus, we do not mean to imply that adding noise increases total information about the stimulus. It is possible that nonlinearly-induced phase locking may contain additional stimulus information that can not be encoded in firing rate modulations, however a specific decoding strategy would be necessary to access such information. If instead

a simple rate code decoder is assumed then signal transmission is improved. However as stimulus amplitude is further increased phase locking will eventually return, and it is possible that the system is using this phase-locking as well as the mean firing rate in a population code. Finally, it should be noted that we used a Gaussian white noise low-pass filtered with a cutoff of 50 Hz, and simply increased the noise intensity until the desired spiking CV values were achieved. Other cutoff frequencies were explored and it was found that for lower cutoff frequencies larger noise intensities were required (and vise versa) to achieve the same CV values. Although this could be investigated more thoroughly, more experimental data will be necessary in order to constrain more detailed models of the origin of VN neuron variability.

3.1 Introduction

The vestibular system provides information about head motion relative to space that is necessary for maintaining posture, computing spatial orientation, and perceiving self-motion. Peripheral vestibular afferents encode the detailed time course of either horizontal rotations, vertical rotations, or linear acceleration through changes in their firing rates and spike timing [26, 38, 101, 102]. These afferents project unto neurons within the vestibular nuclei (VN) [133–135]. *In vitro* studies have established that VN neurons in mammals are classified into two main subpopulations (type A and type B) that differ in their responses to current input as well as action potential shape [136–139]. In response to depolarizing current steps, type A neurons show a sustained tonic response while the type B neurons display spike frequency adaptation. Type B neurons moreover display a resonance at frequencies within the behaviorally

relevant range that increases the tendency of small amplitude, high-frequency synaptic inputs to trigger non-linear firing behavior in the form of synchronization to the peaks of the input [27, 140]. This synchronization severely limits the range of input frequencies and amplitudes for which the activity of type B neurons accurately follows the input [94, 140, 141]. In contrast, type A neurons, despite also displaying a resonance, tend to follow the time course of current injection accurately for a much wider range of stimulus amplitudes [27, 140].

In contrast, the results of *in vivo* experiments have shown that the firing of many VN neurons accurately follows the time course of sensory stimulation over the behaviorally relevant frequency range (0-20 Hz) [35, 39]. While this result is at odds with those of *in vitro* studies, it is consistent with the fact that eye movement produced by the vestibuloocular reflex (VOR), which is largely driven by the activities of VN neurons, has a very short latency and is accurate over this same frequency range [92, 142]. How can the same neurons display nonlinear responses such as synchronization *in vitro* and yet accurately follow the time course of sensory input *in vivo*? The discrepancy can be dramatic. For example, Floccular target neurons (FTNs) have been shown to correspond to a subpopulation of type B VN neurons [143, 144] that display the strongest tendency for nonlinear synchronization *in vitro*, yet do not display such synchronization in response to sensory input *in vivo* [39].

Here we test the hypothesis that the apparent discrepancy between VN response dynamics in the *in vitro* and *in vivo* conditions can be explained by an increase in trial-to-trial variability under *in vivo* vs. *in vitro* conditions. To do so, we used

a simplified biophysical model that has been previously used to describe VN neuron activity *in vitro* [94]. We show that this model displays membrane potential oscillations that give rise to a resonance in the membrane potential response. This resonance is transferred to the spiking response and causes nonlinear synchronization to sinusoidal current injections over a wide range of frequencies (0-20 Hz). We then mimicked the high-conductance state that is typical of *in vivo* conditions in our model by increasing the membrane conductance. Moreover, we mimicked their large resting discharge rates by increasing the bias current. Interestingly, both of these changes in parameter values were not sufficient to remove this synchronization that thus severely limits the range of inputs for which our model's response follows the input accurately. However, we show that adding noise to our model in order to mimic the resting discharge variability displayed by VN neurons *in vivo* can be sufficient to eliminate synchronization over the full range of behaviorally relevant frequencies.

3.2 Results

Our biophysical model is based on the Hodgkin-Huxley formalism and consists of a single compartment endowed with several membrane conductances (see Methods and Figure 3.1). Note that a full biophysical justification of the model can be found elsewhere [27, 94]. Although previous studies have shown that this model could display a resonance in its spiking response to sinusoidal current injections [94], they have not systematically explored its dependence on different parameters as well as the interactions between different membrane conductances that underlies its generation.

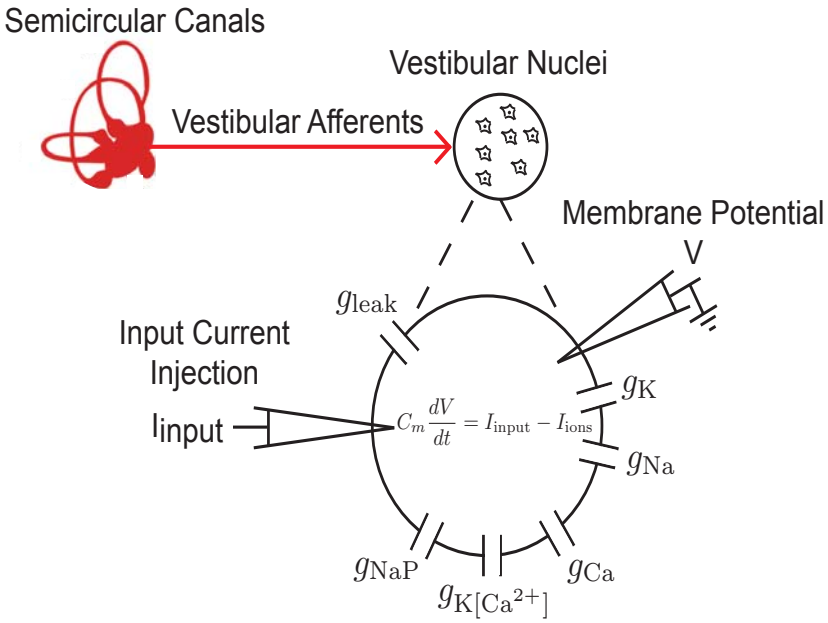

Figure 3.1. Vestibular anatomy and model description. Schematic of peripheral vestibular system, indicating projections from semi-circular canals to the vestibular nuclei (VN). VN neurons were modeled using the Hodgkin-Huxley formalism with several membrane conductances as shown. Sensory input was mimicked by somatic current injection. This figure is copied from Schneider et al. [132].

As it has been previously shown that resonances in the spiking response could be caused by resonances in the membrane potential [145], we first investigated the model's capacity to display membrane potential oscillations in response to current input. To do so, we first turned off the spiking sodium and rectifier potassium conductances by setting their maximum conductances values to zero (i.e. $\bar{g}_{\text{Na}} = \bar{g}_{\text{K}} = 0$ mS/cm^2). We note that this approach is valid for the parameter values used here (see Methods section 3.4).

3.2.1 Intrinsic membrane conductances give rise to damped membrane potential oscillations in the presence of perturbations

It is well known that damped or sustained membrane potential oscillations can arise from the interplay between several membrane conductances including voltage gated calcium channels [146]. The magnitude of these oscillations is furthermore strongly dependent on the amount of depolarizing current bias [145]. As such, we varied both the maximum calcium conductance $\bar{g}_{\mathrm{Ca}}$ and the bias current I_{bias} in our model. We first studied the membrane potential response to step current injections as these have been previously used to demonstrate the presence of membrane potential oscillations [146].

Our results show that the model can display damped membrane potential oscillations with different magnitudes and frequencies for a wide range of I_{bias} and $\bar{g}_{\mathrm{Ca}}$ values (Figures 3.2 A,B,C). We characterized this dependency by systematically varying both I_{bias} and $\bar{g}_{\mathrm{Ca}}$ over a wide range of values and quantified the amplitude of these damped oscillations by computing an oscillation index (see Methods). Further, we computed the oscillation frequency from the squared magnitude of the Fourier transform of the response (see Methods section 3.4). Our results show that, for a given value of the maximum calcium conductance $\bar{g}_{\mathrm{Ca}}$, the oscillation index displays a maximum as a function of the bias current I_{bias} (Figure 3.2 D). The oscillation frequency displayed qualitatively similar behavior to that of the oscillation index (Figure 3.2 E). We note that the oscillation frequency was mostly within the behaviorally relevant range found in natural vestibular stimuli (0-20 Hz) [147]. This indicates that the model can display calcium induced damped membrane potential oscillations, the magnitude and frequency of which are highly dependent on the level

of depolarizing bias current I_{bias}. We note that qualitatively similar results were obtained when varying the persistent sodium conductance $\bar{g}_{\text{NaP}}$ (Figure 3.S1). The results agree with the known effects of persistent sodium, namely to depolarize the membrane and amplify the resonant behavior [146].

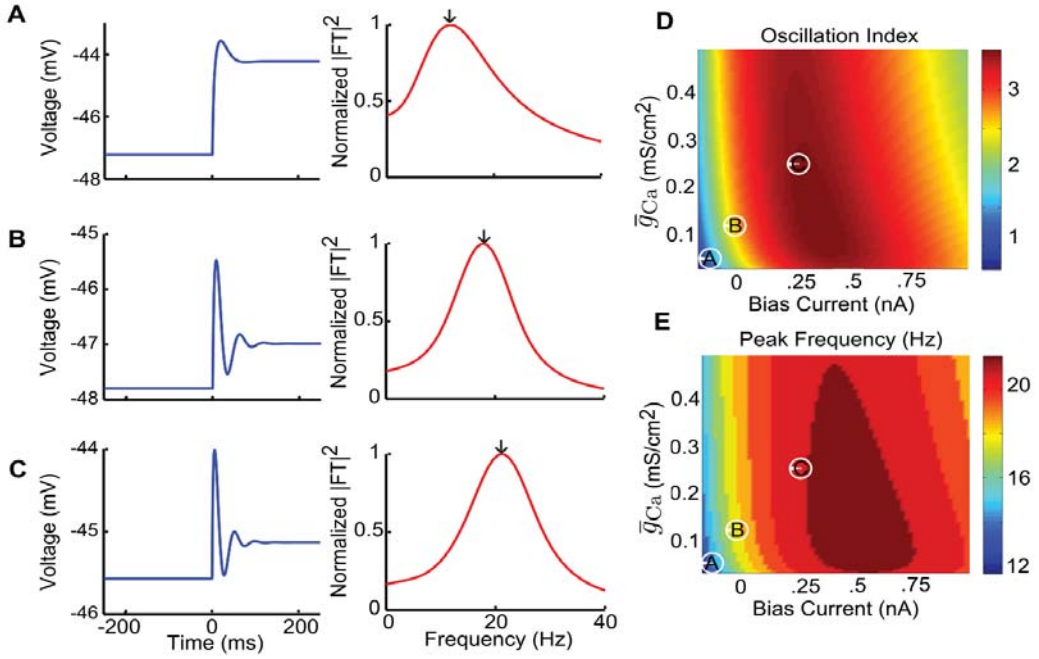

Figure 3.2. The model displays damped membrane potential oscillations in response to step current input. The model's membrane potential response to step current input was characterized for a physiologically plausible range of bias current and calcium conductance values. A-C) Example membrane voltage responses and the normalized squared magnitude of their Fourier transforms. These correspond to parameter values as follows: A) $I_{\text{bias}} = -0.1$ nA, $\bar{g}_{\text{Ca}} = 0.05$ mS/cm^2, B) $I_{\text{bias}} = 0$ nA, $\bar{g}_{\text{Ca}} = 0.125$ mS/cm^2, and C) $I_{\text{bias}} = 0.25$ nA, $\bar{g}_{\text{Ca}} = 0.25$ mS/cm^2. D) Oscillation index (see Methods) measuring the strength of the oscillation in the subthreshold response as a function of I_{bias} and $\bar{g}_{\text{Ca}}$. E) The peak frequency component of the squared magnitude of the responses' Fourier transforms as a function of I_{bias} and $\bar{g}_{\text{Ca}}$. The parameter values corresponding to panels A,B,C are also shown. Other parameter values were: $\bar{g}_{\text{NaP}} = 0.05$ mS/cm^2, $\bar{g}_{\text{KCa}} = 1$ mS/cm^2, and $\sigma = 0$ nA. This figure is copied from Schneider et al. [132].

It is well known that neurons receive massive synaptic bombardment under *in vivo* conditions, which gives rise to a high-conductance state [148, 149]. Mathematically, the increased membrane conductance under such synaptic bombardment can

be mimicked by increasing the leak conductance $\bar{g}_{\text{leak}}$ and by adding an appropriate amount of bias current [145, 150]. As such, we characterized the oscillation index and frequency as a function of both the leak conductance $\bar{g}_{\text{leak}}$ and the bias current I_{bias}. Although increasing the leak conductance $\bar{g}_{\text{leak}}$ decreased the oscillation amplitude, it also decreased the oscillation frequency to values that were contained within the behaviorally relevant frequency range (Figures 3.3 A,B,C). These changes were furthermore seen for a wide range of bias current I_{bias} values. We observed that the oscillation index decreased as a function of the leak conductance $\bar{g}_{\text{leak}}$ for a given value of I_{bias} (Figure 3.3 D). In contrast, the oscillation index displayed a maximum as a function of I_{bias} for a given value of $\bar{g}_{\text{leak}}$ (Figure 3.3 D). The oscillation frequency again displayed qualitatively similar behavior to that of the oscillation index as a function of both $\bar{g}_{\text{leak}}$ and I_{bias} and remained within the behaviorally relevant range (Figure 3.3 E). As such, we conclude that an increased leak conductance is not sufficient to eliminate our model's tendency to display membrane potential oscillations. These oscillations could potentially be detrimental to the model's ability to accurately encode the timecourse of current injections as their frequency is within the behaviorally relevant range. In order to better understand the source of these oscillations, we performed a standard perturbation analysis in our model around the resting membrane potential (see Methods). Our results show that the linearized model gave rise to oscillation indices and frequencies that were quantitatively similar to those obtained with the full model (compare Figures 3.2,3.3 with Figure 3.S2). Moreover, computing the eigenvalues of the Jacobian matrix of the linearized system revealed that they all had a negative real part. As such, the membrane potential

oscillations are stable as our model has a stable fixed point. This is consistent with the damped oscillations that we observed in response to steps (Figure 3.2).

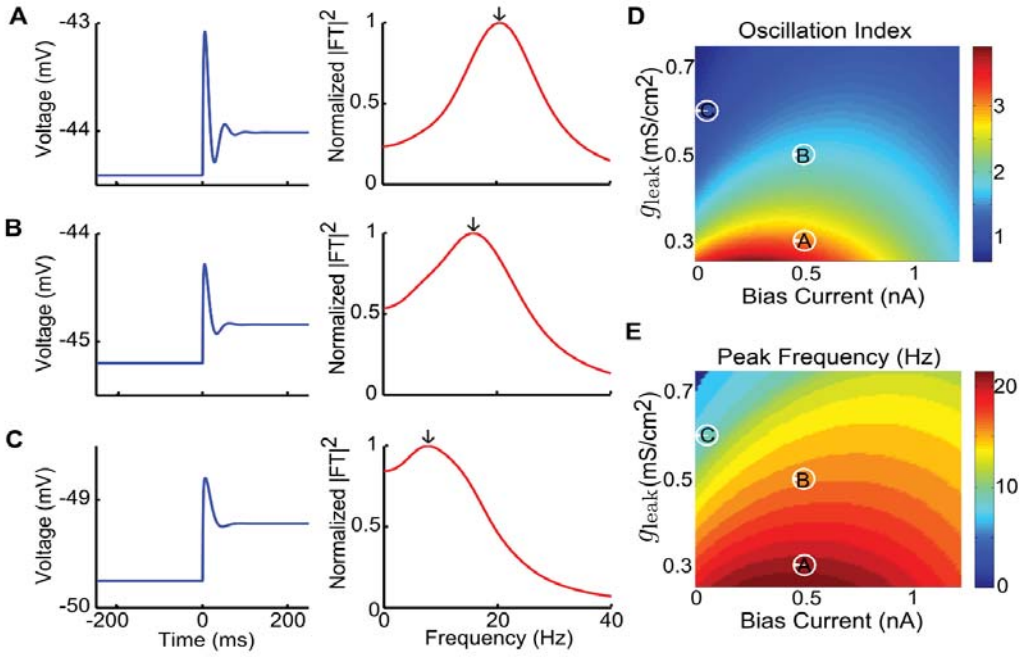

Figure 3.3. Effects of increased leak conductance on membrane potential oscillations. The model's membrane potential response to step current input was characterized for physiologically plausible ranges of bias current and leak conductance values. A-C) Example responses and the squared magnitude of their Fourier transforms. These correspond to parameter values as follows: A) $I_{\text{bias}} = 0.5$ nA, $\bar{g}_{\text{leak}} = 0.3$ mS/cm^2, B) $I_{\text{bias}} = 0.5$ nA, $\bar{g}_{\text{leak}} = 0.5$ mS/cm^2, and C) $I_{\text{bias}} = 0.1$ nA, $\bar{g}_{\text{leak}} = 0.6$ mS/cm^2. D) Oscillation index as a function of I_{bias} and $\bar{g}_{\text{leak}}$. E) The peak frequency component of squared magnitude of the response's Fourier transform as a function of I_{bias} and $\bar{g}_{\text{leak}}$. The parameter values corresponding to panels A,B,C are also shown. Other parameter values were $\bar{g}_{\text{NaP}} = 0.05$ mS/cm^2, $\bar{g}_{\text{KCa}} = 1$ mS/cm^2, $\bar{g}_{\text{Ca}} = 0.25$ mS/cm^2, and $\sigma = 0$ nA. This figure is copied from Schneider et al. [132].

3.2.2 Membrane potential oscillations induce a resonance in the spiking activity.

We next investigated whether the membrane potential oscillations induced a resonance in the membrane potential response and whether this resonance causes a resonance in the spiking activity. As such, we used a zap stimulus (i.e. a sinusoidal waveform with a constant amplitude and a frequency that increases linearly as a function of time; Figure 3.4A) as an input to our model. Such inputs are frequently used to characterize resonant behavior [151, 152]. Our results show that the model does display a resonance in the membrane potential in response to zap current injection for different values of $\bar{g}_{\text{leak}}$ and I_{bias} (Figures 3.4 B,C,D). We note that these responses show asymmetries, which is to be expected since we are using a nonlinear model. We characterized this resonance by an oscillation index that quantifies its magnitude (see Methods) as well as its frequency (i.e. the zap frequency for which the membrane potential oscillation is maximal). Our results show that both the oscillation index and frequency computed from the model's response to zap currents had qualitatively similar dependencies on $\bar{g}_{\text{leak}}$ and I_{bias} to those of the oscillation index and frequency computed from the model's response to step currents (compare Figures 3.4E,F to Figures 3.3D,E, respectively).

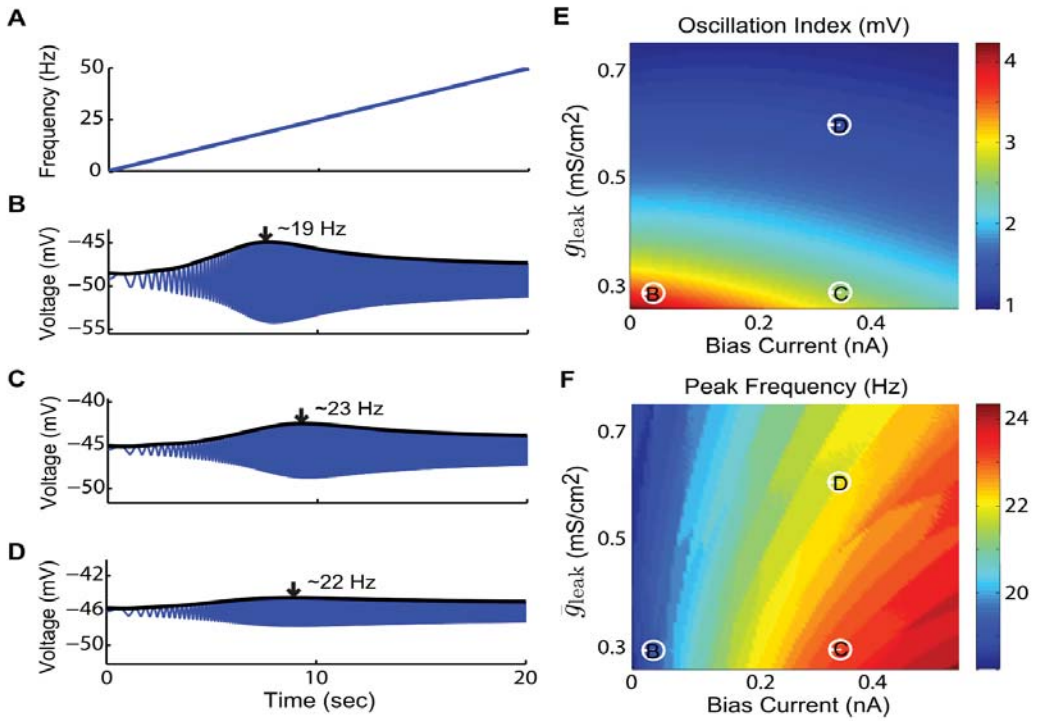

Figure 3.4. Membrane potential responses to zap current input are greatest for a given frequency. The model's membrane potential response to zap currents is greatest for a given input frequency. The magnitude of the response and the input frequency for which it occurs vary with both I_{bias} and $\bar{g}_{\text{leak}}$. A) Instantaneous frequency of the zap stimulus frequency as a function of time. B-D) Example membrane voltage responses as a function of time, corresponding to parameter values as follows: B) $I_{\text{bias}} = 0.05$ nA, $\bar{g}_{\text{leak}} = 0.3$ mS/cm^2, C) $I_{\text{bias}} = 0.35$ nA, $\bar{g}_{\text{leak}} = 0.3$ mS/cm^2, and D) $I_{\text{bias}} = 0.35$ nA, $\bar{g}_{\text{leak}} = 0.6$ mS/cm^2. The envelope of each response is fit with a black curve with an arrow marking the peak in the response and the associated instantaneous frequency. E) Oscillation index (see Methods) as a function of I_{bias} and $\bar{g}_{\text{leak}}$. F) Oscillation frequency as a function of I_{bias} and $\bar{g}_{\text{leak}}$. The parameter values corresponding to panels B,C,D are also shown. Other parameters values were $\bar{g}_{\text{NaP}} = 0.05$ mS/cm^2 and $\bar{g}_{\text{Na}} = \bar{g}_{\text{K}} = 0$ mS/cm^2. This figure is copied from Schneider et al. [132].

How does resonant behavior in the membrane potential relate to resonant behavior in the spiking activity? We investigated this by turning on the spiking conductances (i.e. $\bar{g}_{\mathrm{Na}} = 10$ mS/cm^2, $\bar{g}_{\mathrm{K}} = 2$ mS/cm^2) and by studying the variations in the instantaneous firing rate in response to zap current injection. Our model displayed differential resonant behavior in its spiking activity in its response to zap current injection as a function of the leak conductance $\bar{g}_{\mathrm{leak}}$ and the bias current I_{bias} (Figures 3.5 A, B, C, D). We note that these responses also show asymmetries, which is to be expected since we are using a nonlinear model. In general, parameter values that gave rise to resonance in the membrane potential also gave rise to resonance in the spiking activity (compare Figures 3.4 B,C,D with Figures 3.5 B,C,D, respectively). We further characterized the resonance in the spiking activity by an oscillation index that quantifies its magnitude (see Methods) as well as its frequency (i.e. the zap frequency for which the ensuing variation in the instantaneous firing rate is maximal). Our results show that the oscillation index and frequency computed from the spiking activity had dependencies on $\bar{g}_{\mathrm{leak}}$ and I_{bias} that followed qualitatively similar trends to those of the oscillation index and frequency computed from the membrane potential (compare Figures 3.5 E,F to Figures 3.4 E,F, respectively). Note, however, that the spiking resonance frequency varied over a wider range than the membrane potential resonance. Importantly, the resonance in the spiking regime persisted over a wide range of parameter values and its frequency overlapped with the behaviorally relevant range.

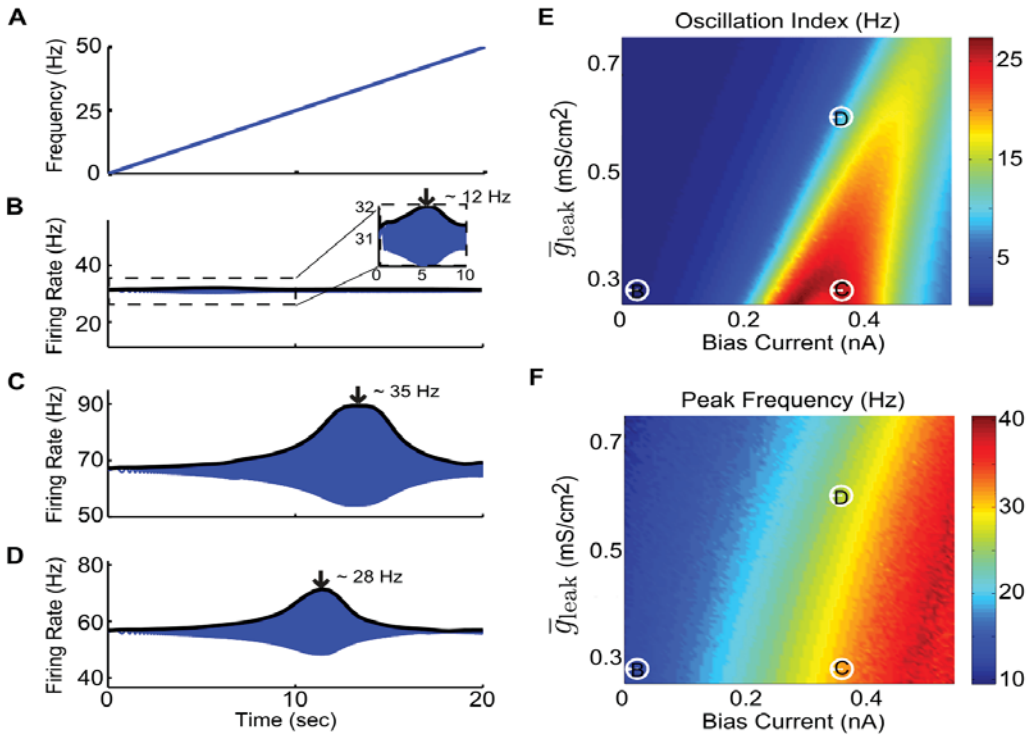

Figure 3.5. Spiking responses to zap current input display a resonance. The model's spiking response to zap current input also displays a resonance whose intensity and frequency vary with both I_{bias} and $\bar{g}_{\text{leak}}$. A) Instantaneous stimulus frequency as a function of time. B-D) Example instantaneous firing rates as a function of time. These correspond to parameter values as follows: B) $I_{\text{bias}} = 0.05$ nA, $\bar{g}_{\text{leak}} = 0.3$ mS/cm^2, C) $I_{\text{bias}} = 0.35$ nA, $\bar{g}_{\text{leak}} = 0.3$ mS/cm^2, and D) $I_{\text{bias}} = 0.35$ nA, $\bar{g}_{\text{leak}} = 0.6$ mS/cm^2. The envelope of the response is fit with a black curve with an arrow marking the location of the maximum response amplitude. E) Oscillation index as a function of I_{bias} and $\bar{g}_{\text{leak}}$. F) Oscillation frequency as a function of I_{bias} and $\bar{g}_{\text{leak}}$. The parameter values corresponding to panels B,C,D are also shown. All other parameters had the same values as previously described except $\bar{g}_{\text{Na}} = 10$ mS/cm^2 and $\bar{g}_{\text{K}} = 2$ mS/cm^2. This figure is copied from Schneider et al. [132].

3.2.3 Increasing variability promotes faithful encoding of the stimulus time course through changes in firing rate

It is expected that the resonance in the spiking activity will lead to nonlinear synchronization of the response with the peaks of the input current that is expected to be detrimental to the faithful encoding of the stimulus' time course through changes in firing rate. This synchronization occurs because of the tendency of excitable systems to display n:m phase locking (i.e. fire n spikes per m cycles of forcing) in response to sinusoidal stimuli [153–155]. We thus characterized the model's response to sinusoidal current injections that mimicked the waveforms of sinusoidal sensory stimuli used experimentally *in vivo* [35,39,92,147,156–159] and systematically varied the frequency of stimulation between 0 and 25 Hz. Our results show that the model tends to display phase locking for high (> 12 Hz) frequencies (Figures 3.6A,B,C). We therefore quantified the model's accuracy at encoding the detailed time course of sinusoidal current injections through changes in firing rate by computing the variance accounted for (VAF, see Methods). Our results show that the VAF was high (≈ 1) for a wide range of I_{bias} values and stimulus frequencies below 5 Hz indicating a strong tendency for faithful encoding of the current stimulus' time course (Figure 3.6D). Increasing the baseline firing rate by increasing the bias current widened the range of stimulus frequencies for which our model displayed negligible phase locking and could faithfully encode the detailed time course of sinusoidal input from 0-5 Hz to 0-10 Hz (Figure 3.6D). However, we observed low VAF values (< 0.1) for stimulus frequencies above 10 Hz for a wide range of I_{bias} values. In order to test whether these low VAF values corresponded to parameter regimes for which our model displays phase locking, we computed a phase locking index (PLI) (see

Methods). As expected, we observed that parameter regimes that gave rise to high VAF also gave rise to low PLI values and vice-versa (compare Figures 3.6 D and 3.6 E). This strong negative correlation between PLI and VAF for a wide range of I_{bias} and stimulus frequencies within the natural frequency range (0-20 Hz) shows that the low VAF values correspond to a strong tendency for phase locking.

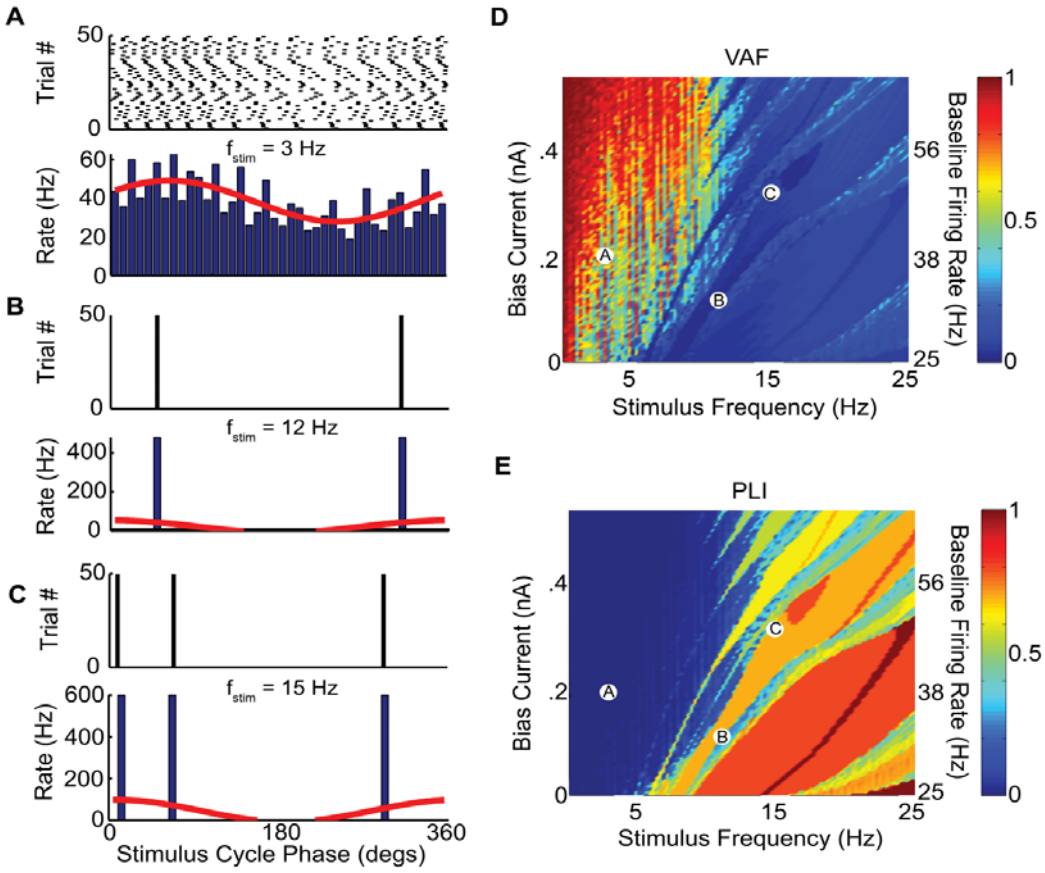

Figure 3.6. Synchronization to sinusoidal input and its consequences on faithful encoding of this input through changes in firing rate. We characterized the model's response to sinusoidal current injections with different frequencies using the phase histogram. A-C) Three example raster plots (top) and phase histograms (bottom) for different values of I_{bias} and f_{stim}. These correspond to parameter values as follows: A) $I_{\text{bias}} = 0.2$ nA, $f_{\text{stim}} = 3$ Hz, B) $I_{\text{bias}} = 0.1$ nA, $f_{\text{stim}} = 12$ Hz, and C) $I_{\text{bias}} = 0.3$ nA, $f_{\text{stim}} = 15$ Hz. Also shown are the best fit sinusoidal curve to each phase histogram (red). D) Variance accounted for (VAF) as a function of I_{bias} and f_{stim}. E) Phase locking index (PLI) characterizing the model's tendency to synchronize to the sinusoidal current as a function of I_{bias} and f_{stim}. It is seen that the VAF is low for parameters for which the PLI is high and vice-versa. The parameter values corresponding to panels A,B,C are also shown. Additional parameters were the same as described previously except $\bar{g}_{\text{leak}} = 0.6$ mS/cm^2. This figure is copied from Schneider et al. [132].

Our simulation results are largely contrary to recordings from VN neurons performed *in vivo*. Indeed, many VN neurons accurately follow the time course of vestibular stimuli through changes in firing rate and do not display synchronization or phase locking for frequencies between 0 and 25 Hz [39]. As our modeling results described above were obtained for high values of $\bar{g}_{\text{leak}}$ and were robust to increases in the bias current I_{bias}, it is unlikely that the discrepancy between our model results and experimental recordings from VN neurons *in vivo* is due to a change in membrane conductance or the fact that VN neurons might be in a depolarized state *in vivo*. Thus, while our results show that increasing the bias current I_{bias} such that the firing rate increases to values seen *in vivo* did increase the range of frequencies for which our model could faithfully encode the time course of sinusoidal input, this alone was not sufficient to eliminate nonlinear synchronization for the full range of frequencies found in natural vestibular stimuli (Figures 3.6D,3.6E,3.7A).

Thus, we hypothesized that the increased trial-to-trial variability that is characteristic of *in vivo* conditions [148, 149] might explain this discrepancy. It is expected that such variability will limit phase locking by inducing firing at all phases of the input and thus promote the faithful encoding of the stimulus waveform by changes in firing rate (see [121] for review). We thus addressed the specific question of whether the levels of resting discharge variability displayed by VN neurons *in vivo* are sufficient to account for the suppression of nonlinear phase locking, which is observed *in vitro*, thereby allowing faithful encoding of the stimulus' time course through changes in firing rate.

In order to test this hypothesis, we systematically varied both the bias current I_{bias} as well as the noise intensity within the experimentally observed ranges of baseline firing rates (Figure 3.7A) and resting discharge variability as quantified by the coefficient of variation (CV) (Figure 3.7B), respectively. We note that previous studies have shown that VN neurons displayed values of CV in their resting discharge ranging from 0.05 to 0.7 [35,39] and resting discharge firing rates between 6 and 170 Hz [35, 39, 157]. Furthermore, we also explored the effects of such increased noise intensities on the model's firing rate resonance, via repeated presentation of the zap stimulus for the same range of bias current values and noise intensities. For higher bias currents (0.4 nA) corresponding to the baseline firing rates seen under *in vivo* conditions ($\sim$ 50 Hz), the addition of noise is seen to reduce the oscillation index (Figure 3.7C). Addition of noise also decreased the oscillation frequency to values near the behaviorally relevant range (Figure 3.7D). As an aside, we note that, for low values of bias current (0.1 nA), we observed a sharp increase followed by a decrease in the oscillation frequency (Figure 3.7D). This sharp increase at low noise intensities is consistent with previous studies showing that, for low noise, model neurons have a resonance at the spontaneous firing rate, while for higher noise intensities, the resonance frequency shifts to lower values [145]. We do not further explore this regime since VN neurons typically have baseline firing rates under *in vivo* conditions that are outside those for which this regime is observed.

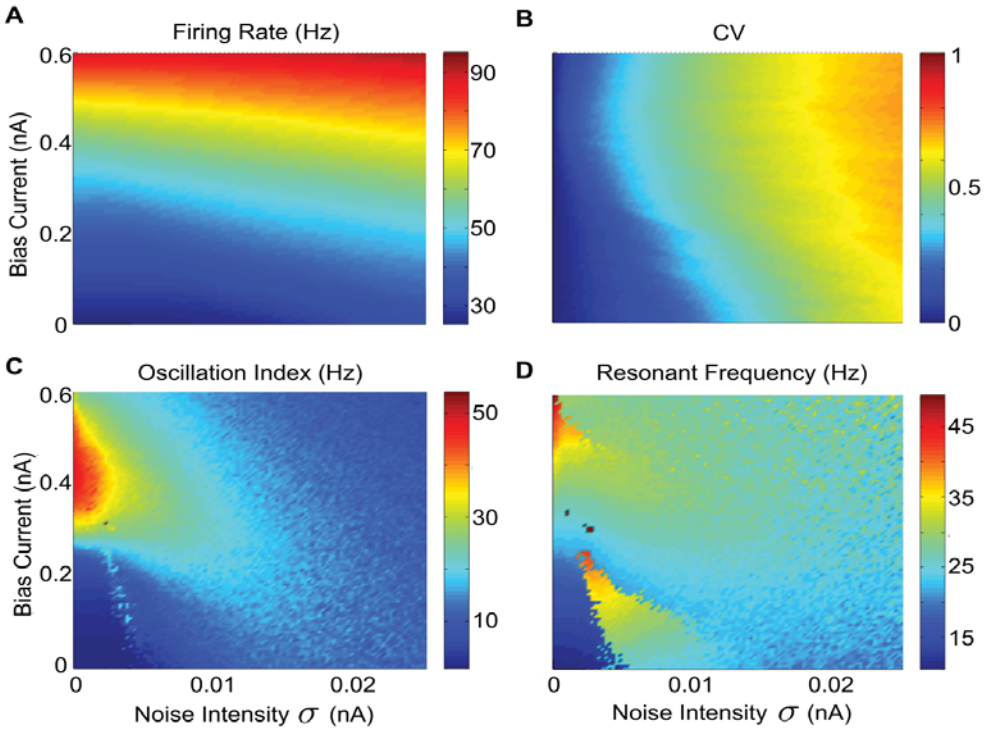

Figure 3.7. Effects of the bias current and noise intensity on resting discharge rate and variability, and resonance strength and frequency. The effects of the bias current I_{bias} and noise intensity σ on the resting discharge rate and variability as quantified by the coefficient of variation (CV) were explored. A) Resting discharge rate as a function of I_{bias} and σ. B) CV as a function of I_{bias} and σ. Parameter values were the same as those previously described. C) Oscillation index from zap stimuli as a function of I_{bias} and noise intensity σ. D) Oscillation frequency as a function of I_{bias} and noise intensity σ. This figure is copied from Schneider et al. [132].

We first recomputed phase histograms in response to sinusoidal current injection (Figures 3.8A,B,C) for the same range of I_{bias} and stimulation frequencies used before but with the addition of noise with a low intensity that gave rise to low resting discharge CV values (0.04-0.24) and with bias currents giving rise to firing rates

between 25-80 Hz in the absence of stimulation. We note that these overlap with the experimentally observed ranges of values [39]. We observed that this noise increased the range of stimulus phases that elicited spiking for higher stimulus frequencies, which reduced phase locking (compare Figures 3.8B,C with Figures 3.6B,C, respectively). However, this noise was not sufficient to completely eliminate phase locking as can be seen from the low VAF and high PLI values observed for high (> 8 Hz) stimulation frequencies for a wide range of I_{bias} values (Figures 8D,E respectively).

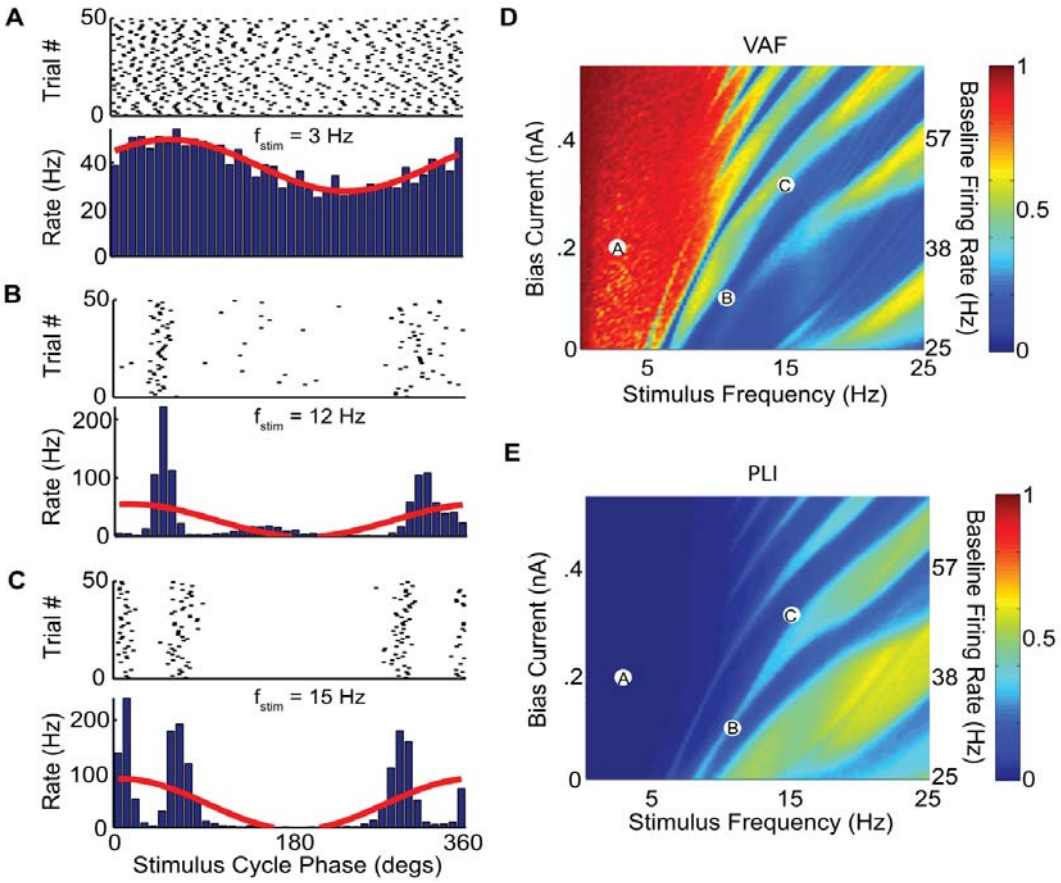

Figure 3.8. Effects of low intensity noise on synchronization to sinusoidal input and its consequences on faithful encoding of this input through changes in firing rate. We characterized the model's response to sinusoidal current injections with different frequencies using the phase histogram as before. A-C) Three example raster plots (top) and phase histograms (bottom) for the same parameter values used in Figure 6 with the best sinusoidal fits (red). D) VAF as a function of I_{bias} and f_{stim}. E) PLI as a function of I_{bias} and f_{stim}. It is seen that low intensity noise somewhat disrupts phase locking but that there are still ranges of parameter values for which the model displays significant phase locking. The parameter values corresponding to panels A,B,C are also shown. Parameter values were the same as those previously described except for $\sigma = 0.0022$ nA. This figure is copied from Schneider et al. [132].

We next performed simulations with a higher noise intensity giving rise to higher resting discharge CV values (0.5-0.7) and bias current giving rise to firing rates from 35-85 Hz. Our results show that the phase histograms in response to sinusoidal current injection were all sinusoidal in shape, even for parameters that gave rise to phase locking in the absence of noise (compare Figures 3.9A,B,C with Figures 3.6A,B,C, respectively). This indicates a lack of phase locking as every phase of the input can now elicit spiking. We recomputed the VAF as a function of I_{bias} and stimulus frequency and found large (> 0.7) values over the entire range explored (Figure 3.9D). Consequently, the model displayed negligible phase locking as quantified by the PLI (Figure 3.9E). Note that the range of values of VAF and PLI used in Figures 3.9D and 3.9E, respectively, were the same as those used previously (compare Figures 3.9D,E with Figures 3.6D,E and Figures 3.8D,E, respectively). As such, this noise intensity was sufficient to eliminate nonlinear phase locking and thereby give rise to faithful encoding of the stimulus waveform through changes in firing rate for all stimulus frequencies within the behaviourally relevant range.

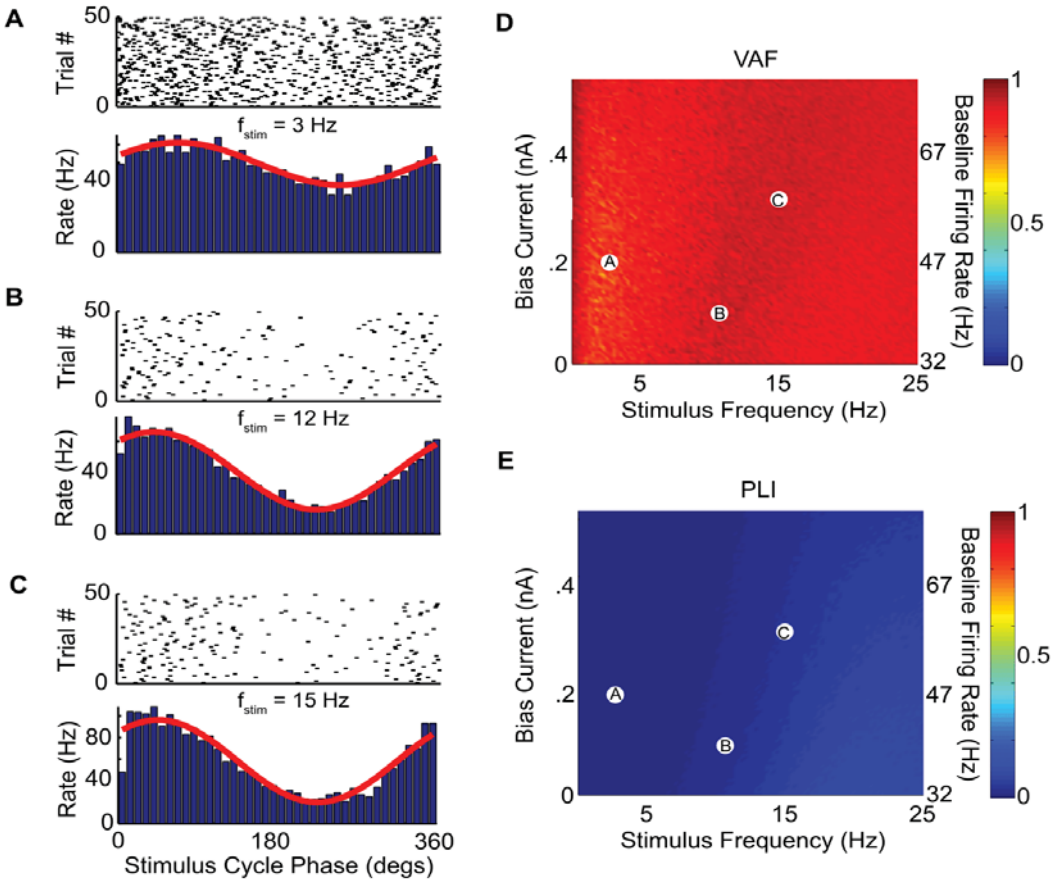

Figure 3.9. Effects of high intensity noise on synchronization to sinusoidal input and its consequences on faithful encoding of this input through changes in firing rate. We characterized the model's response to sinusoidal current injections with different frequencies using the phase histogram as before. A-C) Three example raster plots (top) and phase histograms (bottom) for the same parameter values used in Figure 3.8 with the best sinusoidal fits (red). D) VAF as a function of I_{bias} and f_{stim}. E) PLI as a function of I_{bias} and f_{stim}. It is seen that high intensity noise eliminates phase locking and promotes faithful encoding of the input waveform by changes in firing rate as can be seen from the sinusoidal phase histograms, high VAF values, and negligible PLI values. The parameter values corresponding to panels A,B,C are also shown. Parameter values were the same as those previously described except for $\sigma = 0.0225$ nA. This figure is copied from Schneider et al. [132].

In order to verify the robustness of our results, we also computed a second measure of nonlinear synchronization, the nonlinearity index (NI, see Methods), that is based on the ratio of the Fourier coefficient amplitude squared at the second harmonic to that at the stimulus frequency. This measure had qualitatively similar behavior to that of the PLI measure as a function of the bias current I_{bias}, stimulus frequency, and noise intensity (compare Figure 3.S3 to Figures 3.6,3.8,3.9).

Finally, in order to test that these results were not an artifact of our using current input, we used conductance input rather than current input stimuli in our model. The effect of noise on phase locking in this model (Figure 3.S4) were in qualitative agreement with those shown in Figures 3.6,3.8, and 3.9, illustrating the robustness of our main result to the type of input used. We note that this outcome was expected given that increasing the membrane conductance alone was not sufficient to completely eliminate phase locking over the behaviourally relevant frequency range.

The effects of noise intensity on our model's ability to accurately encode the time course of sinusoidal current injections through changes in firing rate are summarized in Figure 3.10. While the PLI rapidly decreases as a function of increasing noise intensity, the VAF rapidly increases (Figure 3.10A). For comparison, the resulting firing rate and CV values in the absence of stimulation are also shown for the same noise intensities (Figure 3.10B). Because high noise intensities were sufficient to eliminate nonlinear phase locking from our model, we used linear systems analysis to characterize the relationship between input and output in our model. Specifically, we computed the gain (i.e. the coefficient relating input and output) as a function

of I_{bias} and stimulus frequency. Our results show that the gain increases smoothly as a function of stimulation frequency for a given value of I_{bias} in the presence of high noise but not so when noise is not present (Figures 3.10C, D). This result is important as previous studies conducted *in vivo* have shown that VN neurons generally display increasing gains as a function of stimulus frequency [35, 39]. Our results therefore suggest that the high-pass filtering characteristics seen in most VN neurons *in vivo* which are due, at least in part, to an intrinsic resonance. This resonance is attenuated by the high resting discharge variability that results from the intense convergent synaptic input that the cell receives under *in vivo* conditions.

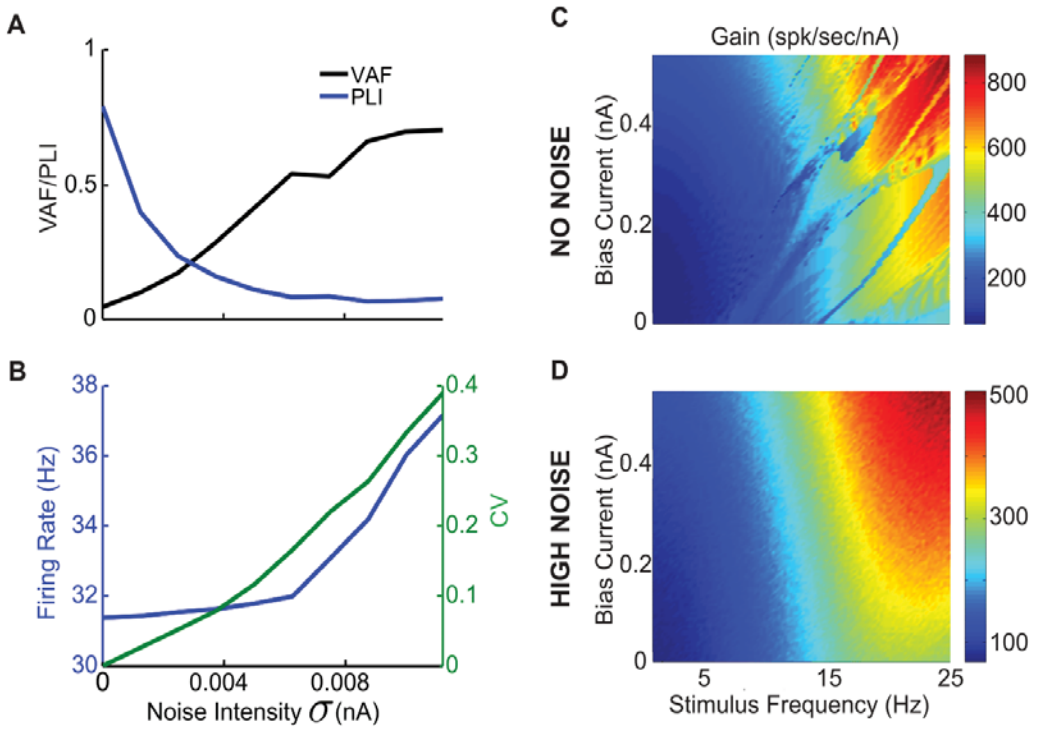

Figure 3.10. Effects of varying noise intensity on the VAF and PLI. A) Increasing noise intensity results in decreased PLI and consequently increased VAF values for $I_{\text{bias}} = 0.1$ nA and $f_{\text{stim}} = 12$ Hz. B) Increasing noise intensity also results in increased resting (ie $S(t) = 0$) discharge rate as well as increased spiking variability as quantified by CV. C) Gain obtained from our model with no noise ($\sigma = 0$ nA) as a function of I_{bias} and f_{stim}. D) Gain obtained from our model with high noise intensity ($\sigma = 0.0225$ nA) as a function of I_{bias} and f_{stim}. It is seen that for a given value of I_{bias} the gain increases as a function of the input frequency f_{stim} until about 22 Hz. This figure is copied from Schneider et al. [132].

3.3 Discussion

3.3.1 Summary of results

The goal of this study was to resolve an apparent discrepancy between the responses of VN neurons to current injection *in vitro* and to sensory input *in vivo*.

VN neurons are prone to display nonlinear responses such as synchronization to the peaks of sinusoidal current injection *in vitro*. In contrast, studies performed *in vivo* have shown that VN neurons can respond to sensory input through changes in firing rate that accurately follow variations in sensory stimulation over a wide frequency range [39]. We investigated the cause for this discrepancy by subjecting a mathematical model based on the Hodgkin-Huxley formalism of *in vitro* VN neuron activity to *in vivo* conditions.

Our results show that this model displays membrane potential oscillations that persisted for a wide range of parameter values. These oscillations give rise to a resonance in the membrane potential which is transmitted to the spike train, causing nonlinear behavior such as synchronization or phase locking over the natural stimulus frequency range (0-20 Hz). It is well known that neural variability resulting from the intense synaptic bombardment to which VN neurons are subjected to *in vivo* will promote faithful encoding of the stimulus waveform through changes in firing rate [121]. As such, we tested the hypothesis that the levels of resting discharge variability seen under *in vivo* conditions could account for the fact that some VN neuron classes do not display synchronization *in vivo*. To do so, we added noise whose intensity was calibrated in order to match the resting discharge variability experimentally observed in VN neurons under *in vivo* conditions. We found that low noise intensities did not completely eliminate phase locking behavior. In contrast, we found that high noise intensities almost completely eliminated phase locking and that our model could now faithfully encode the time course of sinusoidal current injections at frequencies contained within 0-20 Hz for a wide range of input bias

currents. These results are consistent with experimental recordings from VN neurons *in vivo*, suggesting that the addition of noise in the *in vivo* condition underlies the discrepancy between the responses of VN neurons to current injection *in vitro* and to sensory input *in vivo*. Furthermore, they suggest that the vestibular system uses increases in variability to increase the fidelity of encoding by single neurons. This strategy appears to be found across several sensory systems (reviewed in [121]).

3.3.2 Correspondence between anatomy and function in VN

In the present study, we focused on the type B neurons as observed *in vitro*. This is because these neurons display the greatest tendency to respond to sinusoidal current injection with synchronization as well as spike frequency adaptation. In contrast, type A neurons show a sustained tonic response and faithfully follow the time course of sinusoidal current injections that are up to three times larger than those followed by type B neurons [136–140]. The differences between type A and type B neurons are thought to be mediated by differences in the levels of different membrane conductances [27,94]. In particular, type B neurons display larger calcium-activated conductances [140]. Such currents mediate spike frequency adaptation (see [160,161] for review). Theoretical studies have shown that spike frequency adaptation leads to high-pass filtering of time varying stimuli [162–164], which is consistent with our modeling results showing an increased gain for higher frequencies. We note that one could use the same model as was used here in order to mimic the activity of type A VN neurons by changing membrane conductances as was done previously [94]. We predict that a model of type A VN neuron activity would not display phase locking

for the sinusoidal current injections considered here but would display phase locking for larger amplitudes.

In vivo studies have found three major functional neuronal classes in MVN that are based on the responses to voluntary eye movements and passive whole-body rotation: 1) Vestibular-Only (VO) neurons, 2) Position-Vestibular-Pause (PVP) neurons, 3) Floccular Target neurons (FTN). VO neurons project to the spinal cord and are thought to mediate vestibulo-spinal reflexes that control posture [66,165,166], as well as cerebellum and thalamus [167,168], where they are thought to play a role in spatial orientation computation. The vestibular system also generates the vestibulo-ocular reflex (VOR) that functions to effectively stabilize gaze by moving the eye in the opposite direction to the on-going head motion. The three-neuron arcs mediating the VOR are well characterized. The primary pathway consists of projections from afferents to PVP neurons, which in turn project to extraocular motoneurons that control the eye muscles. A secondary pathway is mediated via FTN neurons that receive direct input from the Floccular lobe of the vestibular cerebellum and also project to the extraocular motoneurons. The correspondence between type A and B MVN neurons as observed *in vitro* and the different functional classes observed *in vivo* is not well understood in general. The most direct link that has been made to date is based on the findings of electrophysiological and anatomical studies that suggest a subpopulation of type B neurons receive input from Floccular purkinje cells, such that they most likely correspond to the FTN neurons which have been characterized *in vivo* [143,144]. This correspondence between type B cells and FTN cells, however,

is unexpected since *in vivo* experiments have shown that FTN neurons do not display robust phase locking and instead respond to sinusoidal head rotations through changes in firing rate that scale with stimulus intensity for frequencies spanning the behaviorally relevant range *in vivo* [39]. Thus, our results provide a potential explanation of this discrepancy originating in the intense synaptic bombardment that these neurons receive *in vivo*.

The correspondence between VO and PVP neurons *in vivo* and type A/B neurons *in vitro* is not known. However, previous studies have shown that PVP neurons display nonlinear phase locking behavior in response to high frequency (> 12 Hz) sinusoidal rotations [39]. This is consistent with our modeling results showing that phase locking is not abolished for low noise intensities (Figure 3.8). Our results therefore predict that: i) PVP neurons should have type B like responses *in vitro*; ii) PVP neurons with low resting discharge rates will display a greater tendency for phase locking and, iii): this tendency is a consequence of their low resting discharge variability. Previous studies have reported that VO neurons do not display phase locking dynamics but have only explored frequencies between 0 and 4 Hz [169]. Further studies are needed to explore VO neuron responses to higher stimulus frequencies and might help elucidate their correspondence with either type A or type B neurons.

In conclusion, while it is clear that the filtering properties of VN neurons as observed *in vivo* are shaped by intrinsic mechanisms [140], our simulations are consistent with a growing body of literature emphasizing the role of network mechanisms [164, 170] such as synaptic bombardment that is present under *in vivo* conditions affecting their responses to sensory input.

3.3.3 Sources of variability in VN

What are the sources of resting discharge variability in VN neurons? A unique aspect of the vestibular system, compared to other sensory systems, is that information processing is strongly multisensory and multimodal at the first stage of central processing. This occurs because the vestibular nuclei receive inputs from a wide range of cortical, cerebellar, and other brainstem structures in addition to direct inputs from the vestibular afferents. First, there is complete overlap in the terminal fields of regular and irregular afferents in each of the major subdivisions of the vestibular nuclei [171], and the results of electrophysiological studies have shown that about half of the VN neuron population receive significant input from both afferent classes [133, 134]. Additionally, not only do neurons typically receive convergent input from otolith as well as canals afferents, but there is an impressive convergence of extra-vestibular information within the VN (reviewed in [25]). Notably, sensory inputs encoding somatosensory, proprioceptive, and visual information as well as premotor signals related to the generation of eye and head movements are sent directly to the vestibular nuclei. In alert animals, these extra-vestibular signals strongly modify the processing of vestibular information during our everyday activities, such that this convergence plays an important role in shaping the 'simple' sensory-motor

transformations that mediate vestibulo-ocular and vestibulo-spinal reflexes as well as higher-order vestibular functions, such as self-motion perception and spatial orientation. Thus, as a result of their cortical, cerebellar, and brainstem and afferent input afferents, VN neurons are likely to receive substantial synaptic bombardment *in vivo*. For example, extracellular recordings in the cerebellar flocculus reveal irregularities in the spontaneous simple spikes firing rate of the output neurons (i.e. Purkinje cell) [172]. This provides a clear source of variability to FTN neurons which might explain their lack of synchronization to sensory stimulation as predicted from our modeling results.

3.3.4 Differences between *in vivo* and *in vitro* conditions in VN neuronal activity

Previous reports have found that the high conductance state of neurons *in vivo* can have a significant influence on their processing of synaptic input through changes in intrinsic dynamics [150, 173–175]. Specifically, these changes consist of: 1) increased synaptic input that is dominated by excitation that acts as a net depolarizing bias; 2) increased membrane conductance and; 3) increased variability. In general, bridging the gap between *in vivo* and *in vitro* conditions is not well understood because it is not clear which combination of the three aforementioned effects is responsible for the observed changes in dynamics. For example, both changes in the depolarization bias as well as in variability can alter burst dynamics in thalamocortical neurons [174, 176].

Previous studies have investigated the effects of *in vivo* conditions on the activity of VN neurons [94, 177, 178]. In particular, it has been proposed that heterogeneities might allow for the VN neuron population to accurately encode the time course of

vestibular stimuli while maintaining nonlinear synchronization at the single neuron level [178]. This hypothesis is contrary to more recent experimental results showing that many neurons in the VN, such as FTNs, do not display phase locking *in vivo* [39]. Our results instead predict that increased variability seen under *in vivo* conditions can account for the fact that these neurons accurately follow the time course of vestibular stimuli through changes in their firing rates and that nonlinear behavior such as phase locking occurs because of intrinsic rather than network dynamics.

Moreover, it has been proposed that *in vivo* conditions could be mimicked in VN neurons by increasing the bias current, thereby increasing the firing rate [94, 177]. Our results show that increases in both bias current and membrane conductance are not sufficient to eliminate synchronization for the parameter values used in our model. Instead, our results predict that variability in the form of noise is the main reason for many VN neurons not displaying synchronization *in vivo*. The mechanism by which this noise attenuates synchronization is not by increasing the baseline firing rate but instead by enabling the firing of action potentials at all phases of the stimulus cycle. This prediction can be tested experimentally *in vitro* by mimicking *in vivo* conditions through the dynamic clamp technique [148]. Similar variability-related effects have been observed experimentally in recordings from entorhinal cortical stellate cells *in vitro* [150]. Indeed, these cells show a strong tendency to display subthreshold membrane potential oscillations in the theta range *in vitro* [179] but no significant peak in the theta range has been observed in their activities in awake behaving animals [180]. This suggests that these subthreshold membrane oscillations are strongly attenuated

in vivo. The results of Fernandez and White [150] support this viewpoint as they observed weaker oscillations when they increased conductance and variability through dynamic clamp *in vitro*.

In particular, we note that our model did not include the inward rectifier current I_{h} that is known to be present in VN neurons [144]. While this current has been previously shown to increase the magnitude of membrane potential oscillations [146], it is unlikely to be activated in the depolarized state characteristic of *in vivo* conditions in VN neurons [144]. Indeed, in order to activate I_{h}, the membrane potential must be brought to about 15 mV below the spiking threshold for at least 300 ms [144]. Such a large hyperpolarization leads to a cessation of firing as observed *in vitro* that lasts for at least 300 ms. However, VN neurons are spontaneously active with firing rates of $\sim$ 50 Hz *in vivo* and do not respond to vestibular stimuli (for the intensities typically used in vivo studies) with a complete cessation of firing that lasts 300 ms [35]. Instead, VN neurons smoothly encode variations in head velocity through changes in their firing rate but their firing rates does not reach zero. Thus, it seems unlikely that the membrane potential would reach the values that are necessary to activate I_{h}.

Finally, we note that there exist highly detailed compartmental models of VN neurons that are more morphologically realistic than the model used here [93]. While it would be more realistic to use a detailed compartmental model with an anatomically accurate dendritic tree, such a model would have a significantly greater number of parameters than our current one. Justifying the values used for many of these parameters (i.e. the precise location, strength, and dynamics of afferent synapses

on the dendritic tree) would be non-trivial at best. Based on our results, we can conclude that taking into account the shape of the dendritic tree of VN neurons is not necessary to explain the discrepancy between *in vitro* and *in vivo* results. Nevertheless, future experiments should focus on understanding the effects of dendritic processing in VN neurons.

3.3.5 Stochastic resonance in VN neurons promotes linear coding: functional consequences

Our results have demonstrated that noise can enhance signal transmission in our model VN neuron. Such enhancement of signal transmission by noise is often referred to as stochastic resonance [181–186], a phenomenon by which noise enhances the transmission of a subthreshold signal (i.e. a signal whose intensity is not sufficient to induce spiking activity on its own). We note that our result is, strictly speaking, not stochastic resonance since we chose model parameter values within the suprathreshold regime (i.e. the stimulus could induce action potential firing in the absence of noise). However, in our model, one of the effects of the noise is to induce firing for subthreshold stimulus values. Such effects have been widely discussed before and are commonly referred to as the 'linearization of systems by noise' [121, 187].

While this linearization by noise enables our model VN neuron to faithfully encode the time course of input within the natural frequency range (0-20 Hz), such encoding will only be seen for a finite range of stimulus amplitudes. Indeed, stimuli with larger amplitudes are expected to elicit nonlinear synchronization in VN neurons despite high trial-to-trial variability. In particular, such large amplitude stimuli might lead to activation of I_{h} from the argument above. The putative function of such nonlinear encoding remains a mystery and should be the focus of future studies.

What is the functional role of suppressing synchronization in VN neurons *in vivo*? It is clear that such synchronization in the form of phase locking is used extensively in the auditory system [188–195]. Previous studies have shown that the addition of noise leads to a linearization of the steady state current-response relationship (i.e. the f-I curve) in model neurons [187]. Such linearization of the f-I has also been shown to give rise to gain control mechanisms [196–198] which will extend the dynamic range (i.e. the range of input values that can be coded through a change in output) of a neuron. We propose that increased variability serves to increase the dynamic range of VN neurons and therefore promote more faithful encoding of the stimulus' time course through changes in firing rate over a wider range of vestibular stimulus intensities encountered by the organism in the natural environment. This prediction can be tested *in vitro* using the aforementioned dynamic clamp technique.

3.4 Methods

Model

We used a conductance based Hodgkin-Huxley-type model of VN neuron activity *in vitro* [94,199,200]. The model includes spiking sodium, persistent sodium, delayed rectifier potassium, calcium, and calcium-activated potassium currents. We note that our model did not include the hyperpolarization activated inward rectifier current I_{h} which is present in VN neurons [144] and that addition of this current did not qualitatively affect the nature of our results (data not shown). The model is described by the following system of stochastic differential equations:

$$
\begin{aligned}
C_m\dot{V} &= I_{\text{input}} - I_{\text{ions}} \\
\dot{n} &= [n_\infty(V) - n]/\tau_n(V) \\
\dot{x} &= [x_\infty(V) - x]/\tau_x(V) \\
\dot{C} &= K_p(-I_{Ca}) - R_c\, C \\
\dot{p} &= [p_\infty(V) - p]/\tau_p(V)
\end{aligned}
\tag{3.1}
$$

where $I_{\text{ions}} = I_{\text{Na}} + I_{\text{K}} + I_{\text{K[Ca]}} + I_{\text{Ca}} + I_{\text{NaP}} + I_{\text{L}}$ are the ionic currents, which are given by

$$
\begin{aligned}
I_{\text{Na}} &= \bar{g}_{\text{Na}} m_\infty^3(V)(1-n)(V - V_{\text{Na}}) \\
I_{\text{K}} &= \bar{g}_{\text{K}} n^4 (V - V_{\text{K}}) \\
I_{\text{K[Ca]}} &= \bar{g}_{\text{K[Ca]}} \left(\frac{C}{K_d + C}\right)(V - V_{\text{K}}) \\
I_{\text{Ca}} &= \bar{g}_{\text{Ca}} x^2 \left(\frac{K_c}{K_c + C}\right)(V - V_{\text{Ca}}) \\
I_{\text{NaP}} &= \bar{g}_{\text{NaP}}\, p\, (V - V_{\text{Na}}) \\
I_{\text{L}} &= \bar{g}_{\text{L}}(V - V_{\text{L}}).
\end{aligned}
\tag{3.2}
$$

The dynamical variables are the membrane voltage V, the calcium concentration C, and the activation variables n, x, and p. Although synaptic inputs are most accurately described by fluctuating conductances as described by Destexhe et al. [149], an effective synaptic input [145] can be modeled as an additive current decomposed into three components: a bias current, additive current fluctuations, and a stimulus modulation current. As such, we had $I_{\text{input}} = I_{\text{bias}} + \sigma\xi(t) + S(t)$ where I_{bias} is the

bias current and $S(t)$ is the stimulus current injection. σ is the noise intensity and $\xi(t)$ is low pass filtered (4^{th}-order Butterworth with 50 Hz cutoff) [201] Gaussian white noise with mean zero and standard deviation unity. The activation variables $z \in \{n, x, p\}$ obey the following equation:

$$z_\infty(V) = \frac{1}{1 + \exp\left[-2\, a^{(z)} \left(V - V_{1/2}^{(z)}\right)\right]}. \tag{3.3}$$

Furthermore, while the time constants $\tau_x(V)$ and $\tau_p(V)$ are taken to be independent of the membrane voltage V, the voltage dependent time constant $\tau_n(V)$ is given by

$$\tau_n(V) = \frac{1}{2\lambda \cosh\left[a^{(z)} \left(V - V_{1/2}^{(z)}\right)\right]}. \tag{3.4}$$

Unless otherwise indicated, parameter values were taken as originally tuned [94], and are listed as follows: $\bar{g}_{\text{Na}} = 10$ mS/cm^2, $V_{\text{Na}} = 55$ mV, $V_{1/2}^{(m)} = -33$ mV, $a^{(m)} = 0.055$, $\bar{g}_{\text{K}} = 2$ mS/cm^2, $V_{\text{K}} = -80$ mV, $V_{1/2}^{(n)} = -40$ mV, $a^{(n)} = 0.055$, $\lambda = 0.2$, $\bar{g}_{\text{Ca}} = 0.25$ mS/cm^2, $V_{\text{Ca}} = 124$ mV, $V_{1/2}^{(x)} = -30$ mV, $a^{(x)} = 0.08$, $\tau_x = 10$ ms, $\bar{g}_{\text{K[Ca]}} = 1$ mS/cm^2, $K_p = 0.05$, $K_c = 1$, $K_d = 0.5$, $R_c = 0.05$, $\bar{g}_{\text{NaP}} = 0.05$ mS/cm^2, $V_{\text{NaP}} = 55$ mV, $V_{1/2}^{(p)} = -56$ mV, $a^{(p)} = 0.075$, $\tau_p = 5$ ms, $\bar{g}_{\text{L}} = 0.3$ mS/cm^2, $V_{\text{L}} = -50$ mV, and $C_M = 1$ μF/cm^2. The model equations were integrated numerically using an Euler-Maruyama numerical integration technique [202] with an integration time step of 0.02 ms.

If the time scale at which $\bar{g}_{\text{Na}}$ and $\bar{g}_{\text{K}}$ vary at is much smaller than all other time scales in the model, then one can replace the sodium and potassium currents in equation (1) by their average values during an action potential. This is the case for the parameter values used here. Indeed, the time constant of $\bar{g}_{\text{K}}$ is ~ 0.1 ms

while the minimum time constant of all other processes in our model is 5 ms (note that $\bar{g}_{\mathrm{Na}}$ tracks the membrane potential instantaneously and thus has an effective time constant of zero). We note that, for our parameter values, the average value of summed sodium and potassium currents during an action potential is 0.12 nA, which is an order of magnitude less than the range of bias currents used in this study. As such, our approach of setting $\bar{g}_{\mathrm{Na}} = \bar{g}_{\mathrm{K}} = 0$ mS/cm^2 is valid if one is interested in looking at the dependence of these oscillations on parameter values.

Neurons are known to receive massive amounts of synaptic bombardment from afferent inputs *in vivo*, which puts them into a high-conductance state. Such conditions are characterized by a depolarized and fluctuating membrane potential with a reduction in input resistance (or equivalently an increase in membrane conductance) [149]. Although each individual synaptic input can be accurately modeled by including the presynaptic action potential sequence, the increased membrane conductance and membrane potential fluctuations due to synaptic bombardment onto a neuron can be accurately reproduced by increasing the leak conductance, adding a depolarizing bias current, and adding a noisy current [145, 201, 203]. We note that increasing the leak conductance in order to mimic the increased membrane conductance due to synaptic bombardment is used in dynamic clamp experiments [150].

In order to verify the robustness of our results to more biophysical conditions, we also modeled our sinusoidal stimulus input using an excitatory conductance-based input rather than a simple current input. In this case we used an input current $I_{\mathrm{input}} = I_{\mathrm{bias}} + \sigma\xi(t) + g_{\mathrm{ex}}(t)(V - V_{\mathrm{ex}})$, with the excitatory reversal potential $V_{\mathrm{ex}} = 0$. The excitatory conductance was set to $g_{\mathrm{ex}}(t) = \bar{g}_{\mathrm{ex}}(1 + S(t))$, where $S(t)$ is now a

sinusoid with amplitude of unity, ensuring that $g_{\mathrm{ex}}(t) > 0$. The overall strength of the sinusoidal input is then set by $\bar{g}_{\mathrm{ex}} = 0.07$ mS/cm^2, the value of which was chosen to achieve a comparable firing rate modulation as achieved for equivalent simulations with current input.

3.4.1 Measures

For membrane potential responses to step current inputs, the oscillation index is calculated from the response in the time domain V(t), from the following equation:

$$I_{\mathrm{osc}} = \frac{V_{\mathrm{max}} - V_{\mathrm{min}}}{V_{\mathrm{f}} - V_{\mathrm{i}}}, \tag{3.5}$$

where V_{max} is the maximum voltage occurring after the input step onset, and V_{min} is the minimum voltage that occurs after the maximum. V_i and V_f denote the initial and final values of the voltage, respectively.

In the case of zap current injection, the oscillation index was computed from the envelope of the amplitude modulated membrane voltage response. The envelope was computed by subdividing the membrane potential waveform into windows of length 100 ms and by taking the maximum value within each window. The resulting curve was then low-pass filtered (50^{th}-order low-pass FIR filter with 1.875 Hz cutoff). The oscillation index is then given by the envelope maximum minus the value at t=0. For the spiking activity, the oscillation index is computed in a manner similar to that described above but using the instantaneous firing rate (i.e. the reciprocal of the ISIs) waveform. In that case, each window was 400 ms long and the filter was a 50^{th}-order low-pass FIR filter with 0.625 Hz cutoff.

We also characterized the model's response to sinusoidal current injections that spanned the behaviorally relevant frequency range (0-20 Hz). As done before [94], to convert current density to current, we assume that our model neuron is spherical with a radius of 20 μm, so that 10 μA/cm^2 is equivalent to ~ 0.5 nA. This was done in order to facilitate the comparison of our simulation with experimental data. We used sinusoid amplitudes of $A = 0.13$ nA, as were previously used experimentally *in vitro* [140]. Sinusoidal current injections of a given frequency lasting one cycle were repeatedly presented with the model neuron's initial conditions randomized before each presentation, until 100 seconds of data had been generated for each combination of 100 stimulus frequencies and 100 values of bias current. A cycle histogram was then computed and normalized in order to give the firing rate R(t), as a function of the stimulus phase. The firing rate was then fit to the optimal linear regression model defined as $\hat{\mathrm{R}}(t) = A\sin(2\pi f_{\mathrm{stim}}t + \phi) + B$, as is done experimentally [92, 142, 204]. Although fitting the phase ϕ of $\hat{\mathrm{R}}(t)$ is nonlinear, an optimal linear fit was made for many possible phase values held constant, and the best linear fit taken. The goodness of the fit is then quantified by the variance-accounted-for (VAF) given by the following equation:

$$\mathrm{VAF} = 1 - \frac{\langle(\mathrm{R}(t) - \hat{\mathrm{R}}(t))^2\rangle}{\langle(\mathrm{R}(t) - \langle\mathrm{R}(t)\rangle)^2\rangle}, \tag{3.6}$$

where $\langle ... \rangle = \frac{1}{N}\sum_{i=1}^{N} ...$ with N the number of bins. In the case of a perfect fit, the numerator is equal to zero and the VAF is equal to its maximum value of one. The worst possible fit results in a the minimal VAF of zero. The gain and phase of the response are then calculated as the amplitude of the fit sinusoid normalized by the

amplitude of the stimulus and the phase shift of the fit with respect to that of the stimulus, respectively [92, 142, 204].

The phase locking index (PLI) is computed using the entropy of the cycle histogram [205]. Unlike measures of vector strength [206], this measure can quantify the degree of phase locking present in multi-peaked phase histograms, as present in our case. It is given by:

$$\begin{aligned} \mathrm{PLI} &= 1 - E_0/E_{\max} \\ E_0 &= -\langle P(\phi) \log_2 P(\phi) \rangle \\ E_{\max} &= \log_2 N. \end{aligned} \tag{3.7}$$

where $P(\phi)$ is the probability of firing a spike as a function of stimulus phase. E_0 gives the entropy of the probability distribution and $E_{\max}$ is the maximum entropy possible and is that of a uniform distribution. The PLI thus ranges between 0 and 1. As phase locking is a nonlinear phenomenon, we supplement this measure with the use of an additional more intuitive measure we refer to as a nonlinearity index (NI). This is done by taking the Fourier transform of the firing rate, $\mathrm{R}(t)$, in response to sinusoidal stimulation. We then take the ratio of the magnitudes of the Fourier coefficient squared ($|\mathrm{FC}|^2$) at three times the stimulus frequency divided by that at the stimulus frequency. We thus define NI as:

$$\mathrm{NI} = |\mathrm{FC}|^2_{3f_{\mathrm{stim}}} / |\mathrm{FC}|^2_{f_{\mathrm{stim}}}. \tag{3.8}$$

If the firing rate is a linear function of the sinusoidal stimulus, then it can only contain power at the stimulus' frequency. If there is phase locking, however, then

the magnitude squared of the Fourier coefficients at higher harmonics of the stimulus frequency will be non-zero.

3.4.2 Linearized Model

In the subthreshold regime with spiking sodium and rectifying potassium conductances set to zero, our nonlinear neuron model reduces to the following:

$$\begin{aligned} \dot{V} &= F_V(V, C, x, p) \\ \dot{C} &= F_C(V, C, x) \\ \dot{x} &= F_x(V, x) \\ \dot{p} &= F_p(V, p), \end{aligned} \tag{3.9}$$

where $F_V(V, C, x, p) = [I_{\text{input}} - (I_{\text{Ca}} + I_{\text{K[Ca]}} + I_{\text{NaP}} + I_{\text{Leak}})]/C_m$, $F_C(V, C, x) = K_p(-I_{Ca}) - R_c C$, and $F_x(V, x) = [x_\infty(V) - x]/\tau_x(V)$, and $F_p(V, p) = [p_\infty(V) - p]/\tau_p(V)$. The steady state values of all dynamical variables, V^*, C^*, x^*, and p^*, can then be found numerically by solving the four equations $F_i = 0$, for $i \in \{V, C, x, p\}$. The system can then be linearized in the neighbourhood of these fixed points by Taylor expanding the four functions F_i and keeping only first order terms in the expansions [85]. Redefining the four system variables in terms of their deviation from steady state, $\delta\vec{y} = \vec{y} - \vec{y}^*$ with the vector of dynamical variables defined as $\vec{y} = [V, C, x, p]'$, $\vec{y}^* = [V^*, C^*, x^*, p^*]'$, and ‘$'$’ denotes vector transposition, the linearized system can then be described by the system of equations:

$$\delta\dot{\vec{y}} = M\delta\vec{y} \tag{3.10}$$

where M is the Jacobian, which is given by:

$$M = \left[\begin{array}{cccc} \frac{\partial F_V}{\partial V} & \frac{\partial F_V}{\partial C} & \frac{\partial F_V}{\partial x} & \frac{\partial F_V}{\partial p} \\ \frac{\partial F_C}{\partial V} & \frac{\partial F_C}{\partial C} & \frac{\partial F_C}{\partial x} & 0 \\ \frac{\partial F_x}{\partial V} & 0 & \frac{\partial F_x}{\partial x} & 0 \\ \frac{\partial F_p}{\partial V} & 0 & 0 & \frac{\partial F_p}{\partial p} \end{array} \right]_{\vec{y}=\vec{y}^*} \tag{3.11}$$

Finally, the Matlab function eigs is used to find the four eigenvalues, E_i for $i \in \{1, 2, 3, 4\}$, of the matrix M ordered by their magnitudes. All four eigenvalues have a negative real part implying that the fixed point is stable. However, the last two eigenvalues were complex conjugates of each other, which implies the existence of oscillatory dynamics in the time course of the perturbations as they decay to zero. The frequency of such oscillations is given by the imaginary part of the third or fourth eigenvalues divided by 2π. In order to assess the strength of these oscillations, the linearized model was simulated for step current inputs and the same oscillation index previously used for step current responses was calculated.

3.5 Supporting Information

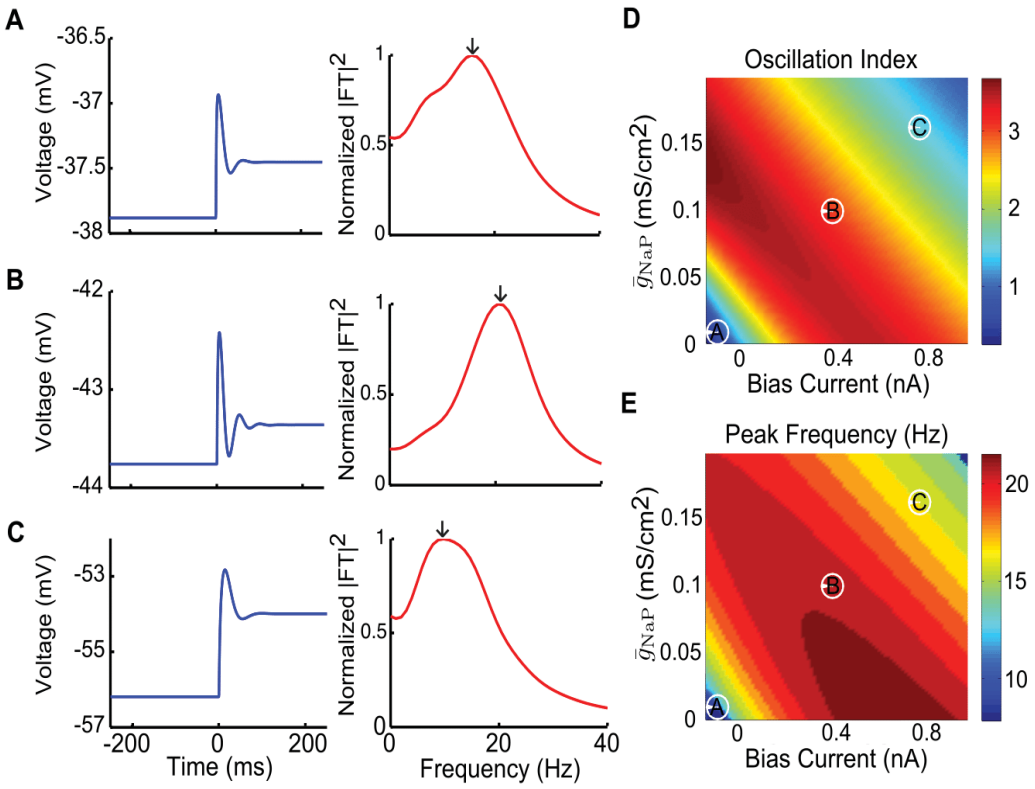

Figure 3.S1. Effects of increased persistent sodium conductance on membrane potential oscillations. The model's membrane potential response to step current input was characterized for physiologically plausible ranges of bias current and persistent sodium conductance values. A-C) Example responses and the normalized squared magnitude of their Fourier transforms. These correspond to parameter values as follows: A) $I_{\text{bias}} = -0.125$ nA, $\bar{g}_{\text{NaP}} = 0.02$ mS/cm^2, B) $I_{\text{bias}} = 0.3625$ nA, $\bar{g}_{\text{NaP}} = 0.098$ mS/cm^2, and C) $I_{\text{bias}} = 0.8$ nA, $\bar{g}_{\text{NaP}} = 0.168$ mS/cm^2. D) Oscillation index as a function of I_{bias} and $\bar{g}_{\text{NaP}}$. E) Oscillation frequency as a function of I_{bias} and $\bar{g}_{\text{NaP}}$. The parameter values corresponding to panels A,B,C are also shown. Other parameter values were $\bar{g}_{\text{Ca}} = 0.25$ mS/cm^2, $\bar{g}_{\text{KCa}} = 1$ mS/cm^2, $\bar{g}_{\text{leak}} = 0.3$ mS/cm^2, and $\sigma = 0$ nA. This figure is copied from Schneider et al. [132].

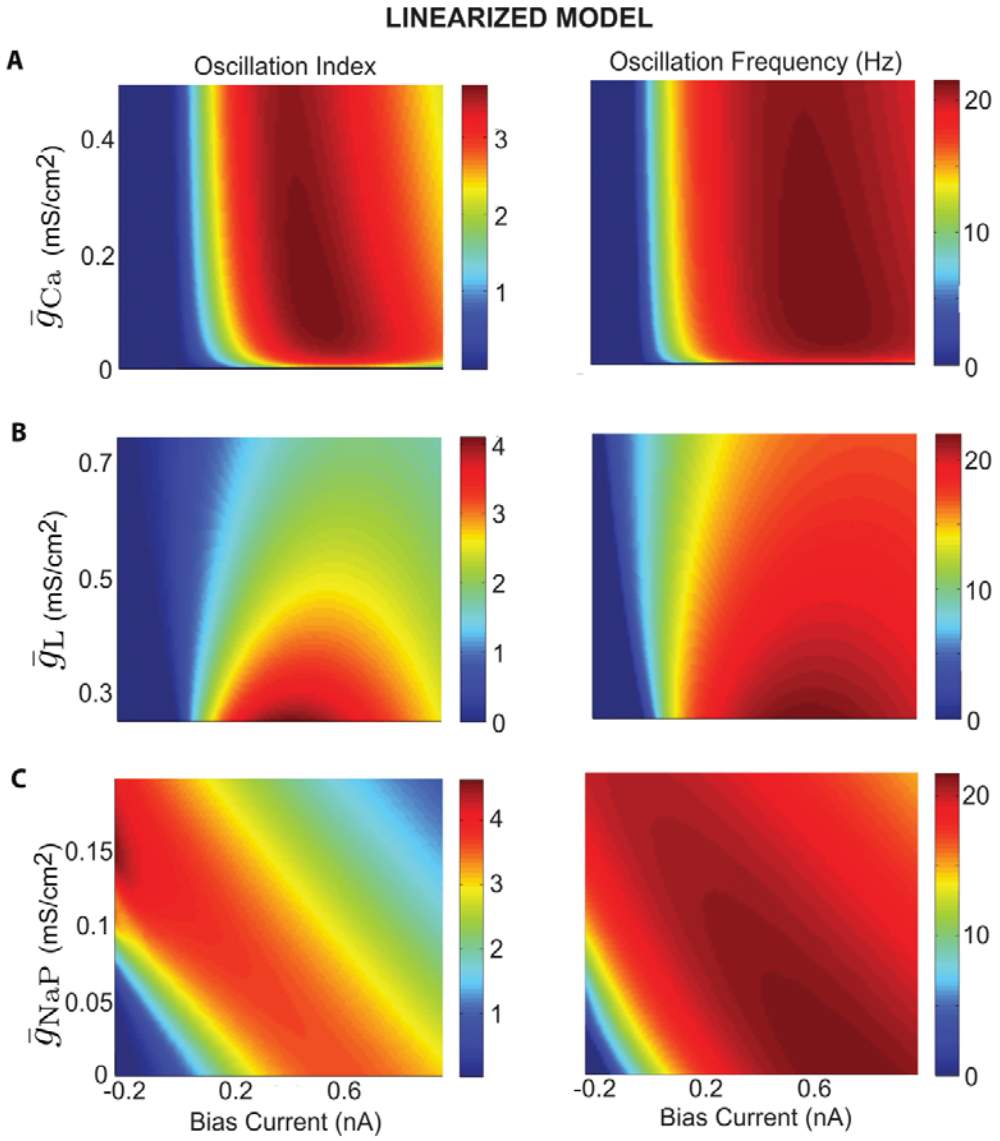

Figure 3.S2. The linearized model's response to step input agrees quantitatively with that of the full model. A) (left) Oscillation index and (right) oscillation frequency as a function of I_{bias} and $\bar{g}_{\mathrm{Ca}}$ for the linearized model. B) (left) Oscillation index and (right) oscillation frequency as a function of I_{bias} and $\bar{g}_{\mathrm{leak}}$ for the linearized model. C) (left) Oscillation index and (right) oscillation frequency as a function of I_{bias} and $\bar{g}_{\mathrm{NaP}}$ for the linearized model. In each case, other parameter values were the same as those used for the full model shown in Figures 3.2,3.3, and 3.S1, respectively. This figure is copied from Schneider et al. [132].

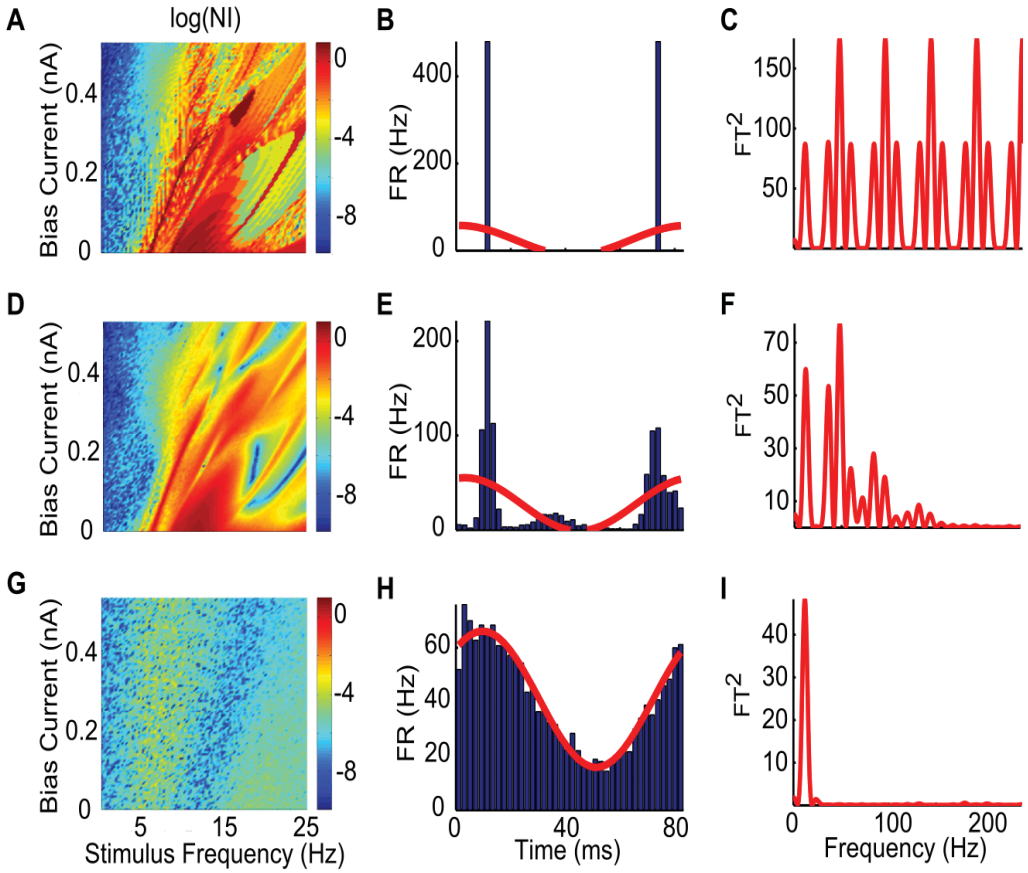

Figure 3.S3. A nonlinearity index (NI) gives qualitatively similar results to those obtained with the PLI measure. A) NI as a function of the bias current I_{bias} and stimulus frequency without noise. B) Example PSTH responses corresponding to $I_{\text{bias}} = 0.1$ nA and $f_{\text{stim}} = 12$ Hz. C) The squared magnitude of the Fourier transform of the PSTH response. D) NI as a function of the bias current I_{bias} and stimulus frequency with low intensity noise. E) Example PSTH responses corresponding to $I_{\text{bias}} = 0.1$ nA and $f_{\text{stim}} = 12$ Hz. F) The squared magnitude of the Fourier transform of the PSTH response. G) NI as a function of the bias current I_{bias} and stimulus frequency with high intensity noise. H) Example PSTH responses corresponding to $I_{\text{bias}} = 0.1$ nA and $f_{\text{stim}} = 12$ Hz. I) The squared magnitude of the Fourier transform of the PSTH response. This figure is copied from Schneider et al. [132].

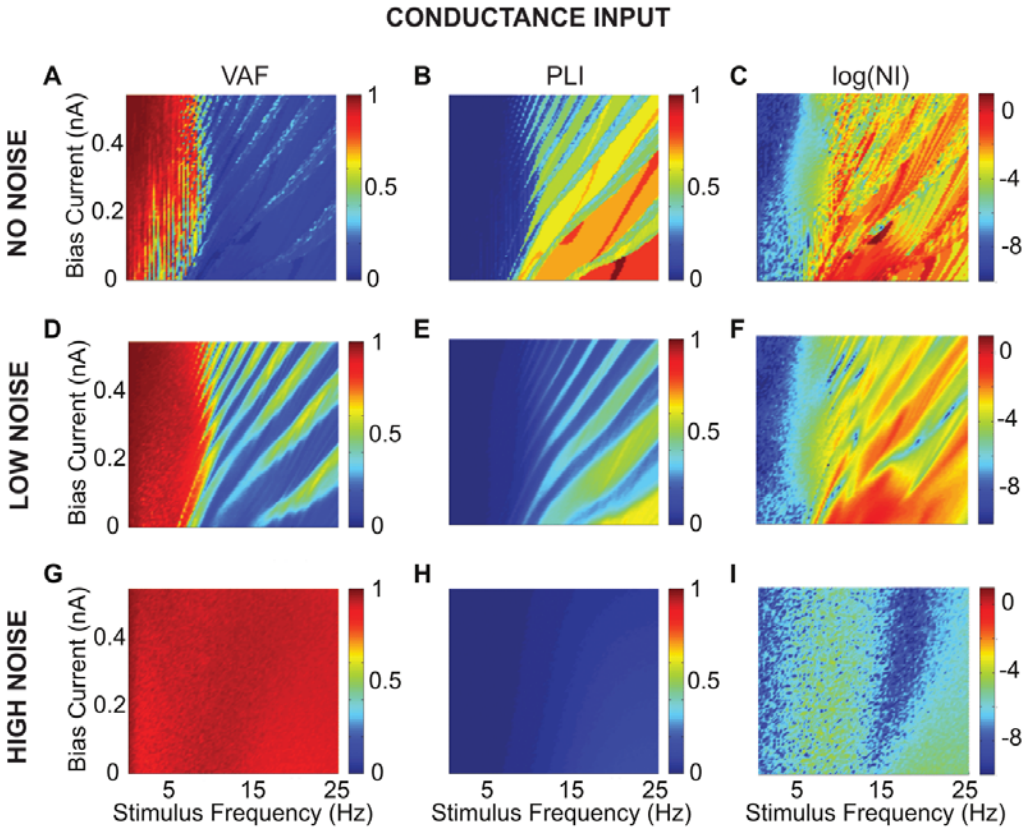

Figure 3.S4. Synchronization to sinusoidal conductance input and the effects of noise. A) VAF as a function of the bias current I_{bias} and stimulus frequency without noise. B) PLI as a function of the bias current I_{bias} and stimulus frequency without noise. C) NI as a function of the bias current I_{bias} and stimulus frequency without noise. D) VAF as a function of the bias current I_{bias} and stimulus frequency with low intensity noise. E) PLI as a function of the bias current I_{bias} and stimulus frequency with low intensity noise. F) NI as a function of the bias current I_{bias} and stimulus frequency with low intensity noise. G) VAF as a function of the bias current I_{bias} and stimulus frequency with high intensity noise. H) PLI as a function of the bias current I_{bias} and stimulus frequency with high noise. I) NI as a function of the bias current I_{bias} and stimulus frequency with high intensity noise. All other parameters values were the same as those used in the equivalent simulations shown in Figures 6, 8, and 9 for current input, with the additional excitatory synaptic conductance $\bar{g}_{\text{ex}} = 0.075$ mS/cm^2. This figure is copied from Schneider et al. [132].

CHAPTER 4
Model vestibular nuclei neurons can exhibit a boosting nonlinearity due to an adaptation current regulated by spike-triggered calcium and calcium-activated potassium channels

In the previous chapter I showed that a conductance-based VN neuron model based on *in vitro* data, could be adapted to reproduce the linear rate encoding of low amplitude stimuli seen *in vivo*. However, In Appendix E, I present a publication [111] showing that VO neurons also exhibit a static boosting nonlinearity in their input-output tuning curves measured *in vivo* (see Figure E.4 in appendices). In this chapter I show that the VN model can indeed produce a similar boosting nonlinearity as found in Massot et al. [111]. I then proceed to find a reduced model that preserves the effect and can reveal its mechanistic origins, by providing an analytic equation for the gain across the boosting nonlinearity. This model will allow for the future exploration of the effects of such a boosting nonlinearity on the encoding of natural stimuli, and the possibility of temporal coding (see Appendix F for additional data analysis linking the boosting nonlinearity to increased temporal precision in spike timing assessed via SR- RR-coherence).

4.1 Introduction

A primary goal of computational neuroscience is to understand the nature of the "neural code" with which sensory information is represented and processed by successive stages of neurons in the nervous system. Sensory neurons were first shown to encode stimulus features such as intensity, in the rate at which they fire action potentials. Accordingly, sensory neurons are often characterized by "tuning curves", which provide a map from a particular stimulus parameter (such as intensity) to the neurons output firing rate [5]. Although linear transformations are known to preserve information, nonlinear transformations are essential for the selective coding of particular stimulus features, as well as using a neurons full information transmission capacity [9]. In the vestibular system, for example, semicircular canal afferents have long been known to primarily encode angular head velocity through firing rate modulations that vary linearly with increasing stimulus amplitude until saturation or rectification occurs [36], whereupon the neuron has reached its maximum or minimum firing rate, respectively. More recently however, *in vivo* studies have shown that neurons in the medial vestibular nuclei (VN) exhibit a boosting nonlinearity in their input-output tuning curves (i.e. firing rate output, versus stimulus, afferent, or bias current input; a.k.a. tuning or f-I curve) [111]. This boosting nonlinearity is characterized by a linear region with a small positive slope for low afferent input currents, and a linear region with higher positive slope for larger afferent inputs, rather than the more common occurrence of a higher slope at low bias currents. *In vitro* studies, on the other hand, measure the membrane potential time course and

have developed a conductance based Hodgkin-Huxley-type VN model, with voltage-activated calcium and calcium-activated potassium channels that produce a specific bidirectional afterhyperpolarization (AHP) [94, 132]. In this paper, a simpler version of this model is shown to produce a boosting nonlinearity similar to that observed experimentally *in vivo* [111], for increased calcium conductances, g_{Ca}, which acts as a bifurcation parameter. In order to shed some light on the underlying mechanisms responsible, a simplified integrate-and-fire (IF) type model is created that is more analytically tractable but preserves the bifurcation structure and boosting nonlinearity under investigation.

It requires a system with at least two variables with nonlinear dynamics to produce action potentials with sodium and potassium currents; the simplicity of IF models is that they replace these spike generating ion channels, with a simpler boundary condition that takes the voltage from threshold back to a reset value [86]. Single variable (i.e. membrane voltage, V) IF models can then be made to have more realistic subthreshold dynamics (which will be required to produce the AHP) by adding back a voltage dependent function, $\psi(V)$. A *linear* "leak" term (giving an LIF) allows the membrane to return to a given resting potential in the absence of stimulation, and a *quadratic* term (giving a QIF) will also add a depolarizing up stroke in the voltage preceding action potentials to better match their shape. A combined linear and exponential function (giving an EIF), has been shown to better fit experimental data [207–209], at a sacrifice to its analytic tractability. Such IF models can be further generalized to include any extra currents, which may require

additional dynamic gating variables, such as spike-triggered adaptation currents (often denoted by W) which serve to decrease V. However, such additional variables also require additional reset conditions, for the change in W upon spiking. The spiking dynamics of such 2-variable (i.e. V,W) adaptive IF models have been extensively studied [210–212], showing that they can produce a variety of spiking behaviors including a similar boosting nonlinearity and a unidirectional AHP [213], for certain parameter combinations.

In this paper, a Hodgkin Huxley (HH) type spiking VN neuron model is reduced to a QIF model generalized to include the calcium and calcium-activated potassium currents, which preserves the bifurcation structureand the boosting nonlinearity observed in the original HH model. The spiking trajectories of the resulting 3-variable adaptive QIF model are then projected into the 2D V-W phase space, revealing an intuitive geometrical picture linking the AHP phase space trajectories with the low gain region of the boosting nonlinearity. Simplifying the models reset conditions and making some additional assumptions, allows for an analytic approximation for the steady state firing rate and its gain (i.e. f-I curve slope) across a similar boosting nonlinearity, as well as the bias current at which the gain is peaked, $\mu = \mu^*$. Although this boosting nonlinearity in the f-I curve of VN neurons has not be experimentally observed *in vitro*, the link with the AHP generation provides the testable prediction that it should be found in the transition to increased bias currents where the AHP no longer occurs.

4.2 Results

4.2.1 HH model produces boosting nonlinearity with AHP and bifurcation through bursting separating low and high gain regions.

Fig. 4.1A shows a schematic of the conductance-based Hodgkin-Huxley (HH) type model (defined by Equations 4.4&4.5 in section 4.4), which was simulated with different calcium conductance strengths, g_{Ca}, over a range of constant bias current injections, μ. Although the full HH model has 4 dynamical variables, example traces of the voltage, V, as well as the gating variable, x, and calcium concentration, C, are shown for different bias currents, and a specific calcium conductance in Fig. 4.1B-D. The dashed green lines indicate a voltage threshold, crossings of which are defined to be spike times, which in turn define a sequence of inter-spike-intervals (ISIs). In panels B&D, red circles indicate regions immediately after spiking that are shown in insets, indicating that the specific AHP in which the voltage changes directions twice, occurs at low bias but not high bias currents. At each bias current value, 1/ISI can be used to give the firing rate, which can be averaged over possibly different ISIs in the case of bursting solutions, such as shown in Fig. 4.1C. These average firing rates are plotted as a function of bias current (known as an f-I curve) in Fig. 4.1E, also with the individual 1/ISIs of the bursts as dots. A boosting nonlinearity (i.e. an increase in gain with an increase in bias current) can be seen to occur for the two highest g_{Ca} vales (cyan and magenta curves), while for the intermediate g_{Ca} value (red curve) the effect is to linearize the f-I curve by reducing the gain at the onset of spiking near $\mu = 0$.

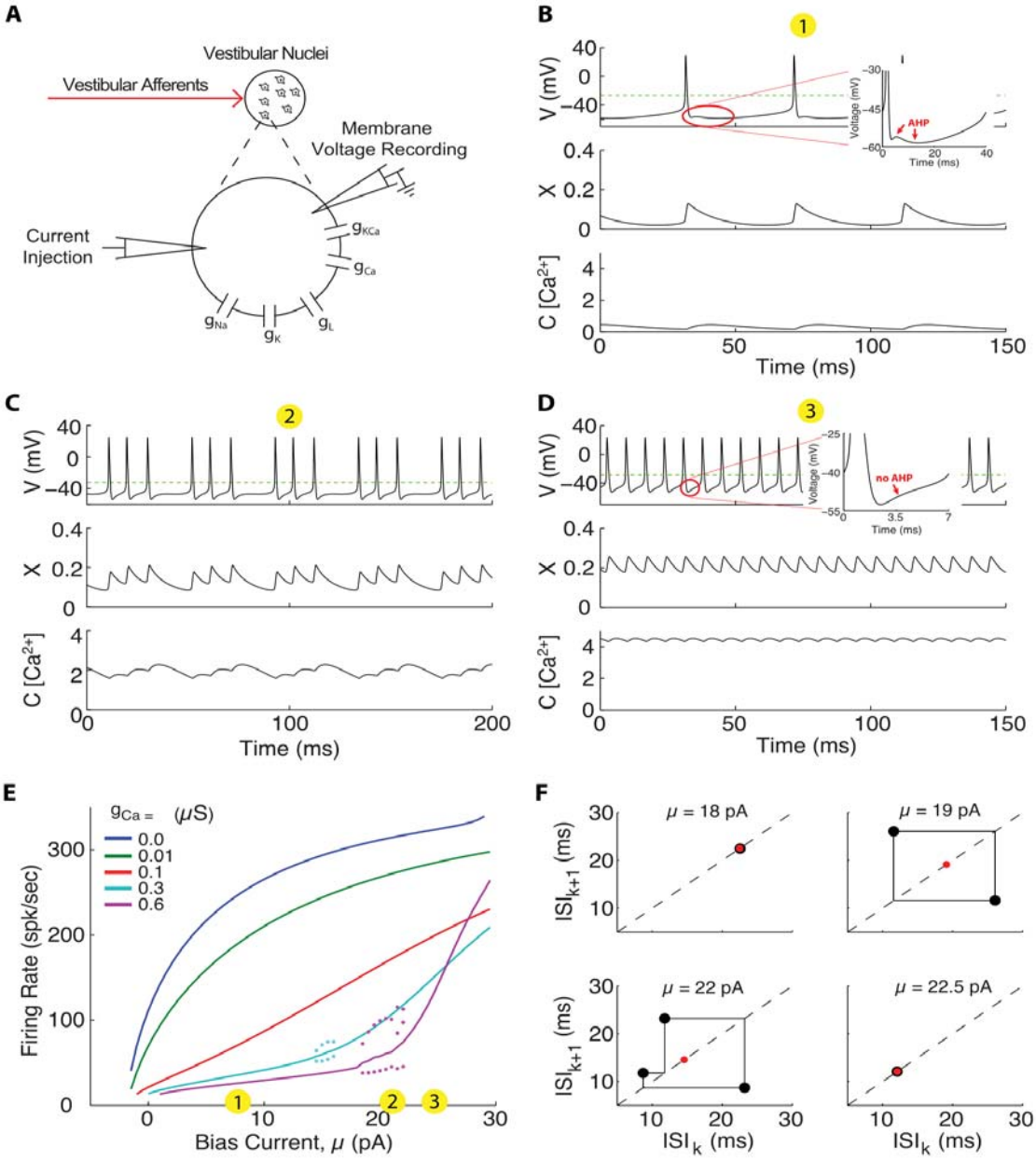

Figure 4.1. Calium and calcium-activated potassium currents induce boosting nonlinearity, AHP, and bifurcation through bursting.

Figure 4.1 ***(previous page).*** (A) A schematic indicating that the neuron model of a vestibular nuclei neuron with conductance-based ion channels as described in Models and Methods Equation 4.5, as well as a constant current injection, which drive the membrane voltage, the "recorded" model output, to generate action potentials. (B-D) Example time series of the simulated membrane voltage, with calcium gating variable, x, and calcium concentration, C, below. Insets show zoom of region preceding spikes either with or without an AHP. Dashed green lines indicate the voltage threshold at which spike times are said to occur. Examples correspond to $g_{Ca} = 0.6$, for the bias current values indicated by the numbered yellow circles in panel E. (E) The firing rate as a function of constant bias current injection, or "f-I curve". Colored lines correspond to the average 1/ISIs for the calcium conductance values indicated, with the colored dots indicating each 1/ISI value of the bursting solutions (i.e. panel C). (F) ISI return maps for four example bias currents with $g_{Ca} = 0.6$, showing how the stable limit cycle ($\mu = 18$) destabilizes into stable 2-spk bursting ($\mu = 19$), and then 3-spk bursting ($\mu = 22$), and back to a stable single spike limit cycle ($\mu = 22.5$). Red dots indicate the mean ISI.

It can also be seen that when the boosting nonlinearity occurs, stable limit cycles of a single ISI are present for sufficiently low or high bias currents, while stable bursting limit cycles (i.e. 2-spk burst, 3-spk burst) appear for intermediate bias current values where the gain (i.e. f-I slope) changes across the boosting nonlinearity. This bifurcation through bursting is characterized by plotting ISI return maps at various bias currents across the bursting region, as are shown in Fig. 4.1F for $g_Ca = 0.6$. From the top right panel stable 2-spk bursting can be seen to transition to stable 3-spk bursting in the lower left panel, before returning to a stable 1-spk limit cycle at higher biases. This appears to be a global "period adding" bifurcation through bursting, however, analysis of the bursting mechanism is beyond the scope of this paper which aims to understand the change in gain across the boosting nonlinearity.

In order to simplify the model and isolate the mechanism underlying this boosting nonlinearity, this HH model was reduced to an analytically tractable integrate-and-fire (IF) type model, which preserves both the boosting nonlinearity and period adding bifurcation.

4.2.2 QIF reduction of HH model can preserve subthreshold bifurcation structure, boosting nonlinearity, and bifurcation through bursting.

To understand the mechanism underlying the HH model's boosting nonlinearity, a reduced integrate-and-fire (IF) type model is generated, that is analytically tractable yet preserves the boosting nonlinearity and underlying bifurcation structure. This was done by replacing the gating variable, n, and related spike generating currents by a nonlinear function, $\psi(V)$, with an additional voltage threshold and reset mechanism, as described in section 4.4. The model's bifurcation structure can be found by calculating the fixed points at each different bias current, which are defined by the zeros of the function $H_1(V, n^*, x^*, C^*)$ (see Equation 4.6). This function is plotted in Fig. 4.2A for $g_{Ca} = 0$ and $g_{Ca} = 0.6$, at an example bias current $\mu = 5$. The green dashed line indicates the voltage threshold used in Fig. 4.1B-D to define the spike times, and the red dashed line indicates the voltage reset value that will be used, which roughly corresponds to the minimum voltage during the action potential in the voltage time series in Fig. 4.1B-D. These curves are shifted up and down with μ and the zero crossings correspond to the HH model's fixed points, with their stability calculated via Equation 4.7. For sufficiently low bias currents, there are three fixed points and the system does not spike spontaneously. As μ is increased the curve is shifted upwards and eventually the two lower fixed points annihilate, generally resulting in the onset of spiking via a saddle-node bifurcation. However, it

is possible for spiking to begin via a Hopf bifurcation, before the two subthreshold fixed points have been annihilated. The fixed point bifurcation diagrams are plotted as a function of bias current for each of the non-zero calcium conductances in Fig. 4.2B, with red dots indicating stable fixed points, and black dots indicating unstable fixed points. The blue lines indicate the maximum and minimum values of the spiking limit cycles, and the onset bifurcation is indicated by a green star for a saddle-node and a green x for an Hopf bifurcation. In the case of the Hopf, the point at which the two remaining unstable subthreshold fixed points annihilate is indicated by cyan stars, which can also be seen to roughly coincide with the region of the bursting solutions. It would appear that the bursting and boosting nonlinearity are closely related to the subthreshold fixed point bifurcation structure, which should be preserved in a reduced IF model.

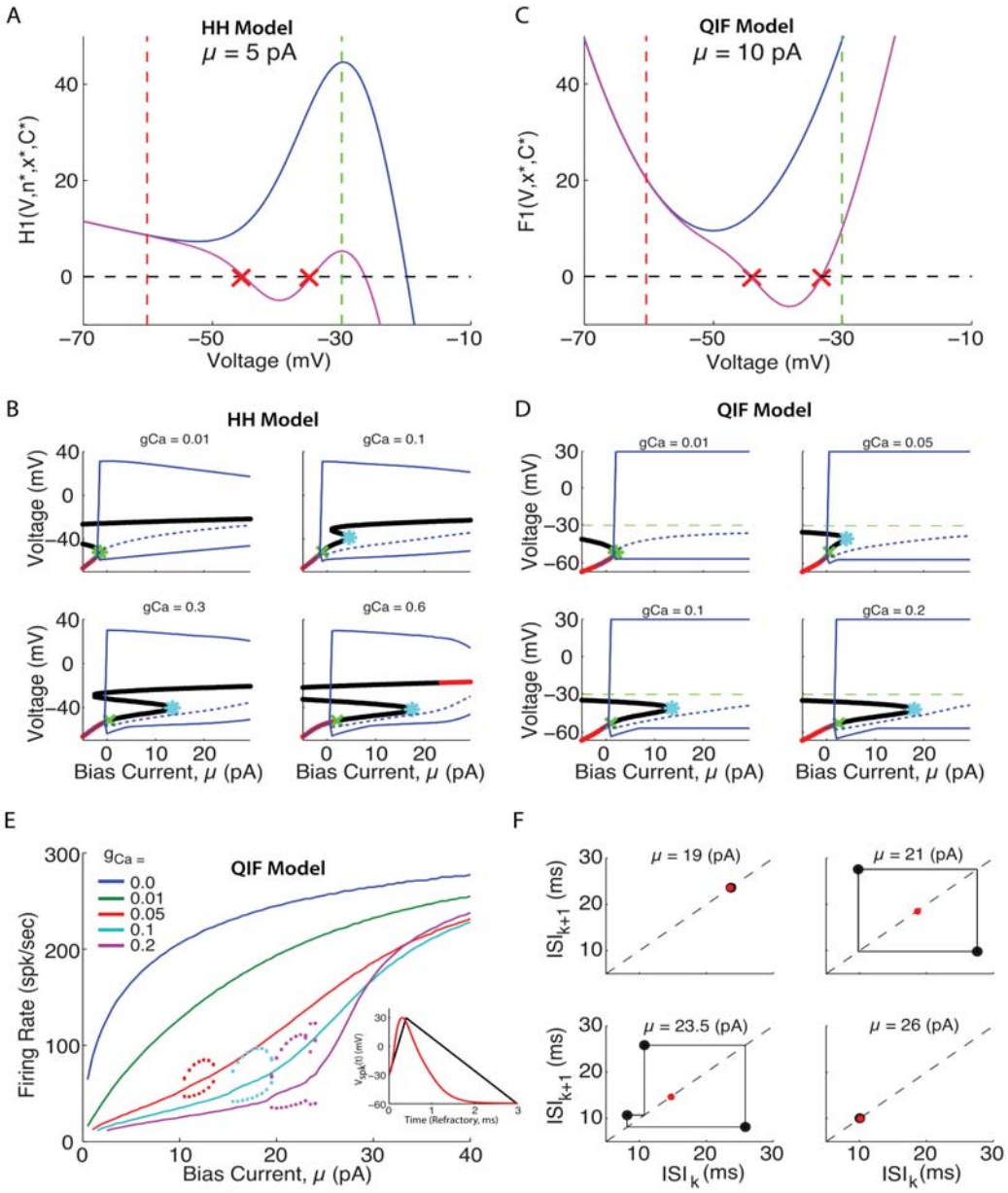

Figure 4.2. Reduced QIF model captures subthreshold bifurcation structure, boosting nonlinearity, and bursting bifurcation of HH model. (A) $H_1(V, n^*, x^*, C^*)$ is plotted for $\mu = 5$, showing how there are either 0 or 2 subthreshold (between the green and red dashed lines) fixed points (i.e. zero crossings), for the $g_{Ca} = 0$ and $g_{Ca} = 0.6$ cases, respectively.

Figure 4.2 ***(previous page).*** (B) Bifurcation diagram for HH model at four different values of g_{Ca} as indicated. Fixed points at each bias current value correspond to zeros of $H_1(V, n^*, x^*, C^*)$, with red indicating stable and black indicating unstable. A green star indicates a saddle-node bifurcation, while a green x indicates an Hopf bifurcation, and a cyan star indicates the annihilation point of the two remaining unstable fixed points. Dashed blue lines indicate the mean voltage, while solid blue lines indicate its maximum and minimum. (C) shows the equivalent $F_1(V, x^*, C^*)$ for the reduced QIF model, for the $g_{Ca} = 0$ and $g_{Ca} = 0.6$ cases, also indicating the two subthreshold fixed points. Green and red dashed lines indicate the voltage threshold and reset, respectively, indicating that the two functions have the same concave shape needed to generate the same subthreshold bifurcation structure. (D) Bifurcation diagram for QIF model at four different values of g_{Ca} as indicated, with fixed points now corresponding to the zeros of $F_1(V, x^*, C^*)$, and additional dashed green lines indicating the voltage threshold. (E) The QIF model f-I curve, with coloured lines and dots as in Fig. 4.1E. Inset shows artificial piecewise linear action potential used to simulate refractory period (black), with an example HH model action potential superimposed (red) for comparison. (F) ISI return maps for four example bias currents with $g_{Ca} = 0.2$, showing how the stable limit cycle undergoes the same period adding bifurcations through bursting as the HH model (see Fig. 4.1F), in the region which separates the low and high gain regions of stable 1-spk firing.

Although and exponential-IF (EIF) model could provide a better fit to $H_1(V, n^*, x^*, C^*)$ in the subthreshold region indicated in Fig. 4.2A, a quadratic-IF (QIF) captures the essential local minimum between threshold and reset necessary to reproduce the two subthreshold fixed points, and has the advantage of being analytically tractable. Although a cubic term could reproduce the entire 'S' shape and high voltage FP, it lies above the voltage threshold and can be ignored for our purposes. Furthermore, a linear function for $\psi(V)$ could not reproduce the two subthreshold fixed points. The two QIF model parameters, g_2 and V_2, can be related to the HH model parameters by linearizing the nonlinear functions in Equation 4.6

and keeping only terms to second order in V, as in Equation 4.12. However, simply choosing values of $g_2 = 0.1$ and $V_2 = -50$ provides a sufficiently good approximation to reproduce the desired phenomena, as can be seen from the resulting function $F_1(V, x^*, C^*)$ (Equation 4.10) plotted in Fig. 4.2C, and bifurcation diagrams in Fig. 4.2D.

The QIF model, defined by Equations 8 in section 4.4, additionally requires an artificial spike waveform to activate the calcium current gating variable, x, as described by Equation 4.9. The resulting f-I curves for this QIF model are shown in Fig. 4.2E, and can be seen to exhibit the desired boosting nonlinearities, as well as the bursting, similarly to the HH model (although for slightly different values of g_{Ca}). In addition, this QIF model exhibits the same period adding bifurcation through bursting as the HH model, as shown by the QIF models ISI return maps (compare Fig. 4.2F and 4.1F). Although the QIF model reproduces the boosting nonlinearity, it also reproduces the same bursting patterns; does this mean that the bursting is necessary to create a boosting nonlinearity?

4.2.3 Does boosting require bursting?

It would appear the the boosting nonlinearity and bursting, depend intimately on the underlying subthreshold bifurcation which occurs near the onset of bursting (see Fig. 4.3A, red Xs). However, these results actually depend significantly on the artificial spike shape used, which defines the reset conditions but does not effect the subthreshold bifurcation structure shown in Fig. 4.2D. The resulting reset condition can be thought of as the amount by which the gating variables change, Δx and ΔC, plotted in Fig. 4.3B, or the reset values themselves, x_{reset} and C_{reset}, plotted in Fig.

4.3C. Are the changes in these reset values with bias current in fact necessary for the model to produce the boosting nonlinearity or bursting? This question can be answered by simplifying the QIF model in these two different ways, choosing fixed values for Δx and ΔC, *or* for x_{reset} and C_{reset}. The resulting f-I curves for each case are shown in Figs. 4.3D&E. In both cases some degree of the boosting nonlinearity can be seen, with a similar bursting occurring in D, but not in E, confirming that one can in fact achieve boosting without bursting.

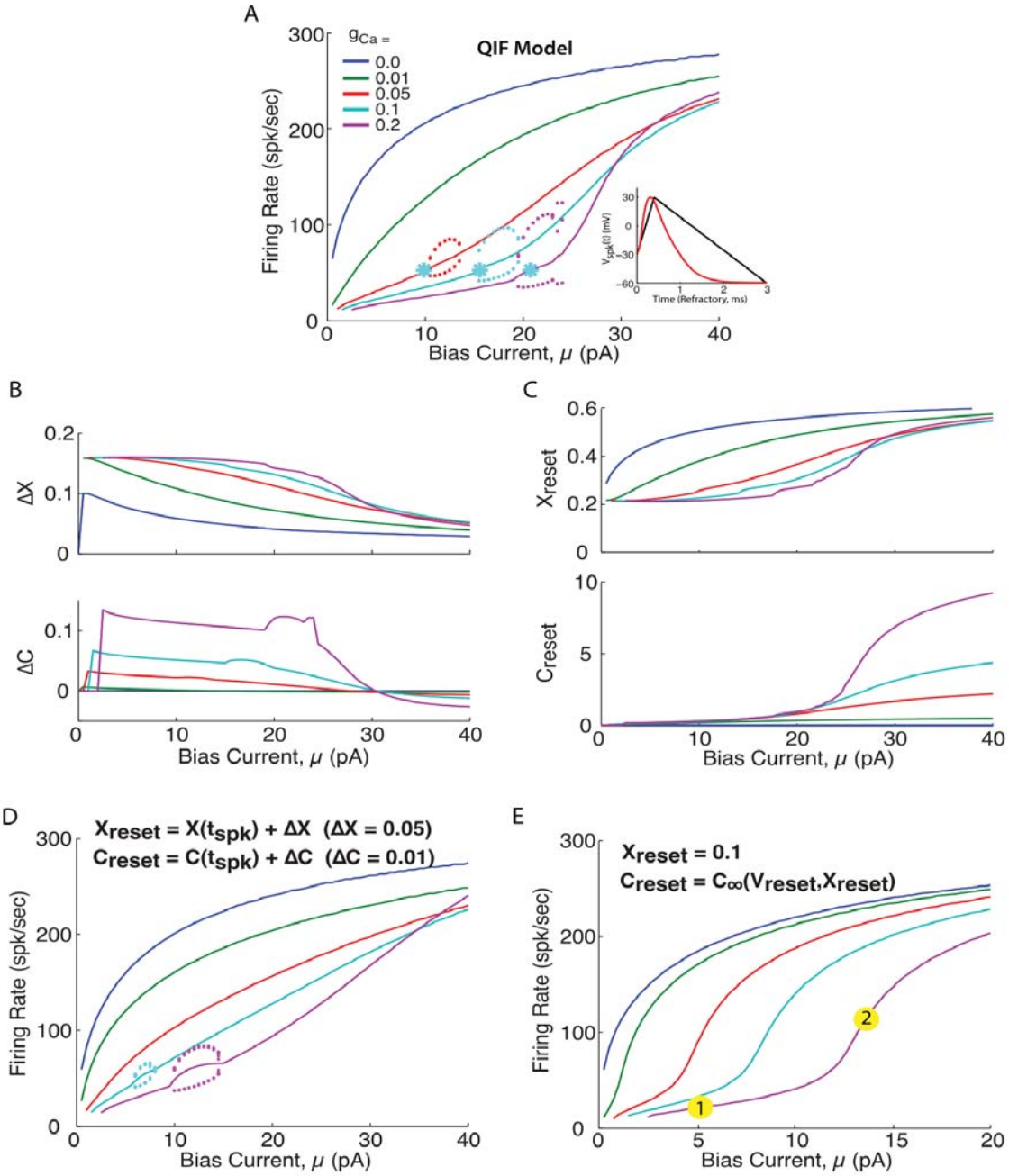

Figure 4.3. Boosting nonlinearity and bursting depend on reset boundary conditions, not only subthreshold bifurcation structure.

Figure 4.3 ***(previous page).*** (A) Firing rate versus μ for the QIF model used in Fig. 4.2E, again with the inset indicating the piecewise linear spike waveform used (black), superimposed with an actual HH model spike (red). Red Xs indicate the bifurcation point of the two subthreshold fixed points which appear to correspond with the onset of bursting. (B) The average Δx and ΔC values generated by the spike shape in A, which change significantly with bias current, μ. (C) The average x_{reset} and C_{reset} values generated by the spike shape in A, also change significantly with bias current. (D) QIF model simulated f-I with fixed Δx and ΔC values for all μ. (E) QIF model simulated f-I with fixed x_{reset} and C_{reset} values, indicates that the boosting nonlinearity can still occur, without any bursting, seemingly independently of the subthreshold bifurcation points, which are the same as in A. Numbered yellow dots indicate examples of low and high gain regions of interest due to boosting nonlinearity most similar in shape to purple f-I curve in panel A.

To understand what is going on, one can think of the QIF model's 3D phase space in V, x, and C. The voltage is bound by the reset and threshold, starting at V_{reset} with particular x_{reset} and C_{reset} values, and evolving in time until it reaches V_{th}. The possible trajectories through this 3D phase space cannot intersect, and are all defined by the system of Equations 4.8, which also defines the subthreshold bifurcation structure. It is how the gating variables are reset that regulates bursting; if the gating variables are changed by a fixed amount at reset, then they must also change by an equal and opposite amount during their phase space trajectory in order to be reset back onto the same trajectory. Otherwise, if the gating variables change by a different amount than the reset, a different trajectory through phase space will be selected, resulting in a different ISI. For fixed gating variable resets, however, the phase space trajectory doesn't matter, the gating variables are always reset to the same values, resulting in the same phase space trajectory and ISI, making bursting impossible.

Although neither of these simplified QIF models capture the physiological realism of the QIF with the artificial spike, they do disentangle the relationship between the boosting nonlinearity, subthreshold bifurcation structure, and bifurcation through bursting. Furthermore, the simplified model in Fig. 4.3E is analytically tractable and will provide a basis for later understanding the model with spike generated reset conditions.

4.2.4 Analytic firing rate and gain curves for the QIF model, with fixed gating variable reset.

To get an analytic expression for the f-I curve and its gain across the boosting nonlinearity, the simplified QIF model with fixed gating variable reset conditions shown in Fig. 4.3E was first considered. As the QIF model is still nonlinear with three dynamic variables, some additional assumptions are needed. Since the original spike generating sodium and potassium channels' gating variable, n, has an average time scale much faster than the additional calcium-related gating variables, x and C, ($\tau_n \approx 1.5ms < \tau_x = 10ms, \tau_C = 20ms$) it can be assumed that the additional gating variables, x and C, are slow compared to the membrane voltage, V. From this they can be set to their mean values which must equal their reset values: $x = \langle x \rangle = x_{reset}$, and $C = \langle C \rangle = C_{reset}$, with $\dot{x} = \dot{C} = 0$. Although this cannot be true during an AHP in which the voltage changes directions and $\dot{V} = 0$ momentarily, it does provide a useful starting place: it reduces the model to a single differential equation in V that can be solved analytically (Equation 4.14), where the additional calcium and calcium-activated potassium currents have been redefined as a single mean adaptation current, $\bar{W}(V)$, defined by Equation 4.13.

For this slow gating variable assumption to hold requires that $\dot{V} > \dot{x} = \dot{C} \approx 0$, which is true as long as the depolarizing "spike generating" current, $\psi(V)$ is greater than the hyperpolarizing adaptation current, $\bar{W}(V)$ (i.e. $\mu + \psi(V) > \bar{W}(V)$, which must be true for sufficiently large μ). This results in a 2D VW phase space, in which the depolarizing current, $\mu + \psi(V)$ is parabolic, and the hyperpolarizing adaptation current, $\bar{W}(V)$ is linear. As such, μ^* can be defined (Equation 4.15) so that if $\mu < \mu^*$ then ψ and $\bar{W}$ intersect, while if $\mu > \mu^*$ they do not (see Fig. 4.4A&B). The simulated trajectories through phase space are superimposed in blue, with blue arrows indicating the direction of the flow from reset to threshold. As long as $\mu > \mu^*$ the slow gating variable approximation holds and Equation 4.14 can be integrated from V_r to V_{th}, resulting in the time interval $\mathcal{I}_0$ (Eqn. 4.17). The approximate trajectory from V_r to V_{th} is superimposed (red curve, $\bar{W}(V)$) in Fig. 4.4B.

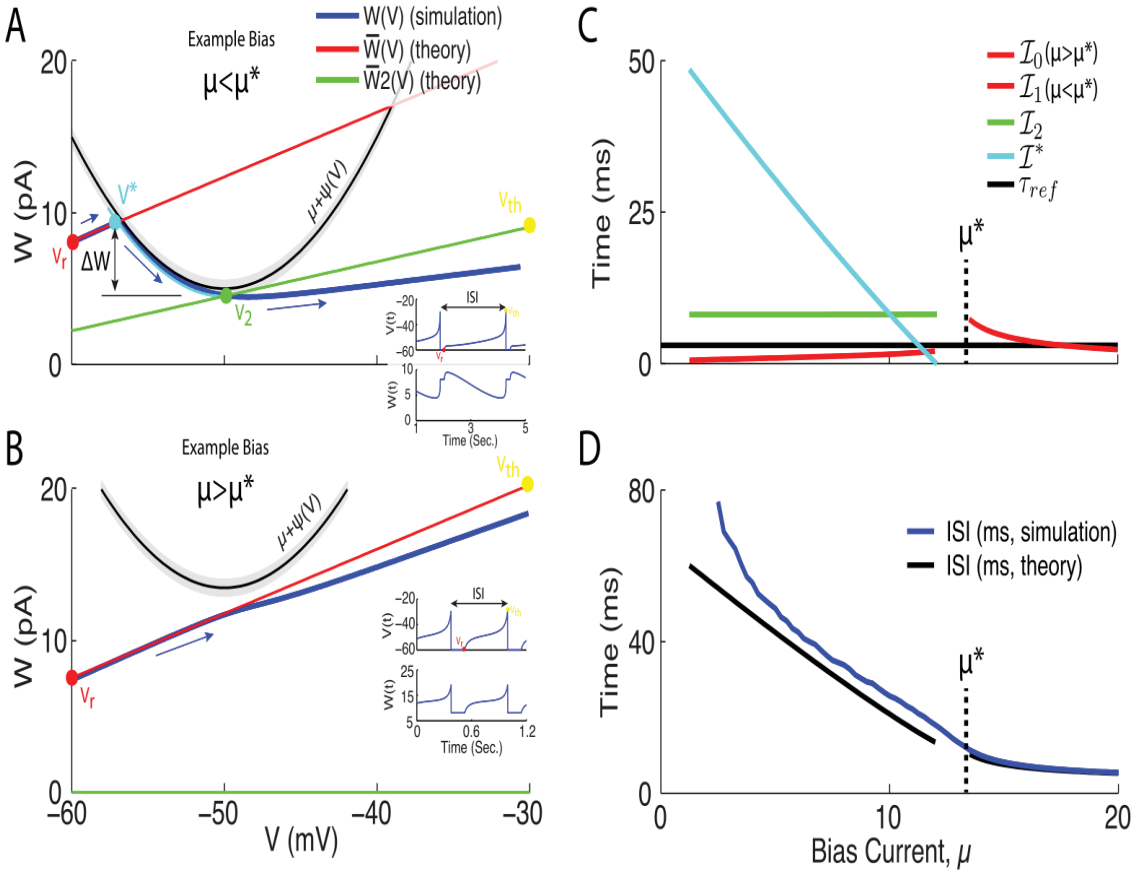

Figure 4.4. WV phase space projection of trajectories at low and high gain μ values, for QIF with $X_r = 0.1$ and $C_r = C_\infty(V_r, X_r)$(see Fig. 4.3E) (A) Example phase space trajectory at bias current, $\mu < \mu^*$, for $g_{Ca} = 0.2$. Simulated trajectory projected into VW phase space (blue) has blue arrows indicating direction of motion in time. The theoretically predicted trajectory starts at the reset voltage, V_{reset} (red dot), and travels along $\bar{W}(V)$ (red line) until it intersects $\mu + \psi(V^*)$ (black line) at V^* (cyan dot). The grey band indicates the region of $|\dot{V}| < \epsilon$. At this point, the x and C variable are free to decay (cyan curve) until W reaches V_2. Then x and C are again fixed and give rise to a new mean adaptation current $\bar{W}^*(V)$ (see Eqn. 4.26, green line) connecting the point V_2 (green dot) and the threshold voltage (yellow dot). Furthermore, the change in W between V^* and V_2 is assumed to be $\Delta W = \bar{W}(V^*) - (\mu - \epsilon)$ as indicated (and assumed by Eqn. 4.23). Insets show V(t) and W(t) as time series.

Figure 4.4 ***(previous page).*** (B) Example trajectory at bias current, $\mu > \mu^*$, for $g_{Ca} = 0.2$. Now $\bar{W}(V)$ (red line) does not intersect $\mu + \psi(V)$, and directly connects V_r (red dot) and V_{th} (yellow dot). (C) The time intervals for the different trajectory components are plotted as a function of bias current (for $g_{Ca} = 0.2$), using colours that match the trajectory components colour in (A) and (B). The vertical dashed line indicates μ^*. (D) The sum of all the predicted intervals shown in (C) results in the predicted ISI (black), and the average ISI of the simulated data (blue) show how the total interval is dominated by $\mathcal{I}^*$ when $\mu < \mu^*$.

For $\mu < \mu^*$, on the other hand, the linear trajectory starting at V_r can be seen to intersect the parabola at a point denoted V^*, defined by Equation 4.18. The ϵ ensures that $F(V) > 0$ between V_r and V^* and can be integrated to give $\mathcal{I}_1$ (Eqn. 4.19). At V^*, then $F(V) \to 0$ and the voltage would come to rest at a fixed point if the slow gating variable assumption *was not* violated; instead the trajectory is now driven by the gating variable dynamics defined by Equation 4.8B&C. If the trajectory were to cross above the parabola, $\mu + \psi(V)$, then $F(V) < 0$ and the voltage would have to decrease until it crosses back; so the only way for the voltage to increase up to threshold, is ultimately by following along under the parabola until it reaches the bottom (located at $V = V_2$, $W = \mu - \epsilon$) where it is free to increase to threshold. The time interval, $\mathcal{I}^*$, for the voltage to travel from V^* to V_2, is calculated in Models and Methods by allowing the gating variables to change and estimating the time for W^* to decay down to $\mu + \psi(V)$ (see Eqns. 4.20-25). In the final segment from V_2 to V_{th} the gating variables are again fixed to their new values, which result in a new $\bar{W}_2$ value and the green linear trajectory shown in Fig. 4.4A, resulting in the interval $\mathcal{I}_2$ (Eqn. 4.27).

Each of these times is calculated for all values of μ and are plotted in Fig. 4.4C. The summed times then give the total ISI, which was compared to the simulated ISIs in Fig. 4.4D. It is clear that at low bias current values the intervals are dominated by $\mathcal{I}^*$ which also has the most significantly nonzero slope. When inverted, the combined intervals defined by Equations 4.17, 4.19, 4.25, and 4.27, give an approximation to the steady state firing rate as a function of bias current:

$$R(\mu) = \begin{array}{r} \dfrac{1}{\mathcal{I}_1 + \mathcal{I}^* + \mathcal{I}_2 + \tau_r}, \text{ for } \mu < \mu^* \\ \dfrac{1}{\mathcal{I}_0 + \tau_r}, \text{ for } \mu > \mu^* \end{array} \tag{4.1}$$

Equation 4.1 is plotted in Fig. 4.5, for both $\tau_r = 3$ ms (solid green and red) as well as $\tau_r = 0$ ms (dashed green and red), superimposed with the firing rate calculated by numerically simulating model Equations 4.8 directly (black). The solid red dots indicate μ^* which can be seen to clearly match the region where the slope of the f-I curves are greatest. For $\mu > \mu^*$ the solid red curves are in very good agreement with the black curve, and the saturation (or reduction in slope) can be seen to be due primarily to the refractory period, τ_r (compare solid and dashed red). $\mu < \mu^*$ the solid green curves are in reasonable agreement with the black curves (considering the additional approximations needed) at least exhibiting the boosting nonlinearity effect, which does not change significantly with τ_r.

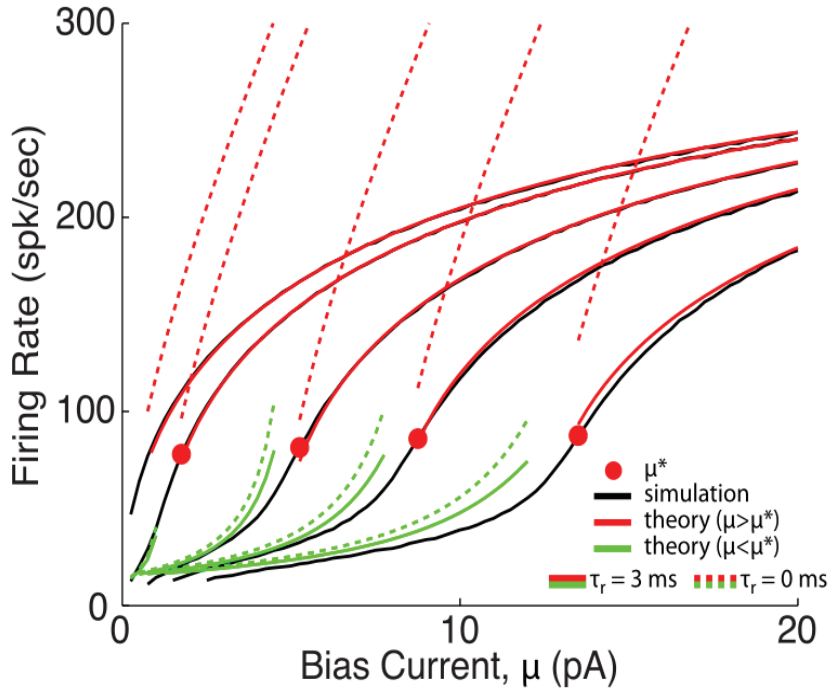

Figure 4.5. Steady state firing rate, simulations and theory: QIF with $X_{reset} = 0.1$ and $C_{reset} = C_\infty(V_{reset}, X_{reset})$. The firing rate is plotted for the numerical simulations in black, with analytic Eqn. 1 in green and red, with solid for $\tau_r = 3$ ms, and dashed for $\tau_r = 0$ ms.

The gain, or slope of the f-I curves, can next be calculated by simply differentiating Equation 4.1 with respect to bias current, $G(\mu) = \partial R(\mu)/\partial\mu$, which is plotted in Figure 4.6 (green and red solid and dashed curves) for comparison with that calculated from the simulated f-I curves (blue). To derive a more intuitive approximate

equation for the gain, the refractory period can be set to zero, $\tau_r = 0$:

$$\begin{aligned} G_-(\mu) &\approx \frac{-1}{(\underbrace{\mathcal{I}_1}_{\approx 0} + \mathcal{I}^* + \underbrace{\mathcal{I}_2}_{\approx 2\pi})^2} \frac{\partial \mathcal{I}^*}{\partial \mu} \\ &\approx \frac{|B|}{[\mu - (2\pi B - A)]^2} \\ &\approx \frac{|B|}{(\mu - \mu^*)^2} \qquad\qquad \text{, for } \mu < \mu^* \end{aligned} \tag{4.2}$$

$$\begin{aligned} G_+(\mu) &= \frac{-1}{\mathcal{I}_0^2} \frac{\partial \mathcal{I}_0}{\partial \mu} \\ &\approx \frac{1}{2\pi} \sqrt{\frac{g_2}{\bar{\mu}}} \\ &= \frac{\sqrt{g_2/4\pi^2}}{[\mu - (W_0 + W_m(V_2 - W_m))]^{1/2}} \quad \text{, for } \mu > \mu^*. \end{aligned} \tag{4.3}$$

For $\mu < \mu^*$, the change in ISI is dominated by the change in $\mathcal{I}^*$ (the segment from V^* to V_2), and $\mathcal{I}_1$ and $\mathcal{I}_2$ are roughly constant by comparison (see Fig. 4.4C). This allows G_- to be reduced to Eqn. 4.2b, which diverges as $\mu \to 2\pi B - A$. Although A and B depend on μ, plugging in numerical values reveals that $2\pi B - A \to \mu^*$ as $\mu \to \mu^*$. For $\mu > \mu^*$ the gain depends only on $\mathcal{I}_0$ and is found to scale as $1/\sqrt{\bar{\mu}}$ from above, similarly to results for the simple QIF model [213], with a rescaled $\bar{\mu}$. In this case the gain diverges when $\bar{\mu} \to 0$ which occurs when $\mu = W_0 + W_m(V_2 - W_m) \simeq \mu^*$, which is also very close to μ^*. This shows that the gain scales as $1/(\mu - \mu^*)^2$ from below and as $1/(\mu - \mu^*)^{1/2}$ from above, and explains why the peak gain should be near $\mu = \mu^*$.

Equations 4.2 & 4.3 are also superimposed in Fig. 4.6, where the dashed yellow and cyan curves are approximations to the dashed green and red curves, and the solid green and red curves are approximations to the blue curve. The dashed yellow

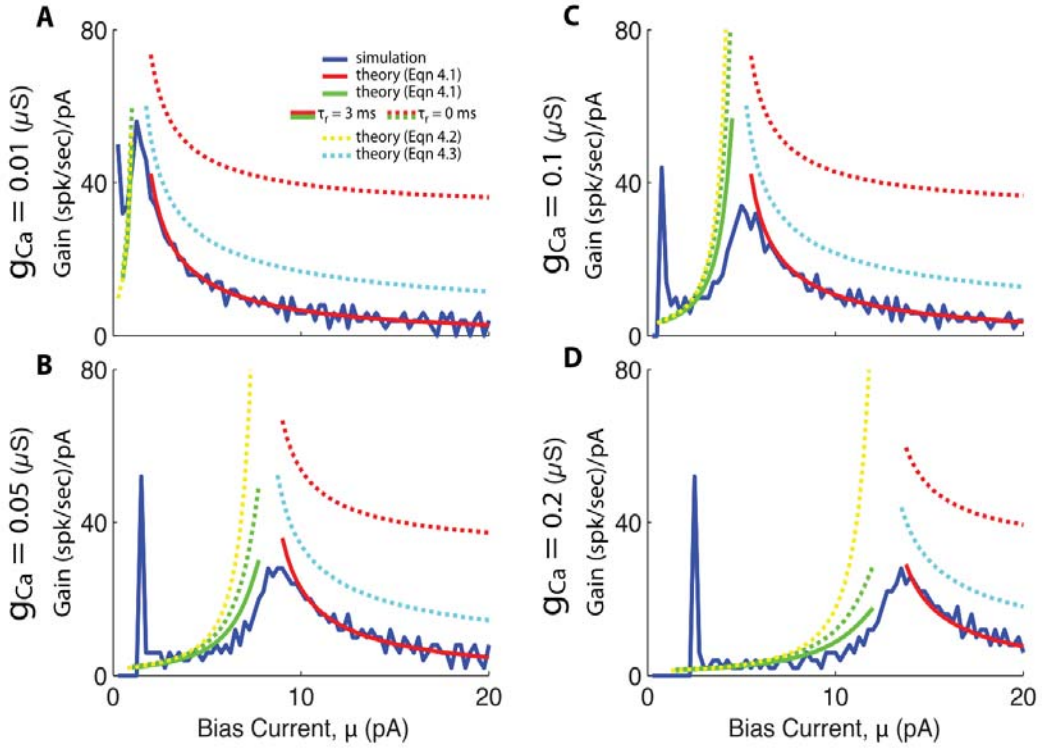

Figure 4.6. f-I curve gain, simulations and theory: QIF with $X_{reset} = 0.1$ and $C_{reset} = C_\infty(V_{reset}, X_{reset})$. The gain (or f-I curve slope) is plotted for the numerically simulated model in blue, with the derivative of Eqn. 4.1 in green and red (solid and dashed). Additionally the approximate gain Eqns. 4.2&3 are superimposed in yellow and cyan dashed lines. The peak of the blue gain curve occurs at μ^* (vertical black line) where the theoretical predictions all diverge. Panels A-D correspond to increasing values of g_{Ca}.

and green curves are in reasonable close agreement, and the solid green does capture the main effect of the boosting nonlinearity (i.e. increase in gain with increasing μ), however ignoring the initial spike in gain at the onset of spiking (blue curves). The solid red curves match the blue curves even better than the green curves (as there were fewer approximations needed). Although the dashed red and cyan curves do differ significantly, it is a roughly constant amount and the cyan curve still captures

the essential scaling features. To quantify the quality of these approximations, the absolute differences of each pair, normalized by the target curve, is plotted in Fig. 4.7. Red and green compare Equation 4.1 with the simulations, and yellow and cyan compare Equations 4.2 & 4.3 with the derivative of Equation 4.1.

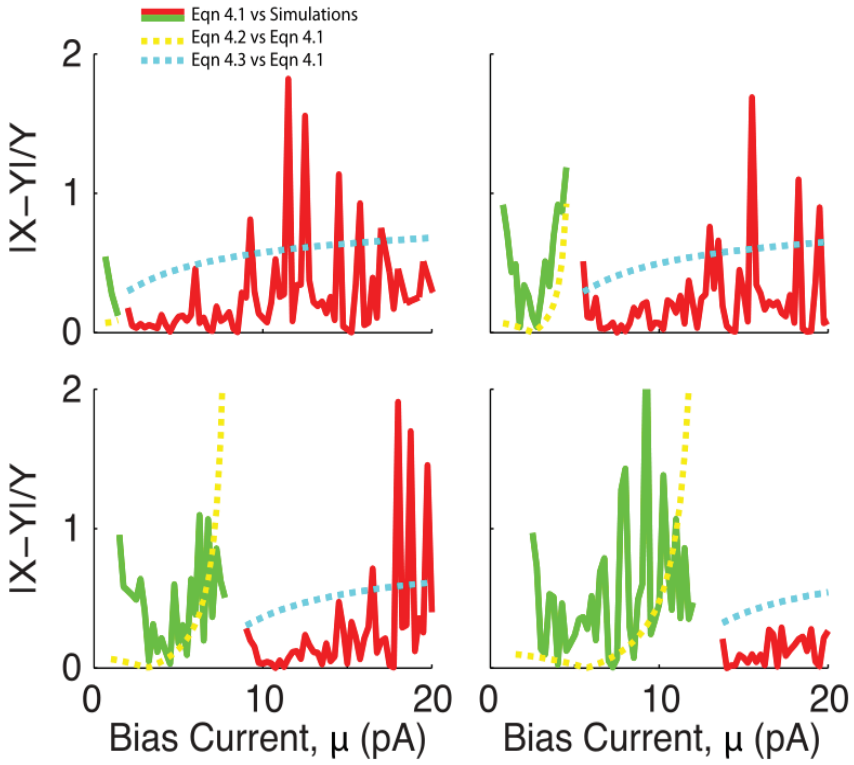

Figure 4.7. Comparison between results from the full theoretical and approximate gain equations. The quality of the full theoretical model is assessed by plotting the absolute difference between the derivative of Eqn. 4.1 and the numerical simulations, normalized by the simulated gain, plotted in green and red for $\mu < \mu^*$ and $\mu > \mu^*$ respectively. Additionally, the approximate gain Eqns. 4.2 and 4.3 are compared to the derivative of Eqn. 4.1 with $\tau_r = 0$, plotted in yellow and cyan dashed curves.

4.2.5 Theoretical firing rate for the QIF model with spike generated resets: convergent iterative predictions

Coming back to the more physiological QIF model with spike generated reset conditions, which reproduces closely the HH model's boosting nonlinearity as well as its bifurcations through bursting, the reset values, x_{reset} and C_{reset}, are no longer given. These reset values may be estimated via an iterative algorithm (see Models and Methods), which may converge to a stable sequence of reset values. In the high bias region where the slow gating variable approximation is valid, a self-consistency condition can be used to generate successive gating variable reset values (and in turn ISIs) similarly to that of Richardson [214]. As described in Models and Methods, because $F(V) > 0$ in this regime, a result of the Fokker-Plank equation can be used to give the probability distribution of the voltage, p(V), which can be used to calculate $x_{reset} = \langle x \rangle$ and $C_{reset} = \langle C \rangle$ [214] according to Equations 4.28-4.30. For low bias values where the slow gating variable approximation is not valid, however, Equation 4.30 no longer holds and the artificial action potential must be used to calculate new reset values.

Letting the algorithm iterate, it may converge to a sequence of identical ISIs (i.e. stable 1-spk limit cycle), a sequence of 2 or more ISIs which repeats (i.e. stable 2- or 3-spk limit cycle; bursting), or even a sequence of ISIs that has no repeating patterns. After 20 iterations of transient ISIs, convergence has generally been reached and the mean and standard deviation of the subsequent sequences of 1/ISIs was used to estimates the f-I curves, as plotted in Fig. 4.8A. The iterative theory can be seen to converge to stable 1-spk limit cycles in the limits of low and high bias current, as well as produce variable ISI sequences (red dashed) near the bursting in the QIF

model (black dashed). The best agreement is actually achieved for the highest value of $g_{Ca} = 0.2$ in the bottom right panel of Fig. 4.8A, where two example bias currents are indicated by yellow dots, which will be considered in the VW phase space below.

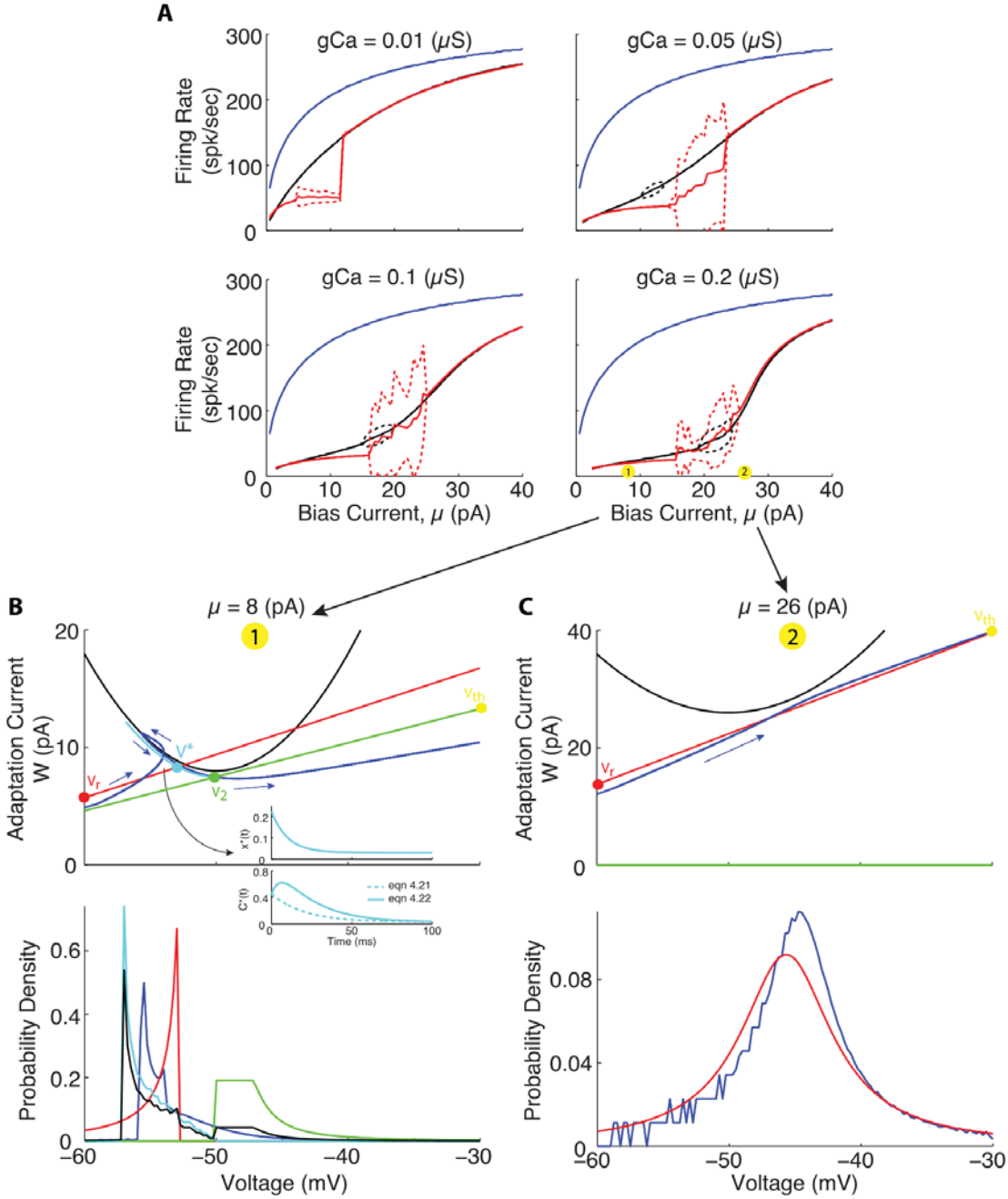

Figure 4.8. WV phase space projection for QIF model with spike waveform, and convergent iterative theoretical predictions for $\mu > \mu^*$ and $\mu \to 0$.

Figure 4.8 ***(previous page).*** (A) Firing rate for QIF with spike waveform, as in Fig. 4.3A, in solid black lines for $g_C a > 0$ (as indicated), and blue curves for $g_C a = 0$. Iteratively estimated theoretical predictions (see Models and Methods for details) are superimposed in red, with solid lines indicating the mean 1/ISI, and dashed lines indicating standard deviation (SD) of 1/ISIs (the bursting patterns will be considered in the next figure). Theory shows excellent agreement above the bursting region where $F(V) > 0$, and reasonable agreement at very low bias currents. Two example bias currents are indicated by numbered yellow circles in the bottom right panel. (B) Low bias example trajectory in VW phase space. Simulated trajectory in blue (with direction of flow indicated by blue arrows), with theoretical trajectory connecting V_{reset} to V^* (red line), then V^* to V_2 (cyan line), and finally V_2 to V_{th} (green line). Inset shows the cyan trajectory in terms of decaying variables $x^*(t)$ and $C^*(t)$, and how Eqn. 4.22 captures the initial increase and then decrease in the calcium concentration, while Eqn. 4.21 does not. Below, the corresponding voltage probability density for the simulated trajectory (blue), and each of the red, cyan, and green segments (independently normalized), as well as their weighted combination (black, see Models and Methods). (C) Same as panel B, but for the high bias example point.

For the stable 1-spike limit cycles in reasonable agreement with the QIF simulations, the low and high bias example trajectories are plotted in the VW phase space in Figs. 4.8B&C. These two trajectories can be seen to have the same fundamental geometry of those in Fig. 4.4: in the high bias region the trajectories do not encounter the parabola, $\mu + \psi$, while for low bias currents, they do. However, in Fig. 4.8B the simulated QIF trajectory (blue curve) crosses the black parabola and changes direction in V, before crossing the parabola again and crossing back over itself (which is only possible since this is really a 3D phase space projected into 2D) before increasing to threshold. It is this trajectory that result in the specific AHP shape in which the voltage changes directions twice. In this case Equation 4.22 must be used to estimate the calcium decay from V^* to V_2, which is compared to

that calculated analytically via Equation 4.21 in the Fig. 4.8B inset (see Models and Methods for details). Once the time interval for each separate component is calculated as described in Models and Methods, the voltage distribution during each segment can be estimated and in the bottom of 8B can be seen to provide a not very accurate match to the simulation (compare black and blue curves), but it does have the marked features of the combined red and cyan peaks. These distributions in 4.8B, however, are not used in the iterative algorithm. For example 2 in the high bias regime (Fig. 4.8C), both V and W can be seen to increase monotonically from reset to threshold, and the resulting voltage distribution is in much better agreement with the simulations.

Although the iterative theory captures the essential phase space geometry to explain the boosting nonlinearity, the results in the regions of bursting are considered next. In Fig. 4.9 (left) the FI curves of the QIF with spike are again plotted, but now with each 1/ISI in the sequences (black dots). Clearly these do not follow the ordered period adding bifurcations see in Figs. 4.1E&4.2E. Although there does appear to be a window of order with a stable 3-spike burst (see Fig. 4.9 right), this 3-spike sequence does not have the same structure as the bursts in Fig. 4.1 and 4.2 (i.e. short-short-long ISI sequences) and may instead be considered an alternation of 1-spk and 2-spk bursts. While the iterative theoretical predictions do capture the low to high gain transition across the boosting nonlinearity, they do fail entirely at capturing the period adding bifurcations through bursting.

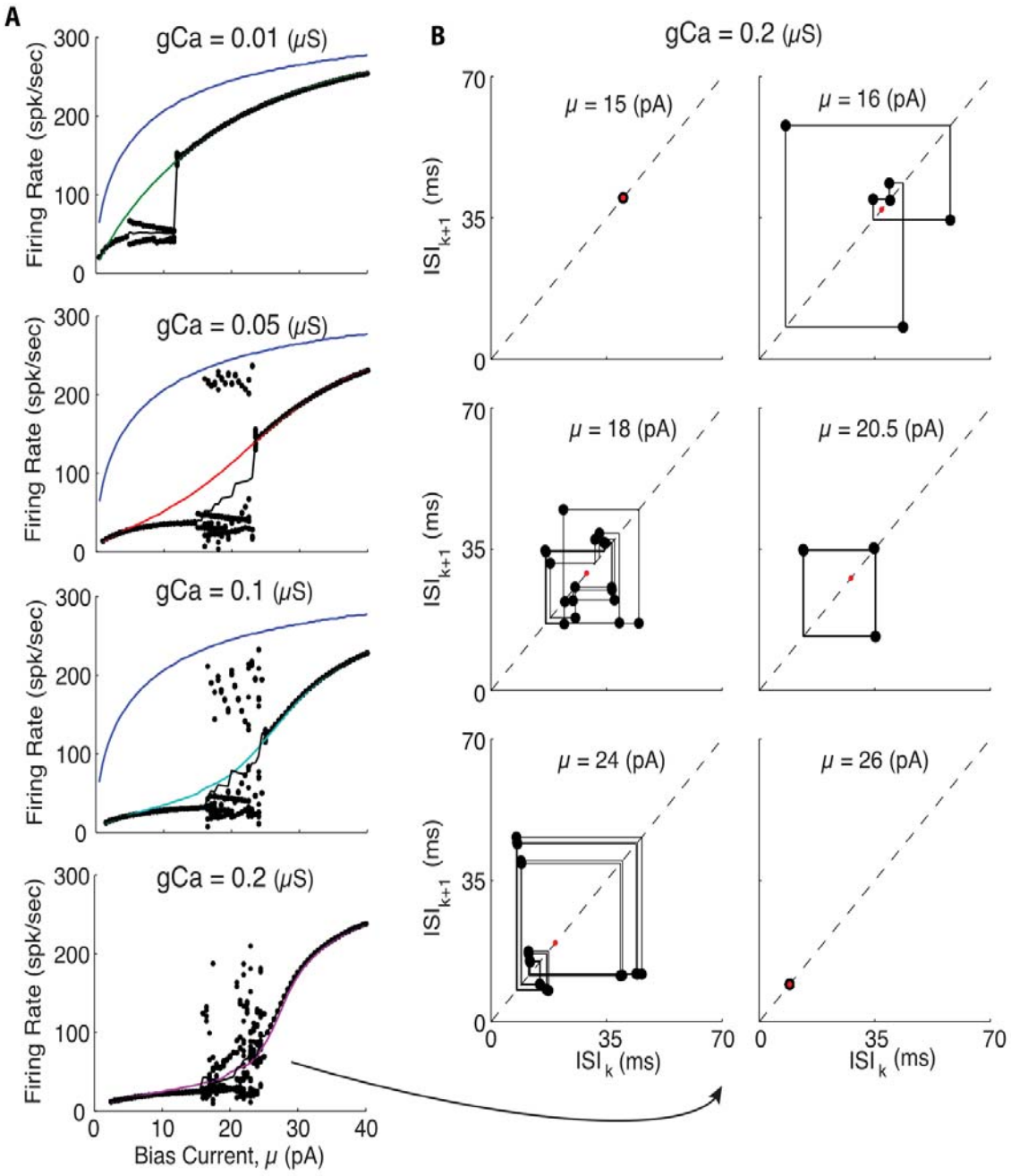

Figure 4.9. Iterative theoretical predictions for QIF model with spike waveform: stable and unstable 1-spike limit cycles.

Figure 4.9 ***(previous page).*** (A) f-I curves for QIF model with spike waveform, each panel comparing $g_{Ca} = 0$ (blue) with $g_{Ca} > 0$ as indicated (color), as well as the theoretical predictions (black). The iterative theory produces a sequence of ISIs, the final 20 are plotted as 1/ISI at each bias (black dots), and their average value versus bias is superimposed (solid black). (B) For the highest g_{Ca} value, ISI return maps are shown for six illustrative bias current values starting with a low bias stable 1-spk limit cycle (top left panel), through bifurcations to aperiodic spiking, with windows of repeating sequences, and back to stable 1-spk limit cycles at high biases (bottom right panel). The same 20 ISIs from A are also plotted in B. It can be seen that at $\mu = 20.5$, a stable sequence of 3 intervals repeats. Similarly, the bottom left panel shows similar sequence of 3 ISIs almost repeats, but 2+ slightly different versions of it repeat, illustrating how regions with stable N-spike ISI sequences transition to other regions with stable M-spike ISI sequences.

4.3 Conclusions

To summarize, in this paper it was shown that a conductance-based Hodgkin-Huxley type vestibular neuron model with high voltage-activated calcium and calcium-activated potassium currents, can exhibit a boosting nonlinearity for increased calcium conductance, g_{Ca}. In addition, the model exhibits a period adding bifurcation through bursting for intermediate bias currents separating the low and high gain regions of the boosting nonlinearity, with an AHP in the low gain region. In order to isolate the mechanism underlying the boosting nonlinearity, the HH model was reduced to a generalized QIF model that preserves the subthreshold bifurcation structure. With an artificial action potential to activate the gating variables, the QIF model reproduces the boosting nonlinearity and the bifurcation through bursting and AHP. To further simplify the model and tease apart the necessary ingredients for a boosting nonlinearity, QIF models were created that use fixed values for, Δx and ΔC, and finally for, x_{reset} and C_{reset}. For this simplified QIF a slow gating variable

approximation was used as a starting point to derive an analytic equation for the f-I curves, and approximate expressions for the gain (i.e. its slope), showing the gain to be peaked at $\mu = \mu^*$. An intuitive geometrical picture of how the trajectories through VW phase space shows that they differ qualitatively in the low and high bias regions of the boosting nonlinearity, and that these two types of trajectories provide the basis for understanding the boosting nonlinearity and deriving an expression for μ^*. Finally, in the case of spike generated reset conditions, it is shown that an iterative algorithm can find stable 1-spk limit cycles that provide reasonable agreement in the limit that $\mu \to 0$, and excellent agreement in the high bias regime.

4.3.1 Comparison to other two- and three-variable adaptive models.

Previously a two-variable adaptive QIF model was studied and found to exhibit a similar boosting nonlinearity [213]. This model used a fixed reset value for its adaptation current, W, such that it would be reset *above* the parabolic function $\mu + \psi(V)$ for low bias, causing the voltage to initially move in the negative direction until it can cross below ψ and begin moving positively, towards threshold. Once μ is increased such that it is greater than W_{reset}, the trajectories are then reset below ψ and increase monotonically towards threshold. This is a very similar mechanism of boosting, whereby spiking trajectories in the low gain region must cross (or come very close to) the V-nullcline, $W^* = \psi(V^*)$, while trajectories in the high gain region do not. This mechanism also results in an AHP in the low gain region, where the voltage initially decreases through a slow minimum, but only changing directions once. However, because phase space trajectories can not cross over themselves, the low gain region only emerges when the reset conditions start the trajectory above

ψ. In the three-variable adaptive QIF model considered here, the projections in the VW plane can cross themselves only because they have an extra dimension due to the x and C variables, and W(x,C). This allows trajectories in the QIF model to start below the V-nullcline, cross up above it, loop back below, cross themselves and off towards threshold. This is what gives my 3-variable QIF model's spikes their signature AHP shape which initially increases before decreasing, unlike two-variable models.

Although the two-variable QIF model of Shlizerman and Holmes does not burst [213], its close relative the adaptive exponential-IF (aEIF, also two-variable) can produce bursting [210, 211], when the adaptation variable reset condition is instead $W_{reset} = W(t_{spk}) + \Delta W$. This produces bursting in a similar way as the adaptive QIF model: multiple short ISIs occur (which do not intersect ψ) with W increasing each time, until W has accumulated enough that the trajectory does intersect ψ and a long ISI occurs, terminating the burst. Although the exponential function in the aEIF model changes the shape of ψ, it does not change the basic concave-up geometry captured by the QIF. As such, it may be expected that the regions of such aEIF models that produce bursts might also indicate the presence of a boosting nonlinearity, however this has not been reported [210, 211]. In addition, although the aEIF model generally uses a simpler linear equation for the dynamics of the adaptation variable such as $\dot{W} = [a(V - V_w) - W]/\tau_w$, it still requires the further simplification that a=0, to compute that $\langle W \rangle = \Delta W$ a priori and apply a slow gating variable assumption for an analytic solution [209, 215].

Finally, Richardson analyzes a three-variable adaptive model very similar to ours [214], with spike-triggered calcium and calcium activated potassium, however he uses an artificial action potential with $V_{max} = 0$, that decays linearly to the reset V_{reset}. He also avoids the problem of not knowing the value of $\langle W \rangle$ by using the slow gating variable assumption and self-consistency criterion to find it iteratively. He does not report a boosting nonlinearity or bursting, but remains in a region of parameter space where $F(V) > 0$ and no AHP [214]. In addition, different spike shapes with the QIF did have a significant effect on whether or not the adaptation currents were strong enough to produce either boosting or bursting, which is one possible explanation for our differing results. However, different values for the conductances g_{Ca} and g_{KCa} are used as well. Although the goal of this study was to understand the mechanisms that produce boosting in the HH model, the ultimate goal is to relate it back to experimental data from the vestibular system, and how it might be functionally relevant.

4.3.2 Correspondence to vestibular nuclei neuron data.

The HH model used in this paper is already a simplified version of the original vestibular nuclei neuron model developed by Av-Ron et al. [94], where only the ion channels necessary to generate the boosting nonlinearity were included. These channels were originally tuned to produce the characteristic bi-directional AHP that goes up and then down before rising to threshold (switching direction twice). This very AHP appears to be a signature that the model would likely produce a boosting nonlinearity (and bursting) if driven to sufficiently high bias currents that the AHP no longer occurs. However, this model was originally developed for *in vitro* preparations

where the average baseline firing rate is much lower (i.e. $\sim 30-50 spk/s$) than in alert behaving animals (i.e. $\sim 60-80 skp/s$) [132]. This may be why such a boosting nonlinearity has not yet been observed *in vitro*. One would expect that if the *in vitro* recordings used current injections large enough that the AHP could no longer occur, that this would also be sufficiently large to reveal a boosting nonlinearity as well, an experimentally testable prediction of this manuscript.

It is also important that neurons are considerably more variable *in vivo*, requiring an additive noise term in the model [132]. Including such increased noise, simulations of the HH model still show the boosting nonlinearity, while the noise is sufficient to disrupt the bursting (not shown). Furthermore, analysis of the data in Massot et al. [111] has shown no evidence of bursting *in vivo*. To further improve the correspondence between the HH model and VN neurons, additive noise could be added to provide the appropriate coefficient-of-variation of the spontaneous spiking activity [111]. However, it is known that different noise intensities may be needed during spontaneous and driven stimulation conditions, as was found for vestibular afferent models [38]. Experimental efforts should therefor be made to measure both the mean firing rate and its variance as functions of bias current, using different stimuli, to further constrain accurate VN neuron models.

4.3.3 Implications for sensory information processing in the vestibular system.

The boosting nonlinearity was originally found in vestibular-only (VO) neurons in VN using narrow band noise stimuli with low (0-5 Hz) and/or high (15-20 Hz) frequency content, and it was found that when presented together the high frequency stimuli masked the response to low frequency stimuli [111]. A linear-nonlinear (LN)

cascade model of the data could explain this masking effect and predict the % attenuation for additional stimuli. The statistics of naturally occurring head movements in primates have since been recorded [95] and indeed been found to have significantly higher power over the low frequency range than the high frequency range, making it unclear whether such masking would occur under natural conditions. This could be explored in a model using stimuli with naturalistic frequency content combined with afferent filters. Additionally, natural stimuli have combinations of angular and linear movements, which could also lead to masking between different axes of motion, rather than different frequency bands within one axis of motion.

It is well known that when neurons are driven across a common rectifying nonlinearity, it can result in increased spiking precision, with information lost about the stimuli in the zero gain region of the nonlinearity which also has a firing rate of zero. It is therefore possible that the boosting nonlinearity could allow the same increased spiking precision, potentially indicative of temporal encoding, to coexist with a standard rate coding since the low gain region still has non-zero gain and firing rate. Further studies with this model could therefore investigate the possibility of simultaneous rate and temporal coding, under natural stimulus conditions.

Finally, it should be pointed out that VO neurons are known to respond robustly to passively applied stimuli (i.e. head movements externally generated by the experimenter), but to show $\sim 70\%$ to the self-generated stimuli studied [114], and that the large majority of natural stimuli recorded by Schneider et al. was indeed self-generated [95]. This suggests a potential role for the boosting nonlinearity: if self-generated stimuli elicit responses that are not sufficiently attenuated and cross

the boosting nonlinearity, an increased level of spiking precision (or population synchrony) could signal a potential problem, without entirely disrupting the linearly decodable information remaining about the stimulus in the firing rate.

4.4 Models and Methods

4.4.1 Full HH model

The Hodgkin-Huxley (HH) type model of a VN neuron developed by Av-Ron et al. [94] and adapted by Schneider et al. [132] is studied in this paper. Specifically, the model includes spiking sodium and potassium currents governed by the single activation variable, n (as in the Morris-Lecar model), as well as a voltage-activated calcium current and calcium-activated potassium current, each governed by the activation variables, x and C, respectively. The additional calcium current, is activated by high voltages that occur during an action potential, and serves primarily to let calcium into the cell with only a small effect on membrane voltage. The additional potassium current, however, is only activated by the calcium that enters the cell when it spikes, and serves to reduce the voltage and prevent spiking. The additional persistent sodium and hyperpolarization-activated currents present in [94, 132] have been removed, as they are not necessary for the model to generate the boosting nonlinearity being investigated. This results in a 4-dimensional spiking neuron model

governed by the following differential equations:

$$\begin{aligned} C_m \frac{dV}{dt} &= H_1(V, n, x, C) = \mu - I_{ions}(V, n, x, C) \\ \frac{dn}{dt} &= H_2(V, n) = [n_\infty(V) - n]/\tau_n \\ \frac{dx}{dt} &= H_3(V, x) = [x_\infty(V) - x]/\tau_x \\ \frac{dC}{dt} &= H_4(V, x, C) = [C_\infty(V, x) - C]/\tau_C. \end{aligned} \tag{4.4}$$

$I_{ions} = I_{Na} + I_K + I_{leak} + I_{Ca} + I_{KCa}$, with $C_\infty = -\frac{K}{R} I_{Ca}$, and the currents are given by the following additional equations:

$$\begin{aligned} I_{Na}(V, n) &= g_{Na} m_\infty^3 (1 - n)(V - V_{Na}) \\ I_K(V, n) &= g_K n^4 (V - V_K) \\ I_{leak}(V) &= g_L (V - V_L) \\ I_{Ca}(V, x) &= g_{Ca} x^2 (V - V_{Ca}) \\ I_{KCa}(V, C) &= g_{KCa} \frac{C}{C + K_d} (V - V_K), \end{aligned} \tag{4.5}$$

where the steady state activation variables obey the following equation: $z_\infty(V) = 1/[1 + \exp[-2a^{(z)}(V - V_{1/2}^{(z)})]]$, for $z \in \{n, x\}$. All parameters are as used by Schneider et al. [132], unless otherwise stated. The calcium current equation I_{Ca} has also been modified from Schneider et al. to remove the calcium saturation term, $\frac{K_r}{C + K_r}$, to further simplify the model while preserving the boosting nonlinearity.

The fixed points (FPs) of the HH model can be found by setting the equations $H_1 = H_2 = H_3 = H_4 = 0$, then solving for, $n^* = n_\infty(V^*)$, $x^* = x_\infty(V^*)$, $C^* = C_\infty(V^*)$, while V^* must be found by plugging these into H_1, and numerically finding

the zeros of

$$H_1(V, n^*, x^*, C^*) = \mu - g_{Na} m_\infty^3(V)(1 - n^*(V))(V - V_{Na}) - g_K n^{*4}(V)(V - V_K) \\ - g_{Ca} x^{*2}(V)(V - V_{Ca}) - g_{KCa} \frac{C^*(V)}{K_d + C^*(V)}(V - V_K) - g_L(V - V_L), \tag{4.6}$$

for a range of bias current values, μ. The stability of the fixed points can then be found by looking at the eigenvalues of the following matrix

$$L_{HH} = \begin{pmatrix} \partial H_1/\partial V & \partial H_1/\partial n & \partial H_1/\partial x & \partial H_1/\partial C \\ \partial H_2/\partial V & \partial H_2/\partial n & 0 & 0 \\ \partial H_3/\partial V & 0 & \partial H_3/\partial x & 0 \\ \partial H_4/\partial V & 0 & \partial H_4/\partial x & \partial H_4/\partial C \end{pmatrix}, \tag{4.7}$$

where the FP is stable if all its eigenvalues have negative real parts.

Setting $g_{Ca} = 0$ (and in turn $C = 0$), it is well known that $H_1(V)$ has a cubic form, with a local minimum at a lower voltage and a local maximum at higher voltage. This shape does not change, but is translated vertically with changes in the bias current, μ. For sufficiently low values of μ there are three fixed points, only that with the lowest voltage is stable, and corresponds to the steady state resting potential. As μ is increased, the two fixed points at lower voltages annihilate in a saddle-node bifurcation at which point there is no stable fixed point, and the model generates action potentials via a stable limit cycle. It is also possible (when $g_{Ca} > 0$) for the lowest voltage fixed point to lose stability via a Hopf bifurcation. In this case the spiking limit cycle can coexist with all three unstable fixed points, with the two lower voltage fixed points annihilating at yet higher values of μ.

4.4.2 Simplified QIF model

In order to find an analytic equation explaining the change in gain of the boosting nonlinearity, a reduced integrate-and-fire (IF) type model is used, that preserves the FP bifurcation structure of the HH model. This is done by removing the gating variable, n, and replacing the currents, $I_L(V) + I_{Na}(V) + I_K(V)$, with a nonlinear function $\psi(V)$, and a voltage threshold and reset. Although simple constant or linear functions can be used for $\psi(V)$, a concave up function is needed to reproduce the second bifurcation of two subthreshold fixed points in the case of the Hopf bifurcation at spiking onset. The simplest of these functions is the quadratic, $\psi(V) = g_2(V-V_2)^2$, resulting in the generalized QIF model, governed by 3 differential equations:

$$\begin{aligned} C_m \frac{dV}{dt} &= F_1(V,x,C) = \mu + \psi(V) - I_{Ca}(V,x) - I_{KCa}(V,C) \\ \frac{dx}{dt} &= F_2(V,x) = [x_\infty(V) - x]/\tau_x \\ \frac{dC}{dt} &= F_3(V,x,C) = [C_\infty(V,x) - C]/\tau_C, \end{aligned} \tag{4.8}$$

where the only new parameters to define are g_2 and V_2.

In addition, the QIF model requires a boundary condition such that when the voltage reaches a threshold, V_{th}, a spike is said to have occurred, and the voltage is returned to a reset value, V_{reset}, for an absolute refractory period, τ_r. However, because the high voltages occurring during the action potential are needed to drive the voltage-activated calcium currents, a simple piece-wise linear function, $V_{spk}(t)$, is used during the refractory period $t_{spk} < t < \tau_r$ (similar to Richardson [214]). The spike shape rises linearly to a maximum, and then decays linearly to the reset voltage

according to

$$\begin{aligned} V_{spk}(t) =& V_{th} + \frac{V_{max} - V_{th}}{t_1} t, \text{ . . . . . for } 0 \leq t < t_1 \\ & V_{max} + \frac{V_r - V_{max}}{\tau_r - t_1}(t - t_1), \text{ . .for } t_1 \leq t < \tau_r \end{aligned} \tag{4.9}$$

where $t = 0$ corresponds to the spike times. In this paper, the spike shape parameters, $V_{max} = 30$ mV, $t_1 = 0.4$ ms, and $\tau_r = 3$ ms are used. This results in the x and C gating variables changing according to $x(t_{spk}) \rightarrow x(\tau_r) = x(t_{spk}) + \Delta x$, and $C(t_{spk}) \rightarrow C(\tau_r) = C(t_{spk}) + \Delta C$, where Δx and ΔC are calculated by plugging Equation 4.9 into Equations 4.8b&c and numerically integrating $x(t)$ and $C(t)$ from t_{spk} to τ_{ref}.

The QIF model can be further simplified by removing $V_{spk}(t)$ and using either fixed Δx and ΔC, or fixed x_{reset} and C_{reset}, resulting in $x(t_{spk} + \tau_r) = x_{reset}$ and $C(t_{spk} + \tau_r) = C_{reset}$. This results in two more parameters, either x_{reset} and C_{reset}, or Δx and ΔC, which must be defined, instead of V_{max} and t_1.

The fixed points (FPs) of this simplified QIF model do not depend on the artificial spike shape or reset boundary conditions, and can be found by setting the equations $F_1 = F_2 = F_3 = 0$, and solving for, $x^* = x_\infty(V^*)$, $C^* = C_\infty(V^*)$, as before, with V^* now being found by plugging these into F_1, and numerically finding the zeros of

$$\begin{aligned} F_1(V, x^*, C^*) = \mu - g_2(V - V_2) - g_{Ca} x^{*2}(V)(V - V_{Ca}) \\ - g_{KCa} \frac{C^*(V)}{K_d + C^*(V)}(V - V_K) = 0. \end{aligned} \tag{4.10}$$

The stability of the fixed points can then be found by looking at the eigenvalues of the following matrix

$$L_{QIF} = \begin{pmatrix} \partial F_1/\partial V & \partial F_1/\partial x & \partial F_1/\partial C \\ \partial F_2/\partial V & \partial F_2/\partial x & 0 \\ \partial F_3/\partial V & \partial F_3/\partial x & \partial F_3/\partial C \end{pmatrix}. \tag{4.11}$$

Although the subthreshold fixed points and their stability depend only on the system of equations 8, the reset values, x_{reset} and C_{reset}, behave as additional bifurcation parameters, similarly to the reset parameters in the adaptive two-variable models studied by Naud et al. [211].

To estimate the QIF model parameters g_2 and V_2 from the HH model, g_{Ca} can be set to zero, and the nonlinear functions in $H_1(V, n^*)$ expanded to second order in V, around its approximate minimum (≈ -50 mV, seen by plotting),

$$\begin{aligned} H_1(V) &= \mu - g_L(V - V_L) - g_{Na} \underbrace{m_\infty^3(V)}_{\approx a_1 + b_1(V+50)} (1 - \underbrace{n_\infty(V)}_{\approx a_2 + b_2(V+50)})(V - V_{Na}) \\ &\quad - g_K \underbrace{n_\infty^4(V)}_{\approx a_3 + b_3(V+50)} (V - V_K), \\ &\approx \mu + k + a(V - h)^2, \end{aligned} \tag{4.12}$$

with $a_1 = m_\infty^3(V = -50)$, $a_2 = n_\infty(V = -50)$, $a_3 = n_\infty^4(V = -50)$, $b_1 = \partial m_\infty^3/\partial V(V = -50)$, $a_2 = \partial n_\infty/\partial V(V = -50)$, and $a_3 = \partial n_\infty^4/\partial V(V = -50)$. Solving for a and h can then be used to estimate g_2 and V_2, however, the values $g_2 = 0.1$ and $V_2 = -50$ mV do a sufficient job to reproduce the HH model's features of interest.

A complete solution of this model would result in $V(t)$, $x(t)$, and $C(t)$, and can result in tonic firing of a single repeated interspike-interval (ISI), or bursts of two or more ISIs in a sequence which repeats, as well as possibly aperiodic spiking with sequences of ISIs which never repeat. In the entire 3D phase space, there is a single trajectory deterministically connecting V_r to V_{th}, for each possible combination of x_{reset} and C_{reset} values which occur at the voltage reset. The trajectories cannot intersect and the entire phase space of trajectories is defined by the system of Equations 8, but the particular trajectory for each ISI is determined by the values of V_{reset}, x_{reset}, and C_{reset}. The x and C values occurring at the voltage threshold may of course be different, and not necessarily result in the same reset values, and may therefore be reset onto a different nearby trajectory in phase space. In my simplified QIF with fixed x_{reset} and C_{reset} reset values, together with V_{reset}, the voltage is reset onto the same trajectory after each spike, resulting in only tonic spiking of a single repeated ISI. In this case the ISI can be estimated analytically, with the values of x_{reset} and C_{reset} defined as model parameters.

4.4.3 Slow gating variable approximation for fixed reset conditions.

The additional gating variables, x and C, have time constants of 10 and 20 ms, compared to the average membrane time constant of $\approx$ 2 ms, and can thus be assumed to vary slowly by comparison (i.e. $\dot{x} \approx \dot{C} \ll \dot{V}$). Although the gating variables may be reset instantaneously during the refractory period following spiking, this approximation only needs hold from the end of the refractory period until the next spike. Additionally subthreshold regions in which this approximation breaks down, such as during an AHP, will be identified and dealt with separately. This

assumption allows the gating variables to be approximated by their initial values, $x \approx x_{reset}$ and $C \approx C_{reset}$. As a result, the additional calcium related currents depend only on V, and can be defined in the adaptation current, $\bar{W}(V)$, as

$$\begin{aligned}
\bar{W}(V) &= I_{Ca}(V, x_r) + I_{KCa}(V, C_r) \\
\bar{W}(V) &= \underbrace{(g_{Ca}x_r^2 + g_{KCa}\frac{C_r}{C_r + K_d})}_{\equiv W_m} V \underbrace{-(g_{Ca}x_r^2 V_{Ca} + g_{KCa}\frac{C_r}{C_r + K_d}V_K)}_{\equiv W_0} \\
\bar{W}(V) &= W_0 + W_m V.
\end{aligned} \tag{4.13}$$

$\bar{W}(V)$ is simply linear in V, always having a positive slope (except when $g_{Ca} = 0$, causing $W_0 = W_m = 0$). This results in the system of Equations in 8, reducing to a single differential equation

$$\frac{dV}{dt} = F(V) = \mu + \psi(V) - \bar{W}(V), \tag{4.14}$$

where $\psi(V) > 0$ represents the spike-generating currents which always drive the membrane voltage *towards* threshold, and $\bar{W}(V) > 0$ represents the calcium and calcium-activated potassium currents which always act to drive the voltage *away* from threshold. It is because $V_K < V_r \leq V \leq V_{th} < V_{Ca}$, that although the calcium current always serves to depolarize the membrane, the stronger calcium-activated potassium current always serves to hyperpolarize the cell.

In the approximate 1D system defined by Equation 4.14, $\mu + \psi(V)$ is a parabola with its minimum at μ, and $\bar{W}(V)$ is a line with positive slope, independent of μ. This gives two possible scenarios: for low enough μ the parabola and line intersect, while for high enough μ the parabola and the line do not intersect. If there is an

intersection, then $F(V) = 0$ at that voltage, and the approximate 1D system should have a fixed point, but since the system is really a 3D system, it only indicates that the slow gating variable approximation breaks down. Although the initial conditions at voltage reset could correspond to a region where $\bar{W} > \psi$, as in [211,213], this does not occur for the model parameters considered in this paper.

Since the parabola is translated linearly with μ, there must always exist a bias current, μ^*, such that $F(V) > \epsilon$ for $\mu > \mu^*$, where the parabola, $\mu + \psi - \epsilon$ and the line, $\bar{W}$ intersect at a single point. The value of ϵ is chosen to be 0.5, small but non-zero, to avoid divergent calculations involving $1/F(V)$. For $g_{Ca} > 0$, the bias current μ^*, can be defined by $F(\mu^*, V) = \epsilon$:

$$\mu^* = \frac{(2g_2V_2 + W_m)^2}{4g_2} - g_2V_2^2 + W_0 + \epsilon. \tag{4.15}$$

For $\mu > \mu^*$, $F(V) > \epsilon$ and it is straightforward to integrate Equation 4.14 from reset to threshold to calculate the ISI (consider this case 1). But for $\mu < \mu^*$, $\dot{V} < \epsilon$ for a range of V in which the slow gating variable assumption cannot be made and Equation 4.14 cannot be used (consider this case 2). It should be noted that in the limit that $g_{Ca} \to 0$, $\mu^* \to \mu$, as expected.

Case 1: $\mu > \mu^*$ and $|\dot{V}| > \epsilon$. With $\mu > \mu^*$ and $|\dot{V}| > \epsilon$, the voltage moves monotonically from reset to threshold, and Equation 4.14 can be integrated to get the time interval

$$\mathcal{I}_0(\mu) = \int_{V_r}^{V_{th}} \frac{dV}{F(V)}. \tag{4.16}$$

Plugging Equation 4.14 into 4.16 results in

$$\begin{aligned}\mathcal{I}_0 &= \int_{V_r}^{V_{th}} \frac{dV}{\bar{\mu} + g_2(V - \bar{V}_2)^2} \\ &= \frac{1}{\sqrt{g_2\bar{\mu}}} \tan^{-1}\left[\frac{\sqrt{g_2\bar{\mu}}(V_{th} - V_r)}{\bar{\mu} + g_2(V_{th} - \bar{V}_2)(V_r - \bar{V}_2)}\right],\end{aligned} \tag{4.17}$$

where the new variables: $\bar{\mu} = \mu - W_0 - W_m(V_2 - W_m)$, $\bar{V}_2 = V_2 + W_m/2g_2$ have been defined. In the limit that $g_{Ca} \to 0$, $\bar{\mu} \to \mu$ and $\bar{V}_2 \to V_2$, and the solution to the to the simple QIF model is recovered [213]. Further letting $g_2 \to 0$, the well known IF model ISI, $\mathcal{I}_{IF} = (V_{th} - V_r)/\mu$, results.

Case 2: $\mu < \mu^*$**.**

Case 2a: $V_r \leq V \leq V^*$**, with** $\dot{V} > \epsilon$**.** For low bias currents, $\mu < \mu^*$, there are two voltages at which the depolarizing current, $\mu + \psi(V)$ is balanced by the hyperpolarizing adaptation current, $\bar{W}(V)$, corresponding to fixed points where $F(V) = 0$. However, at the reset point, (V_r, W_r), F(V) is positive and remains so until the voltage reaches the ϵ-neighbourhood of the lower intersection point, V^*, defined by

$$V^* = \frac{2g_2V_2 + W_m - \sqrt{(2g_2V_2 + W_m)^2 - 4g_2(\mu - \epsilon + g_2V_2^2 - W_0)}}{2g_2}, \tag{4.18}$$

where $F(V^*) = \epsilon$. In this case, the voltage evolves according to Equation 4.14 from V_r up to V^*, with $\bar{\mu} < 0$ in this region, resulting in

$$\begin{aligned}\mathcal{I}_1 &= \int_{V_r}^{V_-^*} \frac{dV}{-|\bar{\mu}| + g_2(V - \bar{V}_2)^2} \\ &= \frac{-1}{2\sqrt{g_2|\bar{\mu}|}} \ln\left|\frac{[1 + \sqrt{g_2/|\bar{\mu}|}(V_-^* - \bar{V}_2)][1 - \sqrt{g_2/|\bar{\mu}|}(V_r - \bar{V}_2)]}{[1 - \sqrt{g_2/|\bar{\mu}|}(V_-^* - \bar{V}_2)][1 + \sqrt{g_2/|\bar{\mu}|}(V_r - \bar{V}_2)]}\right|,\end{aligned} \tag{4.19}$$

with $\bar{\mu}$ and $\bar{V}_2$ defined as in Equation 4.17.

Case 2b: $V^* \leq V \leq V_2$, with $|\dot{V}| < \epsilon$. Once the membrane voltage has reached V^*, $F(V) \leq \epsilon$ and the slow gating variable approximation can no longer be made, and x and C must be allowed to evolve in time. It is assumed that at V^* the gating variables result in an adaptation current $W^* > \mu$, and that they can now decay until the adaptation current, $W^*(t)$, reaches the bottom of the parabola at $\mu - \epsilon$. In this region, $\dot{V} \approx 0$ and $V \approx (V^* + V_2)/2 \equiv \bar{V}^*$, so that one can solve F_2 and F_3 for $x^*(t)$ and $C^*(t)$. Assuming $x^*_\infty \equiv x_\infty(\bar{V}^*)$, Equation 4.8b gives

$$x^*(t) = x^*_\infty - (x^*_\infty - x_r)e^{-t/\tau_x}, \tag{4.20}$$

by requiring $x^*(t = 0) = x_r$. Now to solve Equation 4.8c, one should plug in $x^*(t)$, as calculated above, however to get an analytic solution, it is assumed that $x^*(t) \approx x^*_\infty$, and $C^*_\infty \equiv C_\infty(V^*, x^*_\infty)$ is defined, resulting in

$$C^*(t) = C^*_\infty - (C^*_\infty - C_r)e^{-t/\tau_C}. \tag{4.21}$$

To get a more accurate prediction, Equation 4.8c can be numerically integrated according to

$$C^*_2(t_i) = C^*_2(t_{i-1}) + \Delta t[C_\infty(V^*, x^*(t_{i-1})) - C^*_2(t_{i-1})]/\tau_C, \tag{4.22}$$

with $C^*(t_0) = C_r$, in either case.

The gating variable dynamics in turn cause changes in $W^*(t)$. It is then assumed that $W^*(t)$ decays until it reaches the bottom of the parabola $\mu + \psi(V) - \epsilon$, at V_2.

This time can then be solved for, $W^*(t^*) = \mu - \epsilon$,

$$W^*(t^*) = g_{Ca} \underbrace{x^*(t^*)^2}_{\approx a_1 + b_1 t^*}(V^* - V_{Ca}) + g_{KCa} \underbrace{\frac{C^*(t^*)}{C^*(t^*) + K_d}}_{\approx a_2 + b_2 t^*}(V^* - V_K) = \mu - \epsilon \tag{4.23}$$

by expanding to first order in time. The resulting coefficients are: $a_1 = x_r^2$, $a_2 = C_r/(K_d + C_r)$, and

$$\begin{aligned} b_1 &= \left.\frac{\partial x^*(t)^2}{\partial t}\right|_{t=\tau_x} = \frac{2x^*(\tau_x)(x^*_\infty - x_r)}{\tau_x} e^{-1} \\ b_2 &= \left.\frac{\partial}{\partial t}\left[\frac{C^*(t)}{K_d + C^*(t)}\right]\right|_{t=\tau_C} = \frac{K_d(C^*_\infty - C_r)}{(K_d + C^*(\tau_C))^2 \tau_C} e^{-1}. \end{aligned} \tag{4.24}$$

This allows t^* to be found,

$$\begin{aligned} \mathcal{I}^* = t^* - 0 &= \frac{\mu - \epsilon - [g_{Ca} a_1 (V^* - V_{Ca}) + g_{KCa} a_2 (V^* - V_K)]}{g_{Ca} b_1 (V^* - V_{Ca}) + g_{KCa} b_2 (V^* - V_K)} \\ &= \frac{\mu - \epsilon - A}{B}, \end{aligned} \tag{4.25}$$

where $A \equiv [g_{Ca} a_1 (V^* - V_{Ca}) + g_{KCa} a_2 (V^* - V_K)]$ and $B \equiv g_{Ca} b_1 (V^* - V_{Ca}) + g_{KCa} b_2 (V^* - V_K)$. This shows that A represents the amount of adaptation current, W, when the voltage enters the $\dot{V} < \epsilon$ region at V^*, while B represents rate of change of adaptation current, due to the decay of the gating variables x and C. This gives the simple geometric interpretation that the time interval $\mathcal{I}^*$ is equal to the "distance" that W must travel, divided by the "velocity" at which W travels.

At this point in time, the adaptation current W has decayed to $W(t^*) = \mu - \epsilon$, and $V(t^*) = V_2$, and the voltage is once again free to increase monotonically until threshold.

Case 2c: $V_2 \leq V \leq V_{th}$, with $\dot{V} > \epsilon$. For the remaining trajectory, I require a new adaptation current, $\bar{W}^*$, using the decayed gating variables instead of their initial reset values. However, I also require that $\bar{W}^*(V_2) = \mu - \epsilon$ to have the desired initial conditions, resulting in

$$\begin{aligned} \bar{W}^*(V) &= W_0^* + W_m^* V \\ W_m^* &= g_{Ca} x^*(t^*)^2 + g_{KCa} \frac{C^*(t^*)}{K_d + C^*(t^*)} \\ W_0^* &= \mu - \epsilon - W_m^* V_2. \end{aligned} \tag{4.26}$$

Equation 4.14 can then be integrated from V_2 to V_{th}, resulting in

$$\begin{aligned} \mathcal{I}_2 &= \int_{V_2}^{V_{th}} \frac{dV}{\bar{\mu}^* + g_2(V - \bar{V}_2^*)^2} \\ &= \frac{1}{\sqrt{g_2 \bar{\mu}^*}} \tan^{-1}\left[\frac{\sqrt{g_2 \bar{\mu}^*}(V_{th} - V_2)}{\bar{\mu}^* + g_2(V_{th} - \bar{V}_2^*)(V_2 - \bar{V}_2^*)}\right], \end{aligned} \tag{4.27}$$

where the new variables: $\bar{\mu}^* = \mu - W_0^* - W_m^*(V_2 - W_m^*)$, $\bar{V}_2^* = V_2 + W_m^*/2g_2$ are again defined. Once the voltage has reached threshold, in this case the x and C variables have decayed from their reset values to new values at the occurrence of the new spike, $x(t_{spk}) = x^*(t^*)$ and $C(t_{spk}) = C^*(t^*)$. In this case, the fixed gating variable reset conditions are independent of these threshold values, but in the case of the spike generated resets, they will depend strongly on these threshold values.

4.4.4 Iterative Theoretical Predictions: Stable and Unstable Limit Cycles

For the QIF model with spike generated reset conditions, the values of x_{reset} and C_{reset} are not known. However, with the theory described above, for fixed resets, there are two general types of ISI trajectories: Case 1, $\mu^*(x_{reset}, C_{reset}) < \mu$ in which

$\dot{V} > \epsilon$ and the slow variable approximation holds, and case 2, $\mu^*(x_{reset}, C_{reset}) > \mu$ in which the slow variable approximation is violated and the gating variables are allowed to decay.

For case 1, $\mu > \mu^*$, the slow gating variable assumption is that $x \approx \langle x \rangle = x_{reset}$ and $C \approx \langle C \rangle = C_{reset}$ are constant. In this case, the ISI is easily computed by Equation 4.17, and a simple result of the Fokker-Plank equation corresponding to Equation 4.14, gives the steady state voltage distribution

$$p_0(V) = \frac{1}{F(V)} / \int_{V_r}^{V_{th}} \frac{dV}{F(V)}, \text{ for } V_r < V < V_{th}, \tag{4.28}$$

where the normalization constant is in fact the ISI, $\mathcal{I}_0$. However, this is only the sub-threshold voltage distribution, and does not include the voltage distribution of the action potential, $p_{spk}(V)$, during the refractory period. To get the full voltage distribution these two distributions are combined, weighted according to their fraction of the total ISI:

$$p(V) = A\left[\frac{\mathcal{I}_0}{\mathcal{I}_0 + \tau_r} p_0(V) + \frac{\tau_r}{\mathcal{I}_0 + \tau_r} p_{spk}(V)\right], \tag{4.29}$$

where A is a new normalization coefficient. This leads to the same gating variable self-consistency equations from Equations 4.5b&c as in [214]:

$$\begin{aligned} \langle x \rangle &\approx \int x_\infty(V) p(V)\, dV \\ \langle C \rangle &\approx \int C_\infty(V, x_\infty(V)) p(V)\, dV. \end{aligned} \tag{4.30}$$

In this case the iterative algorithm outputs a voltage distribution, p(V), which is used to estimate the mean gating variables which will be used in the next iteration.

If they again result in $\mu > \mu^*$, the same procedure repeats, and may converge to a stable sequence of a single ISI. If not, the algorithm will proceed to case 2.

If the reset conditions result in case 2, $\mu < \mu^*$, the gating variables will get a chance to decay, as estimated in Models and Methods. Therefore, because the slow gating variable approximation is violated, Equation 4.30 can no longer be used as the self-consistency criterion. Now the artificial action potential must be used to numerically reset the gating variables, and if the amount they decay is stabilized by the amount they are reset, a single trajectory and ISI will repeat. However, if they do not match, a new trajectory will be selected, which may again result in case 2, or take the algorithm back to case 1.

The algorithm may converge to a single repeated ISI, estimated either via case 1 in the high bias regime, or case 2 in the low bias regime, however, the algorithm may also result in a sequence of 2 or more ISIs which repeat periodically (i.e. bursting), or even an aperiodic sequence of ISIs which do not contain any repeating pattern. The sequences of ISIs and gating variable reset values, can be analyzed via the ISI return map, $\phi : ISI_k \to ISI_{k+1}$, to quantify their stability.

CHAPTER 5
Conclusions

5.1 Summary of Results

In this chapter I will first summarize the main results of chapters two through four, and then discuss the big picture conclusions we can draw from considering the vestibular system in the context of optimal coding. I will then consider possible implications of the boosting nonlinearity found in VO neurons and the nature of rate and temporal coding in effect. Finally I will discuss some future directions in which I would continue this line of work.

5.1.1 Irregular afferents are more optimized for the statistics of natural vestibular stimuli than regular afferents

In *chapter 2* we first explore the statistics of the naturalistic stimuli to which the vestibular system is exposed, by recording and characterizing the natural head movements of monkeys. Like other naturalistic stimuli, they were found to have non-Gaussian distributions, with heavy tails characterized by high kurtosis. Furthermore natural stimuli reached velocities and accelerations much greater than those used in the lab. Secondly, we characterize vestibular afferents by fitting them to LN cascade models which predicted that the larger head movements of the distribution tails will result in considerable rectification and saturation. Furthermore, I use information theoretic techniques to show that optimal stimulus distribution for irregular afferents is closer to the natural distribution than that of regular afferents, despite leading to

more rectification. This challenges the traditional view that the vestibular system *is* linear, suggesting that although it behaves primarily linearly, natural stimuli will regularly elicit nonlinearities.

5.1.2 High conductance state of neurons *in vivo* explains differences in behaviour observed *in vitro*

In *chapter 3* we showed that a neuron model developed for type B vestibular nuclei neurons *in vitro* exhibited strong subthreshold oscillations in response to step current stimuli, which translated from a subthreshold resonance to a spiking resonance. These intrinsic cellular dynamics result in the neurons tendency to fire spikes nonlinearly phase-locked to sinusoidal stimuli *in vitro*, over a range of stimulus amplitudes and frequencies which result in linear rate modulations *in vivo*. We show that mimicking the high conductance state of neurons *in vivo* with an increased leak conductance and additive current noise, is sufficient to linearize the neuron model over the required stimulus amplitude and frequency range, allowing it to reproduce the linear rate modulations of VO neurons measured *in vivo*. Although neurons are inherently nonlinear, due to the spike generation mechanism, as well as rectification and saturation, they can still behave linearly for sufficiently small amplitude stimuli. However, it does not make sense to say that a neuron either *is* or *is not* linear, as it depends on the stimulus with which it is driven. For sufficiently large amplitude stimuli, the nonlinear phase locking behavior is expected to re-emerge, despite the noisy high conductance state *in vivo*.

5.1.3 VO model neuron exhibits boosting nonlinearity due to spike-triggered adaptation current governed by calcium and calcium-activated potassium channels

In *chapter 4*, I characterize the effects of the interplay of calcium and calcium activated-potassium channels on the underlying bifurcation structure and resulting f-I curve of the VO neuron model from Chapter 3, showing that increased calcium conductances can result in a boosting nonlinearity in the f-I curve. I reduce the full model to a generalized QIF model, which preserves the boosting nonlinearity and bifurcation structure, with the use of an artificial piecewise linear action potential to mimic the reset conditions of the calcium and calcium-activated potassium currents. By further simplifying the reset conditions I show that a boosting nonlinearity is possible, without resulting in bursting, and derive an analytic equation for the gain, revealing the mechanistic origins of the boosting nonlinearity. By projecting the 3-variable QIF model into the two dimensions of the membrane voltage, V, and spike-triggered adaptation current, W, I show that the phase space trajectories in the low and high bias regions differ qualitatively: at low biases, the trajectories cross the V-nullcline resulting in a bi-directional AHP and low gain, while at high biases, the trajectories are free to increase monotonically to threshold. While the analytic calculations are only possible when the gating variable resets are known, when the artificial action potential is used, an iterative algorithm was shown to converge close to the correct firing rate in the limit of vanishing bias current, and very large bias currents, showing that the original VO model's boosting nonlinearity can still be explained by our simplified theory.

5.2 Optimal Coding in the Vestibular System

5.2.1 Statistical Structure of Natural Stimuli

Similarly to natural stimuli in other sensory systems [5], we found that the probability distributions of natural head movement velocities and accelerations are non-Gaussian as quantified by the increased kurtosis of the distributions. Indeed this was also found for natural head movements in humans [104]. In addition to stimulus probability distributions, such dynamic stimuli are also characterized by their temporal autocorrelation function, or its Fourier transform in the frequency domain. Interestingly, we found linear accelerations to obey a power law (as in many other sensory modalities [5]), while angular rotations do not (see Appendix D). This is also particularly surprising, as a recent publication showed that the natural head movements in *humans* do not obey a power law (for either linear or angular movements), due to low-pass filtering by the biomechanics of the body [104]. This highlights the fact that there are significant differences in the natural head (and likely body) movements of humans and monkeys. For example, humans tend to sit, stand, and walk upright [104], while monkeys spend much more of their time on all fours, resulting in significantly different head movements during locomotion.

5.2.2 Maximizing Mutual Information or Minimizing Energy Consumption

Although we have shown that the optimal stimulus distribution for irregular afferents are better matched to the natural stimulus distributions than regular afferents, it is really due to their resulting response distributions being closer to uniform (i.e. maximizing entropy). However, their response distributions actually differ significantly from uniform, primarily due to afferents spontaneous firing rates, R_0, being

significantly less than the mean of the uniform distribution, $R_{max}/2$. In Appendix B I show that the natural vestibular response distributions for both regular and irregular afferents are most consistent with a fixed mean and variance constraint, that results in the response distribution being peaked at R_0 with a Gaussian shape. Assuming that the mean firing rate is close to R_0, these mean and variance constraints correspond to a constraint on the metabolic energy consumption [17]. Similarly, evidence has been found that neurons in visual cortex exhibit exponential response distributions when stimulated with natural visual scenes [18], corresponding to a mean firing rate constraint on energy consumption.

Constraints on firing rate and energy consumption illustrate a trade-off between increasing information and reducing energy consumption. Furthermore, the data processing inequality states that information in a signal cannot be increased simply by subsequent stages of processing. This paints a natural picture where neurons at the sensory periphery use higher firing rates to ensure as much sensory information as possible enters the brain, with subsequent stages transforming the information into a more efficient representation, that costs less energy (i.e. uses lower firing rates). Indeed, VO neurons do have lower spontaneous firing rates than their afferent inputs ($R_{0,Aff} \approx 100$ spk/s, versus $R_{0,VO} \approx 70$ spk/s). Although this suggests VO cell response distributions would have less mutual information about the stimulus distributions, it has generally been their information rates that are measured using dynamic noise stimuli.

5.2.3 Dynamic Stimuli and the Mutual Information Rate

Vestibular neurons are known to have a finite integration time, with their probability of spiking influenced only by the stimulus values over the previous $\sim 100ms$ [111]. As such, it is their information rates that have been experimentally estimated using broadband stimuli with variance low enough to not elicit significant rectification or saturation. Although VOs were found to transmit less bits per spike [35], the study used broadband noise stimuli with a flat power spectrum from 0-20 Hz, not naturalistic stimuli which many other studies have found to result in greater information rates [5, 12]. It is well known that for dynamic time-dependent stimuli, that the information maximizing transformation is a "whitening" filter [5]. In appendix D I show that the evolutionarily newer irregular afferents have more high-pass gain profiles, and do therefore produce *whiter* responses than regulars. However neither canal or otolith transfer functions result in perfect whitening. Interestingly, canal afferent transfer functions are well described by a simple low-pass filter with two characteristic time constants, while otolith transfer functions require fractional-order transfer functions which have been shown to be equivalent to a weighted linear combination of many filters with different time constants [216]. This different fundamental transfer function structure, may therefore be a reflection of the difference in linear and angular stimulus power spectra, where power law indicates that the otolith stimuli do not have a single characteristic time scale either.

Although irregular afferents clearly perform more whitening than regular afferents, downstream VO neurons receive input from both afferents, with a ratio assumed

to be roughly 50% of each. It is of course possible that VO neurons perform further whitening, as suggested by the masking results and discussion in Appendix E. While some different combinations of "signal" and "masker" amplitude and frequency combinations were explored in Figure E.5, it is also possible for the "masker" to be attenuated by the "signal". This was of course not the case for the data presented in that study, but is possible for naturally occurring stimuli in which power can drop by up to 5 orders of magnitude from 0-20 Hz (see Figure D.1). Furthermore, for natural stimulus power spectra, it is unclear how it should be split into "signal" and "masker" components. Additionally, VO neurons receive convergent afferent inputs from canals and otoliths, so it is also possible that the functional role of the VO nonlinearity could be masking between multimodal inputs. Indeed VO responses to combined linear and rotational movements were recently found to be "sub-additive" [217], which may be a consequence of the boosting nonlinearity.

5.2.4 Functional Constraints: Active versus Passive stimuli

An important functional role of VO neurons is that they respond differently to "active" (i.e. self-generated) and "passive" (i.e. externally generate) head movements, with passive stimuli used to characterize their gains and showing $\sim$ 70% attenuated gains in response to active movements. They are in fact the first stage of processing in the brain to distinguish the two types of movements, and it is considered an essential part of their function in vestibular processing [100]. Interestingly, almost all natural head movements recorded in monkeys were active self generated movements (except a few instances of the monkey jumping for a ledge and missing it). When truly in the wild, however, it is possible they could be carried by another

monkey, swing from a vine, float on a log or raft, hunt prey, escape predators, and of course fight with other monkeys. The amplitude and frequency content of such "passive" head movements is not likely drastically different than those characterized here, but they surely make up a much smaller percentage of the animals total head movements than active movements. It is therefore unlikely that VO neuron responses will form a uniform distribution, if the majority of responses are attenuated. It is however still possible for VO neurons to "whiten" natural stimuli, reducing the correlation time of the spiking response and distributing information more efficiently between fewer spikes. Finally, even if we imagine an optimal response distribution for VO neurons, they receive convergent inputs from canal and otolith afferents making the corresponding optimal stimulus distribution impossible to uniquely define.

Furthermore, with $\sim 70\%$ gain attenuation for all self-generated movements in VO neurons, they will likely not often elicit the boosting nonlinearity, remaining primarily in the linear response range. However, when passive head movements occur, they could be of lower amplitude (i.e. being carried by another monkey) or much larger amplitudes (i.e. fighting, escaping predators, falling from a tree). These larger amplitude passive stimuli, which are surely most relevant to an animals survival, likely do elicit the boosting nonlinearity. Thus during truly natural conditions, VO neurons are likely operating primarily in their linear response regime, with less common large amplitude passive stimuli driving them nonlinearly across the boosting nonlinearity, potentially resulting in temporal coding (as discussed in Appendix F). One question about reafference cancellation in VO cells is why 70-80%? A recent study showed that the cancellation is adaptive to changing conditions [218]; could

the boosting nonlinearity be sending an additional signal to drive the learning until things are attenuated enough to make things linear?

5.3 Coexistence of Rate and Temporal Coding in the Vestibular system

5.3.1 Advantage of a Boosting Nonlinearity

It is well known that when a spontaneously active neuron is driven into rectification, it can lead to a difference in the SR- and $\sqrt{RR}$-coherences, possibly at lower or higher harmonic frequencies to those in the stimulus, indicative of a temporal code [219]. However, such rectification leads to all stimulus values below a certain threshold being mapped onto the same firing rate, 0 spk/s, no longer be distinguishable via a rate code. With a boosting nonlinearity, however, a range of stimulus values that would have lead to rectification can now still be encoded in the firing rate with a lower gain (i.e. gain control; see Appendix E.3.3). We have also shown that such stimuli which elicit the boosting nonlinearity can also generate higher harmonics in their $\sqrt{RR}$-coherence, due to increased spiking precision also potentially resulting in temporal coding (see Appendix F). Thus, unlike normal rectification, a boosting nonlinearity could start to produce increased temporal spiking precision, without completely sacrificing its ability to encode information in its firing rate *simultaneously*.

5.3.2 Role of Variability

Although variability is generally though of as detrimental to information processing, in chapter 3 we showed that in fact the increased variability of VO model neurons prevented them from nonlinearly phase-locking to the stimulus due to their combination of ion channels. These same channels are those that give rise to the

boosting nonlinearity in its f-I curve, and its ability to burst, as shown in Chapter 4. The increased noise, however, disrupts the bursting in the model neuron, and is known to have a similar effect *in vivo* [170]. It is therefore possible that the high degree of variability is necessary for the VO neurons with a boosting nonlinearity to not burst and still primarily employ a rate code for low amplitude stimuli. Furthermore, if populations of neurons have independent variability, then it can often be averaged out in a population code.

5.3.3 Single Neuron versus Population Coding

The increased variability of VO may indeed serve to prevent them from phase-locking or bursting, allowing them to encode stimuli in their firing rate modulations, however it has also been shown to result in single VO cells transmitting significantly less information per second, and per spike, than either afferents [35]. However, as long as this variability is independent across a population of VO cells, it can be averaged out, which appears to be the case for low amplitude stimuli. For larger amplitude stimuli which elicit the boosting nonlinearity, VOs were shown to produce higher harmonics in the $\sqrt{RR}$-coherence due to higher spiking alignment across responses to repeated presentations of the same stimulus (see Appendix F). One can however, easily imagine this was a population of neurons all responding to one presentation of the stimulus, and infer that this translates into a population synchrony, or increased coincident spiking. But a real population of VO cells will have a distribution of properties, from baseline firing rate, gain, and CV, to ion channel concentrations and shapes of boosting nonlinearities [36]. Such heterogeneities across populations can also act as variability, reducing the degree of population synchronization. However,

the vestibular nuclei is also known to contain gap [27] junctions which can couple cells electrically (rather than via slow chemical synapses) which can serve to either promote synchrony or anti-synchrony in different conditions [220].

5.4 Future Directions

The vestibular system has been extensively studied and is well known for its linearity in encoding dynamic stimuli with a rate code. Many people in fact claim the vestibular system *is* linear, and we can see now that for the small amplitude stimuli generally used for its characterization it will indeed behave linearly. However, we have shown that natural head movements are often large enough to drive vestibular afferents out of their linear range, causing it to behave nonlinearly. And in fact central VO neurons in VN, appear to have and additional nonlinearity (beyond rectification or saturation) which has likely evolved for a particular purpose. Furthermore, using a stimulus to show which neurons transmit the most information, is really dependent on which stimuli is used and should be estimated using as natural a stimulus as possible.

One possible future direction would be to stimulate vestibular afferents and VO cells with the naturalistic stimuli that we have recorded in freely moving monkeys, to see if the natural correlation structure and amplitude distributions result in different amounts of information. However, these natural stimuli were almost all self-generated, so applying them passively to the animal in the lab would not be exactly the same. This should not be a problem for afferents, as they are known to respond the same way to passive and active stimuli, and also each respond to a single dimension of motion (i.e. rotations or translations, but not both). However VO

neurons are known to respond differently to active and passive stimuli, and to truly record them in natural conditions the animal would need to be freely moving while recording from the neurons, which poses a huge technical challenge. Furthermore, VO cells receive convergent input from both canal and otolith afferents, and natural movements tend to involve combinations which will activate both afferent classes simultaneously. Generally, experiments showing the attenuated response to active movements, also show the responses to passive application of the same (or as similar as experimentally possible) stimulus profile, which would be virtually impossible (with current lab equiptment) for freely moving monkeys.

An alternative approach would be to continue using artificial stimuli in the lab, but systematically varying stimulus attributes, such as amplitude and frequency content, to map out the neural transformations and see how they may depend on the stimulus applied. In VO cells for example it has been shown that yaw rotations elicit the boosting nonlinearity. However, our analysis would suggest the same result should occur with linear acceleration stimuli as well. Our results from Appendix E consider the possibility of high frequency stimulus masking low frequency stimuli within the same yaw stimulus dimension. Under natural conditions, however, perhaps this nonlinear combination of stimuli would occur for combined stimuli from different movement axes. A recent study in fact found combined rotations and translations of low amplitudes, result in sub-additivity [217]. However, if these combined stimuli had sufficiently large amplitudes to elicit the boosting nonlinearity when combined but not separately, this may be explained by the boosting nonlinearity. Further studies are needed to explore this interesting possibility.

Finally, our VO neuron model which exhibits a boosting nonlinearity similar to that recorded from neurons *in vivo*, was actually developed to model vestibular neurons *in vitro*. However, the *in vitro* studies found no evidence for the actual boosting nonlinearity (unpublished observations). Although the model behaviour and *in vivo* neuron behaviour is quite similar, we have not proven that this is in fact the actual mechanism at play *in vivo*. One way to test this would be to measure the boosting nonlinearity *in vivo*, and then apply a pharmaceutical to block the calcium channels, see that the boosting nonlinearity disappears. This again poses an extreme technical challenge. An alternative would be for the *in vitro* studies to explore a wider range of stimulation protocols in search of the boosting nonlinearity, or alternatively providing concrete evidence that it is not present *in vitro*.

Additionally, further work with the VO neuron model could be done to characterize how it is altered by the effects of the high conductance state of neurons *in vivo*. For example, it is known that such conditions disrupt bursting in neurons *in vivo* [170], simply resulting in increased spiking variability. It is possible however for some signature of bursting to remain, such as negative ISI correlations, or a dependence of firing rate variability with stimulus. Further characterization of the VO models behaviour under noisy *in vivo* conditions could possibly provide a signature which could be experimentally verified. Furthermore, such a model could be used to test the LN model representation of the boosting nonlinearity for increasingly larger amplitude stimuli, as well as some of the predictions about its possible role in temporal coding and population synchronization.

APPENDIX A
Sigmoidal and exponential f-I curve fitting.

In the publication presented in Chapter 2, we used afferent LN models were fit with sigmoidal nonlinearities. However, many neurons exhibit a more asymmetric nonlinearity captured by an exponential function. Additionally, instead of separating linear and nonlinear components into LN models, we can directly plot the firing rate *frequency* versus the stimulus or current *input* (a.k.a. f-I curves) generating a map directly from head velocity stimulus to firing rate response. Such f-I curves are there for dependent on the frequency content of the stimulus used to generate them, with the average frequency-dependent gain captured by the slope of the f-I curve at zero stimulus. In Figure A.1, we show and example neuron fit to a sigmoid and exponential function in panels A and B, as well as the population of regular canal afferent fits to sigmoid, and the population of irregular canal afferent fits to exponentials in panels C and D. Sigmoids were parametrized as in the methods section above, Equation 2.5, which exponential f-I curves were parametrized as,

$$T_{exp}(x) = \max\Big\{c_3[1 - \exp^{-c_1(x-c_2)}], 0\Big\}, \tag{A.1}$$

where the $\max\{,\}$ operation is to ensure the resulting firing rate is always positive. In addition, however, to smooth out the f-I curve near the rectification point, capturing the effects of noisy spiking, convolution with a Gaussian function with an extra parameter for its width, was also used. Panel E shows the fits adjusted-R^2 values,

and that all fits were very good, but for irregular afferents only, exponentials were significantly better than sigmoids. To compare the basic afferent properties, panel F shows the average gain (top) of each population, with irregulars being significantly greater than regulars, the average firing rate at 0 deg/s (i.e. baseline firing rate, middle), and maximum firing rate (bottom) with no significant differences. There parameters are in reasonable agreement with the estimates of these parameters directly from the neural response data, given the frequency content of the stimuli used to generate them, shown in panel G. Although the irregular afferent f-I curves were better fit by exponentials, this was not the case for the LN model nonlinearities which were constrained to have a max slope of ~ 1, due to the separation of the the linear filtering from the nonlinear function.

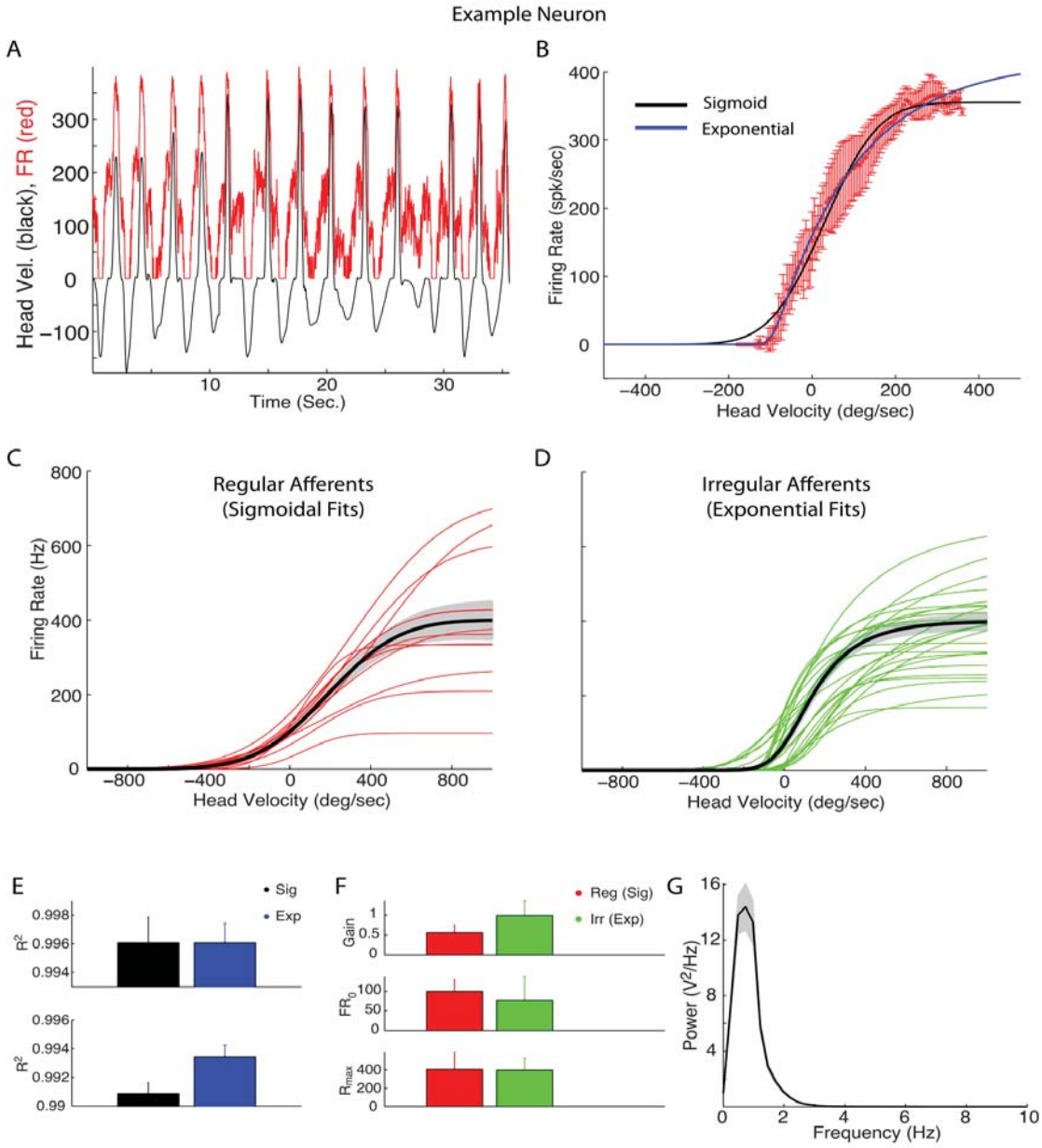

Figure A.1. Sigmoidal versus exponential f-I curve fitting.

Figure A.1 ***(previous page).*** (A) For an example canal afferent neuron, the angular velocity (black) and filtered firing rate response (red) are superimposed, as functions of time. (B) The mean firing rate with SE bars, is plotted as a function of head velocity stimulus, using the same method as in Figure 2.4, but without the linear prediction. Superimposed are the best fit sigmoid and exponential functions, parametrized according to Equation 2.5 and Equation 2.12, respectively. (C) Population of regular afferents fit with sigmoidal functions (red), with mean sigmoid (black) with SE (grey shading). (D) Population of irregular afferents fit with exponential functions (green), with mean sigmoid (black) with SE (grey shading). (E) Population average R^2 values of sigmoidal and exponential fits, showing no significant different for regular afferents, but a significant difference for irregulars ($p < 0.05$). (F) The 3 main parameters of the nonlinearities are compared for regular and irregular fits, with a significant difference for their gains (i.e. max slope (top), $p < 0.05$), and no significant difference for their spontaneous firing rates (i.e. R_0, middle), and no significant difference in R_{max} (bottom). (G) The average frequency content of the stimuli used to generate the f-I curves.

APPENDIX B
Derivation of the optimal stimulus distribution, with and without constraints, in the low noise limit.

The results of the following derivations are outlined in [112], but I include the details of the calculations here for reference.

B.1 The Cramer-Rao Bound

Consider a neuron which transforms a stimulus x into a response y, which is then used to estimate x, $\hat{x}(y)$. If the estimator is *unbiased* then its mean value is equal to the true mean,

$$\int dy\, \hat{x}(y)p(y|x) = \langle \hat{x}(y) \rangle_{p(y|x)} = x. \tag{B.1}$$

If the estimator is *unbiased*, then its variance,

$$\sigma_x^2 = \langle (\hat{x} - x)^2 \rangle_{p(y|x)}, \tag{B.2}$$

is bounded from below,

$$\sigma_x^2 \geq \frac{1}{J(x)}, \tag{B.3}$$

where $J(x) = -\langle \frac{\partial^2}{\partial x^2} \ln p(x|y) \rangle = \langle (\frac{\partial}{\partial x} \ln p(x|y))^2 \rangle$. If the estimator is *efficient* then it saturates the bound. Maximum-likelihood estimators are known to be efficient in the limit of large N observations, where $p(\vec{y}|x)$ is the probability of observing the set of responses $\vec{y}$ (i.e. N independent neurons). In further derivations here, we will need to assume that we are in such a limit.

B.2 Relationship between Fisher and Mutual Information

The mutual information between a stimulus and response is given by

$$I(y,x) = \int dy\, dx\, p(y|x)p(x) \log^2 \frac{p(y|x)}{p(y)}. \tag{B.4}$$

Let us assume that there is a unbiased efficient estimator $\hat{x}(y)$, with $\mu_{\hat{x}} = x$ and $\sigma^2_{\hat{x}} = 1/J(x)$. Since $x \to y \to \hat{x}$, rather than consider the mutual information between x and y, we can start by considering the mutual information between the estimator $\hat{x}$ and its its mean x:

$$I(x,\hat{x}) = \mathcal{H}(\hat{x}) - \int dx\, p(x)\mathcal{H}(\hat{x}|x), \tag{B.5}$$

where $\mathcal{H}(\hat{x}) = -\int d\hat{x}\, p(\hat{x}) \log_2 p(\hat{x})$ is the entropy of the estimator. Since Gaussians maximize entropy for a fixed mean and variance, and conditioning reduces entropy, we have

$$\mathcal{H}(\mathcal{N}(\mu_{\hat{x}}, \sigma^2_{\hat{x}})) \geq \mathcal{H}(\hat{x}) \geq \mathcal{H}(\hat{x}|x), \tag{B.6}$$

where $\mathcal{H}(\mathcal{N}(\mu_{\hat{x}}, \sigma^2_{\hat{x}})) = \frac{1}{2}\log(2\pi e \sigma^2_{\hat{x}}) = \frac{1}{2}\log(\frac{2\pi e}{J(x)})$. We can then rewrite Equation B.5 as,

$$I(\hat{x},x) \geq \mathcal{H}(\hat{x}) - \int dx\, p(x) \underbrace{\frac{1}{2}\log\left(\frac{2\pi e}{J(x)}\right)}_{\geq \mathcal{H}(\hat{x}|x)}. \tag{B.7}$$

Now by the data processing inequality, $I(y,x) \geq I(\hat{x},x)$, which gives

$$I(y,x) \geq \mathcal{H}(\hat{x}) - \int dx\, p(x) \frac{1}{2}\log\left(\frac{2\pi e}{J(x)}\right). \tag{B.8}$$

Finally, if $\hat{x}$ is sharply peaked at its mean (i.e. $J(x) \gg 1$, or $\sigma_x^2 \ll 1$) then $\mathcal{H}(\hat{x}) = \mathcal{H}(x)$, and we can write

$$\begin{aligned} I(y,x) &\geq \mathcal{H}(x) - \int dx\, p(x) \frac{1}{2} \log\left(\frac{2\pi e}{J(x)}\right) \\ &= I_{\text{fisher}}. \end{aligned} \tag{B.9}$$

If $J(x)$ is non-Gaussian, then $I > I_{\text{fisher}}$, however MLEs are known to be Gaussian in the limit of large N. For a single neuron, this is equivalent to a large integration time or small σ limit. We will assume that we are in the small noise limit, and consider effects of high noise intensity separately.

B.3 Calculating Fisher Information

For a neuron with noisy response given by $y = T(x) + \sqrt{V(x)}\eta$, where $P(\eta)$ is a normal distribution with zero mean and unit variance, the conditional probability is given by

$$\begin{aligned} p(y|x) &= \mathcal{N}(T(x), V(x)) \\ &= \frac{1}{\sqrt{2\pi V(x)}} e^{-\frac{(y-T(x))^2}{2V(x)}}, \end{aligned} \tag{B.10}$$

where $V(x) = \sigma^2 g(x)$. This gives rise to:

$$\ln p(y|x) = -\frac{1}{2}\ln(2\pi V(x)) - \frac{1}{2}\frac{(y-T(x))^2}{V(x)} \tag{B.11}$$

$$\begin{aligned}
\frac{\partial}{\partial x}\ln p(x|y) &= \frac{\partial T(x)}{\partial x}\left(\frac{y-T(x)}{V(x)}\right) + \frac{1}{2}\frac{\partial V(x)}{\partial x}\left[\left(\frac{y-T(x)}{V}\right)^2 - \frac{1}{V(x)}\right] \\
&= \frac{\partial T(x)}{\partial x}\left(\frac{\sqrt{V(x)}\eta}{V(x)}\right) + \frac{1}{2}\frac{\partial V(x)}{\partial x}\left[\left(\frac{\sqrt{V(x)}\eta}{V}\right)^2 - \frac{1}{V(x)}\right] \\
&= \frac{\partial T(x)}{\partial x}\left(\frac{\eta}{\sqrt{V(x)}}\right) + \frac{1}{2}\frac{\partial V(x)}{\partial x}\left(\frac{\eta^2-1}{V(x)}\right) \\
&= T'(x)\left(\frac{\eta}{\sigma\sqrt{g(x)}}\right) + \frac{1}{2}\sigma^2 g'(x)\left(\frac{\eta^2-1}{\sigma^2 g(x)}\right) \\
&= \frac{1}{\sigma}\left[\frac{\eta T'(x)}{\sqrt{g(x)}} + \sigma(\eta^2-1)\frac{g'(x)}{2g(x)}\right]
\end{aligned} \tag{B.12}$$

The term on the left is $\mathcal{O}(1)$, while the term on the right is $\mathcal{O}(\sigma)$, and thus in the limit of small σ the first term dominates and the second can be neglected. Letting $y^* = (y-T)/V$, and $(y-T)/\sqrt{2V} = z$, we have $dy = \sqrt{2V}dz$, which gives $y^* = \sqrt{\frac{2}{V}}z$, and

$$\langle(\frac{\partial}{\partial x}\ln p(y|x))^2\rangle = \frac{1}{\sqrt{\pi}}\int dz\left[T'^2\left(\frac{2}{V}\right)z^2\right]e^{-z^2}, \tag{B.13}$$

which results in

$$J(x) = \frac{T'^2}{V}. \tag{B.14}$$

B.4 Information Maximization: The Optimal Stimulus Distribution

In the limit that Equation B.9 is an equality, we have

$$I(y,x) = -\int dx\, p(x)\log p(x) - \int dx\, p(x)\log\sqrt{\frac{2\pi e}{J(x)}}. \tag{B.15}$$

Now if we want to know the stimulus distribution that maximizes $I(x, y)$, then we must solve $\frac{\partial I(x,y)}{\partial p(x)}|_{p(x)=p^*(x)} = 0$, which results in

$$\frac{\partial I(x, y)}{\partial p(x)}|_{p(x)=p^*(x)} = -\ln p^*(x) - \ln e^1 - \ln \sqrt{\frac{2\pi e}{J(x)}} = 0. \tag{B.16}$$

Exponentiating to solve for p^* gives

$$p^*(x) = \sqrt{\frac{J(x)}{2\pi e}}, \tag{B.17}$$

which when normalized results in

$$p_J(x) = \frac{\sqrt{J(x)}}{\int dz \sqrt{J(z)}}, \tag{B.18}$$

which is known as Jeffrey's prior. Then plugging in the equation for J(x), and taking the limit of vanishing noise, the optimal stimulus distribution is reduced to

$$p_{opt}(x) = cT'(x), \tag{B.19}$$

where c is simply the normalization coefficient. In this vanishing noise limit, we find the optimal stimulus distribution to be that which the deterministic transformation y=T(x), results in a uniform response distribution. This is the response distribution which maximizes response entropy, which is equivalent to maximizing information in the vanishing noise limit.

A similar derivation is presented in Bialek's Biophysics: Searching for Principles [221] in section IV-C. Although this derivation appears somewhat simpler, it also makes the assumption that the noise intensity is in the vanishingly small limit, for essentially the same reason of replacing the conditional noise entropy, with that of

a Gaussian. The derivation presented here in fact gives more details underlying this assumption of low noise intensity.

B.5 Entropy Maximization with Constraints

In the limit that of vanishing noise, maximizing information becomes equivalent to maximizing the entropy of the response distribution (see Equation 1.3), $H(y) = -\int dyp(y)\log p(y)$. It is easily shown that the response distribution which maximizes entropy is the uniform distribution from 0 to R_{max} To impose a constraint that the response distribution have a fixed mean and/or variance, we must maximize the following equation,

$$H^*(y) = H(y) - \lambda_0\left(\int dyp(y) - 1\right) - \lambda_1\left(\int dyyp(y) - \mu_y\right) - \lambda_2\left(\int dy(y-\mu_y)^2 p(y) - \sigma_y\right), \tag{B.20}$$

It is well known that with only a constraint on the response mean, the optimal distribution becomes exponential [5], instead of uniform, with its peak at a firing rate of zero. This is perhaps reasonable for cortical neurons that do not fire spontaneously, and with very low mean firing rates ($\sim 1-5spk/s$). However, vestibular afferents have a spontaneous firing rate of $R_0 \sim 100spk/s$, and the natural stimulus distributions show that the most common stimulus is generally to be at rest (i.e. 0 deg/s head velocity). It is therefore most likely that under natural conditions, vestibular afferents most common firing rate is their spontaneous resting rate R_0. Here we see that with both mean and variance constrained to be less than that of the uniform distribution, the optimal response distribution is Gaussian form (possibly with clipped tails)

$$p^*(y) = Ae^{-(y-M)^2/2V}, \tag{B.21}$$

with normalization constant given by

$$A = \frac{2}{\sqrt{2\pi V}[\mathrm{erf}(\frac{M}{\sqrt{2V}}) + \mathrm{erf}(\frac{R_{\max}-M}{\sqrt{2V}})]}, \tag{B.22}$$

due to saturation and rectification of neurons at $y = 0$ and $y = R_{\max}$. Thus, with the usual parametrization of M and V, the response distribution is being constrained to have the following mean and variance:

$$\begin{aligned} \mu_y &= M + AV[e^{-M^2/2V} - e^{-(R_{\max}-M)^2/2V}] \\ \sigma_y^2 &= V[1 - AMe^{-M^2/2V} + A(M - R_{\max})e^{-(R_{\max}-M)^2/2V}] - (\mu_y - M)^2. \end{aligned} \tag{B.23}$$

In the limit where the variance constraint is sufficiently that there is no saturation or rectification, the response distribution has $\mu_r = M$, and $\sigma_r^2 = V$. Although a variance constraint on its own does not effect the mean, and results in a Gaussian response distributions with mean of $R_{max}/2$, the additional mean constraint is needed to lower mean of the Gaussian, without turning it into an exponential peaked at zero. In Figure B.1 panel A shows three sets of constraints, with only a variance constraint and response distributions peaked at $R_{max}/2$ (left), and additional mean constraint resulting in a peak at $R_0 \approx 100$, and an lowered mean constraint resulting in a peak at 0 (right). In the case of only an increasing variance constraint, the mean does not change. However, for the lowered mean constraints there is more rectification (i.e. probability of $R = 0$ spk/s) than saturation (i.e. probability of $R = R_{max}$ spk/s), so as the variance constraint is lowered, the distribution mean also lowers, even when the peak response probability is constrained to remain fixed. In this way, a variance

constraint combined with a mean constraint can still serve the purpose of lowering the mean firing rate and rate of energy consumption.

Once we have chosen a constrained-optimal response distribution, we can then use the nonlinear f-I transformation y = T(x) (defined in Appendix A, and Section 2.2.5), to transform the optimal response distribution into an optimal stimulus distribution, according to

$$p^*(x) = p^*(T(x) = y) \underbrace{T'(x)}_{p_0(x)}, \tag{B.24}$$

where $p_0(x)$ is unconstrained optimal stimulus distribution before normalization. In this Appendix, we use nonlinear transformations from stimulus to response and visa versa, with the 'gain' accounted for by the slope. If we were using an LN model with transfer function filtering, we would also have to use the inverse filters to get from the optimal linear prediction to the optimal stimulus distribution, as done in Section 2.1 above. In Figure B.1 panel B, we show simplified example f-I curves for idealized regular (sigmoidal f-I) and irregular (exponential f-I) afferents, both with $R_{max} = 400$ spk/s, and their firing rate response at zero stimulus aligned to $R_0 = 100$ spk/s, indicated by dashed red lines. The bottom panels then show the optimal stimulus distributions on both linear and logarithmic scales to emphasize the central peak and the tails, respectively. For the unconstrained case, the sigmoidal f-I curve results in a Gaussian optimal stimulus distribution, which has its peak 0 deg/sec, because the uniform response distribution has a mean of $R_{max}/2 > R_0$. On the other hand, the exponential irregular afferent f-I curve results in an asymmetric stimulus distribution which is peaked closer to 0 deg/s, with a longer tail to the

right than the left, due to the asymmetric curvature in the saturating and rectifying regions of the f-I curve. To compare the shape of the optimal distribution tails, on the log scale (bottom right panel) we see that the exponential f-I results in a tail that decays linearly to the right, much more similar to the natural distributions tails. However, the left tail is still parabolic on the left side (as for the sigmoidal f-I) due to the Gaussian smoothing of the f-I. If we now compare the constrained-optimal stimulus distributions, on the linear scale we can see the distributions peaks shift toward the natural distribution peak at the dashed red line, due the the constrained response distributions becoming more peaked at R_0. On the log scale, we can see that the left tails of the optimal stimulus distributions do not change, while the right tails are reduced in length, with some change in shape, reflecting that higher firing rate responses near saturation occur with a reduced probability than the uniform distribution.

Although we have seen that the natural response distribution is more consistent with mean and variance constrained-optimal response distributions, in doing so we have assumed the low or vanishing noise limit, which is poor assumption for the more variable irregular afferents. We next investigate how the optimal stimulus distributions should me adjusted in the high noise limit.

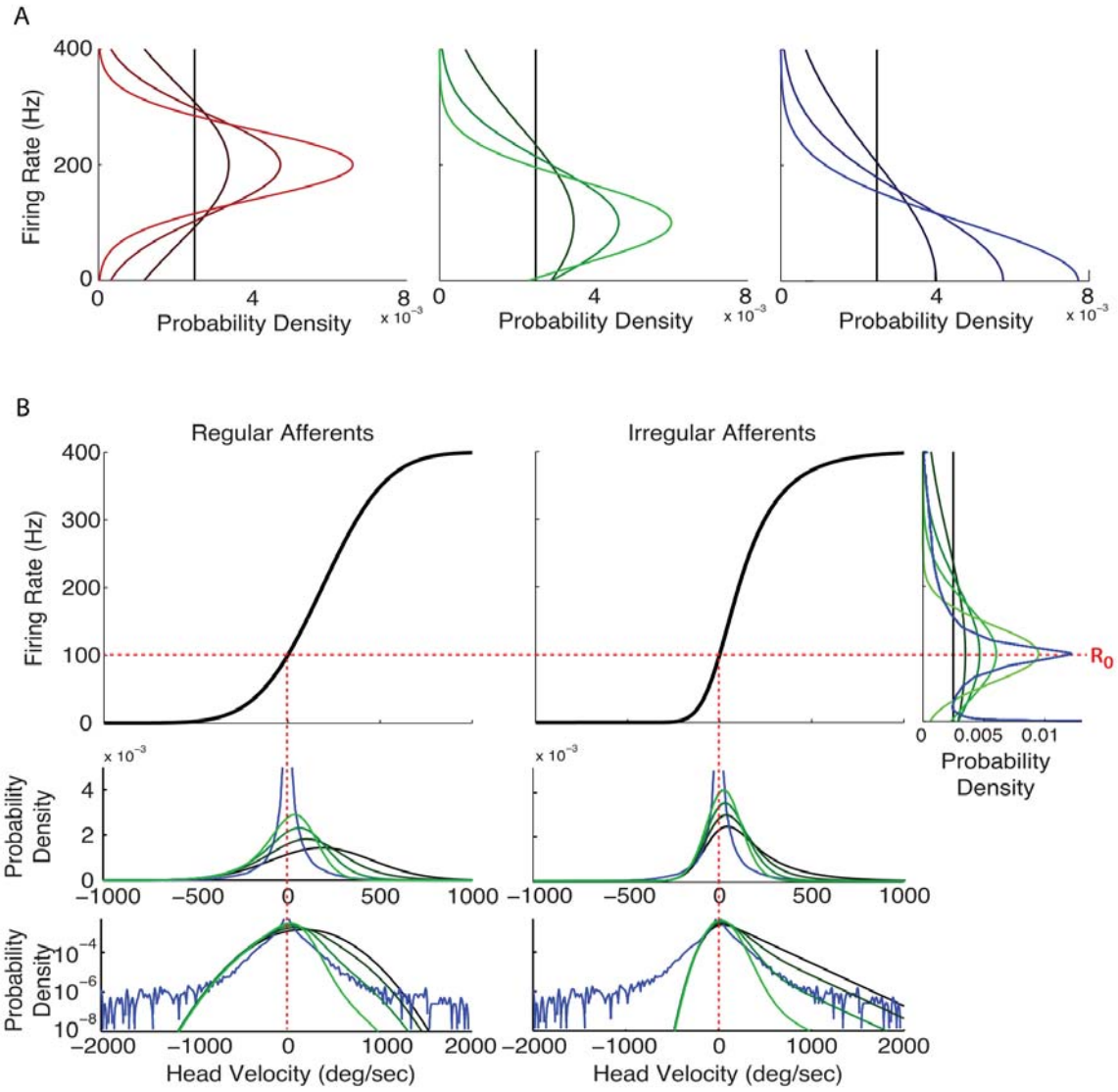

Figure B.1. Vestibular afferents and natural stimulus statistics are more consistent with *constrained* optimal coding.

Figure B.1 ***(previous page).*** (A) Response distributions are plotted for various combination of constraints on μ_y and σ_y^2, with the unconstrained uniform distribution in black. In the left panel, μ_y is not constrained and all distributions have the same mean as the uniform distribution, $\mu_y = R_{max}/2 = 200$ spk/s, and various variance constraints with $\sigma_y^2 < \sigma_{uni}^2$. The middle panel is the same, but now with μ_y chosen such that the resulting in distributions peaked at the afferents spontaneous firing rate, R_0. The right-most panel is again the same, but with μ_y constrained such that the response distributions are peaked at 0. (B) The top left and middle panels show the average f-I curves for regular afferents (sigmoid fit) and irregular afferents (exponential fit), from Figure A.1, with R_{max} parameters adjusted to be equal to 400 spk/sec. The right-most panel show the family of constrained optimal response distributions which result in the distributions peaked at R_0, indicated by a dashed red line. In the bottom two panels, the corresponding optimal stimulus distributions are plotted with linear and logarithmic y-axes for comparison. Superimposed are the natural stimulus distributions for the yaw axis in blue. The vertical dashed red line indicates that a head velocity stimulus of zero results in a firing rate of R_0.

APPENDIX C
Optimal stimulus distribution in the high noise limit: Blahut-Arimoto algorithm

In Chapter 2 and the derivation in Appendix B, the assumption of vanishing noise (i.e. low firing rate variability) is used to calculate the optimal stimulus distribution. However, irregular afferents are known to have high variability relative to regular afferents, and so we now use the Blahut-Arimoto (BA) algorithm to compute the optimal stimulus distribution for increasing levels of variability to quantify the effect on the optimal stimulus distribution.

The mutual information between stimulus and response distributions can be written as

$$I(X,Y) = \underbrace{-\int_{y\in Y} dy\, p(y)\log_2 p(y)}_{H(y)} + \underbrace{\int dx\, p(x)\int dy\, p(y|x)\log_2 p(y|x)}_{H(y|x)}, \qquad \text{(C.1)}$$

where the first term is the response distribution entropy, and the second term is the "noise entropy", which can be neglected when only a deterministic transformation $y = T(x)$ is used. When this transformation is in fact stochastic, such as $y = T(x) + \sigma_y^2\mathcal{N}(0,1)$, where $\mathcal{N}(0,1)$ is a Gaussian distribution with zero mean and unit variance. In this case, $p(y|x)$ is the probability of a response y, given a stimulus value

x, defined as

$$\begin{aligned} p(y|x) &= A(x)e^{(y-T(x))^2/2\sigma_y^2}, \text{ for } 0 \leq y \leq R_{max} \\ &= 0 \ldots\ldots\ldots\ldots \text{ otherwise,} \end{aligned} \tag{C.2}$$

where the additional criterion that $p(y|x) = 0$ for $y > R_{max}$ or $y < 0$, is required when the noise variance is not sufficiently small compared to T(x). In this region, the noise distribution is no longer Gaussian and has a slightly reduced variance. In the limit that $\sigma_y^2 \to 0$, $p(y|x)$ is reduced to a delta function in y, peaked at T(x), and $H(y|x) \to 0$ and our problem reduces to maximizing the response entropy. However, for large σ_y, maximizing mutual information requires a balance of maximizing H(y), while minimizing $H(y|x)$. Although this problem cannot be solved analytically, an iterative scheme known as the Blahut-Arimoto (BA) algorithm has been used to estimate the optimal stimulus distribution [20, 79, 222]. In this case, an initial guess of the uniform *stimulus* distribution is used, and the algorithm iteratively increases/decreases stimulus probability in to increase the overall information transmission, according to

$$q_{n+1}(x_i) = \frac{1}{Z} q_n(x_i) e^{\sum_k q(y_k|x_i) \log_2 \frac{q(y_k|x_i)}{q_n(y_k)}}, \tag{C.3}$$

where $q_n(y_k) = \sum_i q(y_k|x_i) q_n(x_i)$, and Z is a normalization constant to ensure that $\sum_i q_{n+1}(x_i) = 1$. As done by Machens et al. [20], because the resulting stimulus distribution is not unique and often results in discontinuous spikiness, the resulting distribution is low-pass-filtered as much as possible, while preserving 99% information transmission.

In Figure C.1, panel A shows the matrix of the conditional probability distribution $p(y|x)$, a simplified sigmoidal nonlinearity centred at x=0, with $R_{max} = 400$ spk/s, and a constant $\sigma_y = 30$ spk/s, however, we consider cases with a range of values for σ_y, as indicated by the inset in panel C. Panels B and C show the resulting optimal stimulus and resulting response distributions, with those in bold green representing those calculated for the zero noise case, without the BA algorithm. Comparing to the rest of the distributions for increased noise, it is clear what the strategy is: reduce the probability in regions where $T'(x)$ is lower, and increase the stimulus probability in regions where the noise entropy contribution is lowest, due to the rectification and saturation. In panel D, we can see the results on the mutual information, where the BA optimal mutual information (black) can be seen to always be higher than that assuming zero noise, and the difference becomes larger at higher noise levels, although by a very small amount. The amount of mutual information resulting from the use of the natural stimulus distribution is also plotted in cyan for comparison and is considerably lower than both. In the bottom of panel D, we can see the response entropy and noise entropy plotted separately, showing how the response entropy is reduced with increasing noise std for the BA algorithm, which allows its noise entropy (dashed black) to increase by *less* than the dashed red and cyan curves.

Although the optimal stimulus distribution has a significantly different shape for Nsd=30, the resulting change in the predicted information capacity is negligible compared to how much lower the mutual information is for the natural stimulus distribution. This suggests that in high noise conditions, there is a larger family of near

optimal distributions than for the Nsd=0 case, and they consist of distributions with increased probability in the tails. However, because stimulus values that are small or large enough all contribute equally to the response and noise entropy, the algorithm cannot distinguish them, and will spread the stimulus probability distribution as far out into the range of x, as the defining matrix $p(y|x)$ allows. An additional issue with the BA algorithm, is that it uses a projection of the mutual information as a function of stimulus value, $I(x)$, in order to dictate how the probability is altered, however, it is known that this information projection is not unique and that multiple representations result in the same total mutual information $I = \sum_x I(x)$. Finally, considering the conditional response distributions and Equation 2.16 for the mutual information, we can see that it is a weighted average of the KL distance between each different conditional distribution $p(y|x)$, and the entire response distribution p(y), which knows precisely how often each stimulus value occurs in time. However, we have only been considering the mutual information in bits between two static probability distributions. Because vestibular stimuli are highly dynamic in time, it is the mutual information rate that has been experimentally estimated in for vestibular neurons, however, for artificial Gaussian filtered-noise stimuli of a particular intensity [35, 38]. In the next Appendix, we briefly consider the optimal coding of time dependent stimuli.

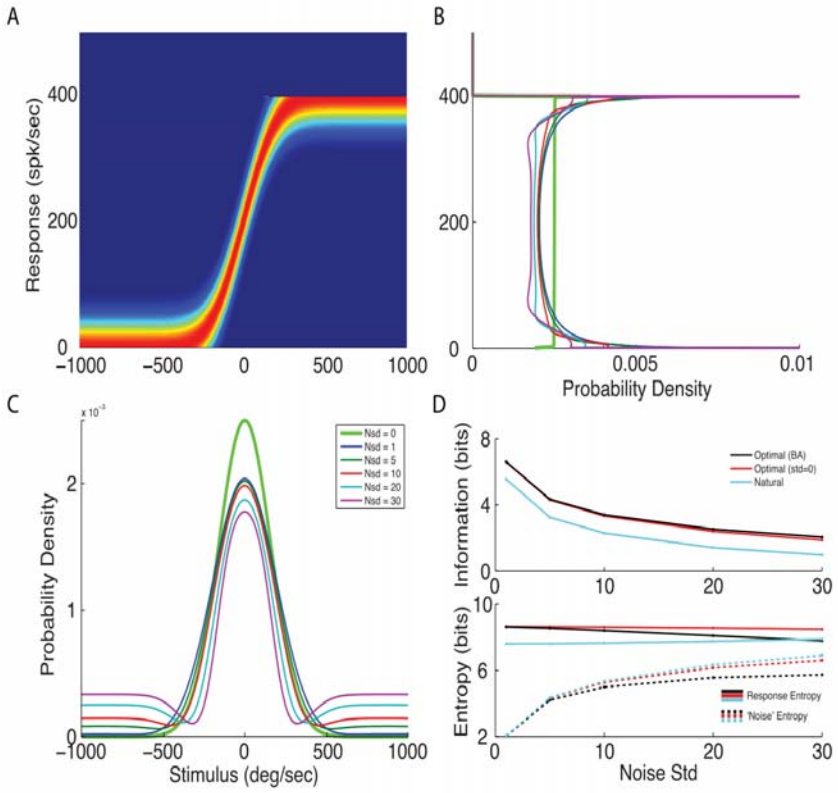

Figure C.1. Optimal stimulus distribution in the high noise limit: Blahut-Arimoto algorithm. (A) The matrix representing the noisy neuronal transformation, $p(r|s)$, for a simplified sigmoid centred at zero, with $R_{max} = 400$ spk/sec, and a constant noise standard deviation (std) of 30 spk/sec. The noise distribution is Gaussian except in regions near rectification and saturation of the mean sigmoidal f-I. (B-C) The optimal stimulus, and corresponding response distributions are plotted for various increased noise std's, computed via the Blahut-Arimoto (BA) algorithm. For comparison, the optimal stimulus distribution with no noise is superimposed in bold green. (D) The information is plotted (top panel) for the optimal distributions computed via the BA algorithm (black), as well as with no noise (red), and the natural yaw stimulus distribution (cyan). The contributing response and 'noise' entropies are plotted (bottom panel) showing how in high noise conditions, the noise entropy is comparable to the response entropy and should not be neglected. Due to the reduced noise entropy at stimuli which result in saturation and rectification, the BA algorithm moves increasing amounts of probability into these regions, where T'(s)=0, which results in reduced response entropy as well as reduced noise entropy.

APPENDIX D
Frequency Content of Natural Stimuli and Whitening

In the previous two appendices and Chapter 2, we have considered the mutual information between the stimulus distribution and resulting response distribution. However, we know that vestibular afferents receive dynamic time varying stimuli and produce time varying responses. In this appendix I consider optimal coding applied to such dynamic stimuli, or maximization of the information rate (i.e. "whitening").

Because the mutual information between two time varying signals is known to increase with the length of the signals, in such cases one generally estimates the information rate, given by Equation 1.6, or the information rate density, Equation 1.7. Although these time series are characterized by their probability distributions, at each point in time that a new values is drawn, it is not necessarily statistically independent from the previous point in time. This correlation time is captured by the Fourier transform, or power spectrum of the signal. So for two time series drawn from the same probability distribution, that with the shorter correlation time, will have the higher entropy rate. In fact, for a given response distribution, the power spectrum which maximizes its entropy rate is a flat, or white power spectrum, for which the signals autocorrelation function is a delta-function, and all point in time are statistically independent. This means that for the optimal neuronal transformation, the response with the greatest information rate, will appear as white noise (as described in detail in Spikes [5]). Of course simply measuring a white noise response

from a neuron does not tell you it is behaving optimally, one must use a naturalistic stimulus and still quantify the mutual information between the stimulus and response in some way. And furthermore one must know what naturalistic stimuli look like. More specifically, the power spectrum of the natural stimuli quantify their characteristic time scale and temporal correlation structure, and an optimal temporal filter will have evolved a gain curve that is precisely tuned to the stimulus power spectrum to result in white noise, known as a "whitening" filter [5].

It is also discussed in Spikes, how natural stimuli tend to follow a power law distribution, which is characterized by a linear power spectrum when plotted on log-log axes [5]. Such natural stimulus power law distributions have been found almost ubiquitously in recorded statistics of natural stimuli, making it particularly striking to learn that natural head movement stimuli in humans, are in fact non-power law and exhibit a characteristic time scale [104]. Furthermore, this study showed that the power spectra of motion stimuli recorded at the subjects feet during running, or fixed to a seat during a metro ride, are in fact power laws as expected, and it is in fact low-pass filtering due to body mechanics which destroy the power-law and result in a characteristic time scale of natural head movement stimuli. To further investigate this result, we here consider the frequency content of natural head movements in monkeys, the power spectra of which are plotted in Figure D.1, on a log-log scale in panel A and a linear scale in panel B. He we find the surprising result that unlike in humans, natural head movement stimuli in monkey do obey a power law for linear accelerations, but not for angular rotations. A dashed black line with slope -4/3 is plotted for the linear accelerations in the top panel, as well as in for the angular

rotations in the bottom of panel A. Although lines could be fit through different regions of the angular motion spectra suggesting it could be piecewise linear, it is quite clear that linear accelerations obey a power law while angular rotations do not. As the previous study in humans found the power law behaviour in the foot motion to be low-pass filtered before causing the head to move, we also compare the power spectra of natural movements for behaviours classified into different activity groups, low, medium, and high (as described in detail in the Methods 2.2 above). Here we see in panel C, that the linear accelerations obey a power law with the same slope, independent of the particular activities being performed. In fact, during the low activity behaviours, the animal is often seated, such that the power law head motion could not possibly originate in the foot (or hand) movements during locomotion, nor the vibrations of the platform on which the monkey was seated (i.e. the monkey did not ride the metro). This suggests that there is a fundamental difference in the head movements of humans and monkeys, as well as the linear and rotational movements. For one thing, humans generally walk upright with gravity pointing in the z-direction, most of the time. Monkeys, on the other hand, tend to walk on all fours, with clearly visual differences in head movement and orientation with respect to gravity. As such, the gravity can simply be subtracted from the z-axis for human data, while for monkeys the gravity vector moves from axis to axis as the head orientation changes, and can not be simply subtracted to give a zero-mean signal. Although we could speculate further as to the bio-mechanical differences between humans and monkeys that cause these differences, we are primarily concerned with

whether or not canal and otolith afferents have been differentially evolved to process these natural stimuli somehow optimally.

Since we already have equations for the well known canal and otolith transfer functions, as defined in the Methods section above, we simply filter the natural stimuli through the transfer functions to predict the afferent firing rate responses (If we wanted to use the angular acceleration stimulus instead of angular velocity, we would simply have to modify the transfer function to take an acceleration input, and the predicted response would be the same). We then plot the resulting response power spectral on log-log scales, with the same power law lines with slope -4/3, for otolith afferents in Figure D.2 panel C, and for canal afferents in panel F. Here we can see that the irregular afferents certainly result in responses that are *whiter* than regular afferents, however they are still far from completely white. So in both cases irregular afferents are more optimal due to their more high-pass gain profiles as compared to the much flatter regular afferent gain profiles (compare panels B and E). However, the fact that linear motion is power-law and angular motion is not, should also be reflected in the shapes of these irregular afferent high-pass gain curves. The canal afferent transfer functions (Equation 2.1) are comprised of two zeros and two poles, with three time constants, to give the canal afferent transfer functions a gain curves up and down at the characteristic frequencies set by the time constants, which are based on the mechanics of the semi-circular canals and inverted pendulum model of the cupula. It is therefore possible that the cupula in different animals have evolved to have different sizes, resulting in different characteristic time scales, that are in some way matched to the characteristic time scales of the angular head

movement. Because the linear acceleration movements obey a power law, they cannot be said to have a single characteristic time scale, and are often referred to as scale-invariant or fractal, exhibiting the same power law structure at different sampling resolutions. Is this fundamental difference in linear accelerations reflected in the otolith transfer function? In fact, otolith transfer functions often require fractional exponents on their zeros, as is the case for our otolith transfer function used in Equation 2.2. Although such fractional-order transfer functions are consistent with fractal calculus (a subject intuitively understood by very few), it has been shown that the linear combination of many filters with a distribution of time-scales can result in fractional-order transfer functions, causing them to have no single characteristic time scale. This lack of characteristic time-scale is precisely what differs between linear head movements and angular head movements, and so it is perhaps not a coincidence that the canal and otolith transfer functions differ in the same way. Although irregular afferent transfer functions clearly do whiten the stimulus more than regular afferents, it is unclear whether this is truly their goal or not. If so, it is possible that subsequent stages of processing by VO neurons in the vestibular nuclei serve to *further whiten* the signals carrying such head movement stimulus information.

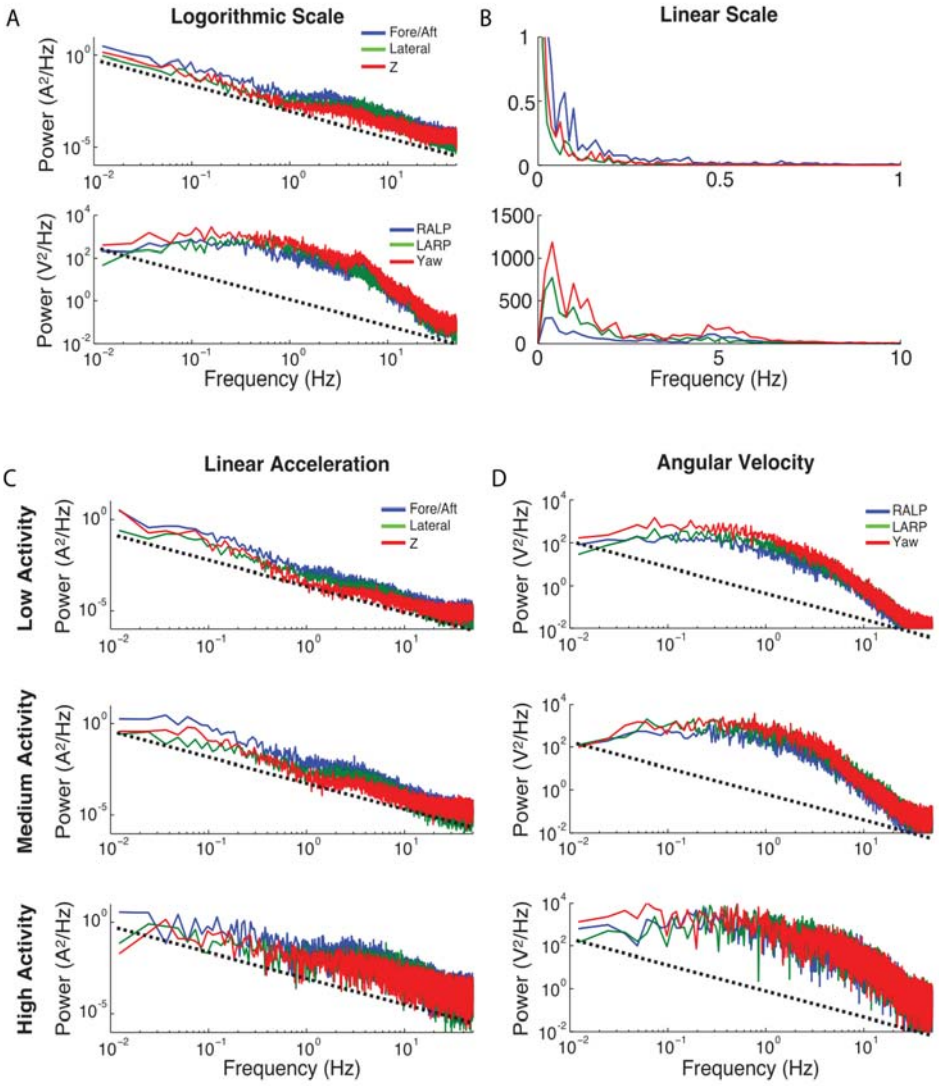

Figure D.1. Linear head accelerations obey a power law, while angular head velocity does not. (A) Frequency content of natural linear head accelerations (top) and angular head velocities (bottom) for all three axes, shown on a log-log scale. Dashed black line has a slope of $\sim -4/3$, indicating a clear power law distribution for linear accelerations, but not for angular rotations. (B) Same frequency spectra as in A, but on a linear scale, to facilitate comparison. (C) Power spectra for linear accelerations on a log-log scale, separated into low (top), medium (middle), and high (bottom) behavioural activities. (D) Same as C, but for angular rotations. Axis scales, and dashed black lines are the same as A to facilitate comparison.

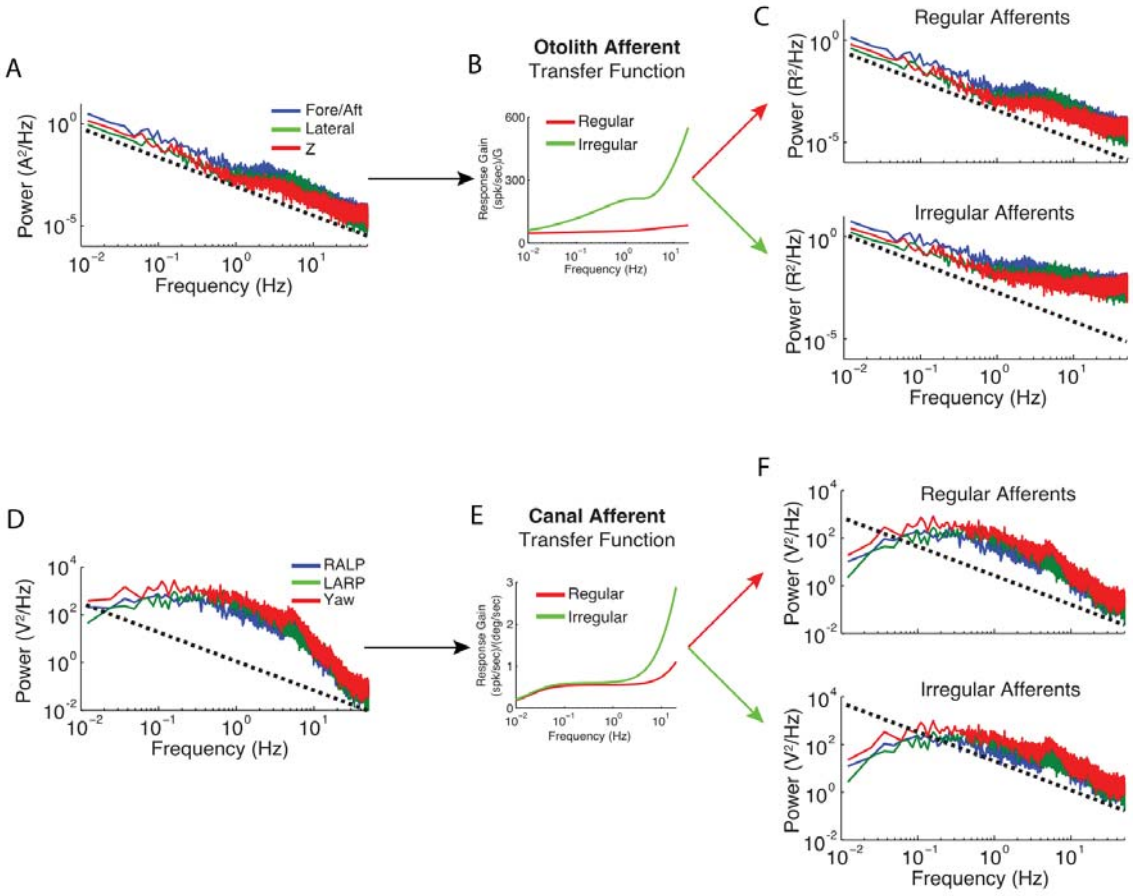

Figure D.2. Irregular afferent transfer functions whiten frequency spectra more than regular, consistent with their being *more* optimal. (A) Power spectra for natural linear head accelerations (as in Figure D.1A), with dashed black line of slope $\sim -4/3$. (B) Head acceleration stimuli are filtered through the regular and irregular otolith transfer functions defined in section 2.1. (C) Power spectra of regular (top) and irregular (bottom) otolith afferent response predictions, with the same dashed black line for comparison. (D-F) Same as A-C, but for natural head rotations and canal afferent transfer functions (also defined in section 2.1).

APPENDIX E
The Vestibular System Implements a Linear-Nonlinear Transformation In Order to Encode Self-Motion

In Chapter 3 we showed that *in vivo* conditions linearized our VO neuron model, explaining VO cells generally linear behaviour observed *in vivo*. However in Figure 1.2E we saw evidence for some nonlinear behaviour *in vivo* as well. In this Appendix, we explicitly test VO cells for nonlinear behaviour, not due to rectification or saturation. To this end, vestibular afferents and VO cells were stimulated with low and high frequency stimuli presented separately, as well as together in combination. As a linear system must respond the same to a stimulus whether presented alone or in combination with another, changes in the gain and stimulus-response (SR) coherence were assessed as a test of linearity. Additionally, we generated input-output curves from the stimulus and response data, and compared its linearity to that of the gain and SR-coherence. Finally, we present a theoretical model to explain how an input-output nonlinearity can result in a nonlinear "masking" of the gain and SR-coherence at low frequencies, when a high frequency stimulus is presented concurrently. This is presented in the form of a published paper in which I am 2nd author, my specific contributions to which are detailed in the Author Contributions section.

E.1 Introduction

Multiple representations of the sensory environment are found across the hierarchical stages of sensory systems [223]. Each of these representations is defined by the activities of a population of neurons in response to their afferent inputs. How neurons decode and then encode sensory information, and the ways in which neural strategies for coding change across successive brain areas, remains a central problem in neuroscience. Studies across sensory systems have shown that representations in higher order brain areas are more efficient because individual neurons detect specific features of sensory input [13, 224–226]. Although theoretical studies predict that more efficient representations are achieved by nonlinear transformations of afferent input [225, 227, 228], to date the nature of these transformations is largely unknown. If nonlinear transformations mediate a more efficient representation of the sensory environment across hierarchical stages of processing, then they should be revealed by experimental approaches specifically designed to probe nonlinear processing. Here, we used the vestibular system as a model to address whether central neurons nonlinearly integrate their afferent inputs in order to give rise to enhanced feature detection. An advantage of the vestibular system, which is essential for providing information about our self-motion and spatial orientation relative to the world, is that the sensory stimulus is relatively easy to describe.

Conventional wisdom is that early vestibular processing is inherently linear. This is supported by numerous studies showing that both afferents and central neurons accurately encode the detailed time course of horizontal rotational head motion through linear changes in firing rate over a wide range of frequencies (reviewed

in [26, 114]; [35]). Further support for this proposal has come from the fact that central vestibular neurons linearly transduce synaptic inputs into changes in firing rate output [229]. Indeed, to date, prior studies have demonstrated remarkable linearity of vestibular behaviours such as the vestibulo-ocular reflex [142, 230–232]. However, all these results are at odds with the expectation that central vestibular neurons achieve more efficient representations of sensory space through nonlinear transformations of their afferent input. Such nonlinear transformations could be advantageous as they would enable vestibular neurons to detect specific features of natural vestibular stimuli. For instance, it would be theoretically beneficial that the central vestibular neurons which mediate vestibulo-spinal reflexes preferentially respond to unexpected transient stimuli, such as those experienced when slipping on ice, in order to optimize compensatory postural responses. A comprehensive re-thinking of the neural code used by the vestibular system is thus necessary to reveal whether more efficient representations of the sensory environment emerge in central vestibular pathways through nonlinear transformations of their afferent input. Notably, prior experiments have characterized early vestibular processing mostly using stimuli that were not designed to systematically probe nonlinear behaviour (e.g., single sinusoids and trapezoids) [26, 35, 114]. In order to test for the existence of such nonlinear transformations, it is necessary to compare neural response to a given stimulus "A" when presented in isolation to that obtained when the same stimulus was presented concurrently with another stimulus "B". If, as suggested by previous studies, central vestibular neurons respond linearly, then we would expect that the response to stimulus "A" should not depend on whether stimulus "B" is present

or not (i.e., the principle of superposition is valid because, by definition, a linear system must be additive). If, instead, central vestibular neurons nonlinearly integrate afferent input, we might expect that the response to stimulus "A" would be altered contingent on the presence of stimulus "B". We explicitly investigated how the neural strategy for coding self-motion changes across the afferent-central neuron synapses by testing whether central vestibular neurons nonlinearly integrate their afferent inputs. We found that, unlike afferents, central vestibular neurons do not obey the principle of superposition because they displayed strong nonlinear responses when sums of low and high frequency stimuli were used. Indeed, the response to low frequency stimuli was strongly attenuated when these were presented concurrently with high frequency stimuli. Through a combination of mathematical modelling and analysis, we show how a static boosting nonlinearity in the input-output relationship can lead to this effect. Our results force a rethinking of the processing of self-motion stimuli in early vestibular pathways. We suggest that nonlinear processing by central vestibular neurons could serve to enhance their coding range and selectivity to high frequency transient self-motion.

E.2 Results

E.2.1 Central Vestibular Neurons Respond Nonlinearly to Self-Motion

We tested response nonlinearity in both central vestibular neurons and afferents by recording their activities in response to a stimulus when presented in isolation and when presented concurrently with another stimulus (Figure E.1A). During experiments, the animal was comfortably seated on a motion platform (Figure E.1B). We first recorded central vestibular neuron responses to random noise stimuli with

frequency content spanning the range of natural head rotations (0-20 Hz) [142]. Specifically, we applied stimuli that spanned two different frequency ranges: low (0-5 Hz) (Figure E.1C, black traces) and high (15-20 Hz) (Figure E.1D, black traces). Both noise stimuli were applied either individually (Figure E.1C,D) or simultaneously (Figure E.1E). The neuronal responses from an example cell to each of these three stimuli are shown by the red traces in Figure E.1C,D,E. We found that, when both stimuli were applied simultaneously, the response was not equal to the sum of the responses to each individual stimulus as would be expected for a linear system. This is because the firing rate modulation in response to the low frequency stimulus when presented alone was much larger than that observed when the high frequency stimulus was presented simultaneously (compare red traces in Figure E.1C,E). In contrast, the firing rate modulation in response to the high frequency stimulus was comparable regardless of whether the stimulus was presented alone or in combination with the low frequency input (compare red traces in Figure E.1D,E). This was reflected in the response power spectrum (compare red traces in the insets of Figure E.1C,E and Figure E.1D,E).

To quantify this effect, we computed the response gain in each condition for our population of central vestibular neurons (see Materials and Methods). Consistent with previous results [35], the neuronal gains of central vestibular neurons were higher for high frequency stimuli (Figure E.1F, compare blue and red traces). However, we found that the population-averaged response gains at low frequencies were significantly attenuated ($\sim$50%) ($p < 10^{-6}$, paired t test, n = 15) when both stimuli are applied simultaneously (Figure E.1F,G). The population-averaged response gains

at high frequencies were, however, unaffected (p= 0.4, paired t test, n = 15) (Figure E.1F,G). Thus, contrary to the common assumption that early vestibular processing is essentially linear, the results above establish that central vestibular neurons respond nonlinearly to sums of low and high frequency head rotations since the principle of superposition is violated. Notably, responses to low frequency self-motion are suppressed in the presence of high frequency self-motion. In contrast, responses to high frequency self-motion are relatively unaffected by the presence of low frequency self-motion. We next asked whether the response nonlinearity that we observed using gain measures would also be evident when using information theoretic measures such as the coherence. Unlike gain measures, coherence measures are computed using the signal-to-noise ratio and thus take variability into account. This is important because previous studies have shown that a given neuron can display qualitatively different frequency tuning depending on whether gain or coherence measures are used [36, 121, 233]. Again, we found that the principle of superposition was violated. Indeed, population-averaged coherence values at low frequencies were significantly lower ($\sim$ 50%) ($p < 0.001$, paired t test, n = 20) when both noise stimuli were presented simultaneously. In contrast, population-averaged coherence values at high (15-20 Hz) frequencies were not significantly different (p =0.87, paired t test, n = 15) (Figure E.S1A, E.S1B, E.S1C). As expected given that there is a one-to-one relationship between coherence and mutual information measures, comparable results were obtained when computing the latter (unpublished data). Thus, taken together, our results using both gain and coherence measures confirm our hypothesis that central vestibular neurons respond nonlinearly to sums of low and high frequency stimuli.

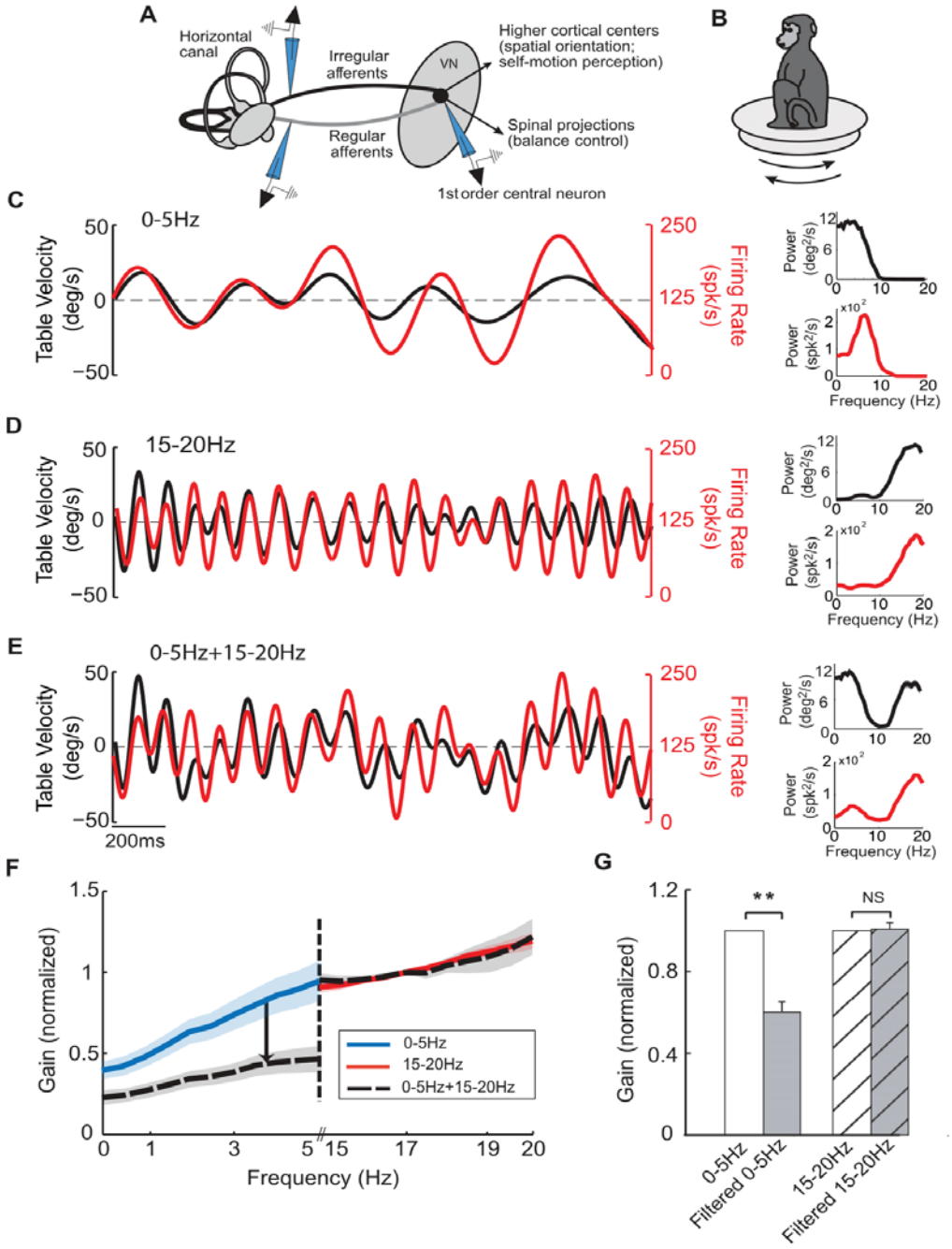

Figure E.1. Central vestibular neurons respond nonlinearly to sums of noise stimuli.

Figure E.1 ***(previous page).*** (A) Vestibular information is transmitted from the sensory end organs through two types of afferents (regular and irregular) that converge on first order central neurons within the vestibular nuclei. (B) During the experiment the monkey was comfortably seated in a chair placed on a motion platform. (C-E) The firing rate (red traces) of an example central vestibular neuron in response to noise stimuli (black traces) whose frequency content spanned 0-5 Hz (C), 15-20 Hz (D), and 0-5 Hz+15-20 Hz (E). The upper insets show the power spectrum of each stimulus, while the lower insets show the power spectrum of the firing rates (red). (F) Population-averaged normalized gains curves for central neurons. Note the attenuated response at low frequency (0-5 Hz, arrow). (G) Population averaged normalized gains for central neurons. Here and in all subsequent figures, the bands (F) and error bars (G) show 1 SEM. The firing rate estimates were obtained by convolving the spike trains with a Kaiser filter (see Materials and Methods). This figure was copied from Massot et al. [111].

We also tested that these nonlinear responses were not specific to the noise stimuli used. Indeed, we found that central vestibular neurons also responded nonlinearly to sums of low and high frequency sinusoidal stimuli. Indeed, when 3 and 17 Hz sinusoidal stimuli were applied simultaneously, the response was not equal to the linear sum of the responses to each individual stimulus (Figure E.S2). We note that this is not due to our filtering the spike trains to obtain the time-dependent firing rate since this effect was also evident in the power spectra from the unfiltered spike trains (Figure E.S3). Further, the observed nonlinear responses of central vestibular neurons were not due to trivial nonlinearities such as rectification (i.e., cessation of firing) or saturation (i.e., the firing rate reaching a plateau at a finite value) since these were not elicited by the stimuli used in this study (Figure E.S4A).

E.2.2 Peripheral Vestibular Afferents Respond Linearly to Sums of Low and High Frequency Motion

Perhaps the simplest explanation for the nonlinear responses of central vestibular neurons shown in Figure E.1 is that they are inherited from their afferent input. Peripheral vestibular afferents display marked heterogeneities in their baseline activity and response to stimulation. Most notably, regularly discharging afferents are characterized by low coefficients of variation (CV) and encode the detailed time course of self-motion as they are broadly tuned to the behaviourally relevant frequency range (0-20 Hz). In contrast, irregularly discharging afferents are characterized by higher CVs and detect fast transient changes in self-motion as they respond preferentially to high frequencies [26, 32, 36, 38]. To address whether the nonlinear responses of central vestibular neurons are inherited from their afferent inputs, we recorded from single regular and irregular afferents using the same random noise stimuli. In contrast to their target central vestibular neurons, neither regular (Figure E.2A) nor irregular afferents (Figure E.2A) displayed significant nonlinearities. Indeed, the population-averaged gain values at low frequencies were not significantly altered by the presence of the high frequency stimulus (regular: p= 0.9, paired t test, n = 5; Figure E.2C; irregular: p= 0.23, paired t test, n = 10; Figure E.2D). Similarly, the population-averaged gain values at high frequencies were not significantly altered by the presence of the low frequency stimulus (regular: p= 0.84, paired t test, n=5; irregular: p =0.19, paired t test, n = 10). We note that the applied stimuli also did not elicit "trivial" nonlinearities in afferents such as rectification or saturation (Figure E.S4B,C) and that similar results were obtained when we instead used the coherence measure (regular: Figure E.S1D,E,F; irregular: Figure E.S1G,H,I). We

note that similar results were observed when using sums of low and high frequency sinusoidal stimuli (unpublished data). Accordingly, unlike central neurons, individual afferents do not respond nonlinearly to sums of low and high frequency stimuli. We quantified the gain attenuation at low frequencies in the presence of the high frequency stimulus for both central vestibular neurons and afferents. While central vestibular neurons displayed strong and significant attenuation ($\sim 50\%$, $p < 0.001$, signrank test, n = 15), both regular and irregular afferents instead displayed weak attenuation ($\sim 10\%$) that was not significantly different from zero (regular: p =0.25, signrank test, n = 5; irregular: p= 0.13, signrank test, n =10) (Figure E.2E). These findings imply that the origin of the response nonlinearity seen in central neurons is due to nonlinear integration of afferent synaptic input.

E.2.3 Central Vestibular Neurons Display Nonlinear Responses to High Frequency But Not Low Frequency Head Rotations When These Are Applied in Isolation

In order to understand how central vestibular neurons nonlinearly integrate their afferent input, we next characterized the relationship between head velocity input and output firing rate for both afferents and central neurons by plotting one as a function of the other. The schematic of the approach used is illustrated in Figure E.3A. If the relationship between input head velocity and output firing rate is linear, then the curve relating the two should be well fit by a straight line. We found that the relationships between head velocity stimuli and peripheral afferent responses were well fit by straight lines. The population-averaged relationships for low and high frequency self-motion obtained for afferents are shown in Figure E.3B and E.3C, respectively. It can further be seen that these relationships are comparable

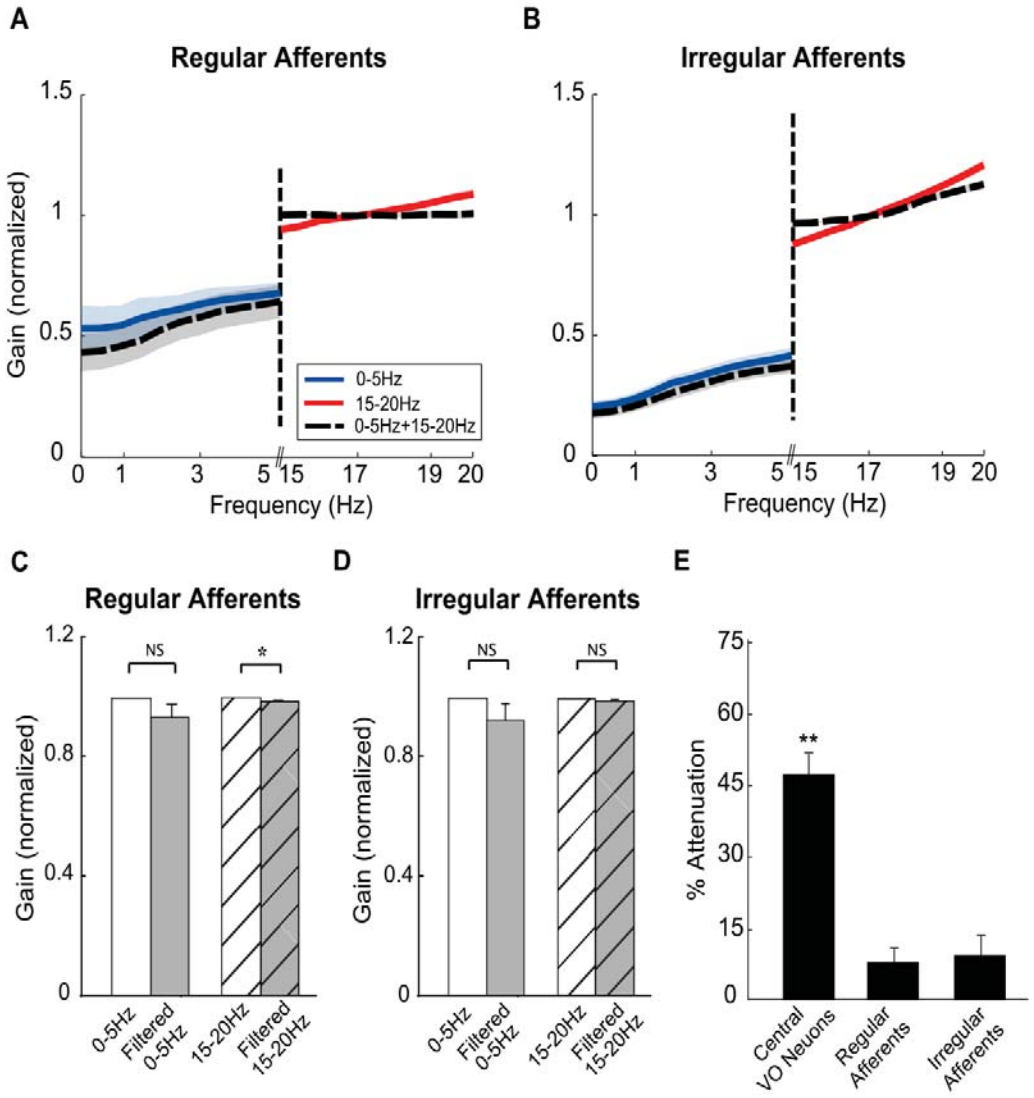

Figure E.2. Afferents respond linearly to sums of noise stimuli. (A, B) Population-averaged normalized gain curves as a function of frequency for regular (A) and irregular (B) afferents. (C, D) Population-averaged normalized gains for regular (C) and irregular (D) afferents. (E) Population averaged attenuation indices for central neurons, regular afferents, and irregular afferents. This figure was copied from Massot et al. [111].

when a given stimulus is applied alone and when it is applied concurrently with the other stimulus (Figure E.3B, E.3C) (low frequency: p =0.93, pairwise t test, n =15; high-frequency: p= 0.89, pairwise t test, n= 15), demonstrating that the principle of superposition applies. This was also seen for single neurons (insets of Figure E.S5). Further, these results were observed for both regular (low frequency: p= 0.59; high frequency: p= 0.58, pairwise t tests, n =5) and irregular (low frequency: p= 0.77; high frequency: p= 0.35, pairwise t tests, n = 10) afferents when considered separately (Figure E.S5). Notably, comparison of Figure E.3B and E.3C further revealed that the afferent gain (i.e., the slope of the input-output relationship) was higher in response to the high as compared to the low frequency stimulus. This observation is consistent with previous studies showing that high frequency head rotations give rise to greater afferent firing rate modulations (reviewed in [26]). We next computed the population-averaged relationships for central vestibular neurons and found that they were well fit by straight lines when the low frequency stimulus was presented alone (Figure E.3D, solid blue curves). We note that this was also true for single neurons (Figure E.S6A, solid blue curve). The head velocity neuronal response relationship (solid black curve) was also linear when low frequency stimulation was applied concurrently with high frequency stimulation (population average: Figure E.3D; single neuron: Figure E.S6A, solid black curves). However, in the combined condition, the slope of the curve (i.e., the gain) was lower (compare solid black and blue traces in Figures E.3D and E.S6A). These results are consistent with our previous analysis of response gain (Figure E.1G), thus confirming our earlier findings.

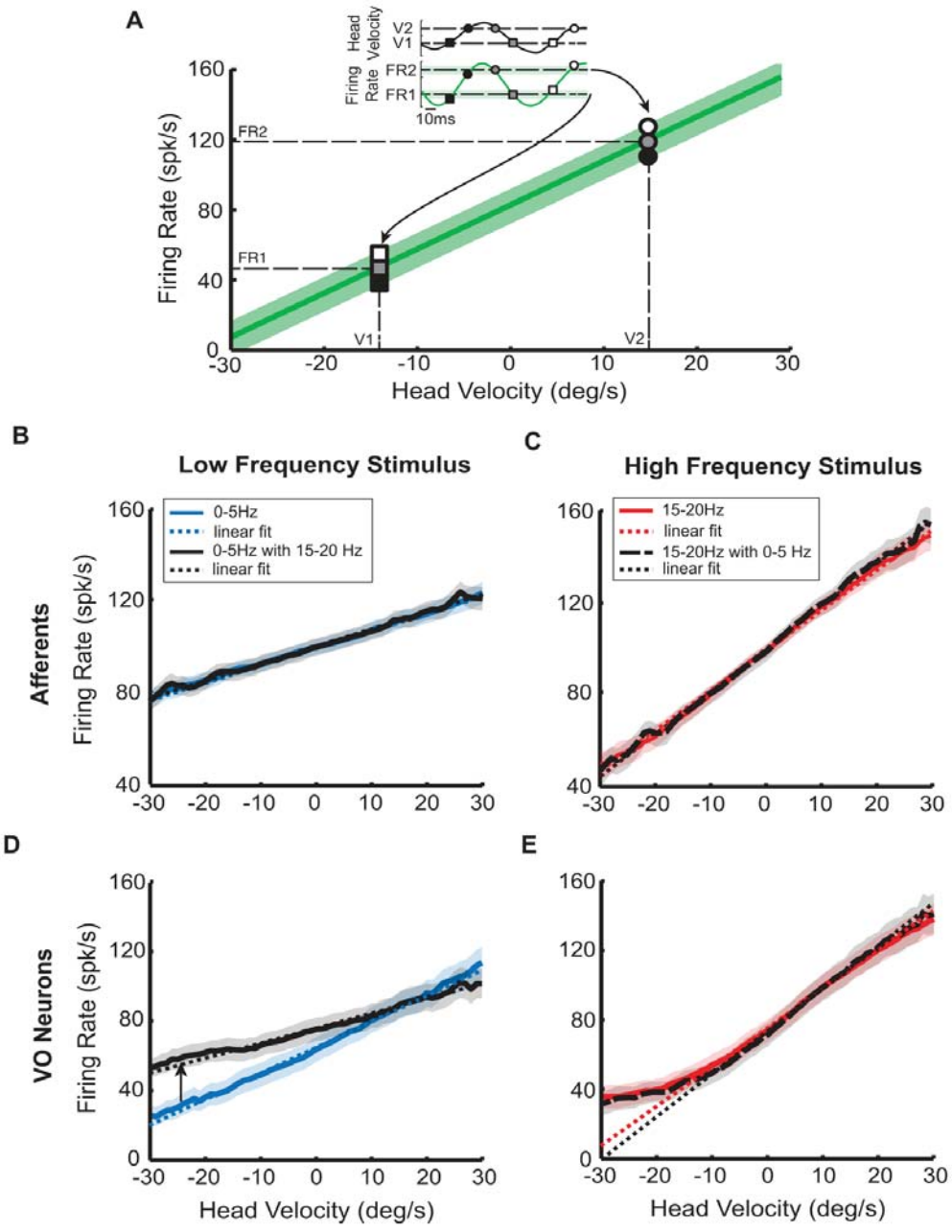

Figure E.3. Central vestibular neurons but not afferents display a nonlinear relationship between output firing rate and input head velocity.

Figure E.3 ***(previous page).*** (A) Output firing rate as a function of head velocity. The inset shows the instantaneous firing rate and the head velocity stimulus as a function of time and the various symbols correspond to different values of the head velocity and the corresponding firing rates. If the firing rate is related linearly to the head velocity stimulus, then the curve relating the two should be well fit by a straight line. The slope of this line is then the response gain. (B) Population-averaged firing rate response as a function of head velocity for afferents when stimulated with 0-5 Hz noise alone (solid blue) and concurrently with 15-20 Hz noise (solid black). In both cases, the curves were well fit by straight lines (dashed lines) and largely overlapped (0-5 Hz alone: $R^2 = 0.99$, slope = 0.70 (spk/s)/(deg/s), y-intercept = 98 spk/s; 0-5 Hz with 15-20 Hz: $R^2 = 0.99$, slope = 0.72 (spk/s)/(deg/s), y-intercept = 98 spk/s). (C) Population-averaged firing rate response as a function of head velocity for afferents when stimulated with 15-20 Hz noise alone (solid red) and concurrently with 0-5 Hz noise (long dashed black). Both curves were again well fit by straight lines (short dashed lines) and largely overlapped (15-20 Hz alone: $R^2 = 0.99$, slope = 1.97 (spk/s)/(deg/s), y-intercept = 102 spk/s; 15-20 Hz with 0-5 Hz: $R^2 = 0.99$, slope = 2.06 (spk/ s)/(deg/s), y-intercept = 102 spk/s). Note, however, the increased slope with respect to panel B. (D) Population-averaged firing rate response as a function of head velocity for central neurons when stimulated with 0-5 Hz noise alone (solid blue) and concurrently with 15-20 Hz noise (solid black). In both cases, the curves were well fit by straight lines (dashed lines) although the solid black curve had a lower slope (i.e. gain) than the solid blue curve (0-5 Hz: $R^2 = 0.98$, slope = 1.56 (spk/s)/(deg/s), y-intercept = 67 spk/s; 0-5 Hz with 15-20 Hz: $R^2 = 0.87$, slope = 0.83 (spk/s)/(deg/s), y-intercept = 81 spk/s). (E) Population-averaged firing rate response as a function of head velocity for central neurons when stimulated with 15-20 Hz noise alone (solid red) and concurrently with 0-5 Hz noise (long dashed black). While both curves were similar and largely overlapped, they were not well fit by straight lines (short dashed lines) that underestimated the firing rate for head velocities <210 deg/s (15-20 Hz: $R^2 = 0.64$, slope = 2.32 (spk/ s)/(deg/s), y-intercept = 79 spk/s; 15-20 Hz with 0-5 Hz: $R^2 = 0.27$, slope = 2.78 (spk/s)/(deg/s), y-intercept = 79 spk/s). We note that central neurons did not display rectification since the firing rate was always above zero. This figure was copied from Massot et al. [111].

In contrast, qualitatively different results were observed for high frequency head rotations. Notably, we found that the relationships between head velocity stimuli and central neuron responses were nonlinear as they were characterized by significantly lower gains (i.e., the slope of the curve) for head velocities less than 210 deg/s as compared to those for head velocities greater than 210 deg/s ($p = 0.01$, pairwise t test, $n = 20$). This was seen for both the population averages (Figure E.3E) and single neurons (Figure E.S6B). We will henceforth refer to the shape of these curves as a boosting nonlinearity [234]. Moreover, the relationships obtained for high frequency head rotations were comparable when the stimulus was presented alone or concurrently with low frequency head rotations ($p = 0.43$, pairwise t test, $n = 20$) (Figures E.3E and E.S6B, compare red and black-dashed traces). Thus, again consistent with our results using gain measures, central vestibular neuron responses were comparable when high frequency stimuli were applied alone or concurrently with low frequency stimuli. Notably, unlike afferents, central vestibular neurons respond nonlinearly to sums of low and high frequency stimuli. Moreover, our analysis of their stimulus input-firing rate output relationships further revealed a boosting nonlinearity characterized by lower slopes for head velocities less than 210 deg/s as compared to those obtained for head velocities greater than 210 deg/s. This nonlinearity was only seen when high frequency stimuli were applied (Figures E.3E and E.S6B).

E.2.4 The Greater Afferent Firing Rate Modulations Elicited by High Frequency Stimuli Elicit Nonlinear Responses in Central Vestibular Neurons

Thus far, we have looked at the relationship between head velocity stimuli and output firing rates for both central neurons and afferents. We found that afferents

responded linearly to both low and high frequency stimuli. In contrast, central neurons responded linearly to low frequency stimuli but nonlinearly to high frequency stimuli. A priori, this effect could be mediated by a dynamic non-linearity that would be activated exclusively under high frequency stimulation (e.g., a network-based mechanism such as feedback input from higher centers). Alternatively, the nonlinearity might be static in nature (e.g., due to intrinsic mechanisms such as voltage-gated conductances) and be preferentially elicited by the afferent input due to high frequency stimulation. Figure E.4A illustrates the sequential processing of low (top) and high (bottom) frequency stimuli when applied in isolation. It is important to note that, for high frequency stimulation, the afferent input to central vestibular neurons will span a greater range (Figure E.4A, compare green traces) because afferents display greater sensitivities (compare Figure E.3B,C). As a result, at the next stage of processing, these larger afferent firing rate modulations should evoke greater central neuron firing rate modulations as compared to those evoked by low frequency head rotations (Figure E.4A, compare purple traces). Thus, if the nonlinearity is static, we predict that (1) the smaller range of afferent firing rates evoked by low frequency stimulation are contained in a region for which the central vestibular neuron input-output relationship is approximately linear, (2) the greater range of afferent firing rates evoked by high frequency stimulation extend into a region of the input-output relationship that elicits the boosting nonlinearity (Figure E.4A, VO neuron box), and as a result, (3) central vestibular neuron output firing rate is then a fixed function of the afferent input firing rate, regardless of whether low or high frequency head rotations are applied in isolation.

To test whether the nonlinearity is static or dynamic, we next experimentally characterized the input-output relationship of central neurons by plotting their output firing rates as a function of their afferent input rather than head velocity. Given that central neurons receive input from many afferents that display significant heterogeneities (see [26] for review), we obtained an estimate of this activity by fitting a linear model to previous data (see Materials and Methods). The input-output relationship obtained for low frequency stimuli was approximately linear (Figure E.4B, blue curve), confirming our first prediction. In addition, the input-output relationship obtained for high frequency stimuli displayed a boosting nonlinearity (Figure E.4B, red curve), such that the slope for afferent inputs less than 90 spk/s was much lower than that for afferent inputs greater than 90 spk/s (Figure E.4B, compare solid and dashed red curves). Thus, the afferent input-central neuron output relationship can be approximated by the piecewise linear function illustrated in Figure E.4A, confirming our second prediction. Moreover, we found that both curves overlapped when only the smaller range of afferent firing rates evoked by low frequency stimuli was considered (Figure E.4B, compare red and blue curves). Accordingly, this finding confirmed our third prediction that central vestibular neuron firing rate is a fixed function of the afferent input firing rate when either low or high frequency head rotations are applied in isolation. Accordingly, there is a striking contrast between the results of this analysis and that of our previous analysis of the relationship between head velocity input and afferent output. Notably, the head velocity input-afferent output relationships obtained for low and high frequency stimulation did not overlap consistently with the known frequency- dependent sensitivities of afferents (Figure

E.4B, inset). Thus, taken together, our results show that central vestibular neuron responses are characterized by a static nonlinearity that is primarily elicited by the greater afferent firing rate modulations caused by high frequency stimuli. We suggest that the intrinsic properties of central vestibular neurons and/or network interactions within this vestibular pathway underlie this boosting nonlinearity (see Discussion).

We next plotted the afferent input-firing rate output relationships obtained when low frequency stimulation was applied alone or concurrently with high frequency stimulation for central vestibular neurons. We found significantly different slopes in both conditions (Figure E.4C, compare black and blue curves and inset). Specifically, central vestibular neuron firing rates in response to afferent firing rates below 110 spk/s were higher when the low frequency stimulus was applied concurrently with the high frequency stimulus than when it was applied alone (Figure E.4C, arrow). We also note that, as can be expected from Figure E.3E, the central vestibular neuron input-output relationships obtained when high frequency stimulation was applied alone or concurrently with low frequency stimulation overlapped (Figure E.4C, red and dashed black curves) and did not differ significantly in their slopes (Figure E.4C, inset), which confirms that central vestibular neurons display a static boosting nonlinearity in response to these stimuli.

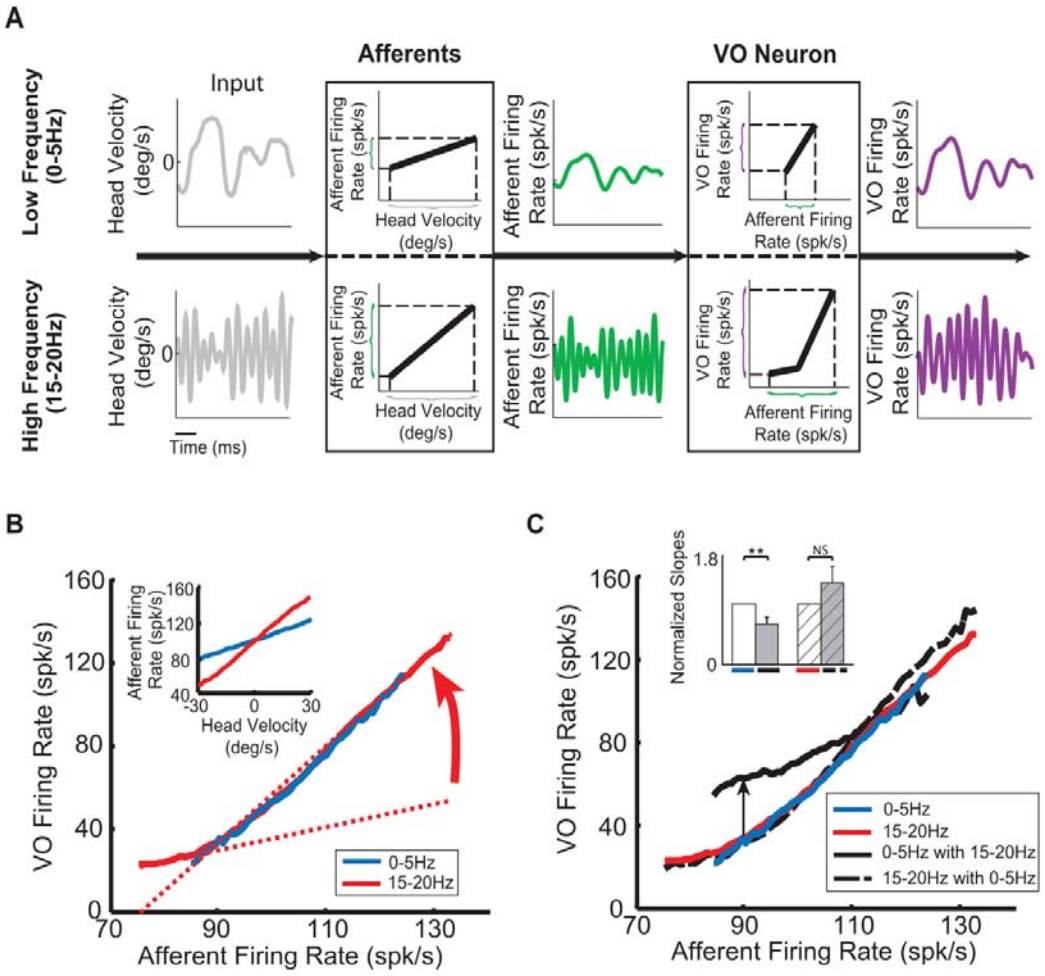

Figure E.4. Central neurons display a static nonlinear relationship between their output firing rate and their afferent input. (A) Low (top) and high (bottom) frequency head velocity stimuli (gray) cause smaller and larger changes in afferent firing rate (green), respectively. These differential changes in afferent firing rate in turn cause differential changes in central neuron firing rate (purple), respectively. Notably, the changes in afferent firing rate caused by high frequency head velocity stimuli are distributed over a greater range and thus elicit nonlinear responses from VO neurons, whereas this is not the case for those caused by low frequency head velocity stimuli. Note that the same scales were used for corresponding panels in the bottom and upper rows.

Figure E.4 ***(previous page).*** (B) Population-averaged firing rates of central VO neurons as a function of afferent firing rate for low (blue) and high (red) frequency noise stimuli presented in isolation. Note that the curve obtained for the low frequency stimulus (blue) extends over a smaller range than that obtained for high frequency (red) stimuli. Further, both curves are linear over the range for which they overlap. Also shown are best linear fits to the portion of the curve below and above 90 Hz (dashed red lines). As such, the curve can be approximated by a piecewise linear function. Inset: population-averaged firing rates of afferents as a function of the head velocity stimulus for low (blue) and high (red) frequency noise stimuli presented alone. (C) Population-averaged firing rates of central VO neurons as a function of afferent input firing rates: (1) for the low frequency stimulus when presented alone (blue) and concurrently with the high frequency stimulus (solid black); (2) for the high frequency stimulus when presented alone (red) and concurrently with the low frequency stimulus (dashed black). Note that the curves obtained in response to the high frequency stimulus when presented alone (red) and when presented concurrently with the low frequency stimulus (dashed black) overlapped before (Figure E.3E) and thus, not surprisingly, also overlap. Note also that only the curve obtained when the low frequency stimulus was presented concurrently with the high frequency stimulus (solid black) does not overlap with the others. This is because the central VO neuron firing rate is higher than that obtained for the low frequency stimulus when applied alone for values lesser than 110 Hz. Inset: population-averaged normalized slopes under all four conditions. The afferent activity was estimated by fitting a linear model to previous experimental recordings from a large population of afferents (see Materials and Methods). This figure was copied from Massot et al. [111].

E.2.5 Modeling and Predicting Central Vestibular Neuron Responses to Sums of Arbitrary Stimuli

Does the static boosting nonlinearity in the input-output relationship of central vestibular neurons account for their nonlinear responses to sums of low and high frequency stimuli? To address this question, we fit the experimentally recorded central vestibular neuron input-output relationship in response to afferent input when a given stimulus was presented in isolation. Since individual central vestibular neurons receive input from a large heterogeneous population of afferents [26], we estimated their average activity by fitting a linear model to existing data (see Materials and Methods). The input-output relationship in response to this stimulus when another stimulus is presented concurrently can then be obtained by averaging (see Materials and Methods). Accordingly, it becomes possible, using this model, to predict the change in the central vestibular neuron input-output relationship to a given stimulus when another stimulus is applied concurrently. Our results show that, when compared to experimental data, this relatively simple model is surprisingly accurate at predicting the change in afferent to central neuron input-output relationship to the low frequency stimulus when the high frequency stimulus is applied concurrently (Figure E.5A, compare solid and dashed curves). The same model also predicts little change in the input-output relationship to the high frequency stimulus when the low frequency stimulus is applied concurrently, consistent with our experimental results (Figure E.5B, compare solid and dashed curves).

Importantly, using this model, we were further able to predict the relative gain attenuation in response to sums of stimuli with given intensities and frequencies within the behaviourally relevant range. It then becomes important to introduce

new terminology to distinguish both stimuli by other means than just their frequency content, as was done until now. Thus, we will henceforth refer to one stimulus as the "signal" and to the other as the "masker". Note that, while the terms "signal" versus "masker" are arbitrary, this division allows us to focus on the coding of one input (i.e., the input designated as the signal). Our model shows stronger attenuation of the response gain to a low frequency signal by maskers with higher frequency content (Figure E.5C). This is because vestibular afferents display gains that increase as a function of frequency. Moreover, our model shows stronger attenuation of the response gain to a given signal by maskers with higher intensity (Figure E.5D). This is because maskers of greater intensities are more effective at eliciting nonlinear responses from central vestibular neurons. Thus, although it is not experimentally feasible to test all combinations of maskers and signals, our model allows us to make testable predictions of how a static nonlinear input-output relationship attenuates central vestibular neuron responses to a given signal in the presence of a masker over the physiologically relevant range of frequencies and intensities. For example, our model makes the prediction that a masker with a given frequency content is equally effective at attenuating the sensitivity to signals with either low or high frequency content (Figure E.5C).

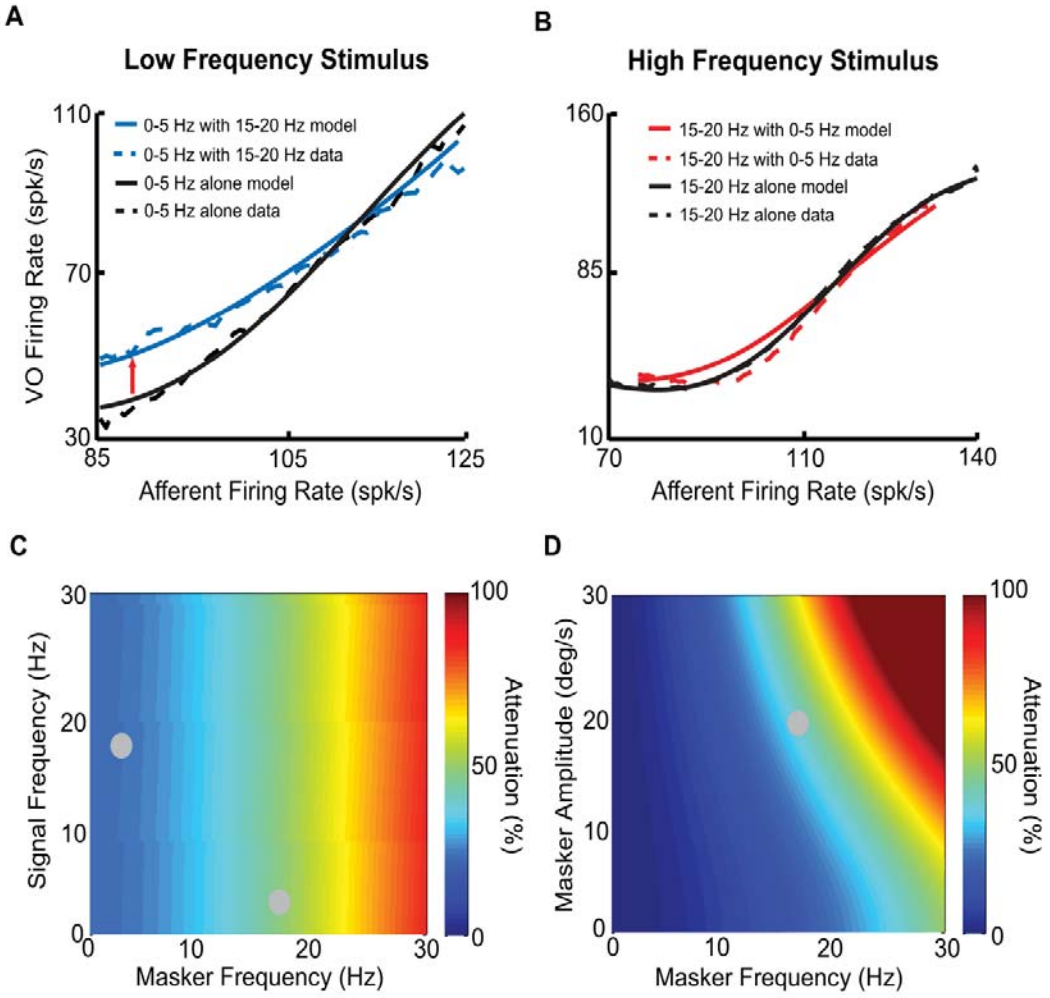

Figure E.5. A simple model accurately predicts nonlinear central VO neuron responses to sums of low and high frequency stimuli. (A) Model (solid) and data (dashed) relationships between afferent firing rate and central VO neuron firing rate when the low frequency stimulus was presented alone (blue) and concurrently with the high frequency stimulus (black). Note that the model accurately reproduces the decrease in slope seen experimentally as evidenced by the large overlap between the model and data curves ($R^2 = 0.92$).

Figure E.5 ***(previous page).*** (B) Model (solid) and data (dashed) relationships between afferent firing rate and VO neuronal firing rate when the high frequency stimulus was presented alone (red) and concurrently with the low frequency stimulus (black). Note that the model also accurately reproduces the lack of change seen experimentally as the model curves largely overlap with the experimental ones ($R^2 = 0.99$). (C) % gain attenuation plotted as a function of signal and masker frequency. The stimulus for which the response is computed is referred to as the signal, while the other stimulus is referred to as the masker. Maskers with higher frequency content lead to greater gain attenuation. (D) % gain attenuation as a function of masker amplitude and frequency. Maskers of greater amplitude and frequency lead to greater gain attenuation. This figure was copied from Massot et al. [111].

E.2.6 A Linear-Nonlinear Cascade Model Verifies That Central Vestibular Neurons Display a Static Boosting Nonlinearity

So far, our data and modelling results show that a static boosting nonlinearity can explain why central neurons display reduced gain to low frequency motion when applied concurrently with high frequency motion. If this is true, then central vestibular neurons should respond nonlinearly to any stimulus that contains high frequencies. Moreover, the form of nonlinearity should be stimulus independent. To test this prediction experimentally, we recorded from afferents and central vestibular neurons during broadband noise stimulation and used a more general approach to characterize their responses. Specifically, we used a linear-nonlinear (LN) cascade model [110] that is illustrated in Figure E.6A (see Materials and Methods). This model assumes that a neuron's firing rate at any instant is a function f of the convolution between the stimulus and an optimal linear filter (i.e., the linear prediction) [110]. The form of the function f can then be estimated by plotting the actual firing rate as a function of the linear prediction (Figure E.6A).

We first applied this model to our afferent data and found that their output firing rates were well predicted by the optimal linear filter alone as all data points were located close to the identity line (R^2 =0.99860.001, n = 15) (Figure E.6B). This was seen for both regular (Figure E.S7A,B) and irregular (Figure E.S7C,D) afferents. Notably, the slope of best straight line fit to the curve (Figure E.6B, red line) was not significantly different from unity (p =0.966, n = 15, pairwise t test).

Qualitatively different results were obtained for central vestibular neurons. Indeed, we found that their output firing rates were not well predicted by the optimal

linear filter alone (Figure E.6C) as evidenced by significant deviations from the identity line (Figure E.S7E,F). Notably, the slope of the best straight line fit to the curve over the range (0-80 Hz) was significantly lower than the slope of the best straight line fit to the curve over the range (80-160 Hz) (p= 0.0014, n = 13, pairwise t test) (Figure E.6C, compare red lines). Additionally, the curve relating the actual firing rate to the linear prediction in response to broadband noise stimuli closely resembled the nonlinear input-output relationship obtained in response to high frequency narrowband noise stimuli (compare Figures E.6C and E.3E), which suggests that the frequency filtering properties of central vestibular neurons are mostly inherited from afferents. The actual responses were well predicted by the full LN model (R^2 = 0.9460.07, n = 13). We also note that the firing rate values extrapolated from the best straight line fit to the curve over the range (80-160 Hz) are negative over the range (0-20 Hz), while the actual firing rate values are of course positive. We shall return to this point in the discussion.

Finally, we compared the curves relating the actual firing rate to the linear prediction for afferents and central vestibular neurons for different stimuli (i.e., low frequency, high frequency, low+high frequency, and broadband noise stimuli). The afferent curves overlapped and were all located close to the identity line (Figure E.S8A), confirming that the responses were well fit by linear models. The curves for central vestibular neurons also overlapped, but exhibited significant deviations from linearity only for stimuli that contained high frequencies (Figure E.S8B). As such, our results using LN models provide additional strong evidence that central vestibular neurons indeed display a static boosting nonlinearity that is preferentially elicited

by the greater afferent firing rate modulations caused by high frequency motion and that their frequency filtering properties are largely inherited from those of afferents.

E.2.7 How Does a Static Boosting Nonlinearity Give Rise to Suppressed Response to Low Frequency Stimuli in the Presence of High Frequency Stimuli?

Our results above have shown that a static boosting nonlinearity can indeed account for the nonlinear responses of central vestibular neurons. Here, we provide an intuitive explanation of how a static boosting nonlinearity leads to the experimentally observed response attenuation to low frequency stimuli when presented concurrently with high frequency stimuli. First, consider a piecewise linear input-output relationship between afferent firing rate and central neuron firing rate such as that illustrated in Figure E.7A. If the afferent input is normally distributed with low intensity such that it is constrained to the right side of the vertex (i.e., the point at which the slope suddenly changes), then the corresponding output firing rate will be linearly related to the afferent input and thus will also be normally distributed (Figure E.7A, distribution and mean plotted in light purple). This is the situation when low frequency stimuli are applied in isolation. In contrast, if a normally distributed afferent input has a greater intensity and thus spans a greater range of values extending past the vertex (e.g., when high frequency stimuli are applied), then the output firing rate will be a nonlinear function of the input and thus will not be normally distributed any longer. This is because the output firing rate distribution has become skewed, thus shifting its mean to higher values than what would be predicted if the input-output relationship were linear (Figure E.7A, distribution and mean plotted in dark purple). Notably, the skew in the input-output distribution will increase as a function of the

input distribution intensity (compare the three distributions in Figure E.7B), which in turn will increase the bias in the mean with respect to what is expected if the distribution was linear (Figure E.7B, inset). We note that, under experimental conditions, the input intensity will increase when the head velocity stimulus increases in either intensity or frequency content.

Why then does a skewed output distribution result in higher sensitivity to the low frequency stimulus when applied in isolation than when applied concurrently with the high frequency stimulus? To answer this question, note that the output firing rate in response to a given value of the afferent input firing rate caused by the low frequency stimulus must be averaged over the normal distribution of values of the high frequency stimulus. This is because both stimuli are not correlated. For a high value of the low frequency stimulus (point 1, Figure E.7C), the distribution of the high frequency stimulus spans the linear range of the piecewise linear input-output relationship. As such, the average output firing rate in response to this value of the low frequency stimulus when presented concurrently with the high frequency stimulus is equal to that obtained when the low frequency stimulus is presented in isolation. However, this is not the case for lower values of the low frequency stimulus (points 2 and 3, Figure E.7C). Indeed, in these cases, the distribution of the high frequency input extends past the vertex. As a consequence, the distribution of output firing rates is skewed as explained above. The average central vestibular neuron output in response to low values of the low frequency stimulus is thus greater than what would be expected if the input-output relationship were linear. Moreover, the skewness becomes greater for lower values of the low frequency stimulus (compare the purple

output distributions corresponding to points 2 and 3, Figure E.7C), resulting in a greater bias in the output firing rate. This bias, in turn, reduces the slope of the input-output relationship between output and input firing rates when the low frequency stimulus is presented concurrently with the high frequency stimulus, as compared to that obtained when the low frequency stimulus is presented in isolation.

Finally, the above argument leads to the crucial question of why central vestibular neurons display similar sensitivities to high frequency stimuli when applied in isolation or concurrently with low frequency stimuli. As illustrated in Figure E.7D, low frequency stimuli will tend to give rise to narrower distributions of afferent input firing rates and thus smaller biases than high frequency stimuli because of the high-pass filtering characteristics of afferents (compare distributions in Figure E.7D and E.7C, respectively), thereby leading to smaller attenuations in sensitivity.

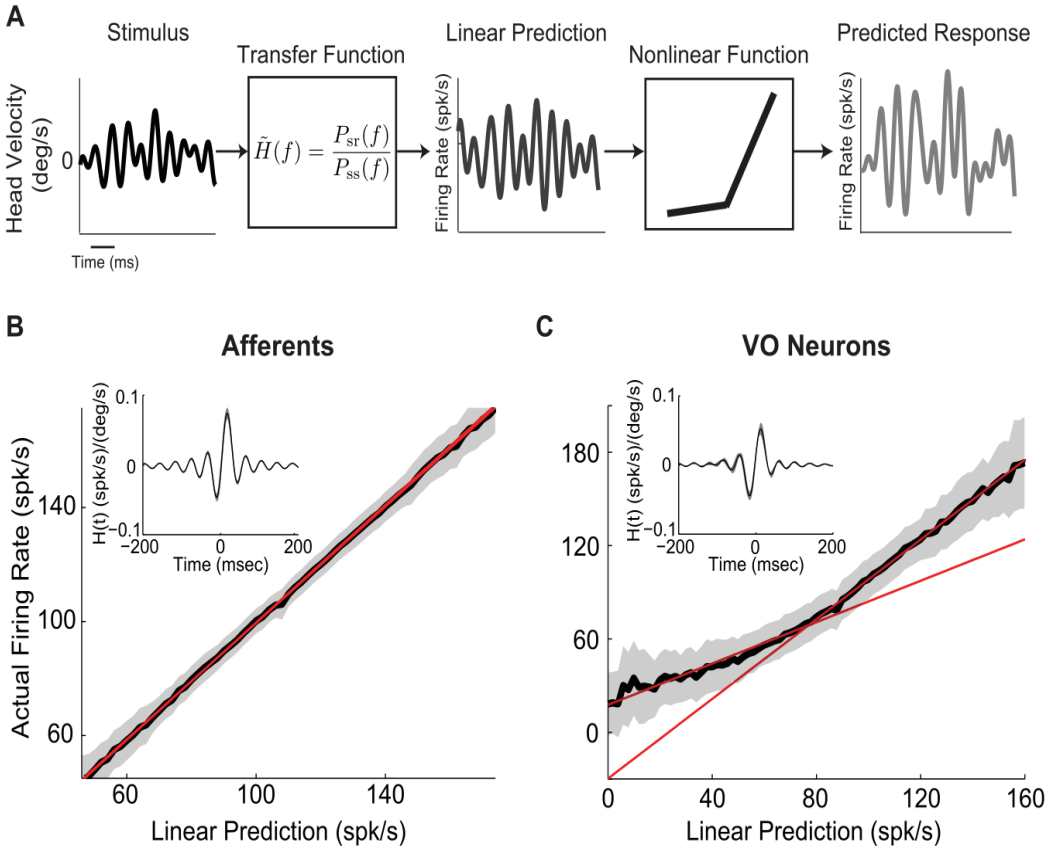

Figure E.6. A linear-nonlinear (LN) cascade model reveals that central vestibular neurons respond nonlinearly to broadband noise stimulation. (A) Schematic showing the LN model's assumptions. The stimulus (left) is convolved with a filter H(t) that is given by the inverse Fourier transform of the transfer function (f) in order to generate the linear predicted firing rate (middle). This linear prediction is then passed through a static function f (which can be linear or nonlinear) to give rise to the predicted output firing rate (right). (B) Population-averaged function f for afferents. Also shown is the best-fit line ($R^2 = 0.9986 \pm 0.001$, n = 15) (red) whose slope did not significantly differ from unity (p = 0.99, n = 15, pairwise t test). Inset: population-averaged filter H(t) for afferents. (C) Population-averaged function f for central VO neurons. Also shown are the best-fit straight lines for the intervals (0-80 Hz) and (80-160 Hz) (red) whose slopes were significantly different from one another (p = 0.0014, n = 13, pairwise t test). Inset: population-averaged filter H(t) for central VO neurons. This figure was copied from Massot et al. [111].

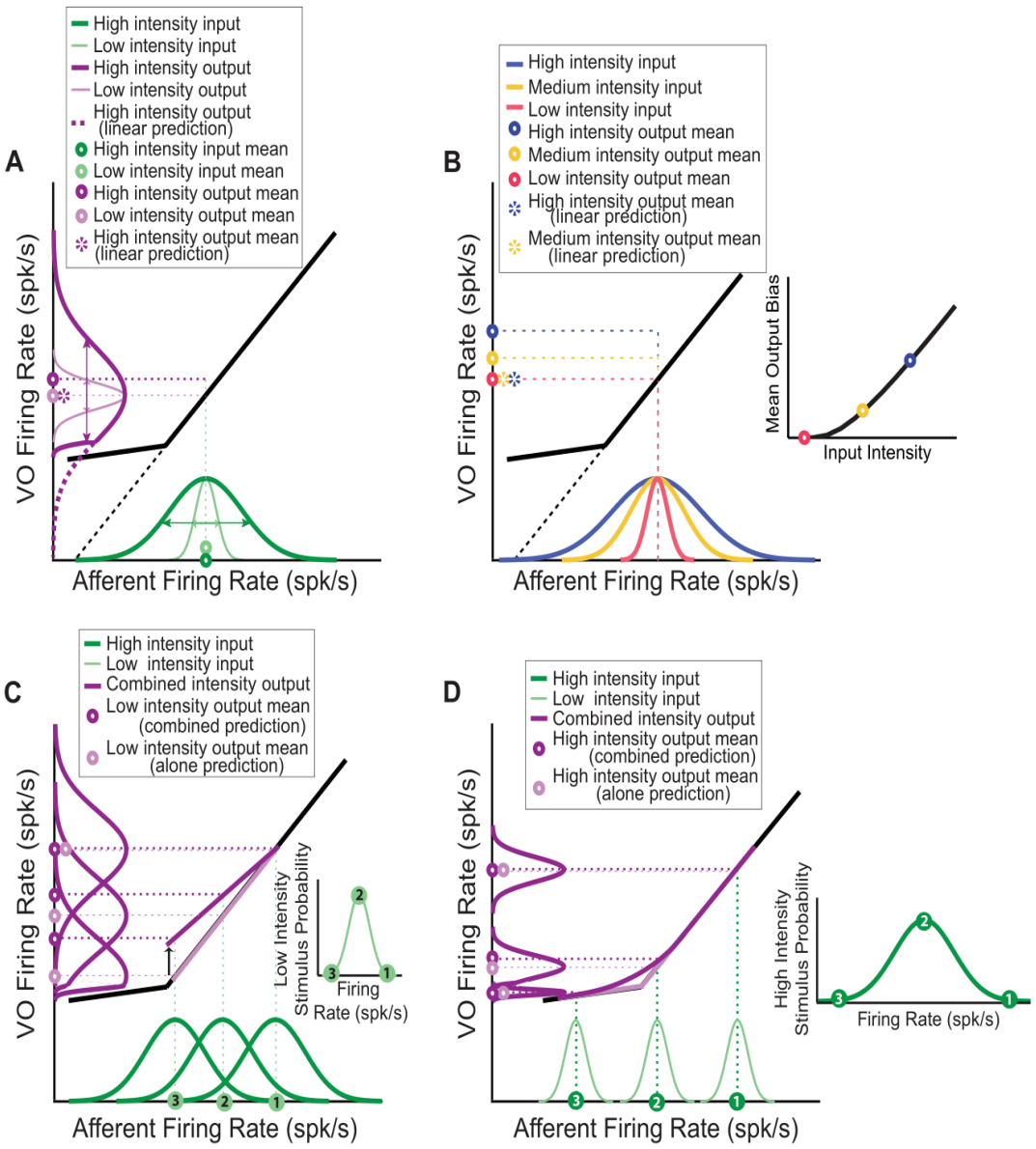

Figure E.7. Schematic showing how a nonlinear static relationship between input and output can lead to attenuated sensitivity to sums of low and high frequency stimuli. (A) Input-output relationship showing a vertex (i.e. a sudden change in slope) (black curve). If we assume that the input is normally distributed with low intensity (i.e. standard deviation) such that all the

Figure E.7 ***(previous page).*** input values are to the right of the vertex (light green distribution on x-axis), then the corresponding output distribution will also be normally distributed (light purple distribution on y-axis). The mean output (light purple circle on y-axis) corresponds to the image of the mean input (dashed purple circle on y-axis; note that the light purple and dashed purple circles were offset for clarity) as both input and output are linearly related. In contrast, for a higher intensity input that extends significantly past the vertex (dark green distribution on x-axis), the corresponding output distribution (dark purple on y-axis) is skewed with respect to the linear prediction (dashed purple on y-axis). The mean output (dark purple circle on y-axis) is thus greater than the linear prediction (dashed purple circle on y-axis). (Note that here and below, we represented the distributions to have the same maximum value in order to emphasize the fact that we are changing the standard deviation.) (B) Increasing the input distribution intensity for a given mean (compare red, yellow, and blue distributions) causes a greater skew in the corresponding output distribution (unpublished data) and thus an increased bias in their means (red, yellow, and blue dots on the y-axis and inset) as compared to the linear prediction (dashed yellow and blue dots on the y-axis). (C) Shifting the mean of the high intensity input distribution to the left (compare points 1, 2, and 3 on the x-axis and the inset) makes it extend to the left of the vertex more and more (compare the green curves on the x-axis), causing greater skewness in the corresponding output distributions (purple curves on the y-axis), which creates a greater bias in the mean (dark purple points on y-axis) with respect to the linear prediction (light purple points on y-axis). As a result, the mean output in response to a given value of the low intensity input (points 1, 2, and 3 on the x-axis) when the high intensity signal is present (dark purple line) has a lower slope (i.e. gain) than when the high intensity signal is absent (light purple line). (D) Shifting the mean of the high intensity input distribution to the left (compare points 1, 2, and 3 on the x-axis and the inset) makes the corresponding distributions of the low intensity input extend to the left of the vertex more and more (green curves on the x-axis), causing greater skewness in the output distribution (purple curves on the y-axis), which creates a greater bias in the mean (dark purple points on y-axis) with respect to the linear prediction (light purple points on y-axis). Note, however, that the bias in the mean will be lower than in (C) since the input distributions now have a lower intensity as explained in (B). Thus, the input-output relationship when the low intensity signal is present (dark purple line) will have a lower slope (i.e. gain) than when the low intensity signal is absent (light purple line) but the effect will be weaker than in (C). This figure was copied from Massot et al. [111].

E.3 Discussion

E.3.1 Summary of Results

What is the neural code used by the brain to represent self-motion (i.e., vestibular) information? We showed that neurons at the first central stage of vestibular processing respond nonlinearly to sums of low and high frequency stimuli. This is because, when stimuli contained low and high frequency motion components, responses to the low frequency component were strongly attenuated. Given that such responses were not observed in afferents, we hypothesized that this occurs because central vestibular neurons nonlinearly integrate their afferent inputs. Computing input-output relationships revealed that afferent firing rates were related linearly to head velocity in all stimulation paradigms. In contrast, the relationship between head velocity and central neuron firing rate was characterized by a significant boosting nonlinearity for high frequency stimulation. Prior studies have shown that higher frequency stimuli elicit greater changes in afferent firing rate than do low frequency stimuli (reviewed in [26]). We hypothesized that this frequency-dependent afferent response plays a vital role in establishing the conditions for which central vestibular neurons will preferentially display nonlinear responses. We confirmed this hypothesis by plotting the central vestibular neuron firing rate output as a function of the afferent firing rate input, and then formulated a model to explain our findings. We then demonstrated the generality of this model by predicting neuronal responses to sums of arbitrary stimuli and conclude that high-pass filtering characteristics displayed by afferents combined with the nonlinear input-output relationship of central vestibular neurons underlie their attenuated responses to low frequency motion when presented

concurrently with high frequency motion. To test that this boosting nonlinearity was indeed static and preferentially elicited by high frequency stimulation, we used LN cascade models to predict responses to broadband noise stimulation. We found that central vestibular neuron responses were well fitted by these models and that the form of the nonlinearity closely matched that obtained for high frequency narrowband noise stimulation with our previous analysis, suggesting that the frequency filtering properties of central vestibular neurons are mostly inherited from that of afferents. Finally, we provided an intuitive explanation as to why a static boosting nonlinearity can lead to the attenuation of the response to low frequency motion in the presence of high frequency motion. Specifically, the nonlinear response of central neurons to high frequency motion creates a skew in the output firing rate distribution, which increases its mean with respect to what would be expected if the input-output relationship was linear. This bias in turn decreases the input-output relationship slope when low frequency motion is presented concurrently with high frequency motion.

E.3.2 Origins of the Nonlinear Processing in Early Vestibular Pathways

While our findings confirm that vestibular afferents display linear responses over a wide frequency range, they further show the novel result that central vestibular neurons respond nonlinearly to sums of low and high frequency stimuli, since they violate the principle of superposition. This is surprising given that previous reports have found that the high conductance state of neurons in vivo can have a significant influence on their processing of synaptic input through linearization in their input-output relations [132, 187, 235, 236], which is thought to extend the neuronal coding

range [11]. Our results further show that the nonlinear responses of central vestibular neurons to sums of low and high frequency self-motion are caused by a static boosting nonlinearity in their input-output relationships. This nonlinearity differs from those (directional asymmetry, soft saturation) described in prior studies examining the responses of these same neurons [237, 238]. We note that our stimuli were designed as to not elicit "trivial" nonlinearities such as rectification and saturation from both afferents and central vestibular neurons but that these will indeed be elicited by high intensity stimuli [109].

What causes the observed boosting nonlinearity in central vestibular neurons? Our results show that this nonlinearity is static, and thus support the hypothesis that it is caused by intrinsic mechanisms such as short-term synaptic plasticity [239], voltage-dependent conductances [140], or the diversity in the innervations patterns of regular versus irregular afferent inputs onto central vestibular neurons [240] rather than network mechanisms such as nonlinear inhibitory connections within the known recurrent feedback loops of the vestibular nuclei/cerebellum [241,242]. It is, however, difficult to determine the exact nature of these mechanisms for several reasons. (1) Intrinsic mechanisms such as synaptic conductance, passive membrane properties, and voltage-gated currents of neurons in the vestibular nuclei have been primarily been studied in mouse and guinea pig (reviewed in [27]) and not in primates. This is important because previous studies have shown significant differences in the activities of rodent and monkey vestibular nuclei neurons in vivo [152]. (2) Most prior characterizations of intrinsic mechanisms were performed under in vitro conditions, whereas the integration properties of vestibular neurons differ significantly in vivo

and in vitro [132]. Thus, further studies involving in vivo intracellular recordings from single primate central vestibular neurons are needed to uncover the mechanisms that mediate the observed nonlinearity.

E.3.3 Consequences of Nonlinear Central Vestibular Processing for Higher Vestibular Pathways and Perception

During everyday activities, such as walking or running, the predominant frequencies of head rotation and translation are within 0.6-10 Hz in both humans [243–245] and monkeys [142, 246]. While significant harmonics up to 15-20 Hz can be present, their magnitude is generally $< 5\%$ of the power found in the predominant frequency range. Taken together, these findings indicate that while active head movements cover a wide range of frequencies, most stimulation occurs at relatively low frequencies. This then leads to the question: What is the functional significance of nonlinear integration of afferent input by central vestibular neurons leading to attenuated responses to the low frequency components of self-motion?

One possibility is that the relative enhancement of high frequency power serves to effectively "whiten" (i.e., flatten) the output power spectrum of sensory neurons during everyday activities. For example, in vision, natural scenes are typically described by a spatial frequency amplitude spectrum that decreases as 1/frequency– or equivalently as a power spectrum that decreases as $1/\text{frequency}^2$ [247, 248]. A widespread view is that early visual neurons are tuned in such a way as to compensate for this decrease. Indeed, whitening would serve to equalize the neural responses across frequencies as originally proposed by Field [247]. Specifically, a neuron tuned to high frequencies would require an increased response gain to produce the same

response as a neuron tuned to low frequencies (reviewed in [249, 250]). This mechanism bears a striking resemblance to preferential encoding of high frequency stimuli by central vestibular neurons demonstrated in the present study. Another possible mechanism that has been proposed to underlie whitening in the visual system is decorrelation [251], which includes neurons with bandpass tuning curves for which a portion of the curve rises with frequency. This latter model is not a likely candidate strategy for early vestibular processing since vestibular afferents and central neurons are characterized by high-pass rather than band-pass tuning.

Another possibility, which relates to the argument above, is that neuronal responses optimize our ability to reflexively respond to transient unexpected events. In particular, central vestibular neurons make descending projections to the spinal cord and mediate the vestibulo-spinal reflexes that ensure stable posture [114]. We note that, to date, the vestibular stimuli experienced during voluntary activities such as walking and running have primarily been quantified while subjects locomoted "in place" [243]. However, these studies might have underestimated the frequency content of natural vestibular stimuli. Indeed, higher frequency stimuli are experienced during natural locomotion since heel strikes can produce vibrations with frequencies as high as 75 Hz [252]. It is likely that these high frequency components are filtered out as the vibration passes up through the body. Thus, the enhanced neural responses to high frequency motion could be an effective coding strategy for countering the biomechanical filtering properties of the body segments during unexpected postural perturbations. Indeed, recent studies have demonstrated such frequency-specific filtering of vestibular-evoked postural responses in humans [253]. It is also

noteworthy that central vestibular neurons are also much less responsive to active than passive motion [147, 156]. Accordingly, their response selectivity is likely to optimize our ability to reflexively respond to unexpected transient events. For example, if standing while riding the metro, or walking/running, one is likely to experience sudden stops or unexpected motion for which it is vital to generate compensatory postural reflexes.

Yet another possibility is that the nonlinear responses of central vestibular neurons constitute an adaptation mechanism that preserves the coding of both low and high frequency components of self-motion by preventing rectification (i.e., a complete cessation of firing). Specifically, such adaptation would serve to enhance the coding range by allowing responses to higher stimulus intensities through gain control. Gain control has been widely observed across systems and can be caused by multiple mechanisms [10, 11, 196, 254]. Further studies that focus on how central vestibular neurons adapt to changes in natural self-motion stimuli are needed to investigate this possibility.

Finally, the central vestibular neurons that were the focus of the present study make contributions to higher-order vestibular processing including the computation of self-motion perception, spatial orientation (reviewed in [25]). However, to date, prior studies of self-motion perception [255] have focused on responses to motion containing frequencies < 5 Hz and thus have only probed the lower portion of the physiologically relevant frequency range (i.e., 0-20 Hz) [142]. Accordingly, it is unlikely that the nonlinearities observed in the present study would have been significantly evoked in these studies. Interestingly, several studies have reported that

perceptual responses to low frequency vestibular input are enhanced by a network property, termed velocity storage, which functions to lengthen the time constant of the vestibuloocular reflex [256–258]. This mechanism is mediated via reciprocal connections between the vestibular cerebellum and nuclei, and its dynamics are encoded in the responses of single central neurons. Our results predict that central neurons would exhibit dynamics consistent with velocity storage but that the amplitude of this effect should be reduced when low and high frequency stimuli are applied concurrently. Future experiments will be needed to investigate how the response selectivity of central vestibular neurons shapes postural responses as well as the perception of self-motion and spatial orientation.

E.3.4 The Emergence of Feature Extraction: Function and General Principles Across Systems

As an alternative to the whitening hypothesis mentioned above, theoretical studies suggest that a common underlying principle of sensory processing is that the representation of information becomes more efficient in higher brain centers because neurons in these areas respond more selectively to specific features of natural sensory stimuli. This principle, commonly referred to as "sparse coding", has been investigated in different sensory systems (see [259] for a review). Some of the most compelling evidence for a sparse code comes from experiments using stimuli resembling those which would be encountered during natural vision in primary visual cortex [260] and area V4 [261]. Parallel findings in the auditory [262], somatosensory [263], and olfactory [264] systems have provided further evidence that sensory processing is generally characterized by an increase in sparseness at higher levels. Here we focused on understanding the mechanisms underlying integration of afferent

input by central vestibular neurons. While the linear filtering properties of central vestibular neurons and afferents were similar, confirming our previous results [35], we have shown here that a static nonlinearity causes a decreased response to low frequency stimuli in the presence of high frequency stimuli in central vestibular neurons but not afferents. We propose that this decreased response to the low frequency components of self-motion corresponds to feature detection in that it enables central vestibular neurons to respond selectively to the high frequency components. This is consistent with our previous results showing that individual central vestibular neurons transmit less information about the detailed time course of the stimulus than individual afferents [35]. We suggest that this enhanced feature selectivity displayed by central vestibular neurons could constitute a signature of sparse coding and that further sparsening occurs at subsequent levels of processing.

Our findings also suggest the intriguing possibility that central vestibular neurons implement gain control through divisive normalization, similar to that previously shown to occur in the visual [265], auditory [266], and olfactory [267]systems (see [268] for a review). In sensory systems for which neurons are tuned to different features of complex natural stimuli, divisive normalization provides an efficient nonlinear coding strategy that can reduce dependencies between stimulus features. Specifically, when multiple features are present in a given stimulus, the activity of a neuron tuned to a given feature is obtained by normalizing the response to that feature presented in isolation by the summed activity of neighbouring neurons tuned to the other features. As a result, an advantage is that divisive normalization effectively implements sensory gain control such that the neural response to a given feature is

adaptively attenuated when other features are present. The attenuated response to low frequency head rotations that we observed in central vestibular neurons when these are presented concurrently with high frequency head rotations could be a signature of divisive normalization. Further studies are, however, needed to fully test this hypothesis and to understand the functional implications of the relatively negligible attenuation that was seen for high frequency stimulation. Finally, our results provide evidence for a nonlinear mechanism that enables the preferential attenuation of the response to a given stimulus when multiple stimuli are presented at the same time. Such responses to stimuli consisting of sums of low and high frequency components are also seen in other systems and may thus be a general feature of sensory processing. For example, simultaneous masking presents some similarities with the effect described here as the presence of a high frequency sound can significantly degrade the perception of a low frequency sound [125, 269, 270]. Further, non-classical receptive field stimulation can strongly attenuate the responses to low but not high frequency input [260, 271]. We hypothesize that mechanisms similar to those described here might mediate these effects in other systems.

E.4 Materials & Methods

Three macaque monkeys (two Macaca mulatta and one Macaca fascicularis) were prepared for chronic extracellular recording using aseptic surgical techniques [35, 272, 273]. All procedures were approved by the McGill University Animal Care Committee and were in compliance with the guidelines of the Canadian Council on Animal Care.

E.4.1 Data Acquisition

The experimental setup and methods of data acquisition have been previously described for both vestibular afferents [36, 38, 274] and vestibular nuclei neurons [35, 147]. We used standard techniques to perform single unit recordings from 18 vestibular afferents [35, 106, 274] that innervate the horizontal semicircular canals and 21 vestibular-only (VO) neurons [35, 147, 272] in the medial vestibular nuclei that were sensitive to horizontal rotations. Resting discharge regularity in afferents was quantified by the normalized coefficient of variation (CV^*) [35, 108]. Vestibular afferents with a $CV^* < 0.15$ were classified as regular, whereas those with a $CV^* \geq 0.15$ were classified as irregular as done previously [36, 38, 275]. As such, 5 afferents were classified as regular and the remaining 13 were classified as irregular. VO neurons were classified as either type I or type II depending on whether they are excited or inhibited by rotations towards the ipsilateral side, respectively [276]. 9 VO neurons were type I and 12 were type II. Data from both groups were pooled as no notable difference was observed when quantifying their responses to the stimuli used here (unpublished data).

E.4.2 Experimental Design

We used two classes of head velocity stimuli to characterize the responses of vestibular afferents and central neurons to horizontal rotations. The first class of stimuli consisted of noise stimuli characterized by a Gaussian distribution of angular velocities with zero mean and standard deviation (SD) of 20 deg/s each lasting 80 s. We used four different noise stimuli whose frequency content spanned the frequency range of natural vestibular stimuli (0-20 Hz) [142]: (1) low-pass filtered

Gaussian white noise (8th order Butterworth, 5 Hz cutoff frequency), henceforth referred to as the low frequency noise stimulus; (2) band-pass filtered Gaussian white noise (4th order Butterworth, 15-20 Hz band), henceforth referred to as the high frequency noise stimulus; (3) the linear sum of the low and high frequency noise stimuli; and (4) low-pass filtered Gaussian white noise (8th order Butterworth, 20 Hz cutoff frequency), henceforth referred to as the broadband noise stimulus. Our noise stimulation protocol consisted of the low frequency stimulus by itself, then the high frequency stimulus by itself, then the linear sum of the two, and finally the broadband noise stimulus. The second class of stimuli consisted of single frequency sinusoidal rotations each lasting 80 s, of amplitude 15 deg/s and frequencies 3 Hz and 17 Hz, henceforth referred to as the low and high frequency sinusoidal stimuli, respectively. These frequencies were chosen because they span the frequency range of natural vestibular stimuli (0-20 Hz) [142]. Our stimulation protocol consisted of delivering the low frequency sinusoidal stimulus, then the high frequency sinusoidal stimulus, and then the linear sum of the two.

E.4.3 Traditional Linear System Analysis

For the analysis of responses to sinusoidal stimuli s(t), the spike train from each neuron was converted into a binary sequence r(t) with a bin width of 1 ms. The value of any given bin was set to 1 if it contained an action potential and 0 otherwise, as done previously [38]. This binary sequence was then convolved with a Kaiser window with cutoff frequency 0.1 Hz above the stimulus frequency to obtain an estimate of the time dependent firing rate $f_{measured}(t)$ [277, 278]. The response gain was then computed by fitting a first order model $f_{fit}(t) = b + g * s(t - t_d)$ to the data. Here b

is the bias, g is the gain, and td is the latency, respectively. We used a least squares regression to find the best fit parameter values that provide the maximum variance accounted for (VAF) given by $1 - [var[f_{fit}(t) - f_{measured}(t)]/var(f_{measured}(t))]$. Here var is the variance and $f_{measured}(t)$ represents the actual firing rate [156, 272]. For noise stimuli, the stimulus waveform s(t) was also sampled with timesteps of 1 ms. The response sensitivity was computed from the gain $G(f) = |P_{sr}(f)/P_{ss}(f)|$, where $P_{sr}(f)$ is the cross-spectrum between the stimulus s(t) and binary sequence r(t), and $P_s s(f)$ is the power spectrum of the stimulus s(t). All spectral quantities (i.e., power-spectra and cross-spectra) were estimated using multitaper techniques with 8 Slepian functions [279]. Estimates of gain for low (0-5 Hz) and high (15-20 Hz) frequencies were obtained by averaging the gain curves G(f) between 0 and 5 Hz and between 15 and 20 Hz, respectively.

E.4.4 Coherence Measures

We also used the coherence function to measure the neural response to the noise stimuli used in this study. The coherence is defined by:

$$C(f) = \frac{|P_{sr}(f)|^2}{P_{ss}(f)P_{rr}(f)} \tag{E.1}$$

Here $P_{rr}(f)$ is the power spectrum of the response $r(t)$. Based on the number of trials and tapers used in this study, the confidence limit for the magnitude of the coherence being significantly different from zero at the p= 0.05 level is 0.097 [197, 279] and all neurons in our dataset displayed maximum coherence values that were greater than 0.097 for at least one of the stimulation protocols. It is important to note that, unlike the sensitivity G(f), the coherence is based on the signal-to-noise ratio

$SNR(f) = C(f)/[1 - C(f)]$ and thus takes neural variability into account [121]. As such, measuring the response using gain and coherence measures can sometimes give qualitatively different results [38, 233, 280]. The coherence is also related to a lower bound on the mutual information [80] that measures the amount of information that can be decoded linearly [81].

E.4.5 Stationarity

We tested that the neural responses to both sinusoidal and noise stimuli were stationary in the following way. We divided each recorded neural response r(t) into 4 epochs of length 20 s and computed the mean firing rate, gain, and coherence in each epoch. We found that these did not differ significantly from one another for all neurons in our dataset and all stimuli ($p < 0.05$, oneway ANOVAs).

E.4.6 Normalization

All gain and coherence measures were normalized in the following way. The curves in response to the high frequency stimuli (noise or sinusoidal) were normalized by their values at 17 Hz. The curves in response to low frequency stimuli were also normalized by these values. The curves obtained in response to the sum of the low and high frequency stimuli were normalized by their values at 17 Hz.

E.4.7 Attenuation

We quantified response gain attenuation by:

$$\%attenuation = 100 \cdot \frac{G_{stim,alone} - G_{stim,together}}{G_{stim,alone}} \tag{E.2}$$

where $G_{stim,alone}$ is the gain in response to stimulus "stim" when it is presented by itself and $G_{stim,together}$ is the gain in response to stimulus "stim" when it is presented concurrently with another stimulus. We also quantified coherence response attenuation by:

$$\%attenuation = 100\frac{C_{stim,alone} - C_{stim,together}}{C_{stim,alone}} \tag{E.3}$$

where $C_{stim,alone}$ is the coherence in response to stimulus "stim" averaged over the stimulus's frequency range when it is presented by itself and $C_{stim,together}$ is the coherence in response to stimulus "stim" averaged over the stimulus's frequency range when it is presented concurrently with another stimulus.

E.4.8 Input-Output Relationships

We quantified the output as the time varying firing rate, which was obtained by filtering the response r(t) using a Kaiser filter with cutoff frequency 5 Hz above the highest frequency contained in the stimulus input [277]. We then computed the cross-correlation function between the filtered response and the horizontal head velocity stimulus s(t) and noted the lag at which it was maximal. This lag was then used to align the response r(t) with the stimulus s(t). We then plotted r(t) as a function of s(t) and took the average of values in bins of 1 deg/s. To quantify whether these curves were well-fit by a straight line, we performed a linear least-squares fit over the range 10 to 20 deg/s and computed R^2 over the range 230 to 220 deg/s.

E.4.9 Rescaled Input-Output Relationships

We rescaled input-output relationships in order to plot the output firing rate of VO neurons as a function of the input afferent firing rate. Because central vestibular

neurons receive input from a heterogeneous population of afferents, we estimate the afferent input firing rate in the following manner. First, we took the average gain curves of regular and irregular afferents as a function of frequency obtained by Sadeghi et al. [36] since this corresponds, to the best of our knowledge, to the largest dataset on primate vestibular afferents. We then fit these curves using the following expression [32, 89, 281]:

$$G_{est}(f) = \frac{AuT_c(1+uT_1)}{(1+uT_c)(1+uT_2)} \tag{E.4}$$

where $u = 2\pi f$. Here T_c and T_2 are the long and short time constants of the torsion-pendulum model of canal biomechanics and T_1 is proportional to the ratio of acceleration to velocity sensitivity of the afferent response. Similar models have more recently been shown to provide an accurate description of canal afferent responses in monkeys [275, 282] up to 20 Hz [92], in chinchillas [89, 90] and mice [283]. We used A =0.428 (spk/s)/ (deg/s), $T_1 = 0.015$ s, T_2= 0.003 s, and $T_c = 5.7$ s to fit the average gain curve for regular vestibular afferents [32]. A was adjusted to match the data of Sadeghi et al. [36] under control conditions. To fit the average gain curve of irregular afferents, we used A= 0.765 (spk/s)/(deg/s), T_1= 0.0085 s, T_2= 0.003 s, and T_c =5.7 s. A and T_1 were adjusted to match the average gain curve for C and D-irregulars from Sadeghi et al.'s [36] data under control conditions since C and D-irregulars were encountered with roughly equal probability [36]. The input afferent firing rate is then given by:

$$r_{aff}(s) = G_{aff}s + bias \tag{E.5}$$

$$G_{aff} = \frac{G_{reg} + G_{irreg}}{2} \tag{E.6}$$

where G_{reg} and G_{irreg} are the gains of regular and irregular afferents averaged over the stimulus's frequency content, respectively, and Gaff is the average between the two values. We took the average since about 50% of afferents encountered were regular and the other 50% were irregular in Sadeghi et al.'s [36] dataset. We used a bias of 104.30 spk/s, which corresponds to the average baseline firing rate of the afferent population observed experimentally [36].

E.4.10 Model

Our model assumes that VO neurons display a static input-output relationship with respect to their afferent input. We estimated this relationship by fitting a 6th order polynomial to the input-output relationship obtained experimentally with the high frequency noise stimulus. As a result, the output firing rate of the VO neuron is given by:

$$r_{VO}(r_{aff}) = F[r_{aff}] \tag{E.7}$$

where r_{VO} is the VO neuron's firing rate, r_{aff} is the afferent firing rate, and F is the estimate of the static input-output relationship. We now consider the input s to consist of two stimuli. We will refer to one stimulus as the "signal" and to the other as the "masker". Note that, while the terms "signal" versus "masker" are arbitrary, this division allows us to focus on the coding of one input (i.e. the input designated as the signal). The VO neuron's response to the signal and masker stimuli is then given by:

$$\begin{aligned} r_{VO}(\text{signal} + \text{masker}) &= F[r_{aff}(\text{signal} + \text{masker})] \\ &= F(G_{aff,signal}\text{signal} + G_{aff,masker}\text{masker} + \text{bias}) \end{aligned} \tag{E.8}$$

where $G_{aff,signal}$ and $G_{aff,masker}$ are the afferent gains to the signal and masker, respectively. These are obtained by averaging the afferent gains over the signal and masker's frequency contents, respectively. In order to obtain the VO neuron's firing rate as a function of the signal alone, it is necessary to average over the distribution of values that can be taken by the masker. As signal and masker are not correlated, this distribution is equal to the probability distribution of the masker, which is taken to be normal with mean 0 and standard deviation σ_{masker}, thus:

$$P(masker) = \frac{1}{\sigma_{masker}\sqrt{2\pi}} e^{-\frac{masker^2}{2\sigma_{masker}}} \tag{E.9}$$

The VO neuron's firing rate is then given by:

$$r_{VO}(signal) = \langle r_{VO}(signal + masker)\rangle_{masker} \tag{E.10}$$

$$= \int_{-\infty}^{\infty} dx r_{VO}(signal + x)P(x) \tag{E.11}$$

where x is the masker. The integral was evaluated numerically using a Riemann sum approximation with binwidth 1 deg/s. This model can then be used to predict the VO neuron's input-output relationship when arbitrary signal and masker stimuli are used. In order to get some intuition, we expanded F into a Taylor series in equation (12) to obtain:

$$\begin{aligned} r(signal) =& \langle F(G_{signal}signal + bias)\rangle_{masker} + G_{masker}F' \\ & (G_{signal}signal + bias)\langle masker\rangle_{masker} + \frac{G_{masker}^2}{2}F'' \\ & (G_{signal}signal + bias)\langle masker^2\rangle_{masker} + \ldots \end{aligned} \tag{E.12}$$

where F' and F'' are the first and second derivatives of F, respectively. The first term simply corresponds to the firing rate when no masker is present (i.e., $\sigma^2_{masker} = 0$) and the term $\langle masker^n \rangle_{masker}$ is equal to the n^{th} order moment of the Gaussian distribution P(masker). In particular, all moments for n odd are equal to zero (this comes from the fact that the distribution is symmetric with respect to its mean) while the second moment is simply equal to the variance σ^2_{masker}. Neglecting all higher order moments gives:

$$r_{VO}(signal) = r_{VO,0}(signal) + \frac{\sigma^2_{masker} G^2_{aff,masker}}{2} F''(G_{signal} signal + bias) \quad \text{(E.13)}$$

where $r_{VO}(signal)$ is the VO neuron's firing rate for a given value of the signal in the presence of the masker and $r_{VO,0}(signal)$ is the firing rate for the same value of the signal when the masker is absent (i.e., $\sigma^2_{masker} = 0$). Inspection of Equation E.14 shows that the masker has no effect on the output firing rate $r_{VO}(signal)$ if F is a linear function, as we then have $F''(x) = 0$ for any x. Further, the sign of the correction depends solely on the sign of the second derivative since all other terms are positive. As such, the masker will increase the average firing rate in response to the signal in regions where F is convex and decrease it in regions where F is concave. The amount by which the firing rate increases/decreases grows in magnitude with the masker variance σ^2_{masker} but also depends on the gain of the afferents to the masker $G_{aff,masker}$. Since the afferents display gains that increase as a function of frequency, maskers with higher frequency content will lead to a greater correction in firing rate than maskers with lower frequency content for a given variance σ^2_{masker}. Equation E.14 then allows us to evaluate the percentage attenuation in gain by taking its

derivative and evaluating it at signal = 0 and substituting the result into Equation E.2:

$$\%attenuation = -100 \times \frac{\frac{\sigma^2_{masker} G^2_{masker}}{2} F'''(bias)}{F'(bias)} \tag{E.14}$$

where F"' is the third derivative of F.

E.4.11 Linear Nonlinear Cascade Model

We used a linear-nonlinear (LN) cascade model [110] to characterize the response properties of both afferents and VO neurons to noise stimuli. This model predicts that a neuron's firing rate predicted at any instant is a function f of the linear firing rate r_{linear} plus the baseline firing rate r_{bias}. The linear firing rate is obtained by convolving the stimulus with the optimal linear filter H(t). Thus, we have:

$$r_{predicted}(t) = f(r_{linear}(t)) \tag{E.15}$$

$$r_{linear}(t) = r_{bias} + (H \star s)(t) \tag{E.16}$$

where "*" denotes the convolution operation and H(t) is the inverse Fourier transform of the transfer function $\tilde{H}(f) = P_{sr}(f)/P_{ss}(f)$. We estimated f by plotting the actual firing rate r(t), which was computed as described above, as a function of the linear prediction r_{linear} [110]. To quantify whether these curves were well-fit by a straight line, we performed a linear least-squares fit over the ranges 80-120 and 100-140 spk/s for central VO neurons and afferents, respectively. We then computed the R^2 over the ranges -17-120 and 20-140 spk/s for central VO neurons and afferents, respectively. In practice, H(t), r_{bias}, and f were all computed using the first half of the recorded activity for a given neuron. We then compared the predicted firing rate $r_{predicted}(t)$ computed using Equation E.16 against the actual firing rate r(t) for

the second half of the recorded activity and quantified the goodness-of-fit of the LN model by computing R^2.

E.4.12 Statistics

Values are reported as mean 6 STD in the text. Error bars or gray bands represent 1 SEM. Throughout, "**" and "*" indicate statistical significance using a paired t test at the p =0.01 and p =0.05 levels, respectively. "NS" indicates that the p value was above 0.05.

E.5 Supporting Information

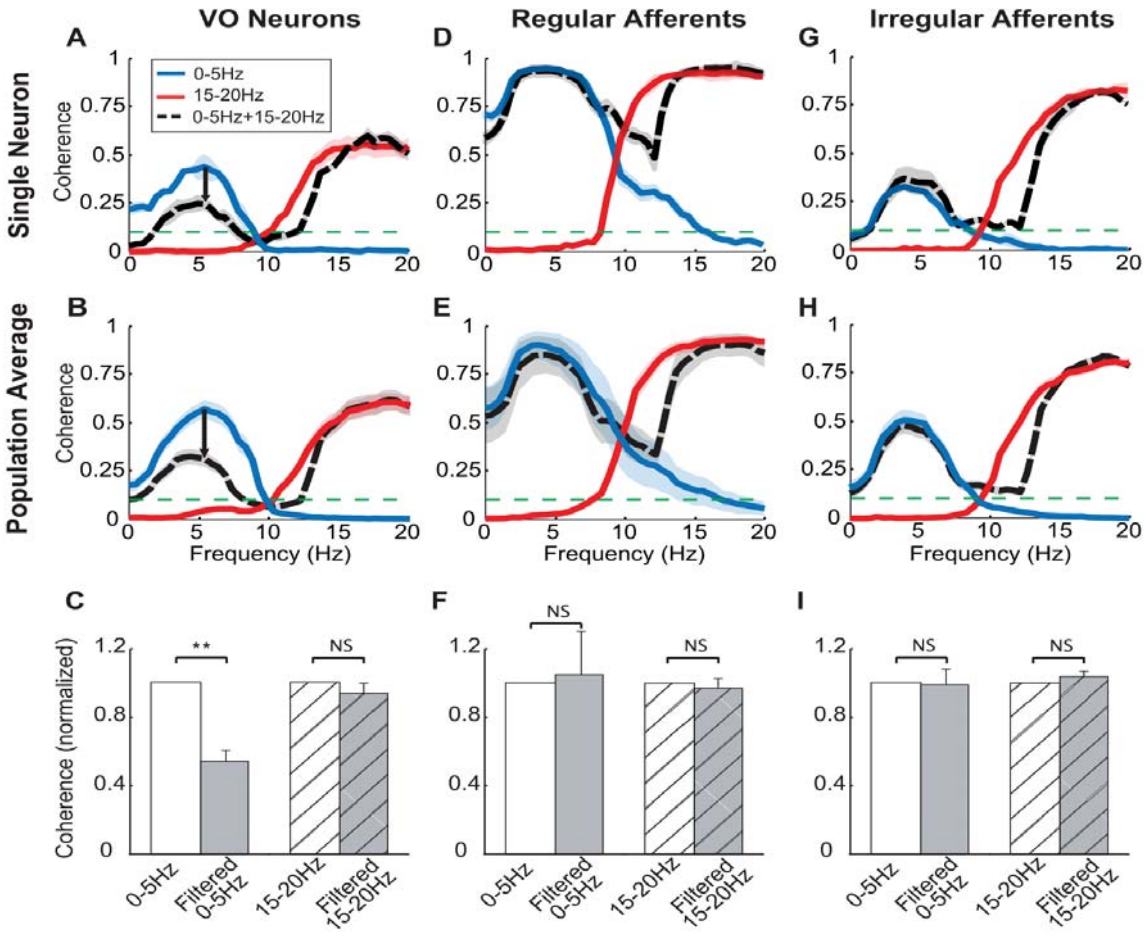

Figure E.S1. Central VO neurons but not afferents respond nonlinearly to sums of low and high frequency noise stimuli as quantified by coherence measures. (A, B) Coherence curves as a function of frequency for an example VO neuron (A) and averaged over the population (B). (C) Population-averaged average normalized coherence values for central VO neurons. (D, E) Coherence curves as a function of frequency for an example regular afferent (D) and averaged over the population (E). (F) Population-averaged average normalized coherence values for regular afferents. (G, H) Coherence curves as a function of frequency for an example irregular afferent (G) and averaged over the population (H). (I) Population-averaged average normalized coherence values for irregular afferents. This figure was copied from Massot et al. [111].

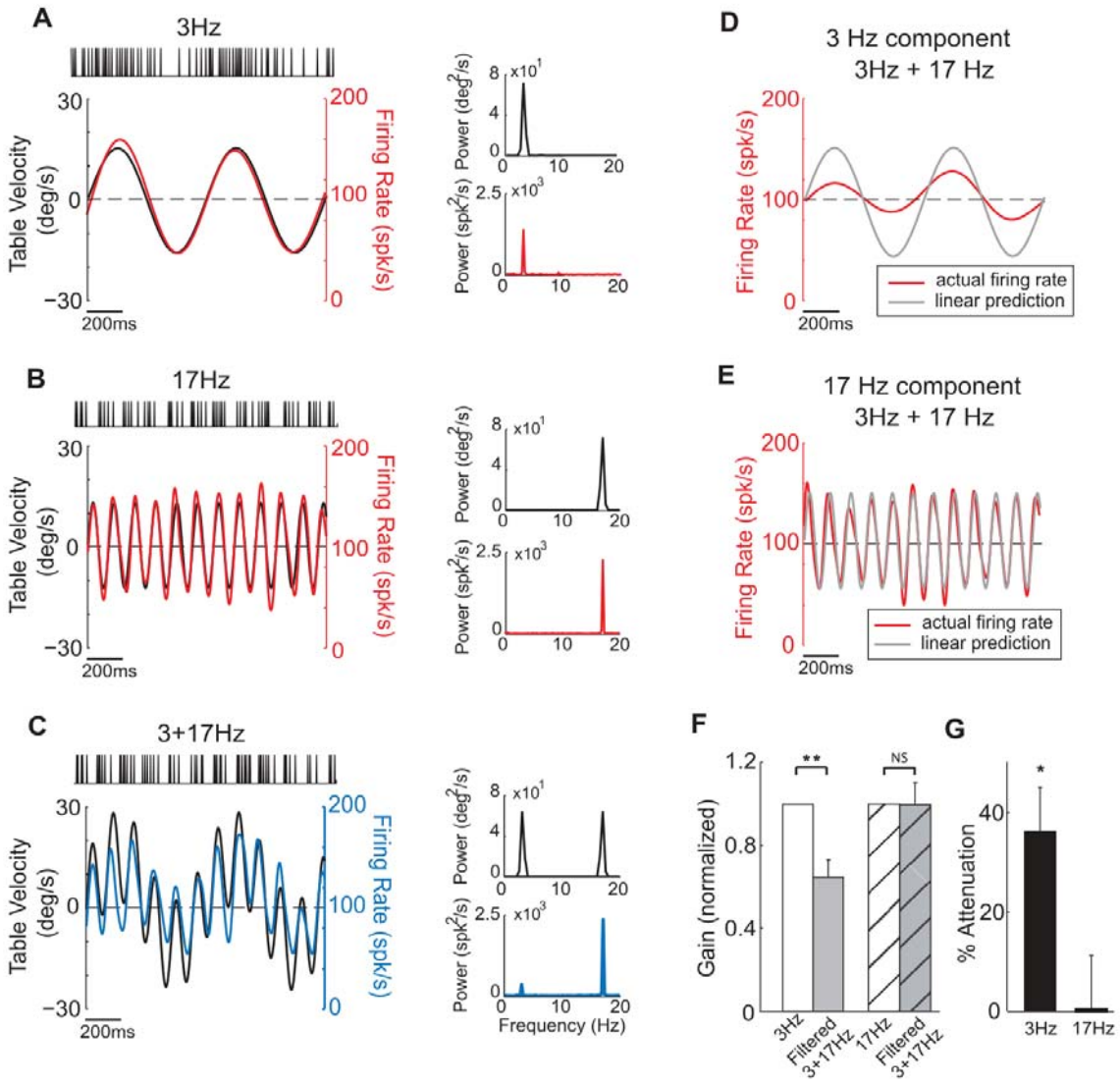

Figure E.S2. Central vestibular neurons respond nonlinearly to sums of sinusoidal stimuli.

Figure E.S2 ***(previous page).*** (A+C) Example central vestibular neuron responses to 3 Hz (A), 17 Hz (B), and 3+17 Hz (C) sinusoidal rotations. The insets show the power spectra of the input stimuli (black) and output firing rate (red and blue). (D, E) Comparison between the actual response and that predicted from a linear system for the same example neuron for the 3 Hz (D) and 17 Hz (E) components of 3+17 Hz stimulation. (F) Population-averaged normalized gains for central VO neurons. Note the gain for 3 Hz is strongly attenuated in the presence of 17 Hz (p=1023, paired t test, n = 11). In contrast, the gain at 17 Hz was not significantly altered by simultaneously presenting the 3 Hz stimulus (p = 0.97, paired t test, n = 8). (G) Population-averaged percentage attenuation at low (3 Hz) and high (17 Hz) for central neurons. The firing rate estimates were obtained by convolving the spike trains with a Kaiser filter (see Materials and Methods). This figure was copied from Massot et al. [111].

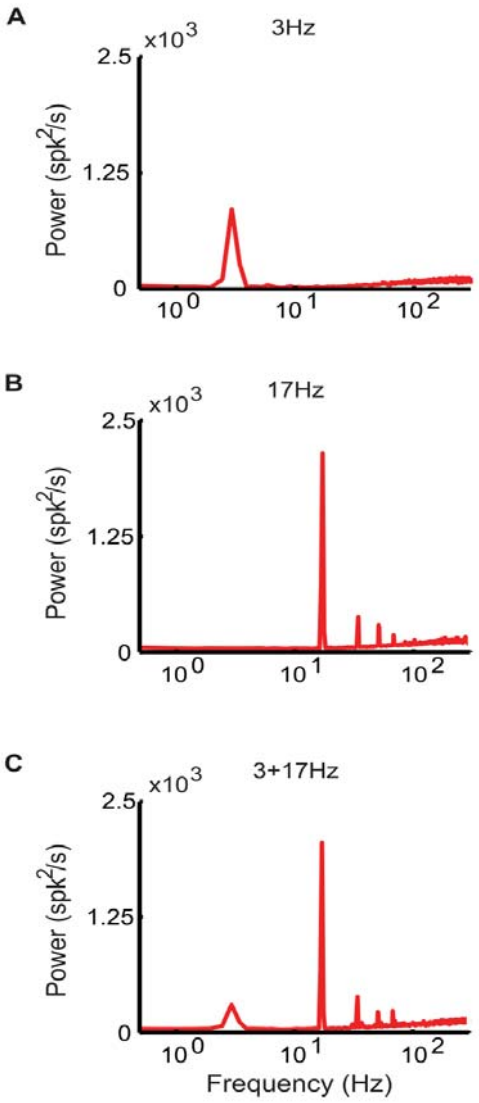

Figure E.S3. Analysis of unfiltered spike trains confirms that central vestibular neurons respond nonlinearly to sums of sinusoidal stimuli. (A-C) Spike train power spectra for the same example central VO neuron shown in Figure E.S2 to 3 Hz (A), 17 Hz (B), and 3+17 Hz (C) sinusoidal rotations. Note that the power at 3 Hz was lower for 3+17 Hz than for 3 Hz stimulation and that the power at 17 Hz for 17 Hz stimulation was similar to that for 3+17 Hz stimulation. This figure was copied from Massot et al. [111].

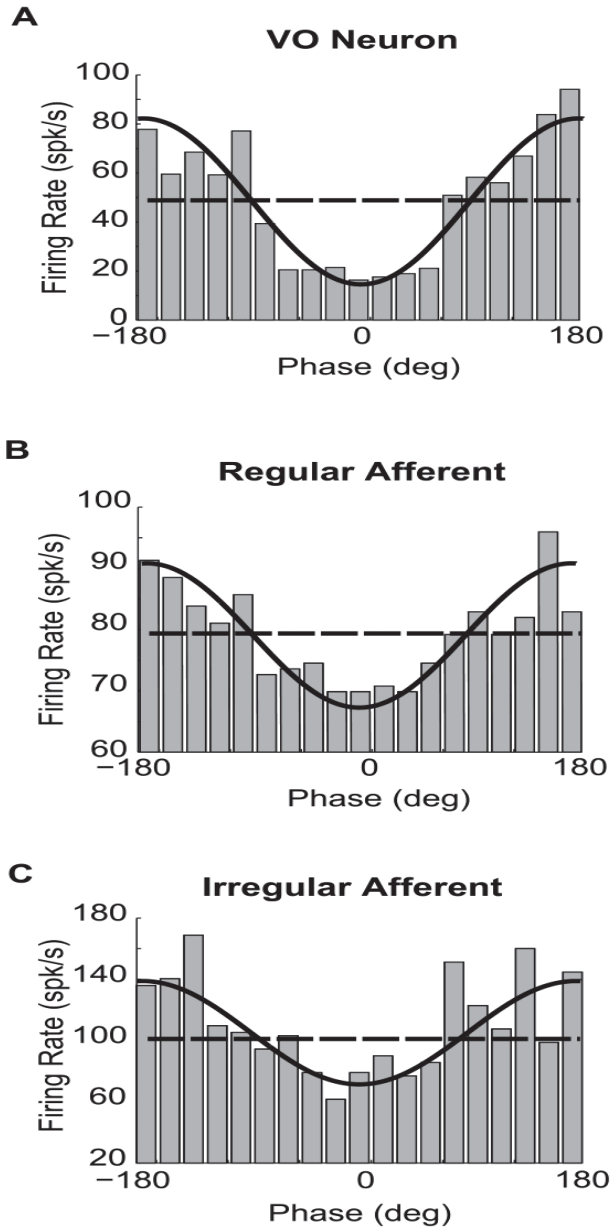

Figure E.S4. Central VO neurons as well as afferents do not show rectification and/or saturation when stimulated by the low and high frequency head rotations used in this study.

Figure E.S4 ***(previous page).*** (A-C) Phase histograms for an example VO neuron (A), regular afferent (B), and irregular afferent (C). The solid curves show the best sinusoidal fits. The dashed lines indicate the mean firing rates. Note that in no case do the histograms display either saturation or rectification. The population-averaged percentage of bins in the phase histograms corresponding to values less than 5% of the mean was 0 in more than 98% of cases, indicating no significant rectification. This was also true for 3 Hz and 3+17 Hz sinusoidal rotation (unpublished data) and for all neurons in the population. The population-averaged Variance-Accounted-For (VAF) of the sinusoidal fit for all three types of neurons was not significantly different between the different sinusoidal stimuli ($p=0.15$, t tests). This was also true for the noise stimuli (unpublished data). This figure was copied from Massot et al. [111].

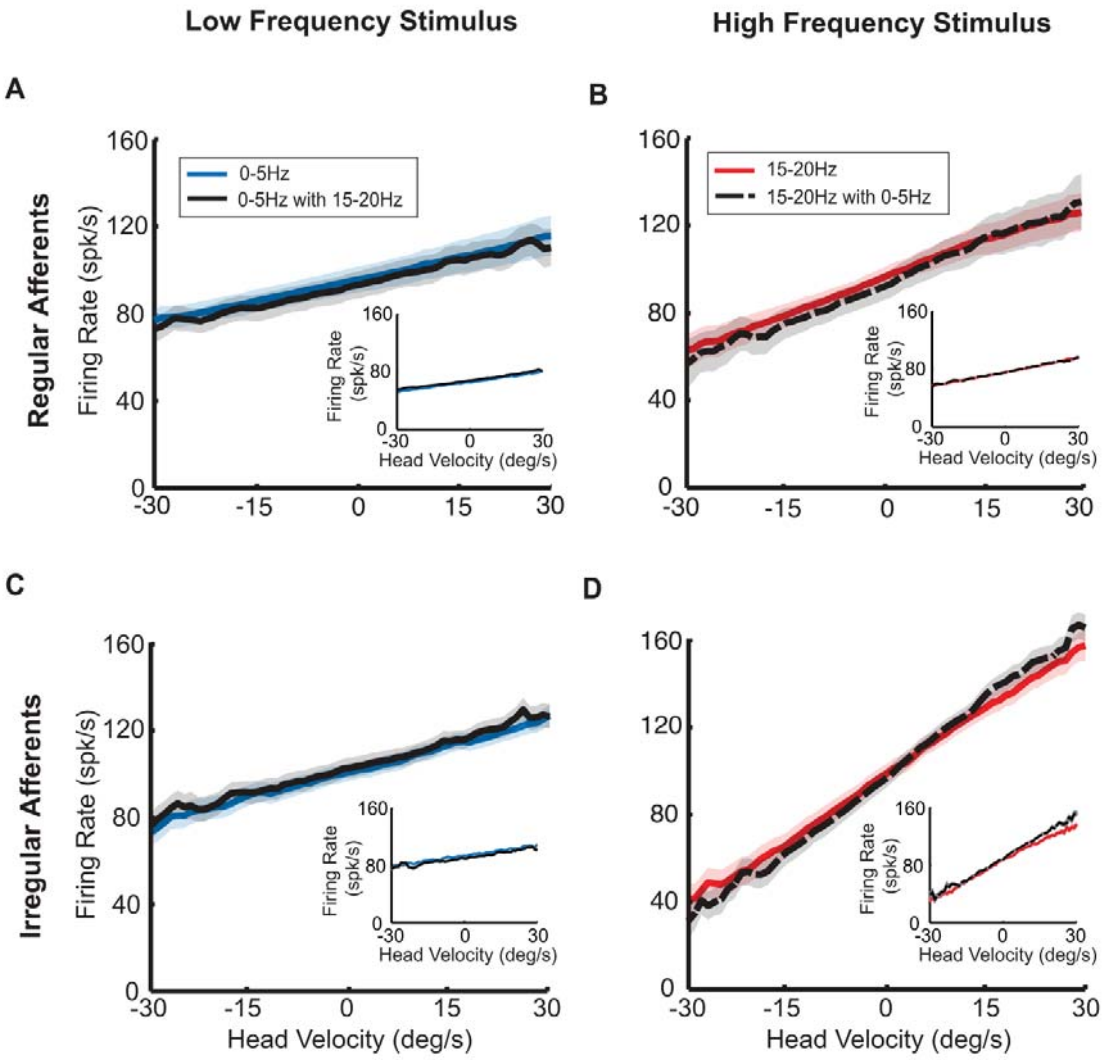

Figure E.S5. Afferents display a linear relationship between output firing rate and input head velocity. (A) Population-averaged firing rate as a function of head velocity for regular afferents when the low frequency (0-5 Hz) noise stimulus was applied in isolation (blue) and concurrently with the high frequency (15-20 Hz) noise stimulus (black). Inset: firing rate as a function of head velocity for an example regular afferent.

Figure E.S5 ***(previous page).*** (B) Population-averaged firing rate as a function of head velocity for regular afferents when the high frequency (15-20 Hz) noise stimulus was applied in isolation (red) and concurrently with the low frequency (0-5 Hz) noise stimulus (dashed black). Inset: firing rate as a function of head velocity for the same regular afferent. (C) Population-averaged firing rate as a function of head velocity for irregular afferents when the low frequency (0-5 Hz) noise stimulus was applied in isolation (blue) and concurrently with the high frequency (15-20 Hz) noise stimulus (black). Inset: firing rate as a function of head velocity for an example irregular afferent. (C) Population-averaged firing rate as a function of head velocity for irregular afferents when the high-frequency (15-20 Hz) noise stimulus was applied in isolation (red) and concurrently with the low frequency (0-5 Hz) noise stimulus (dashed black). Inset: firing rate response as a function of head velocity for the same irregular afferent. This figure was copied from Massot et al. [111].

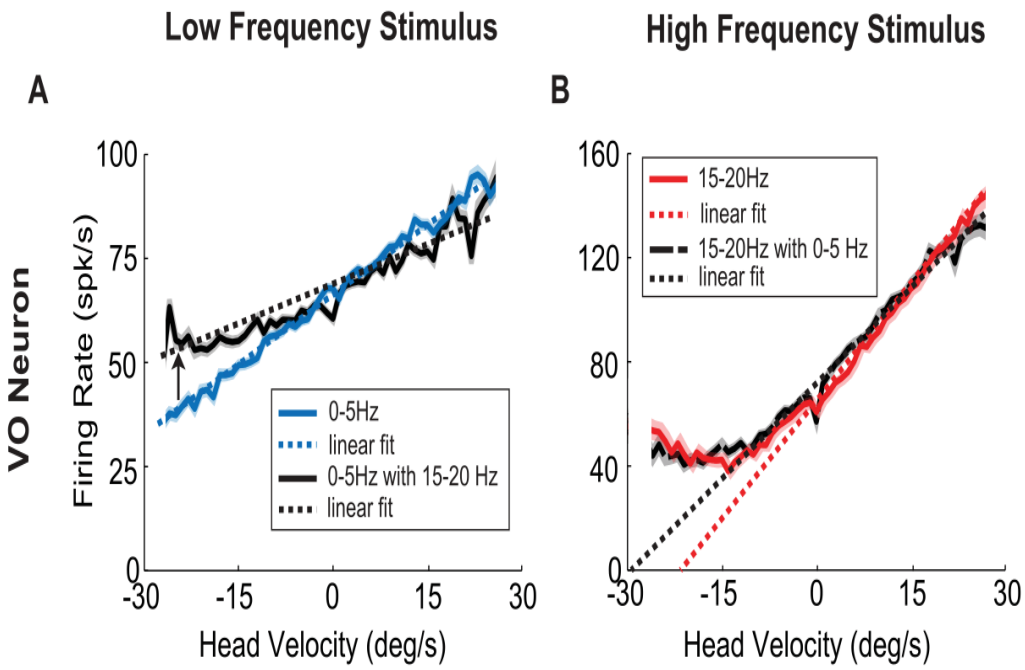

Figure E.S6. Individual central neurons display nonlinear responses. (A) Firing rate as a function of head velocity for an example central VO neuron when the low frequency (0-5 Hz) noise stimulus was applied in isolation (blue) and concurrently with the high frequency (15-20 Hz) noise stimulus (black). Both curves were well fit by straight lines (dashed lines). (B) Firing rate as a function of head velocity for the same example central VO neuron when the high frequency (15-20 Hz) noise stimulus was applied in isolation (red) and concurrently with the low frequency (0-5 Hz) noise stimulus (long dashed black). Note that both curves were not well fit by straight lines (short dashed lines). This figure was copied from Massot et al. [111].

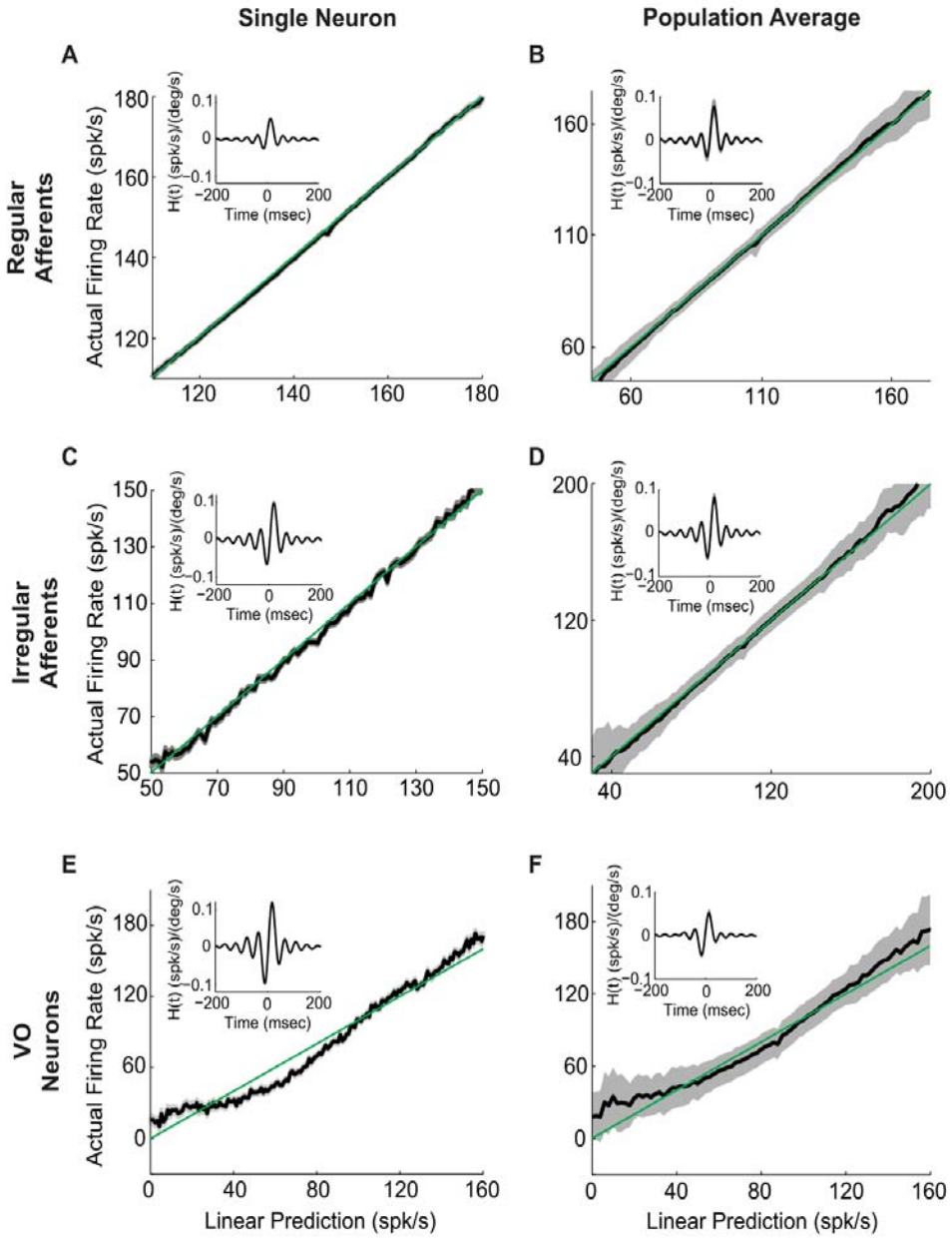

Figure E.S7. Characterization of central VO neurons and afferents by LN cascade models. (A) Actual firing rate as a function of the linear prediction for an example regular afferent. Inset: the filter H(t) for this same afferent.

Figure E.S7 ***(previous page).*** (B) Population-averaged actual firing rate as a function of the linear prediction for regular afferents. Inset: population-averaged filter H(t) for regular afferents. (C) Actual firing rate as a function of the linear prediction for an example irregular afferent. Inset: the filter H(t) for this same afferent. (D) Population-averaged actual firing rate as a function of the linear prediction for irregular afferents. Inset: population averaged filter H(t) for irregular afferents. (E) Actual firing rate as a function of the linear prediction for an example central VO neuron. Inset: the filter H(t) for this same VO neuron. (F) Population-averaged actual firing rate as a function of the linear prediction for central VO neurons. Inset: population-averaged filter H(t) for central VO neurons. Throughout, the identity line is shown in green. This figure was copied from Massot et al. [111].

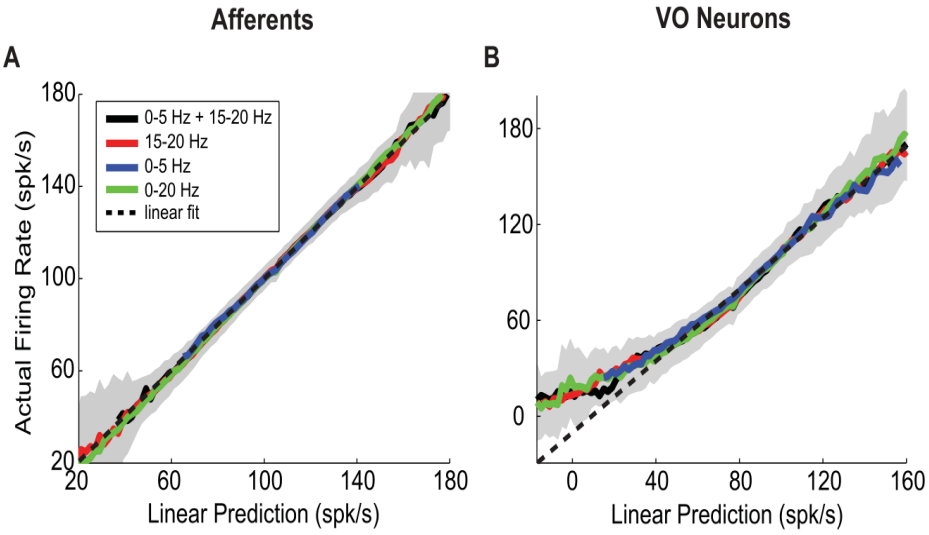

Figure E.S8. LN analysis reveals that central vestibular neurons but not afferents display a static nonlinearity in response to different self-motion stimuli. (A) Population-averaged actual firing rate as a function of the linear prediction for afferents in response to 0-20 Hz noise (green), 0-5 Hz noise (blue), 15-20 Hz noise (red), and 0-5 Hz+15-20 Hz noise (black). Note that all the curves are linear and overlap but that the blue curve extends over a narrower range than all the others. All the curves were further well fit by straight lines ($R^2 = 0.99$ in all cases). (B) Population-averaged actual firing rate as a function of the linear prediction for central VO neurons in response to 0-20 Hz noise (green), 0-5 Hz noise (blue), 15-20 Hz noise (red), and 0-5 Hz+15-20 Hz noise (black). Note that all the curves overlap but that the blue curve extends over a narrower range than all the others. As such, the blue curve is relatively better fit by a straight line (0-5 Hz: $R^2 = 0.91$; 15-20 Hz: $R^2 = 0.58$; 0-5 Hz+15-20 Hz: $R^2 = 0.37$; 0-20 Hz: $R^2 = 0.62$). This figure was copied from Massot et al. [111].

E.6 Author Contributions

The author(s) have made the following declarations about their contributions: Conceived and designed the experiments: KEC MJC. Performed the experiments:

CM. Analyzed the data: CM ADS. Contributed reagents/materials/analysis tools: CM ADS MJC. Wrote the paper: KEC MJC.

In the appendix of this chapter, I present additional analysis on some of the data presented in the publication, whereby I compute the RR-coherence as well as the SR-coherence, which can be used to assess whether neural responses contain additional information that cannot be decoded linearly. This is a signature of potential temporal coding, which is investigated by performing a spike timing jitter analysis. These additional analysis explicitly test whether and how VO neurons might use a temporal code when driven nonlinearly by large amplitude or high frequency stimuli.

APPENDIX F
Coherence and spike timing jitter analysis reveal potential for temporally encoded information that cannot be decoded linearly.

In this appendix, I perform additional analysis on the low (0-5 Hz) and high (15-20 Hz) frequency noise stimuli (and elicited responses) used in the publication presented in this chapter. As the stimuli consisted of four repeated identical segments, we compare the SR-coherence (Equation 1.9), with the RR-coherence (Equation 1.10). It has previously been shown that C_{rr} has a value between zero and one, and quantifies the strength to which the responses elicited by repeated presentations of the same stimulus are correlated with each other [81]. It was also shown that $\sqrt{C_{rr}}$ measure the maximum possible fraction of the response that can be reproduced by an optimal encoding filter, which is in general nonlinear. This results in the inequality, $0 \leq C_{sr} \leq \sqrt{C_{rr}} \leq 1$, which reflects the fact that C_{sr} says how well the optimal linear model can recover the stimulus from the response, while the difference $\sqrt{C_{rr}} - C_{sr}$ captures whether there is additional information in the responses that cannot be decoded linearly. As such, C_{sr} and $\sqrt{C_{rr}}$, are related to lower and upper bounds on the signal-to-noise ratio (SNR), via $SNR(f) = C(f)/(1 - C(f))$, which can then be used to give lower and upper bounds on the mutual information rate density, via

$$I(f) = -\log_2\big[1 - C(f)\big], \tag{F.1}$$

where use of C_{sr} results in $I_{lower}(f)$, and use of $\sqrt{C_{rr}}$ results in $I_{upper}(f)$ [80,284–287]. However, because this is in fact an indirect estimate of the mutual information with several caveats, we simply present and consider the SR- and $\sqrt{RR}$-coherences, to asses whether the neural responses contain additional information about the stimulus, which cannot be decoded with the optimal linear filter.

To further asses the nature of this additional information and how it may be contained in the spike timing of neural responses, we use a spike-timing jitter analysis [38, 288]. Jitter randomly drawn from a Gaussian distribution with zero mean and standard deviation, σ_J, was added to each spike time. Because stimuli used have a maximum frequency content of 20 Hz, the stimulus and firing rate response from 0-20Hz, vary on a timescale of 50 ms or slower. One might therefore expect jitter with $\sigma_J < 10$ ms to have no effect on stimulus encoding, however unpublished observations have found that $\sigma_J = 5$ ms is sufficient to reduce the neurons 'gain', $G(f) = |P_{sr}(f)|/P_{ss}(f)$, implying that jitter can effect coding at time scales significantly greater than the jitter itself [35, 38].

To investigate the nature of the neural code, and how it changes when vestibular neurons are driven out of their linear range, by large amplitude stimuli, we consider both the $C_{sr}(f)$ as well as $\sqrt{C_{rr}}$, in combination with the f-I curves (calculated as in the publication presented above). It has previously been shown that when a stimulus results in rectification of varying degrees, this can produce additional peaks in $\sqrt{C_{rr}}$ which are outside of the stimulus frequency range (and therefore not contained in $C_{sr}(f)$), at both lower frequencies as well as higher harmonic frequencies [219]. In Figure F.1 we show that when regular afferents, irregular afferents, and VO cells,

subject to the same low and high frequency noise stimuli (as defined in the publication above), it is only VOs that show $\sqrt{C_{rr}}$ peaks above and below the stimulus frequency range, however *none* of the stimuli result in rectification. By also plotting the f-I curves, we can see that although none show any rectification, it is in fact the VOs in response to only the high frequency stimulus which appears nonlinear. In panel D, we quantify the difference $\sqrt{C_{rr}} - C_{sr}$, averaged across frequency, and across cell populations, separately for each stimulus and cell type. The dashed black line indicates the difference which is significantly different from zero with a confidence of 95%, which is clearly only for the VOs and high frequency stimulus. To quantify the nonlinearity in the f-I curves, for each cell in the populations, a line was fit separately to the left and right sides (i.e. for positive stimuli and negative stimuli), and the difference in slope, $m_2 - m_1$ is averaged across the populations of different cell types and two stimulus types, which are plotted in panel E. Here we can see that again it is only the VOs which are significantly nonlinear, for the high frequency stimulus. The rectifying nonlinearity considered by Savard et al. is comparable having a region of zero slope, and a region of positive slope, however for the boosting nonlinearity the low slope region need not have a slope of 0, nor correspond to rectified responses of 0 spk/s. Now the FI curves are calculated using the filtered spike trains (i.e. R(t)) and therefore quantifies whether the transformation from continuous stimulus S(t) to continuous firing rate, R(t), are linear or nonlinear, but do not tell us anything about potential temporal coding: A rate code can be linear or nonlinear. A temporal code, on the other hand, requires a nonlinear transformation to reliably position spike times at a smaller timescale than that contained in the stimulus. The coherences,

however, are computed using the binary sequences of spike times, and can therefore capture information possibly contained within spike timing patterns.

To identify any temporally encoded information, due to the boosting nonlinearity, we investigate how C_{sr} and $\sqrt{C_{rr}}$ are affected by the addition of spike time jitter. It has already been shown that jitter with $\sigma_J = 2$ ms is enough to reduce C_{sr} [35,38], however we also consider how it reduces $\sqrt{C_{rr}}$ as well. In Figure F.2 panel A, I show how both C_{sr} and $\sqrt{C_{rr}}$ are reduced by jitter with $\sigma_J = 2.4$ ms. We can see that it clearly the coherence for regular afferents with is reduced most significantly, which has lead some to conclude that regulars are more likely using a temporal code than irregulars [38]. Another study further showed that regular afferents do in fact lose SR-coherence faster than regular afferents, as jitter is added from distributions of increasing σ_J. However, they also showed that if the jitter SD is normalized by the afferents spontaneous spike timing SD, σ_0, the C_{sr} decay curves then overlap. In panel B, we therefore plot the C_{sr} as a functions of both σ_J (left panels) as well as σ_J/σ_0. Here we do indeed see that the coherence is lost from the regular afferents faster than the irregulars which in turn decay faster than irregulars, for both stimulus types. However, we know that regulars also have lower spontaneous spiking variability than irregulars, with irregulars having less than VOs. When the jitter is normalized by this spontaneous spiking variability, we do find that the curves all overlap much better for the low frequency stimuli, however, we in fact find the opposite, with VOs loosing coherence sooner than irregulars, which are soon than regulars, when the high frequency stimulus is used. This in fact would suggest that it is really VOs that are using a temporal code. However, any information captured by the C_{sr}

can be decoded linearly. We next consider how the difference $\sqrt{C_{rr}} - C_{sr}$ are affected by jitter. In panel C, we plot this difference, averaged over different frequency bands, capturing the frequencies lower and higher than those contained by the stimulus. As one would expect, these differences are destroyed with less jitter for higher frequency bands, requiring more jitter for lower bands. However, these differences appear reasonably constant for very low σ_J (i.e. from $10^{-1} < \sigma_J < 10^0$), compared to C_{sr} alone over this range. This suggests that for such very small jittering, both C_{sr} and $\sqrt{C_{rr}}$ decay by similar amounts.

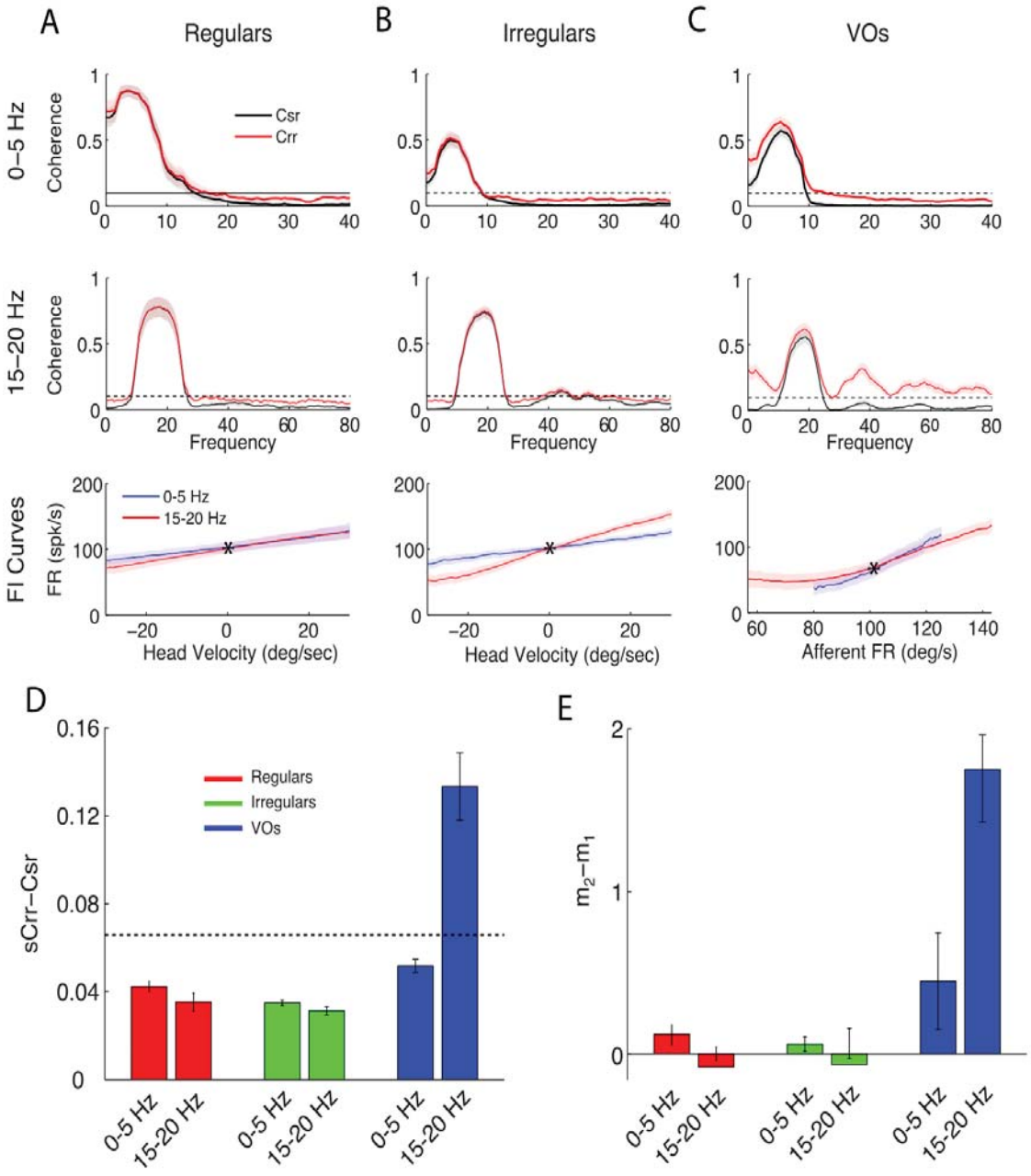

Figure F.1. Stimuli which elicit nonlinear range of FI curve of VO neurons, results in information which can not be linearly decoded.

Figure F.1 ***(previous page).*** For regular afferents (A), irregular afferents (B), and VO neurons (C), we plot the population averaged SR-coherence (black) and $\sqrt{RR}$-coherence (red) for low frequency (0-5 Hz) noise stimuli (top), and high frequency (15-20 Hz) noise stimuli (middle), and the resulting FI curves using each superimposed in red and blue, respectively (bottom). Population standard error (SE) is indicated by light bands around the means. Horizontal dashed black lines at 0.1 indicate that the coherence is nonzero with 95% confidence. In the bottom panels, the black star indicates the spontaneous firing rate of the neuron with a stimulus of zero. In (D) we plot the difference $\sqrt{C_{rr}} - C_{sr}$ averaged over frequency, for both the low and the high frequency stimuli, and all three cell types. The dashed black line now indicates a significant difference at $0.1/\sqrt{2}$, and clearly only the difference for VOs and high frequency stimuli is significantly different from zero. Error bars indicate SE. (E) For the FI curves of each cell in the population averages shown, a line is fit to both the left and right sides of the star, and the population averaged differences in their slopes, $m_1 - m_2$, is plotted for both stimulus types, and all three cell types. Error bars indicated SE. Again it is only the for the high frequency stimuli and the VOs that the difference is significant from zero.

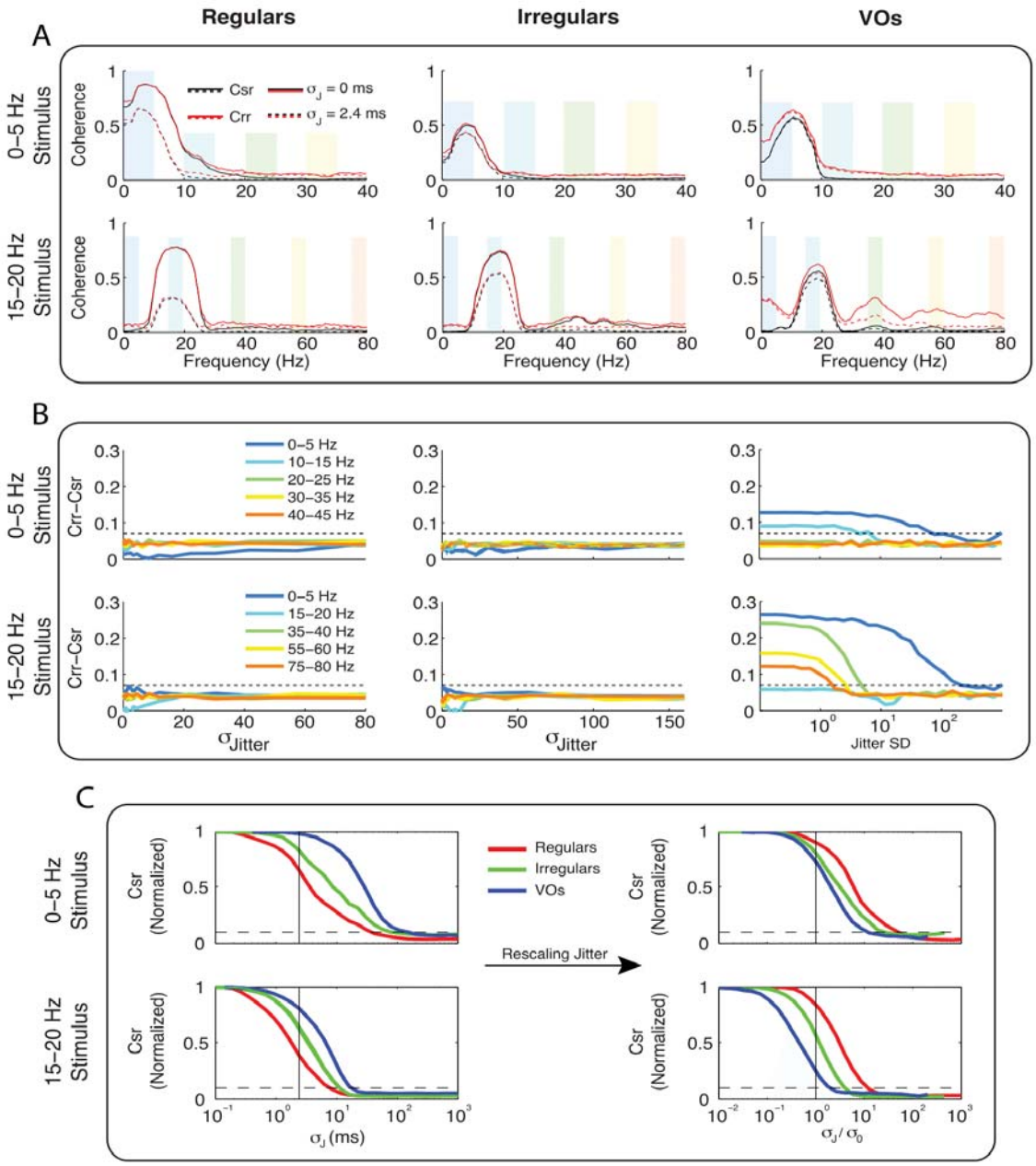

Figure F.2. Spike timing jitter analysis reveals nature of temporally encoded information.

Figure F.2 ***(previous page).*** (A) For all three cell types, we again plot the population averaged SR-coherence (black) and $\sqrt{RR}$-coherence (red) for low frequency (0-5 Hz) noise stimuli (top), and high frequency (15-20 Hz) noise stimuli (bottom), with no jitter added (solid lines) and with spike timing jitter added from a Gaussian distribution with $\sigma_J = 2.4$ ms (dashed lines). Vertical coloured bands indicate either the frequency band of the stimulus, or equally spaced higher (and one lower) frequency bands, intended to capture the peaks in the $\sqrt{RR}$-coherence for high frequency stimuli and VOs. (B) The difference $\langle \sqrt{C_{rr}} - C_{sr} \rangle$ averaged over the different frequency bands, versus increasing σ_J, using a log scale for the x-axis. (C) In the left panels we plot the normalized SR-coherence as a function of σ_J for all three cell types, in response to both the low frequency stimulus (top) and the high frequency stimulus (bottom). It can be seen that the C_{sr} of regular afferents begin to drop sooner than irregulars, and both drop off sooner than VO cells, for both stimulus types. In the right panels, the SR-coherences are again plotted, but as a function of jitter std normalized by the by the ISI std during spontaneous firing, σ_J/σ_0. After normalization, for low frequency stimulus (top) the curves almost overlap for all cell types, while for the high frequency stimulus (bottom) it is now the VO cells which start to drop soonest, and regular afferents last.

References

1. E. D. Adrian, "The impulses produced by sensory nerve endings: Part I.," *The Journal of Physiology*, vol. 61, pp. 49–72, Mar. 1926.

2. E. D. Adrian and Y. Zotterman, "The impulses produced by sensory nerve-endings: Part II. The response of a Single End-Organ.," *The Journal of Physiology*, vol. 61, pp. 151–171, Apr. 1926.

3. E. D. Adrian and Y. Zotterman, "The impulses produced by sensory nerve endings: Part 3. Impulses set up by Touch and Pressure.," *The Journal of Physiology*, vol. 61, pp. 465–483, Aug. 1926.

4. E. D. Adrian, "The impulses produced by sensory nerve-endings: Part 4. Impulses from Pain Receptors.," *The Journal of Physiology*, vol. 62, pp. 33–51, Oct. 1926.

5. F. Rieke, D. Warland, R. de Ruyter van Steveninck, and W. Bialek, *Spikes: Exploring the Neural Code*. MIT Press, Sept. 1997.

6. F. Theunissen and J. P. Miller, "Temporal encoding in nervous systems: a rigorous definition," *Journal of Computational Neuroscience*, vol. 2, pp. 149–162, 1995.

7. L. D. Landau and E. M. Lifshitz, *Mechanics*. Course in Theoretical Physics Vol. 1, Butterworth Heinemann, Jan. 1976.

8. H. B. Barlow, "Possible principles underlying the transformation of sensory messages," in *Sensory communication*, pp. 217–234, MIT Press, 1961.

9. S. Laughlin, "A simple coding procedure enhances a neuron's information capacity," *Z. Naturforsch*, no. 36, pp. 910–912, 1981.

10. A. Fairhall, G. D. Lewen, W. Bialek, and R. R. de Ruyter van Steveninck, "Efficiency and ambiguity in an adaptive neural code," *Nature*, vol. 412, pp. 787–792, 2001.

11. B. Wark, B. Lundstrom, and A. Fairhall, "Sensory adaptation," *Current opinion in neurobiology*, vol. 17, pp. 423–429, Aug. 2007.

12. F. Rieke, D. Bodnar, and W. Bialek, "Naturalistic stimuli increase the rate and efficiency of information transmission by primary auditory afferents," *Proceedings: Biological Sciences*, pp. 259–265, 1995.

13. B. A. Olshausen and D. Field, "Emergence of simple-cell receptive field properties by learning a sparse code for natural images," *Nature*, vol. 381, no. 13, pp. 607–609, 1996.

14. J. Zylberberg, J. T. Murphy, and M. R. DeWeese, "A sparse coding model with synaptically local plasticity and spiking neurons can account for the diverse shapes of V1 simple cell receptive fields," *PLoS Computational Biology*, vol. 7, no. 10, 2011.

15. H. B. Barlow, "Redundancy reduction revisited," *Network: Computation in Neural Systems*, vol. 12, no. 3, pp. 241–253, 2001.

16. S. Laughlin, "Energy as a constraint on the coding and processing of sensory information," *Current opinion in neurobiology*, pp. 475–480, 2001.

17. S. Laughlin, R. van Steveninck, and J. Anderson, "The metabolic cost of neural information," *Nature Neuroscience*, vol. 1, no. 1, pp. 36–41, 1998.

18. R. Baddeley, L. Abbott, M. Booth, F. Sengpiel, T. Freeman, E. A. Wakeman, and E. T. Rolls, "Responses of neurons in primary and inferior temporal visual cortices to natural scenes," *Proceedings of the Royal Society B: Biological Sciences*, vol. 264, pp. 1775–1783, 1997.

19. D. Ruderman, "The statistics of natural images," *Network: Computation in Neural Systems*, vol. 5, pp. 517–548, 1994.

20. C. K. Machens, T. Gollisch, O. Kolesnikova, and A. V. M. Herz, "Testing the efficiency of sensory coding with optimal stimulus ensembles," *Neuron*, vol. 47, pp. 447–456, 2005.

21. F. Rieke, D. Warland, and W. Bialek, "Coding efficiency and information rates in sensory neurons," *EPL (Europhysics Letters)*, vol. 22, p. 151, 2007.

22. F. Rieke, D. Bodnar, and W. Bialek, "Naturalistic Stimuli Inrease the Rate and Efficiency of Information Transmission by Primary Auditory Afferents,"

Proceedings of the Royal Society of London B, vol. 262, pp. 259–265, Sept. 2011.

23. C. K. Machens, H. Schütze, A. Franz, O. Kolesnikova, M. B. Stemmler, B. Ronacher, and A. V. M. Herz, "Single auditory neurons rapidly discriminate conspecific communication signals," *Nature*, vol. 6, no. 4, pp. 341–342, 2003.

24. E. Salinas, "How behavioral constraints may determine optimal sensory representations," *PLoS Biology*, vol. 4, no. 12, p. e387, 2006.

25. D. E. Angelaki and K. E. Cullen, "Vestibular System: The Many Facets of a Multimodal Sense," *Annual Reviews Neuroscience*, vol. 31, pp. 125–150, 2008.

26. J. M. Goldberg, "Afferent diversity and the organization of central vestibular pathways," *Experimental Brain Research*, vol. 130, no. 3, pp. 277–297, 2000.

27. H. Straka, N. Vibert, P.-P. Vidal, L. Moore, and M. B. Dutia, "Intrinsic membrane properties of vertebrate vestibular neurons: function, development and plasticity," *Progress in neurobiology*, vol. 76, pp. 349–392, 2005.

28. M. Jamali, S. G. Sadeghi, and K. E. Cullen, "Response of Vestibular Nerve Afferents Innervating Utricle and Saccule During Passive and Active Translations," *Journal of Neurophysiology*, vol. 101, pp. 141–149, Nov. 2008.

29. R. A. Eatock and J. E. Songer, "Vestibular hair cells and afferents: two channels for head motion signals," *Annual review of neuroscience*, vol. 34, pp. 501–534, 2011.

30. C. Fernandez and J. Goldberg, "Physiology of peripheral neurons innervating otolith organs of the squirrel monkey. II. Directional selectivity and force-response relations," *Journal of Neurophysiology*, vol. 39, no. 5, pp. 985–995, 1976.

31. C. Fernández and J. M. Goldberg, "Physiology of peripheral neurons innervating otolith organs of the squirrel monkey. III. Response dynamics," *Journal of Neurophysiology*, vol. 39, pp. 996–1008, Sept. 1976.

32. C. Fernandez and J. M. Goldberg, "Physiology of peripheral neurons innervating semicircular canals of the squirrel monkey. II. Response to sinusoidal

stimulation and dynamics of peripheral vestibular system," *Journal of Neurophysiology*, vol. 34, pp. 661–675, July 1971.

33. J. M. Goldberg, *The Vestibular System. A Sixth Sense*, Oxford University Press, 2012.

34. R. Eatock and A. Lysakowski, "Mammalian vestibular hair cells," in *Vertebrate Hair Cells*, pp. 384–442, Springer, 2006.

35. C. Massot, M. J. Chacron, and K. E. Cullen, "Information transmission and detection thresholds in the vestibular nuclei: single neurons vs. population encoding," *Journal of Neurophysiology*, vol. 105, pp. 1798–1814, Apr. 2011.

36. S. Sadeghi and L. Minor, "Response of vestibular-nerve afferents to active and passive rotations under normal conditions and after unilateral labyrinthectomy," *Journal of Neurophysiology*, vol. 97, pp. 1503–1514, 2007.

37. R. Kalluri, J. Xue, and R. A. Eatock, "Ion channels set spike timing regularity of mammalian vestibular afferent neurons," *Journal of Neurophysiology*, vol. 8, pp. 80–90, 2010.

38. S. G. Sadeghi, M. J. Chacron, M. C. Taylor, and K. E. Cullen, "Neural Variability, Detection Thresholds, and Information Transmission in the Vestibular System," *Journal of Neuroscience*, vol. 27, no. 4, pp. 771–781, 2007.

39. R. Ramachandran and S. G. Lisberger, "Neural Substrate of Modified and Unmodified Pathways for Learning in Monkey Vestibuloocular Reflex," *Journal of Neurophysiology*, vol. 100, pp. 1868–1878, Aug. 2008.

40. J. Ventre and S. Faugier-Grimaud, "Projections of the temporo-parietal cortex on vestibular complex in the macaque monkey (Macaca fascicularis).," *Experimental brain research Experimentelle Hirnforschung Expérimentation cérébrale*, vol. 72, no. 3, pp. 653–658, 1988.

41. S. Faugier-Grimaud and J. Ventre, "Anatomic connections of inferior parietal cortex (area 7) with subcortical structures related to vestibulo-ocular function in a monkey (Macaca fascicularis).," *The Journal of Comparative Neurology*, vol. 280, pp. 1–14, Feb. 1989.

42. S. Akbarian, O. J. Grüsser, and W. O. Guldin, "Corticofugal connections between the cerebral cortex and brainstem vestibular nuclei in the macaque

monkey.," *The Journal of Comparative Neurology*, vol. 339, pp. 421–437, Jan. 1994.

43. K. Fukushima, "Corticovestibular interactions: anatomy, electrophysiology, and functional considerations.," *Experimental brain research Experimentelle Hirnforschung Expérimentation cérébrale*, vol. 117, pp. 1–16, Oct. 1997.

44. H. Shimazu and C. M. Smith, "Cerebellar and labyrinthine influences on single vestibular neurons identified by natural stimuli.," *Journal of Neurophysiology*, vol. 34, pp. 493–508, July 1971.

45. R. R. Batton, A. Jayaraman, D. Ruggiero, and M. B. Carpenter, "Fastigial efferent projections in the monkey: an autoradiographic study.," *The Journal of Comparative Neurology*, vol. 174, pp. 281–305, July 1977.

46. S. C. Carleton and M. B. Carpenter, "Distribution of primary vestibular fibers in the brainstem and cerebellum of the monkey.," *Brain Research*, vol. 294, pp. 281–298, Mar. 1984.

47. Y. Homma, S. Nonaka, K. Matsuyama, and S. Mori, "Fastigiofugal projection to the brainstem nuclei in the cat: an anterograde PHA-L tracing study.," *Neuroscience research*, vol. 23, pp. 89–102, Aug. 1995.

48. G. Xiong and M. Matsushita, "Connections of Purkinje cell axons of lobule X with vestibulocerebellar neurons projecting to lobule X or IX in the rat," *Experimental Brain Research*, vol. 133, pp. 219–228, July 2000.

49. J. Voogd, A. H. Epema, and J. A. Rubertone, "Cerebello-vestibular connections of the anterior vermis. A retrograde tracer study in different mammals including primates.," *Archives italiennes de biologie*, vol. 129, pp. 3–19, Jan. 1991.

50. T. Langer, A. F. Fuchs, C. A. Scudder, and M. C. Chubb, "Afferents to the flocculus of the cerebellum in the rhesus macaque as revealed by retrograde transport of horseradish peroxidase.," *The Journal of Comparative Neurology*, vol. 235, pp. 1–25, May 1985.

51. D. Bukowska, "Cerebellovestibular projection from the posterior lobe cortex in the rabbit: an experimental study with the retrograde HRP method. II. Zonal organization.," *Acta neurobiologiae experimentalis*, vol. 55, no. 1, pp. 35–47, 1995.

52. D. Bukowska, "Cerebellovestibular projection from the posterior lobe cortex in the rabbit: an experimental study with the retrograde HRP method. I. Topographical relationships.," *Acta neurobiologiae experimentalis*, vol. 55, no. 1, pp. 23–34, 1995.

53. J. Tan, A. H. Epema, and J. Voogd, "Zonal organization of the flocculovestibular nucleus projection in the rabbit: a combined axonal tracing and acetylcholinesterase histochemical study," *The Journal of Comparative Neurology*, vol. 356, pp. 51–71, June 1995.

54. L. Cazin, M. Magnin, and J. Lannou, "Non-cerebellar visual afferents to the vestibular nuclei involving the prepositus hypoglossal complex: an autoradiographic study in the rat.," *Experimental brain research Experimentelle Hirnforschung Expérimentation cérébrale*, vol. 48, no. 2, pp. 309–313, 1982.

55. M. Magnin, J. H. Courjon, and J. M. Flandrin, "Possible visual pathways to the cat vestibular nuclei involving the nucleus prepositus hypoglossi.," *Experimental brain research Experimentelle Hirnforschung Expérimentation cérébrale*, vol. 51, no. 2, pp. 298–303, 1983.

56. O. Pompeiano, "Spinovestibular relations: anatomical and physiological aspects.," *Progress in Brain Research*, vol. 37, pp. 263–296, 1972.

57. O. Pompeiano, "Vestibulospinal relations: vestibular influences on gamma motoneurons and primary afferents.," *Progress in Brain Research*, vol. 37, pp. 197–232, 1972.

58. O. Pompeiano, "Cerebellar control of the vestibular pathways to spinal motoneurons and primary afferents.," *Progress in Brain Research*, vol. 37, pp. 391–410, 1972.

59. O. Pompeiano, "Reticular control of the vestibular nuclei: physiology and pharmacology.," *Progress in Brain Research*, vol. 37, pp. 601–618, 1972.

60. A. Gottesman-Davis, M. Shao, J. C. Hirsch, and K. D. Peusner, "Electrophysiological properties of morphologically-identified medial vestibular nucleus neurons projecting to the abducens nucleus in the chick embryo," *Neuroscience*, vol. 172, pp. 494–509, Jan. 2011.

61. A. Strassman, S. M. Highstein, and R. A. McCrea, "Anatomy and physiology of saccadic burst neurons in the alert squirrel monkey. I. Excitatory burst

neurons.," *The Journal of Comparative Neurology*, vol. 249, pp. 337–357, July 1986.

62. A. Strassman, S. M. Highstein, and R. A. McCrea, "Anatomy and physiology of saccadic burst neurons in the alert squirrel monkey. II. Inhibitory burst neurons," *The Journal of Comparative Neurology*, pp. 358–380, June 1986.

63. C. A. Scudder and A. F. Fuchs, "Physiological and behavioral identification of vestibular nucleus neurons mediating the horizontal vestibuloocular reflex in trained rhesus monkeys.," *Journal of Neurophysiology*, vol. 68, pp. 244–264, July 1992.

64. C. A. Scudder and A. F. Fuchs, "The error signal for modification of vestibuloocular reflex gain.," *Annals of the New York Academy of Sciences*, vol. 656, pp. 884–885, May 1992.

65. V. J. Wilson, R. M. Wylie, and L. A. Marco, "Projection to the spinal cord from the medial and descending vestibular nuclei of the cat," *Nature*, vol. 215, June 1967.

66. C. Abzug, M. Maeda, B. W. Peterson, and V. J. Wilson, "Cervical branching of lumbar vestibulospinal axons.," *The Journal of Physiology*, vol. 243, pp. 499–522, Dec. 1974.

67. A. M. Rubin, S. R. Liedgren, L. M. Odkvist, A. C. Milne, and J. M. Fredrickson, "Labyrinthine and somatosensory convergence upon vestibulospinal neurons.," *Acta Oto-Laryngologica*, vol. 86, pp. 251–259, Aug. 1978.

68. R. Boyle and O. Pompeiano, "Responses of vestibulospinal neurons to neck and macular vestibular inputs in the presence or absence of the paleocerebellum.," *Annals of the New York Academy of Sciences*, vol. 374, pp. 373–394, 1981.

69. R. Boyle and O. Pompeiano, "Convergence and interaction of neck and macular vestibular inputs on vestibulospinal neurons.," *Journal of Neurophysiology*, vol. 45, pp. 852–868, May 1981.

70. R. Boyle and O. Pompeiano, "Relation between cell size and response characteristics of vestibulospinal neurons to labyrinth and neck inputs.," *The Journal of Neuroscience*, vol. 1, pp. 1052–1066, Sept. 1981.

71. Y. Shinoda, T. Ohgaki, T. Futami, and Y. Sugiuchi, "Vestibular projections to the spinal cord: the morphology of single vestibulospinal axons ," *Progress in Brain Research*, vol. 76, pp. 17–27, Apr. 1988.

72. Y. Shinoda, T. Ohgaki, Y. Sugiuchi, and T. Futami, "Structural basis for three-dimensional coding in the vestibulospinal reflex. Morphology of single vestibulospinal axons in the cervical cord.," *Annals of the New York Academy of Sciences*, vol. 545, pp. 216–227, 1988.

73. T. Shiroyama, T. Kayahara, Y. Yasui, J. Nomura, and K. Nakano, "Projections of the vestibular nuclei to the thalamus in the rat: a Phaseolus vulgaris leucoagglutinin study.," *The Journal of Comparative Neurology*, vol. 407, pp. 318–332, May 1999.

74. C. d. Waele, B. x. r. P, L. J, P. T. B. Huy, and V. P, "Vestibular projections in the human cortex," *Experimental Brain Research*, vol. 141, pp. 541–551, Dec. 2001.

75. R. A. McCrea, G. T. Gdowski, R. Boyle, and T. Belton, "Firing behavior of vestibular neurons during active and passive head movements: vestibulospinal and other non-eye-movement related neurons.," *Journal of Neurophysiology*, vol. 82, pp. 416–428, July 1999.

76. R. A. McCrea and C. Chen-Huang, "Signal processing related to the vestibulo-ocular reflex during combined angular rotation and linear translation of the head.," *Annals of the New York Academy of Sciences*, vol. 871, pp. 65–80, May 1999.

77. O. J. Grüsser, M. Pause, and U. Schreiter, "Localization and responses of neurones in the parieto-insular vestibular cortex of awake monkeys (Macaca fascicularis).," *The Journal of Physiology*, vol. 430, pp. 537–557, Nov. 1990.

78. O. J. Grüsser, M. Pause, and U. Schreiter, "Vestibular neurones in the parieto-insular cortex of monkeys (Macaca fascicularis): visual and neck receptor responses.," *The Journal of Physiology*, vol. 430, pp. 559–583, Nov. 1990.

79. T. M. Cover and J. A. Thomas, *Elements of Information Theory*. Wiley, 2nd ed., Dec. 2006.

80. A. Borst and F. E. Theunissen, "Information theory and neural coding," *Nature Neuroscience*, vol. 2, no. 11, pp. 947–957, 1999.

81. J. C. Roddey, B. Girish, and J. P. Miller, "Assessing the performance of neural encoding models in the presence of noise," *Journal of Computational Neuroscience*, vol. 8, no. 2, pp. 95–112, 2000.

82. N. Brunel and M. C. W. van Rossum, "Lapicque's 1907 paper: from frogs to integrate-and-fire," *Biological Cybernetics*, vol. 97, pp. 337–339, Oct. 2007.

83. A. V. M. Herz, T. Gollisch, C. K. Machens, and D. Jaeger, "Modeling single-neuron dynamics and computations: a balance of detail and abstraction," *Science (New York, NY)*, vol. 314, p. 80, 2006.

84. A. L. Hodgkin and A. F. Huxley, "Propagation of Electrical Signals Along Giant Nerve Fibres," *Proceedings of the Royal Society B: Biological Sciences*, Oct. 1952.

85. S. H. Strogatz, *Nonlinear Dynamics and Chaos*. Perseus Books Publishing, Westview Press, Cambridge, 1994.

86. E. M. Izhikevich, *Dynamical Systems in Neuroscience: The Geometry of Excitability and Bursting*. The MIT Press, June 2010.

87. E. Marder, "Colloquium Paper: Variability, compensation, and modulation in neurons and circuits," *Proceedings of the National Academy of Sciences*, vol. 108, pp. 15542–15548, Sept. 2011.

88. D. E. Angelaki and J. D. Dickman, "Spatiotemporal processing of linear acceleration: primary afferent and central vestibular neuron responses.," *Journal of Neurophysiology*, vol. 84, pp. 2113–2132, Oct. 2000.

89. T. E. Hullar, C. C. Della Santina, T. Hirvonen, D. M. Lasker, J. P. Carey, and L. B. Minor, "Responses of irregularly discharging chinchilla semicircular canal vestibular-nerve afferents during high-frequency head rotations.," *Journal of Neurophysiology*, vol. 93, pp. 2777–2786, May 2005.

90. T. E. Hullar and L. Minor, "High-frequency dynamics of regularly discharging canal afferents provide a linear signal for angular vestibuloocular reflexes," *Journal of Neurophysiology*, vol. 82, pp. 2000–2005, 1999.

91. C. Smith and J. Goldberg, "A stochastic afterhyperpolarization model of repetitive activity in vestibular afferents," *Biological Cybernetics*, vol. 54, no. 1, pp. 41–51, 1986.

92. R. Ramachandran and S. G. Lisberger, "Transformation of vestibular signals into motor commands in the vestibuloocular reflex pathways of monkeys," *Journal of Neurophysiology*, vol. 96, no. 3, pp. 1061–1074, 2006.

93. R. Quadroni and T. Knöpfel, "Compartmental models of type A and type B guinea pig medial vestibular neurons," *Journal of Neurophysiology*, vol. 72, no. 4, pp. 1911–1924, 1994.

94. E. Av-Ron and P. P. Vidal, "Intrinsic membrane properties and dynamics of medial vestibular neurons: a simulation," *Biological Cybernetics*, vol. 80, no. 6, pp. 383–392, 1999.

95. A. D. Schneider, M. Jamali, J. Carriot, M. J. Chacron, and K. E. Cullen, "The Increased Sensitivity of Irregular Peripheral Canal and Otolith Vestibular Afferents Optimizes their Encoding of Natural Stimuli," *The Journal of neuroscience : the official journal of the Society for Neuroscience*, vol. 35, pp. 5522–5536, Apr. 2015.

96. M. G. Metzen and M. J. Chacron, "Weakly electric fish give behavioral responses to envelopes naturally occurring during movement: implications for neural processing," *The Journal of experimental biology*, vol. 101, pp. 102–113, 2013.

97. F. Attneave, "Some informational aspects of visual perception.," *Psychological Review*, vol. 61, pp. 183–193, May 1954.

98. E. Simoncelli and B. A. Olshausen, "Natural image statistics and neural representation," *Annual review of neuroscience*, vol. 24, pp. 1193–1216, 2001.

99. J. Wallman, J. Velez, B. Weinstein, and A. E. Green, "Avian vestibuloocular reflex: adaptive plasticity and developmental changes.," *Journal of Neurophysiology*, vol. 48, pp. 952–967, Oct. 1982.

100. K. E. Cullen, "The neural encoding of self-motion," *Current opinion in neurobiology*, vol. 21, pp. 587–595, Aug. 2011.

101. R. A. Baird, G. Desmadryl, C. Fernandez, and J. M. Goldberg, "The Vestibular Nerve of the Chinchilla. II. Relation Between Afferent Response Properties

and Peripheral Innervation Patterns in the Semicircular Canals," *Journal of Neurophysiology*, vol. 60, no. 1, pp. 182–203, 1988.

102. C. Fernandez, R. A. Baird, and J. M. Goldberg, "The Vestibular Nerve of the Chinchilla. I. Peripheral Innervation Patterns in the Horizontal and Superior Semicircular Canals," *Journal of Neurophysiology*, vol. 60, no. 1, pp. 167–181, 1988.

103. M. Jamali, J. Carriot, M. J. Chacron, and K. E. Cullen, "Strong Correlations between Sensitivity and Variability Give Rise to Constant Discrimination Thresholds across the Otolith Afferent Population," *The Journal of neuroscience : the official journal of the Society for Neuroscience*, vol. 33, pp. 11302–11313, July 2013.

104. J. Carriot, M. Jamali, M. J. Chacron, and K. E. Cullen, "Statistics of the vestibular input experienced during natural self-motion: implications for neural processing.," *The Journal of neuroscience : the official journal of the Society for Neuroscience*, vol. 34, pp. 8347–8357, June 2014.

105. A. Dale and K. E. Cullen, "The nucleus prepositus predominantly outputs eye movement-related information during passive and active self-motion.," *Journal of Neurophysiology*, vol. 109, pp. 1900–1911, Apr. 2013.

106. S. G. Lisberger and T. A. Pavelko, "Vestibular signals carried by pathways subserving plasticity of the vestibulo-ocular reflex in monkeys.," *The Journal of Neuroscience*, vol. 6, pp. 346–354, Feb. 1986.

107. J. Carriot, J. X. Brooks, and K. E. Cullen, "Multimodal integration of self-motion cues in the vestibular system: active versus passive translations.," *The Journal of neuroscience : the official journal of the Society for Neuroscience*, vol. 33, pp. 19555–19566, Dec. 2013.

108. J. Goldberg and C. Smith, "Relation between discharge regularity and responses to externally applied galvanic currents in vestibular nerve afferents of the squirrel monkey," *Journal of Neurophysiology*, vol. 51, no. 6, pp. 1236–1256, 1984.

109. S. G. Sadeghi, J. M. Goldberg, L. B. Minor, and K. E. Cullen, "Effects of canal plugging on the vestibuloocular reflex and vestibular nerve discharge during passive and active head rotations.," *Journal of Neurophysiology*, vol. 102, pp. 2693–2703, Nov. 2009.

110. E. Chichilnisky, "A simple white noise analysis of neuronal light responses," *Network: Computation in Neural Systems*, vol. 12, no. 2, pp. 199–213, 2001.

111. C. Massot, A. Schneider, M. Chacron, and K. Cullen, "The Vestibular System Implements a Linear–Nonlinear Transformation In Order to Encode Self-Motion," *PLoS Biology*, vol. 10, no. 7, p. e1001365, 2012.

112. N. Brunel and J. P. Nadal, "Mutual information, Fisher information, and population coding," *Neural Computation*, vol. 10, pp. 1731–1757, 1998.

113. M. McDonnell and N. Stocks, "Maximally informative stimuli and tuning curves for sigmoidal rate-coding neurons and populations," *Physical Review Letters*, vol. 101, 2008.

114. K. Cullen and J. E. Roy, "Signal processing in the vestibular system during active versus passive head movements," *Journal of Neurophysiology*, vol. 91, pp. 1919–1933, 2004.

115. J. M. Goldberg and C. Fernández, "Conduction times and background discharge of vestibular afferents.," *Brain Research*, pp. 545–550, Nov. 1977.

116. X. Si, M. M. Zakir, and J. D. Dickman, "Afferent innervation of the utricular macula in pigeons.," *Journal of Neurophysiology*, vol. 89, pp. 1660–1677, Mar. 2003.

117. J. Xue and E. H. Peterson, "Hair bundle heights in the utricle: differences between macular locations and hair cell types.," *Journal of Neurophysiology*, vol. 95, pp. 171–186, Jan. 2006.

118. A. Steinacker, *Sensory processing and ionic currents in vestibular hair cells.* Springer Handbook of Auditory Research, Springer New York, Nov. 2004.

119. P. Domenici, E. M. Standen, and R. P. Levine, "Escape manoeuvres in the spiny dogfish (Squalus acanthias).," *The Journal of experimental biology*, vol. 207, pp. 2339–2349, June 2004.

120. P. Domenici and R. Blake, "The kinematics and performance of fish fast-start swimming," *The Journal of experimental biology*, vol. 200, pp. 1165–1178, Apr. 1997.

121. R. B. Stein, E. R. Gossen, and K. E. Jones, "Neuronal variability: noise or part of the signal?," *Nature Review Neuroscience*, vol. 6, pp. 389–397, May 2005.

122. A. A. Faisal, L. Selen, and D. M. Wolpert, "Noise in the nervous system," *Nature Reviews Neuroscience*, vol. 9, pp. 292–303, 2008.

123. T. Takahashi, A. Moiseff, and M. Konishi, "Time and intensity cues are processed independently in the auditory system of the owl.," *The Journal of Neuroscience*, vol. 4, pp. 1781–1786, July 1984.

124. D. Oertel, "The role of timing in the brain stem auditory nuclei of vertebrates.," *Annual Review of Physiology*, vol. 61, pp. 497–519, 1999.

125. S. Gelfand, *Hearing: An Introduction to psychological and physiological acoustics.* Colchester: CRC Press, June 2004.

126. D. Marr, *Vision: A Computational Investigation into the Human Representation and Processing of Visual Information.* New York: The MIT Press, July 2010.

127. M. S. Livingstone and D. H. Hubel, "Psychophysical evidence for separate channels for the perception of form, color, movement, and depth.," *The Journal of Neuroscience*, vol. 7, pp. 3416–3468, Nov. 1987.

128. W. H. Merigan and J. H. Maunsell, "How parallel are the primate visual pathways?," *Annual review of neuroscience*, vol. 16, pp. 369–402, 1993.

129. C. E. Carr and L. Maler, *Electroreception in gymnotiform fish: central anatomy and physiology.* Electroreception, Wiley: New York, Nov. 1986.

130. C. Bell and L. Maler, *Central neuroanatomy of electrosensory systems in fish.* Electroreception, Springer: New York, Nov. 2005.

131. M. Kawasaki, *Physiology of tuberous electrosensory systems.*, vol. 21 of *Electroreception*. Springer: New York, 2005.

132. A. Schneider, K. Cullen, and M. Chacron, "In vivo Conditions Induce Faithful Encoding of Stimuli by Reducing Nonlinear Synchronization in Vestibular Sensory Neurons," *PLoS Computational Biology*, vol. 7, no. 7, 2011.

133. R. Boyle, J. M. Goldberg, and S. M. Highstein, "Inputs from Regularly and Irregularly Discharging Vestibular Nerve Afferents to Secondary Neurons in Squirrel Monkey Vestibular Nuclei. III. Correlation with Vestibulospinal and Vestibuloocular Output Pathways.," *Journal of Neurophysiology*, vol. 68, pp. 471–484, 1992.

134. J. M. Goldberg, S. M. Highstein, A. K. Moschovakis, and C. Fernandez, "Inputs From Regularly and Irregularly Discharging Vestibular Nerve Afferents to Secondary Neurons in the Vestibular Nuclei of the Squirrel Monkey. I. An Electrophysiological Analysis," *Journal of Neurophysiology*, vol. 58, pp. 700–718, Oct. 1987.

135. S. M. Highstein, J. M. Goldberg, A. K. Moschovakis, and C. Fernández, "Inputs From Regularly and Irregularly Discharging Vestibular Nerve Afferents to Secondary Neurons in the Vestibular Nuclei of the Squirrel Monkey. II. Correlation with Output Pathways of Secondary Neurons.," *Journal of Neurophysiology*, vol. 58, pp. 719–738, 1987.

136. M. Serafin, C. de Waele, A. Khateb, P. P. Vidal, and M. Mühlethaler, "Medial vestibular nucleus in the guinea-pig," *Experimental Brain Research*, vol. 84, pp. 426–433, 1991.

137. A. R. Johnston, N. K. MacLeod, and M. B. Dutia, "Ionic conductances contributing to spike repolarization and after-potentials in rat medial vestibular nucleus neurones.," *The Journal of Physiology*, vol. 481, pp. 61–77, 1994.

138. M. B. Dutia, R. B. Lotto, and A. R. Johnston, "Post-natal Development of Tonic Activity and Membrane Excitability in Mouse Medial Vestibular Nucleus Neurones," *Acta Otolaryngologica (Stockh) Suppl.*, vol. 520, pp. 101–104, 1995.

139. M. B. Dutia and A. R. Johnston, "Development of action potentials and apamin-sensitive after-potentials in mouse vestibular nucleus neurones," *Experimental Brain Research*, vol. 118, pp. 148–154, 1998.

140. L. Ris, M. Hachemaoui, N. Vibert, E. Godaux, P. P. Vidal, and L. E. Moore, "Resonance of spike discharge modulation in neurons of the guinea pig medial vestibular nucleus," *Journal of Neurophysiology*, vol. 86, no. 2, pp. 703–716, 2001.

141. S. du Lac and S. G. Lisberger, "Cellular Processing of Temporal Information in Medial Vestibular Nucleus Neurons," *Journal of Neuroscience*, vol. 15, no. 12, pp. 8000–8010, 1995.

142. M. Huterer and K. E. Cullen, "Vestibuloocular reflex dynamics during high-frequency and high-acceleration rotations of the Head on Body in Rhesus Monkey," *Journal of Neurophysiology*, vol. 88, pp. 13–28, 2002.

143. A. L. Babalian and P. P. Vidal, "Floccular Modulation of Vestibuloocular Pathways and Cerebellum-Related Plasticity: An In Vitro Whole Brain Study," *Journal of Neurophysiology*, vol. 84, no. 5, pp. 2514–2528, 2000.

144. C. Sekirnjak and S. du Lac, "Intrinsic firing dynamics of vestibular nucleus neurons," *Journal of Neuroscience*, vol. 22, no. 6, pp. 2083–2095, 2002.

145. M. J. E. Richardson, N. Brunel, and V. Hakim, "From subthreshold to firing-rate resonance," *Journal of Neurophysiology*, vol. 89, pp. 2538–2554, 2002.

146. B. Hutcheon and Y. Yarom, "Resonance, oscillation and the intrinsic frequency preferences of neurons," *Trends in Neurosciences*, vol. 23, pp. 216–222, 2000.

147. J. E. Roy and K. E. Cullen, "Dissociating self-generated from passively applied head motion: neural mechanisms in the vestibular nuclei," *Journal of Neuroscience*, vol. 24, no. 9, pp. 2102–2111, 2004.

148. A. Destexhe, M. Rudolph, J. M. Fellous, and T. J. Sejnowski, "Fluctuating synaptic conductances recreate in vivo-like activity in neocortical neurons," *Neuroscience*, vol. 107, no. 1, pp. 13–24, 2001.

149. A. Destexhe, M. Rudolph, and D. Paré, "The high-conductance state of neocortical neurons in vivo," *Nature Reviews Neuroscience*, vol. 4, pp. 739–751, Sept. 2003.

150. F. R. Fernandez and J. A. White, "Artificial Synaptic Conductances Reduce Subthreshold Oscillations and Periodic Firing in Stellate Cells of the Entorhinal Cortex," *Journal of Neuroscience*, vol. 28, no. 14, pp. 3790–3803, 2008.

151. B. Hutcheon, R. M. Miura, Y. Yarom, and E. Puil, "Low-threshold calcium current and resonance in thalamic neurons: a model of frequency preference," *Journal of Neurophysiology*, vol. 71, no. 2, p. 583, 1994.

152. M. Beraneck, S. Pfanzelt, I. Vassias, M. Rohregger, N. Vibert, P. P. Vidal, L. E. Moore, and H. Straka, "Differential Intrinsic Response Dynamics Determine Synaptic Signal Processing in Frog Vestibular Neurons," *Journal of Neuroscience*, vol. 27, pp. 4283–4296, Apr. 2007.

153. C. Ascoli, M. Barbi, S. Chillemi, and D. Petracchi, "Phase-locked Responses in the Limulus Lateral Eye. Theoretical and Experimental Investigation," *Biophysical Journal*, vol. 19, pp. 219–240, 1977.

154. A. Rescigno, R. B. Stein, R. L. Purple, and R. E. Poppele, "A neuronal model for the discharge patterns produced by cyclic inputs," *Bulletin of Mathematical Biophysics*, vol. 32, pp. 337–353, 1970.

155. R. B. Stein, A. S. French, and A. V. Holden, "The frequency response, coherence, and information capacity of two neuronal models," *Biophysical Journal*, vol. 12, pp. 295–322, 1972.

156. J. E. Roy and K. E. Cullen, "Selective processing of vestibular reafference during self-generated head motion," *Journal of Neuroscience*, vol. 21, no. 6, pp. 2131–2142, 2001.

157. J. E. Roy and K. E. Cullen, "Vestibuloocular reflex signal modulation during voluntary and passive head movements," *Journal of Neurophysiology*, vol. 87, no. 5, pp. 2337–2357, 2002.

158. J. E. Roy and K. E. Cullen, "Brain stem pursuit pathways: dissociating visual, vestibular, and proprioceptive inputs during combined eye-head gaze tracking," *Journal of Neurophysiology*, vol. 90, pp. 271–290, 2003.

159. S. G. Sadeghi, D. E. Mitchell, and K. E. Cullen, "Different neural strategies for multimodal integration: comparison of two macaque monkey species," *Experimental Brain Research*, vol. 195, pp. 45–57, 2009.

160. P. Sah, "Ca2+-activated K+ currents in neurones: types, physiological roles and modulation," *Trends in Neurosciences*, vol. 19, no. 4, pp. 150–154, 1996.

161. E. S. L. Faber and P. Sah, "Calcium-Activated Potassium Channels: Multiple Contributions to Neuronal Function," *The Neuroscientist*, vol. 9, pp. 181–194, 2003.

162. J. Benda and A. V. M. Herz, "A Universal Model for Spike-Frequency Adaptation," *Neural Computation*, vol. 15, pp. 2523–2564, 2003.

163. J. Benda, A. Longtin, and L. Maler, "Spike-Frequency Adaptation Separates Transient Communication Signals from Background Oscillations," *Journal of Neuroscience*, vol. 25, no. 9, pp. 2312–2321, 2005.

164. C. Rössert, H. Straka, S. Glasauer, and L. E. Moore, "Frequency-domain analysis of intrinsic neuronal properties using high-resistant electrodes," *frontiers in Neuroscience*, vol. 3, no. 64, pp. 1–12, 2009.

165. G. T. Gdowski and R. A. McCrea, "Integration of vestibular and head movement signals in the vestibular nuclei during whole-body rotation.," *Journal of Neurophysiology*, vol. 82, pp. 436–449, July 1999.

166. Y. Shinoda, T. Ohgaki, T. Futami, and Y. Sugiuchi, "Vestibular projections to the spinal cord: the morphology of single vestibulospinal axons," *Vestibulospinal Control of Posture and Locomotion, Elsevier*, vol. 76, pp. 17–27, 1988.

167. H. Meng, P. J. May, J. D. Dickman, and D. E. Angelaki, "Vestibular signals in primate thalamus: properties and origins," *Journal of Neuroscience*, vol. 27, no. 50, pp. 13590–13602, 2007.

168. V. Marlinski and R. A. McCrea, "Self-motion signals in vestibular nuclei neurons projecting to the thalamus in the alert squirrel monkey," *Journal of Neurophysiology*, vol. 101, pp. 1730–1741, 2009.

169. J. D. Dickman and D. E. Angelaki, "Dynamics of vestibular neurons during rotational motion in alert rhesus monkeys," *Experimental Brain Research*, vol. 155, pp. 91–101, 2004.

170. O. A. Akerberg and M. J. Chacron, "In vivo conditions influence the coding of stimulus features by bursts of action potentials," *Journal of Computational Neuroscience, DOI 10.1007/s10827-011-0313-4*, 2011.

171. F. Sato, H. Sasaki, N. Ishizuka, S. I. Sasaki, and H. Mannen, "Morphology of single primary vestibular afferents originating from the horizontal semicircular canal in the cat," *The Journal of Comparative Neurology*, vol. 290, pp. 423–439, 1989.

172. F. E. Hoebeek, J. S. Stahl, A. M. v. Alphen, M. Schonewille, C. Luo, M. Rutteman, A. M. J. M. v. d. Maagdenberg, P. C. Molenaar, H. H. L. M. Goossens,

M. A. Frens, and C. I. D. Zeeuw, "Increased noise level of Purkinje cell activities minimizes impact of their modulation during sensorimotor control," *Neuron*, vol. 45, pp. 953–965, 2005.

173. A. Destexhe and D. Paré, "Impact of Network Activity on the Integrative Properties of Neocortical Pyramidal Neurons In Vivo," *Journal of Neurophysiology*, vol. 81, pp. 1531–1547, 1999.

174. J. Wolfart, D. Debay, G. Le Masson, A. Destexhe, and T. Bal, "Synaptic background activity controls spike transfer from thalamus to cortex," *Nature Neuroscience*, vol. 8, no. 12, pp. 1760–1767, 2005.

175. N. Toporikova and M. J. Chacron, "SK channels gate information processing in vivo by regulating an intrinsic bursting mechanism seen in vitro," *Journal of Neurophysiology*, vol. 102, no. 4, pp. 2273–2287, 2009.

176. S. M. Sherman and R. W. Guillery, "The role of the thalamus in the flow of information to the cortex," *Philosophical Transactions of the Royal of London B*, vol. 357, pp. 1695–1708, 2002.

177. L. E. Moore, M. Hachemaoui, E. Idoux, N. Vibert, and P. P. Vidal, "The linear and non-linear relationships between action potential discharge rates and membrane potential in model vestibular neurons," *Nonlinear Studies*, vol. 11, no. 3, pp. 423–447, 2004.

178. T. M. Hospedales, M. C. W. v. Rossum, B. P. Graham, and M. B. Dutia, "Implications of noise and neural heterogeneity for vestibulo-ocular reflex fidelity," *Neural Computation*, vol. 20, no. 3, pp. 756–778, 2008.

179. A. Alonso and R. R. Llinás, "Subthreshold Na+-dependent theta-like rhythmicity in stellate cells of entorhinal cortex layer II," *Nature*, vol. 342, pp. 175–177, Nov. 1989.

180. L. M. Frank, E. N. Brown, and M. A. Wilson, "A Comparison of the Firing Properties of Putative Excitatory and Inhibitory Neurons from CA1 and the Entorhinal Cortex," *Journal of Neurophysiology*, vol. 86, pp. 2029–2040, 2001.

181. A. Longtin, "Stochastic resonance in neuron models," *Journal of Statistical Physics*, vol. 70, no. 1, pp. 309–327, 1993.

182. F. Moss, L. M. Ward, and W. G. Sannita, "Stochastic resonance and sensory information processing: a tutorial and review of application," *Clinical Neurophysiology*, vol. 115, pp. 267–281, 2004.

183. L. Gammaitoni, P. Hänggi, P. Jung, and F. Marchesoni, "Stochastic resonance," *Reviews of Modern Physics*, vol. 70, no. 1, pp. 0034–6861, 1998.

184. K. Wiesenfeld and F. Moss, "Stochastic resonance and the benefits of noise: from ice ages to crayfish and SQUIDs," *Nature*, vol. 373, pp. 33–36, 1995.

185. F. Jaramillo and K. Wiesenfeld, "Mechanoelectrical transduction assisted by Brownian motion: a role for noise in the auditory system," *Nature Neuroscience*, vol. 1, no. 5, pp. 384–388, 1998.

186. P. Cordo, J. T. Inglis, S. Verschueren, J. J. Collins, D. M. Merfeld, S. Rosenblum, S. Buckley, and F. Moss, "Noise in human muscle spindles," *Nature*, vol. 383, pp. 769–770, 1996.

187. M. Stemmler, "A single spike suffices: the simplest form of stochastic resonance in model neurons," *Network: Computation in Neural Systems*, vol. 7, pp. 1–30, Nov. 1996.

188. J. E. Rose, J. F. Brugge, D. J. Anderson, and J. E. Hind, "Phase-locked response to low-frequency tones in single auditory nerve fibers of the squirrel monkey," *Journal of Neurophysiology*, vol. 30, no. 4, pp. 769–793, 1967.

189. R. A. Lavine, "Phase-locking in response of single neurons in cochlear nucler complex of the cat to low-frequency tonal stimuli," *Journal of Neurophysiology*, vol. 34, no. 3, pp. 467–483, 1971.

190. G. Crow, A. L. Rupert, and G. Moushegian, "Phase locking in monaural and binaural medullary neurons: implications for binaural phenomena," *Journal of Acoustical Society of America*, vol. 64, no. 2, pp. 493–501, 1978.

191. A. R. Palmer and I. J. Russell, "Phase-locking in the cochlear nerve of the guinea-pig and its relation to the receptor potential of inner hair-cells," *Hearing research*, vol. 24, pp. 1–15, 1986.

192. S. B. C. Dynes and B. Delgutte, "Phase-locking of auditory-nerve discharges to sinusoidal electric stimulation of the cochlea," *Hearing research*, vol. 58, pp. 79–90, 1992.

193. C. Köppl, "Phase locking to high frequencies in the auditory nerve and cochlear nucleus magnocellularis of the barn owl, Tyto alba," *Journal of Neuroscience*, vol. 17, no. 9, pp. 3312–3321, 1997.

194. M. N. Wallace, T. M. Shackleton, and A. R. Palmer, "Phase-locked responses to pure tones in the primary auditory cortex," *Hearing research*, vol. 172, pp. 160–171, 2002.

195. A. N. Temchin and M. A. Ruggero, "Phase-locked responses to tones of chinchilla auditory nerve fibers: implications for apical cochlear mechanics," *Journal of the Association for Research in Otolaryngology : JARO*, vol. 11, pp. 297–318, June 2010.

196. F. S. Chance, L. F. Abbott, and A. D. Reyes, "Gain Modulation from Background Synaptic Input," *Neuron*, vol. 35, pp. 773–782, 2002.

197. R. W. Berg, A. Alaburda, and J. Hounsgaard, "Balanced Inhibition and Excitation Drive Spike Activity in Spinal Half-Centers," *Science (New York, NY)*, vol. 315, p. 390, 2007.

198. C. van Vreeswijk and H. Sompolinsky, "Chaos in neuronal networks with balanced excitatory and inhibitory activity," *Science (New York, NY)*, vol. 274, no. 5293, p. 1724, 1996.

199. E. Av-Ron, H. Parnas, and L. A. Segel, "A minimal biophysical model for an excitable and oscillatory neuron," *Biological Cybernetics*, vol. 65, pp. 487–500, 1991.

200. E. Av-Ron, H. Parnas, and L. A. Segel, "A basic biophysical model for bursting neurons," *Biological Cybernetics*, vol. 69, pp. 87–95, 1993.

201. A. Manwani and C. Koch, "Detecting and estimating signals in noisy cable structures, I: Neuronal noise sources," *Neural Computation*, vol. 11, no. 8, pp. 1797–1829, 1999.

202. P. E. Kloeden and E. Platen, "Numerical Solution of Stochastic Differential Equations," *Springer, Berlin*, 1999.

203. M. J. E. Richardson and W. Gerstner, "Synaptic shot noise and conductance fluctuations affect the membrane voltage with equal significance," *Neural Computation*, vol. 17, no. 4, pp. 923–947, 2005.

204. J. X. Brooks and K. E. Cullen, "Multimodal Integration in Rostral Fastigial Nucleus Provides an Estimate of Body Movement," *Journal of Neuroscience*, vol. 29, pp. 10499–10511, Aug. 2009.

205. Y. Kajikawa and T. A. Hackett, "Entropy analysis of neuronal spike train synchrony," *Journal of Neuroscience Methods*, vol. 149, pp. 90–93, 2005.

206. K. V. Mardia and P. E. Jupp, *Directional statistics*. Wiley, Chichester, 1999.

207. L. Badel, S. Lefort, R. Brette, C. C. H. Petersen, W. Gerstner, and M. J. E. Richardson, "Dynamic I-V Curves Are Reliable Predictors of Naturalistic Pyramidal-Neuron Voltage Traces," *Journal of Neurophysiology*, vol. 99, pp. 656–666, Feb. 2008.

208. N. Fourcaud-Trocmé, D. Hansel, C. van Vreeswijk, and N. Brunel, "How spike generation mechanisms determine the neuronal response to fluctuating inputs," *The Journal of Neuroscience*, vol. 23, no. 37, pp. 11628–11640, 2003.

209. L. Hertäg, J. Hass, T. Golovko, and D. Durstewitz, "An Approximation to the Adaptive Exponential Integrate-and-Fire Neuron Model Allows Fast and Predictive Fitting to Physiological Data.," *Frontiers in Computational Neuroscience*, vol. 6, p. 62, 2012.

210. R. Brette and W. Gerstner, "Adaptive exponential integrate-and-fire model as an effective description of Neuronal Activity," *Journal of Neurophysiology*, vol. 94, pp. 3637–3642, 2005.

211. R. Naud, N. Marcille, C. Clopath, and W. Gerstner, "Firing patterns in the adaptive exponential integrate-and-fire model," *Biological Cybernetics*, vol. 99, no. 4-5, pp. 335–347, 2008.

212. J. Touboul and R. Brette, "Dynamics and bifurcations of the adaptive exponential integrate-and-fire model," *Biological Cybernetics*, vol. 99, pp. 319–334, Nov. 2008.

213. E. Shlizerman and P. Holmes, "Neural dynamics, bifurcations, and firing rates in a quadratic integrate-and-fire model with a recovery variable. I: Deterministic behavior.," *Neural Computation*, vol. 24, pp. 2078–2118, Aug. 2012.

214. M. J. E. Richardson, "Dynamics of populations and networks of neurons with voltage-activated and calcium-activated currents," *Physical Review E*, vol. 80, no. 2, p. 021928, 2009.

215. L. Hertäg, D. Durstewitz, and N. Brunel, "Analytical approximations of the firing rate of an adaptive exponential integrate-and-fire neuron in the presence of synaptic noise," *Frontiers in Computational Neuroscience*, vol. 8, 2014.

216. T. Anastasio, "The fractional-order dynamics of brainstem vestibulo-oculomotor neurons," *Biological Cybernetics*, pp. 69–79, 1994.

217. J. Carriot, M. Jamali, J. X. Brooks, and K. E. Cullen, "Integration of Canal and Otolith Inputs by Central Vestibular Neurons Is Subadditive for Both Active and Passive Self-Motion: Implication for Perception," *The Journal of neuroscience : the official journal of the Society for Neuroscience*, vol. 35, pp. 3555–3565, Feb. 2015.

218. J. X. Brooks, J. Carriot, and K. E. Cullen, "Learning to expect the unexpected: rapid updating in primate cerebellum during voluntary self-motion," *Nature Neuroscience*, vol. 18, pp. 1310–1317, Aug. 2015.

219. M. Savard, R. Krahe, and M. J. Chacron, "Neural heterogeneities influence envelope and temporal coding at the sensory periphery," *Neuroscience*, vol. 172, pp. 270–284, Jan. 2011.

220. T. J. Lewis and J. Rinzel, "Dynamics of spiking neurons connected by both inhibitory and electrical coupling.," *Journal of Computational Neuroscience*, vol. 14, pp. 283–309, May 2003.

221. W. Bialek, *Biophysics: Searching for Principles*. Princeton University Press, Apr. 2012.

222. C. Machens, "Adaptive sampling by information maximization," *Physical Review Letters*, vol. 88, no. 22, pp. 2281041–2281044, 2002.

223. D. C. Van Essen, C. H. Anderson, and D. J. Felleman, "Information processing in the primate visual system: an integrated systems perspective.," *Science (New York, NY)*, vol. 255, pp. 419–423, Jan. 1992.

224. H. B. Barlow, "Single units and sensation: a neuron doctrine for perceptual psychology," *Perception*, vol. 1, pp. 371–394, 1972.

225. E. T. Rolls and M. J. Tovee, "Sparseness of the neuronal representation of stimuli in the primate temporal visual cortex," *Journal of Neurophysiology*, vol. 73, no. 2, pp. 713–726, 1995.

226. T. Hromádka, M. R. DeWeese, and A. M. Zador, "Sparse representation of sounds in the unanesthetized auditory cortex," *PLoS Biology*, vol. 6, no. 1, 2008.

227. D. Attwell and S. B. Laughlin, "An Energy Budget for Signaling in the Grey Matter of the Brain," *Journal of cerebral blood flow and metabolism : official journal of the International Society of Cerebral Blood Flow and Metabolism*, pp. 1133–1145, Oct. 2001.

228. F. P and M. Young, *Sparse Coding in the Primate Cortex*. The Handbook of brain theory and neural networks, Cambridge: MIT Press, Nov. 1995.

229. M. W. Bagnall, L. E. Mcelvain, M. Faulstich, and S. du Lac, "Frequency-independent synaptic transmission supports a linear vestibular behavior.," *Neuron*, vol. 60, pp. 343–352, Oct. 2008.

230. D. Robinson, "Adaptive gain control of vestibuloocular reflex by the cerebellum," *Journal of Neurophysiology*, vol. 39, no. 5, p. 954, 1976.

231. P. D. Pulaski, D. S. Zee, and D. A. Robinson, "The behavior of the vestibuloocular reflex at high velocities of head rotation.," *Brain Research*, pp. 159–165, Nov. 1981.

232. L. Minor, D. M. Lasker, D. D. Backous, and T. E. Hullar, "Horizontal vestibuloocular reflex evoked by high-acceleration rotations in the squirrel monkey. I. Normal responses," *Journal of Neurophysiology*, pp. 1254–1270, 1999.

233. M. J. Chacron, L. Maler, and J. Bastian, "Electroreceptor neuron dynamics shape information transmission," *Nature Neuroscience*, vol. 8, pp. 673–678, May 2005.

234. J. De La Rocha, B. Doiron, E. Shea-Brown, K. Josić, and A. Reyes, "Correlation between neural spike trains increases with firing rate.," *Nature*, vol. 448, pp. 802–806, Aug. 2007.

235. B. Ermentrout, "Linearization of FI curves by adaptation," *Neural Computation*, vol. 10, pp. 1721–1729, 1998.

236. B. Doiron, A. Longtin, N. Berman, and L. Maler, "Subtractive and divisive inhibition: effect of voltage-dependent inhibitory conductances and noise," *Neural Computation*, vol. 13, no. 1, pp. 227–248, 2001.

237. S. Musallam and R. D. Tomlinson, "Asymmetric integration recorded from vestibular-only cells in response to position transients," *Journal of Neurophysiology*, vol. 88, pp. 2104–2113, 2002.

238. S. D. Newlands, N. Lin, and M. Wei, "Response Linearity of Alert Monkey Non-Eye Movement Vestibular Nucleus Neurons During Sinusoidal Yaw Rotation," *Journal of Neurophysiology*, vol. 102, pp. 1388–1397, 2009.

239. D. M. Broussard, "Dynamics of glutamatergic synapses in the medial vestibular nucleus of the mouse.," *The European journal of neuroscience*, vol. 29, pp. 502–517, Feb. 2009.

240. A. Popratiloff and K. D. Peusner, "Otolith fibers and terminals in chick vestibular nuclei.," *The Journal of Comparative Neurology*, vol. 502, pp. 19–37, May 2007.

241. D. Malinvaud, I. Vassias, I. Reichenberger, C. Rossert, and H. Straka, "Functional Organization of Vestibular Commissural Connections in Frog," *Journal of Neuroscience*, vol. 30, p. 3310, Mar. 2010.

242. P. Wulff, M. Schonewille, M. Renzi, L. Viltono, M. Sassoè-Pognetto, A. Badura, Z. Gao, F. E. Hoebeek, S. van Dorp, W. Wisden, M. Farrant, and C. De Zeeuw, "Synaptic inhibition of Purkinje cells mediates consolidation of vestibulo-cerebellar motor learning," *Nature*, vol. 12, pp. 1042–1049, 2009.

243. G. Grossman, R. Leigh, L. Abel, D. Lanska, and S. Thurston, "Frequency and velocity of rotational head perturbations during locomotion," *Experimental Brain Research*, vol. 70, no. 3, pp. 470–476, 1988.

244. T. Pozzo, A. Berthoz, and L. Lefort, "Head stabilization during various locomotor tasks in humans. I. Normal subjects.," *Experimental brain research Experimentelle Hirnforschung Expérimentation cérébrale*, vol. 82, no. 1, pp. 97–106, 1990.

245. T. Pozzo, A. Berthoz, and L. Lefort, "Head stabilization during various locomotor tasks in humans," *Experimental Brain Research*, vol. 82, no. 1, pp. 97–106, 1990.

246. M. Armand and L. Minor, "Relationship between time-and frequency-domain analyses of angular head movements in the squirrel monkey," *Journal of Computational Neuroscience*, vol. 11, no. 3, pp. 217–239, 2001.

247. D. Field, "Relations between the statistics of natural images and the response properties of cortical cells," *J. Opt. Soc. Am. A*, vol. 4, no. 12, pp. 2379–2394, 1987.

248. G. J. Burton and I. R. Moorhead, "Color and spatial structure in natural scenes.," *Applied optics*, vol. 26, pp. 157–170, Jan. 1987.

249. D. J. Field and N. Brady, "Visual sensitivity, blur and the sources of variability in the amplitude spectra of natural scenes," *Vision Research*, vol. 37, pp. 3367–3383, Dec. 1997.

250. D. J. Graham, D. M. Chandler, and D. J. Field, "Can the theory of "whitening" explain the center-surround properties of retinal ganglion cell receptive fields?," *Vision Research*, vol. 46, pp. 2901–2913, Sept. 2006.

251. J. J. Atick and A. N. Redlich, "What does the retina know about natural scenes?," *Neural Computation*, pp. 196–210, 1992.

252. S. R. Simon, I. L. Paul, J. Mansour, M. Munro, P. J. Abernethy, and E. L. Radin, "Peak dynamic force in human gait," *Journal of Biomechanics*, vol. 14, pp. 817–822, Jan. 1981.

253. C. J. Dakin, B. L. Luu, K. van den Doel, J. T. Inglis, and J.-S. Blouin, "Frequency-specific modulation of vestibular-evoked sway responses in humans.," *Journal of Neurophysiology*, vol. 103, pp. 1048–1056, Feb. 2010.

254. J. S. Rothman, L. Cathala, V. Steuber, and R. A. Silver, "Synaptic depression enables neuronal gain control.," *Nature*, vol. 457, pp. 1015–1018, Feb. 2009.

255. L. Grabherr, K. Nicoucar, F. W. Mast, and D. M. Merfeld, "Vestibular thresholds for yaw rotation about an earth-vertical axis as a function of frequency.," *Experimental Brain Research*, vol. 186, pp. 677–681, Apr. 2008.

256. T. Okada, E. Grunfeld, J. Shallo-Hoffmann, and A. M. Bronstein, "Vestibular perception of angular velocity in normal subjects and in patients with congenital nystagmus.," *Brain*, vol. 122 (Pt 7), pp. 1293–1303, July 1999.

257. A. M. Bronstein, E. A. Grunfeld, M. Faldon, and T. Okada, "Reduced self-motion perception in patients with midline cerebellar lesions.," *NeuroReport*, vol. 19, pp. 691–693, Apr. 2008.

258. G. Bertolini, S. Ramat, J. Laurens, C. J. Bockisch, S. Marti, D. Straumann, and A. Palla, "Velocity storage contribution to vestibular self-motion perception in healthy human subjects.," *Journal of Neurophysiology*, vol. 105, pp. 209–223, Jan. 2011.

259. B. A. Olshausen and D. Field, "Sparse coding of sensory inputs," *Current opinion in neurobiology*, vol. 14, pp. 481–487, 2004.

260. W. E. Vinje and J. L. Gallant, "Sparse coding and decorrelation in primary visual cortex during natural vision.," *Science (New York, NY)*, vol. 287, pp. 1273–1276, Feb. 2000.

261. E. T. Carlson, R. J. Rasquinha, K. Zhang, and C. E. Connor, "A sparse object coding scheme in area V4.," *Current biology : CB*, vol. 21, pp. 288–293, Feb. 2011.

262. M. R. DeWeese, M. Wehr, and A. M. Zador, "Binary spiking in auditory cortex," *Journal of Neuroscience*, vol. 23, no. 21, pp. 7940–7949, 2003.

263. M. Brecht and B. Sakmann, "Dynamic representation of whisker deflection by synaptic potentials in spiny stellate and pyramidal cells in the barrels and septa of layer 4 rat somatosensory cortex.," *The Journal of Physiology*, vol. 543, pp. 49–70, Aug. 2002.

264. G. Laurent, "Olfactory network dynamics and the coding of multidimensional signals," *Nature Reviews Neuroscience*, vol. 3, pp. 884–895, Nov. 2002.

265. D. J. Heeger, "Normalization of cell responses in cat striate cortex.," *Visual neuroscience*, vol. 9, pp. 181–197, Aug. 1992.

266. O. Schwartz and E. Simoncelli, "Natural signal statistics and sensory gain control," *Nature Neuroscience*, vol. 4, no. 8, pp. 1–11, 2001.

267. S. R. Olsen, V. Bhandawat, and R. I. Wilson, "Divisive Normalization in Olfactory Population Codes," *Neuron*, vol. 66, pp. 287–299, Apr. 2010.

268. M. Carandini and D. J. Heeger, "Normalization as a canonical neural computation," *Nature Reviews Neuroscience*, pp. 1–12, Nov. 2011.

269. A. Gutschalk, C. Micheyl, and A. J. Oxenham, "Neural correlates of auditory perceptual awareness under informational masking.," *PLoS Biology*, vol. 6, p. e138, June 2008.

270. J. C. Makous, R. M. Friedman, and C. J. Vierck, "A critical band filter in touch.," *The Journal of Neuroscience*, vol. 15, pp. 2808–2818, Apr. 1995.

271. M. Chacron, B. Doiron, L. Maler, A. Longtin, and J. Bastian, "Non-classical receptive field mediates switch in a sensory neuron's frequency tuning," *Nature*, vol. 423, pp. 77–81, 2003.

272. P. A. Sylvestre and K. E. Cullen, "Quantitative analysis of abducens neuron discharge dynamics during saccadic and slow eye movements," *Journal of Neurophysiology*, vol. 82, pp. 2612–2632, Nov. 1999.

273. S. G. Sadeghi, L. B. Minor, and K. E. Cullen, "Dynamics of the horizontal vestibuloocular reflex after unilateral labyrinthectomy: response to high frequency, high acceleration, and high velocity rotations.," *Experimental brain research Experimentelle Hirnforschung Expérimentation cérébrale*, vol. 175, pp. 471–484, Nov. 2006.

274. K. E. Cullen and L. B. Minor, "Semicircular canal afferents similarly encode active and passive head-on-body rotations: implications for the role of vestibular efference.," *The Journal of neuroscience : the official journal of the Society for Neuroscience*, vol. 22, p. RC226, June 2002.

275. A. Haque, D. E. Angelaki, and J. D. Dickman, "Spatial tuning and dynamics of vestibular semicircular canal afferents in rhesus monkeys.," *Experimental brain research Experimentelle Hirnforschung Expérimentation cérébrale*, vol. 155, pp. 81–90, Mar. 2004.

276. F. Duensing and K. Schaefer, "The activity of ngle neurons in the region of the vestibular nuclei in horizontal acceleration, with special reference to vestibular nystagmus.," *Arch Psychiatr Nervenkr Z Gesamte Neurol Psychiatr*, pp. 225–252, June 1958.

277. S. Cherif, K. Cullen, and H. Galiana, "An improved method for the estimation of firing rate dynamics using an optimal digital filter," *Journal of Neuroscience Methods*, vol. 173, pp. 165–181, Aug. 2008.

278. A. Oppenheim and R. Schafer, *Discrete-time Signal Processing*. Englewood Cliffs, NJ: Prentice Hall., June 1989.

279. M. Jarvis and P. Mitra, "Sampling properties of the spectrum and coherency of sequences of action potentials," *Neural Computation*, vol. 13, no. 4, pp. 717–749, 2001.

280. B. Lindner, D. Gangloff, A. Longtin, and J. E. Lewis, "Broadband coding with dynamic synapses.," *The Journal of neuroscience : the official journal of the Society for Neuroscience*, vol. 29, pp. 2076–2088, Feb. 2009.

281. S. G. Sadeghi, L. B. Minor, and K. E. Cullen, "Multimodal integration after unilateral labyrinthine lesion: single vestibular nuclei neuron responses and implications for postural compensation.," *Journal of Neurophysiology*, vol. 105, pp. 661–673, Feb. 2011.

282. L. B. Minor and J. M. Goldberg, "Vestibular-nerve inputs to the vestibulo-ocular reflex: a functional-ablation study in the squirrel monkey.," *The Journal of Neuroscience*, vol. 11, pp. 1636–1648, June 1991.

283. D. M. Lasker, G. C. Han, H. J. Park, and L. B. Minor, "Rotational responses of vestibular-nerve afferents innervating the semicircular canals in the C57BL/6 mouse.," *Journal of the Association for Research in Otolaryngology : JARO*, vol. 9, pp. 334–348, Sept. 2008.

284. M. J. Chacron, "Nonlinear Information Processing in a Model Sensory System," *Journal of Neurophysiology*, vol. 95, pp. 2933–2946, Jan. 2006.

285. R. Krahe, J. Bastian, and M. J. Chacron, "Temporal Processing Across Multiple Topographic Maps in the Electrosensory System," *Journal of Neurophysiology*, vol. 100, pp. 852–867, June 2008.

286. G. Marsat and G. S. Pollack, "Effect of the Temporal Pattern of Contralateral Inhibition on Sound Localization Cues," *Journal of Neuroscience*, vol. 25, pp. 6137–6144, June 2005.

287. J. W. Middleton, A. Longtin, J. Benda, and L. Maler, "Postsynaptic Receptive Field Size and Spike Threshold Determine Encoding of High-Frequency

Information Via Sensitivity to Synchronous Presynaptic Activity," *Journal of Neurophysiology*, vol. 101, pp. 1160–1170, Mar. 2009.

288. L. M. Jones, "Robust Temporal Coding in the Trigeminal System," *Science (New York, NY)*, vol. 304, pp. 1986–1989, June 2004.